

# **Properties of the Host Galaxies of Type Ia Supernovae in the SDSS-II Supernova Survey**

by

**Mathew Smith**

THE THESIS IS SUBMITTED IN PARTIAL FULFILMENT OF THE REQUIREMENTS FOR  
THE AWARD OF THE DEGREE OF  
DOCTOR OF PHILOSOPHY  
OF THE  
UNIVERSITY OF PORTSMOUTH

October, 2008

# Copyright

© Copyright 2008 by **Mathew Smith**. All rights reserved.

The copyright of this thesis rests with the Author. Copies (by any means) either in full, or of extracts, may not be made without the prior written consent from the Author.

*“I exist just to make you happy”*

# Abstract

This thesis presents new measurements of the properties of type Ia supernovae. For this, I use data collected from the first two years of the SDSS-II Supernova Survey, which carried out a photometric search for supernovae for three months (Sept. - Nov.) of 2005 to 2007. Overall,  $\simeq 500$  type Ia events were spectroscopically confirmed with densely sampled (approximately once every 4 days) multi-colour light-curves in the redshift range  $0 < z < 0.4$ . The survey also discovered several hundred type Ia events with well-measured light-curves that do not have a spectroscopic observation. In this thesis, I shall present the search pipelines and algorithms used to carry out this survey, with special attention to the spectroscopic follow-up activities.

Starting with a sample of 15,000 transient objects discovered by the SDSS-II Supernova Survey, I make numerous cuts in the data to obtain a complete sample of type Ia supernovae that is free of selection bias. I also determine the efficiency of the survey as a function of redshift. Using this sample, and the measured efficiency function, I determine the volumetric type Ia supernova rate to be  $r_V = 2.24 \pm 0.49 \times 10^{-5} \text{ SNe yr}^{-1} \text{ Mpc}^{-3} h_{70}^3$  in the redshift range  $z < 0.12$  assuming a flat cosmology with  $\Omega_M = 0.3, \Omega_\Lambda = 0.7$  and  $H_0 = 70 \text{ km s}^{-1} \text{ Mpc}^{-1}$ .

The main focus of this thesis is the host galaxy properties of the type Ia events. These allow us to constrain the type Ia progenitor system and investigate the diversity in the type Ia population. We find that the rate of type Ia supernovae is lower in passive galaxies than galaxies with recent star-formation activity. Further to this, we find that a supernova rate purely dependent on the stellar mass of the host galaxy is ruled out, and another component is required. We obtain a better fit for “two-component” model, with one “delayed” component dependent on the stellar mass, and one “prompt” component proportional to the level of star-formation activity. However, a gradient of unity for the “delayed” component, is not favoured, as found in the literature, and a better fit is  $\text{SNR}_{\text{Ia}} = A \times M^{\frac{1}{2}} + B \times \text{SFR}$ , where  $M$  is the stellar mass of the and  $\text{SFR}$  is the current star-formation rate.

A “two-component” model for the type Ia supernova rate indicates that the observed properties of type Ia supernovae are related to their host galaxy. We consider the photometric properties of the type Ia population, and find significant evidence that the distribution of the “stretch” parameter is different for type Ia events that occur in passive galaxies when compared to star-forming galaxies. This is in agreement with results in the literature. We find that the brightest events are seen in star-forming galaxies. There is no indication that the extinction distribution of type Ia’s is related to the host galaxy type, suggesting that the dust content of the host galaxy maybe a sub-dominant component to this parameter.

Finally, we consider residuals from the best fit cosmology to the Hubble diagram. We find, with a high level of significance, that the mean residual offset from the best-fit is different for supernovae in passive galaxies when compared to star-forming galaxies; with the “passive supernovae” appearing brighter than would be expected from the best fit cosmological model. This is shown to be partially dependent on the extinction prior chosen in the light-curve fitting, with these “passive supernovae” requiring a different prior than star-forming events. We find some evidence that supernovae in passive galaxies are less scattered about the best-fit cosmology than those in star-forming events, but the result is dependent on the details of the sample selection.

Overall, the results in this thesis confirm there is a diversity in the type Ia population, but we have not yet fully understood it.

# Preface

The work in this thesis was carried out at the [Institute of Cosmology and Gravitation](#), University of Portsmouth, United Kingdom, and was carried out in collaboration with the SDSS-II Supernova Survey, of which I am a collaboration member (see [Frieman et al. \(2008a\)](#) for details).

The results of Chapter [3](#) were obtained in collaboration with Dr. Benjamin Dilday, while the results of Chapter [7](#) were obtained in collaboration with Dr. Hubert Lampeitl.

# Acknowledgements

I would like to thank my supervisor Prof. R. C. Nichol for his guidance, patience and support during my PhD, and all members of the Institute of Cosmology and Gravitation (both past and present) for their help and encouragement.

Special thanks goes to Kishore Ananda, Frederico Arroja, Steven Bamford, Iain Brown, Chris Clarkson, Jim Cresswell, Edd Edmondson, Tomasso Giannantonio, Ben Hoyle, Hubert Lampeitl, Elisabetta Majerotto, Kelly Nock, Janine Pforr, Cristiano Sabiu, Fabio Silva, Mehri Torki and, of course Prina Patel.

All of this of course would not be possible without the presence Maria Soledad Caceres Merino, Deirdre, Adam, Rosemary and Seb in my life.

Funding for the SDSS and SDSS-II was provided by the Alfred P. Sloan Foundation, the Participating Institutions, the National Science Foundation, the U.S. Department of Energy, the National Aeronautics and Space Administration, the Japanese Monbukagakusho, the Max Planck Society, and the Higher Education Funding Council for England.

The SDSS was managed by the Astrophysical Research Consortium for the Participating Institutions. The Participating Institutions were the American Museum of Natural History, Astrophysical Institute Potsdam, University of Basel, Cambridge University, Case Western Reserve University, University of Chicago, Drexel University, Fermilab, the Institute for Advanced Study, the Japan Participation Group, Johns Hopkins University, the Joint Institute for Nuclear Astrophysics, the Kavli Institute for Particle Astrophysics and Cosmology, the Korean Scientist Group, the Chinese Academy of Sciences (LAMOST), Los Alamos National Laboratory, the Max-Planck-Institute for Astronomy (MPIA), the Max-Planck-Institute for Astrophysics (MPA), New Mexico State University, Ohio State University, University of Pittsburgh, University of Portsmouth, Princeton University, the United States Naval Observatory, and the University of Washington.

# Table of Contents

<b>Abstract</b>	<b>iii</b>
<b>Preface</b>	<b>v</b>
<b>Acknowledgements</b>	<b>vi</b>
<b>1 Introduction</b>	<b>1</b>
1.1 The Standard Model of Cosmology . . . . .	1
1.1.1 The Cosmological Model and the Friedmann Equations . . . . .	1
1.1.2 The Contents of the Universe . . . . .	4
1.1.3 Distances in Cosmology . . . . .	6
1.2 Supernovae - Definitions and Classifications . . . . .	8
1.2.1 Spectral Classification of Supernovae . . . . .	9
1.2.2 The Light-Curves of Type Ia Events . . . . .	11
1.3 The Physics of Type Ia Supernovae . . . . .	14
1.4 Type Ia Supernova Surveys . . . . .	16
1.4.1 Dark Energy . . . . .	16
1.5 Measurements of Type Ia Supernova Diversity and the Supernova rate . . . . .	21
1.5.1 The Type Ia Supernova Rate . . . . .	21
1.5.2 The Type Ia Population . . . . .	23
1.6 Description of this Work . . . . .	27
<b>2 The SDSS-II Supernova Survey</b>	<b>28</b>
2.1 Survey Aims and Description . . . . .	28
2.1.1 Survey Aims . . . . .	28
2.1.2 Technical Summary of the SDSS-II Survey . . . . .	30
2.2 Survey Observations . . . . .	32
2.2.1 Stripe 82 . . . . .	32
2.2.2 The Search Pipeline . . . . .	32
2.2.3 Spectroscopic Follow-up . . . . .	40

2.2.4	Final Photometry . . . . .	45
2.3	Results from the SDSS-II Supernova Survey . . . . .	47
<b>3</b>	<b>The Complete SDSS-II Supernova Survey Sample</b>	<b>53</b>
3.1	Introduction . . . . .	53
3.2	Correcting for Incompleteness . . . . .	55
3.2.1	The Bayesian Light-Curve Fitter . . . . .	56
3.2.2	The Search Photometry Criteria . . . . .	56
3.2.3	MLCS . . . . .	58
3.2.4	The SMP Selection Criteria . . . . .	64
3.2.5	The “Complete” Sample . . . . .	66
3.3	Estimating Survey Efficiency . . . . .	76
3.3.1	Artificial Images . . . . .	76
3.3.2	Monte-Carlo Simulations . . . . .	77
3.4	The Volumetric Type Ia Supernova Rate . . . . .	80
3.5	Summary . . . . .	84
<b>4</b>	<b>Derived Properties of the Complete Supernova Sample</b>	<b>86</b>
4.1	Introduction . . . . .	86
4.2	Galaxy Data . . . . .	87
4.3	Determining the Supernova Host Galaxies . . . . .	88
4.4	Determining the Properties of the Host Galaxies . . . . .	89
4.4.1	Fitting Spectral Energy Distributions to Galaxy Data . . . . .	89
4.4.2	Derived Properties . . . . .	93
4.5	The Comparison Field Sample . . . . .	97
4.5.1	Derived Properties of the Comparison Field Sample . . . . .	97
4.6	Incompleteness of the Field Sample . . . . .	98
4.7	Systematic Uncertainties . . . . .	99
4.8	Details of the Galaxies in our Sample . . . . .	101
<b>5</b>	<b>Host Properties of Type Ia Supernovae</b>	<b>105</b>
5.1	Introduction . . . . .	105
5.2	The Mass and Star-Formation Rate Distribution of Supernova Ia Hosts . . . . .	106
5.2.1	The Colour-Magnitude Distribution of Type Ia Hosts . . . . .	107
5.3	The Type Ia Supernova Rate as a Function of Galaxy Type . . . . .	109
5.3.1	The Effect of Our Selection Criteria and Various Cuts on the Passive Rate . . . . .	115
5.3.2	The Effect of SED errors on the Passive Rate . . . . .	116
5.4	The Supernova Ia Rate as a Function of Host Galaxy Mass . . . . .	121

5.4.1	The Effect of Our Selection Criteria and Various Cuts on these Results . . . . .	124
5.4.2	Estimating the Errors on these Measurements . . . . .	125
5.5	The “A+B” Model . . . . .	135
5.6	The Supernova Ia Rate as a Function of Host Galaxy Star Formation Rate	139
5.6.1	The Effect of Our Selection Criteria and Various Cuts on these Results . . . . .	144
5.6.2	Estimating Errors . . . . .	144
5.7	Bivariate Fit . . . . .	147
5.8	Comparison to Other Results . . . . .	153
<b>6</b>	<b>Supernova Properties as a Function of Host Galaxy Properties</b>	<b>156</b>
6.1	Introduction . . . . .	156
6.2	Investigating the Light-Curve Decline Rate as a Function of Host Galaxy Type . . . . .	158
6.2.1	The Delta Distribution of Type Ia Supernovae . . . . .	159
6.2.2	The $x_1$ and stretch distributions of Type Ia Supernovae . . . . .	162
6.2.3	Summary . . . . .	169
6.3	Extinction and Colour in the Supernova . . . . .	172
6.3.1	The $A_V$ distribution of type Ia SNe . . . . .	172
6.3.2	The Colour Correction of type Ia SNe . . . . .	175
6.3.3	Summary . . . . .	177
6.4	The Effect of the $A_V$ Prior on the Results . . . . .	178
6.4.1	Using a Flat $A_V$ Prior . . . . .	178
6.4.2	Using No $A_V$ Prior . . . . .	182
6.4.3	Summary . . . . .	187
6.5	The Effect of the cuts . . . . .	187
6.6	Comparison with other results . . . . .	188
6.7	Conclusions . . . . .	190
<b>7</b>	<b>Effect of Host Galaxy Properties on the Hubble Diagram</b>	<b>194</b>
7.1	Introduction . . . . .	194
7.2	Sample Selection . . . . .	195
7.3	Hubble Diagram for Confirmed Events . . . . .	197
7.4	Hubble Diagram for Events with a Spectroscopic Redshift . . . . .	202
7.5	Altering the $A_V$ Distribution for Passive Galaxies . . . . .	205
7.6	Comparison to SALT2 . . . . .	206
7.6.1	SALT2 Analysis for Confirmed Events . . . . .	211

7.6.2	SALT2 Analysis for Objects with a Spectroscopic Redshift . . . .	215
7.7	Conclusions . . . . .	218
<b>8</b>	<b>Conclusions</b>	<b>221</b>
8.1	The Type I Supernova Rate . . . . .	221
8.1.1	The Volumetric Type Ia Supernova Rate . . . . .	221
8.1.2	The Type Ia Supernova Rate as a Function of Host Galaxy Prop- erties . . . . .	222
8.2	Photometric Properties of Type Ia Supernovae . . . . .	223
8.3	Hubble Diagram Residuals . . . . .	224
8.4	Future Work . . . . .	225
<b>A</b>	<b>The Accuracy of the Photometric Redshift estimates for the Host Sample</b>	<b>227</b>
<b>B</b>	<b>Comparison of the Derived Measurements from PÉGASE.2 with Other Mea- surements</b>	<b>232</b>
B.1	Introduction . . . . .	232
B.2	The Mass Estimates . . . . .	233
B.3	The Star-Formation Rate Estimates . . . . .	233
<b>C</b>	<b>The Differences in Derived Properties when the Redshift is Known Com- pared to When it is Left Free</b>	<b>240</b>
C.1	Introduction . . . . .	240
C.2	Differences . . . . .	241
C.3	Summary . . . . .	245
<b>D</b>	<b>The Influence on the Rest-Wavelength Coverage of the SDSS Filter Bands</b>	<b>248</b>
D.1	Introduction . . . . .	248
D.2	The GALEX survey . . . . .	249
D.3	The Difference Between Six and Five Filters . . . . .	250
D.4	Summary . . . . .	250
<b>E</b>	<b>Other SED Templates</b>	<b>254</b>
E.1	The Maraston Galaxy Templates . . . . .	254
E.2	Analysis of the Maraston Models . . . . .	255
E.2.1	The Difference Between the PEGASE and Maraston Models as a Function of Apparent Magnitude . . . . .	255
<b>F</b>	<b>The Effect of the Observed Offset</b>	<b>260</b>

<b>G List of Supernovae</b>	<b>263</b>
<b>H Properties of the Host Galaxies in this Analysis</b>	<b>271</b>
<b>References</b>	<b>287</b>

# List of Tables

3.1	The number of candidates that pass the selection criteria at various stages as discussed in §2.2.2, §3.2.2 and §3.2.4 . . . . .	69
3.2	Values of the volumetric type Ia supernova rate for different values of the maximum redshifts considered. . . . .	84
4.1	The eight PÉGASE scenarios used for our SED fitting process. . . . .	94
5.1	Distribution of Objects in the Final Sample . . . . .	107
5.2	Values of the Passive Rate for Various Samples . . . . .	114
5.3	Values of Passive Rate with Systematics . . . . .	117
5.4	Values of the Gaussian standard deviation for the four systematic tests described in §5.3.2 . . . . .	120
5.5	Values of how the supenova rate varies as a function of host galaxy mass with Systematics . . . . .	127
5.6	Values of the Gaussian centres and standard deviations for the parameters described in §5.4 for the four systematic tests described in §5.4.2 . . . . .	127
5.7	Values on how the parameters described in §5.6 change with systematic tests . . . . .	145
5.8	Values of the Gaussian centres for the parameters described in §5.6 for the four systematic tests described in §5.6.2 . . . . .	148
6.1	Gaussian parameters for the MLCS2k2 $\Delta$ parameter . . . . .	159
6.2	Gaussian parameters for the SALT2 $x_1$ parameter . . . . .	164
6.3	Gaussian parameters for the SALT2 stretch parameter when converted from the SALT2 $x_1$ parameter . . . . .	166
6.4	Gaussian parameters for the SALT2 $x_1$ parameter when converted from the MLCS2k2 $\Delta$ parameter using a low redshift approximation . . . . .	169
6.5	Gaussian parameters for the SALT2 stretch parameter when converted from the MLCS2k2 $\Delta$ parameter using a low redshift approximation . . . . .	170
6.6	Gaussian parameters for the MLCS2k2 $A_v$ parameter . . . . .	173
6.7	Gaussian parameters for the SALT2 colour parameter . . . . .	177

6.8	Gaussian parameters for the MLCS $A_V$ parameter when a Flat $A_V$ prior is used in the light-curve fitting procedure . . . . .	179
6.9	Gaussian parameters for the MLCS $\Delta$ parameter when a Flat $A_V$ prior is used in the light-curve fitting procedure . . . . .	180
6.10	Test statistics for the MLCS $\Delta$ and $A_V$ parameters when a Flat $A_V$ prior is used . . . . .	182
6.11	Gaussian parameters for the MLCS $A_V$ parameter when No $A_V$ prior is used in the light-curve fitting procedure . . . . .	183
6.12	Gaussian parameters for the MLCS $\Delta$ parameter when No $A_V$ prior is used in the light-curve fitting procedure . . . . .	184
6.13	Test statistics for the MLCS $\Delta$ and $A_V$ parameters when No $A_V$ prior is used . . . . .	186
6.14	Gaussian outputs for various parameters when only objects with a spectroscopic redshift are considered . . . . .	189
6.15	Gaussian outputs for various parameters when only spectroscopically confirmed objects are considered . . . . .	189
6.16	Test statistics for various parameters when only objects with a spectroscopic redshift are considered . . . . .	189
6.17	Test statistics for various parameters when only spectroscopically confirmed objects are considered . . . . .	190
7.1	The distribution of objects that pass our cosmological fit, and selection criteria described §3.2.4 and §3.2.2, as a function of host galaxy type for both the low and high redshift samples. . . . .	199
7.2	Gaussian fitting parameters for the three distributions shown in Figure 7.2. The values for the complete dataset ( $0 < z < 0.5$ ), and that of a low redshift cut-off, ( $0 < z < 0.25$ ) are given. . . . .	199
7.3	K-S and A-D test statistics for the residuals from the best-fit cosmology to the Hubble diagram (shown in Figure 7.2). . . . .	201
7.4	Gaussian fitting parameters for the three distributions shown in Figure 7.2. The values for the complete dataset ( $0 < z < 0.5$ ) and a low redshift, ( $0 < z < 0.25$ ) are given. . . . .	204
7.5	K-S and A-D test statistics for the residuals from the best-fit to the Hubble diagram (shown in Figure 7.2). . . . .	204
7.6	Gaussian fitting parameters for the three distributions shown in Figure 7.6. These objects have been fitted with a standard $A_V$ prior for star-forming objects, and a steeper exponential for passive galaxies. . . . .	209

7.7	K-S and A-D test statistics for the residuals from the best-fit to the Hubble diagram (shown in Figure 7.6). These objects have been fitted with a standard $A_V$ prior for star-forming objects, and a steep exponential for passive galaxies. . . . .	210
7.8	Gaussian fitting parameters for the three distributions shown in Figure 7.8. The values for the complete dataset ( $0 < z < 0.5$ ), and that of a low redshift cut-off, ( $0 < z < 0.25$ ) are given. . . . .	214
7.9	K-S and A-D test statistics for the residuals from the best-fit cosmology to the Hubble diagram (shown in Figure 7.8) for the SALT2 light-curve fitter. . . . .	216
7.10	Gaussian fitting parameters for the three distributions shown in Figure 7.10. The values for the complete dataset ( $0 < z < 0.5$ ), and that of a low redshift cut-off, ( $0 < z < 0.25$ ) are given. . . . .	217
7.11	K-S and A-D test statistics for the residuals from the best-fit cosmology to the Hubble diagram (shown in Figure 7.10) for the SALT2 light-curve fitter. . . . .	220
F.1	Values for the parameters described in this work when different comparison field samples are considered. . . . .	262
G.1	List of objects passing the selection criteria described in §3.2 . . . . .	270
H.1	List of galaxies and their derived properties including Mass, SFR and sSFR. . . . .	287

# List of Figures

1.1	Spectra of type Ia supernovae, 1998aq, 1999aa and 1999by at $B$ -band maximum. This figure is from <a href="#">Matheson et al. (2008)</a> . . . . .	10
1.2	Spectra of the ‘branch normal’ type Ia supernovae, 1998bu. The figure shows the observed spectral evolution of this event and is from <a href="#">Matheson et al. (2008)</a> . . . . .	12
1.3	Uncorrected type Ia light-curves for a sample of nearby events. The figure is re-printed from <a href="#">Hamuy et al. (1996d)</a> . . . . .	13
1.4	Hubble Diagram of type Ia supernovae as measured by the SCP and HzSST. The bottom panel shows the residuals from an open Universe with $\Omega_M = 0.3$ . This figure is taken from <a href="#">Frieman et al. (2008b)</a> . . . . .	17
1.5	Current measurement of the Hubble diagram of type Ia supernovae. This figure is taken from <a href="#">Kowalski et al. (2008)</a> . . . . .	19
1.6	Current constraints of the cosmological parameters, $\omega$ and $\Omega_M$ . This figure is taken from <a href="#">Kowalski et al. (2008)</a> . . . . .	20
1.7	The velocity gradient and $\mathcal{R}(\text{SiII})$ compared to the light-curve decline rate parameter for a set of low redshift supernovae. . . . .	25
2.1	Measured SDSS filter response functions shown at an airmass of 1.3. . . . .	31
2.2	Right ascension versus epoch for the southern half of “stripe 82” during the 2006 observing season of the SDSS-II Supernova Survey . . . . .	33
2.3	The number of imaging scans on the northern and southern strips for the 2005 and 2006 observing seasons of the SDSS-II Supernova Survey . . . . .	34
2.4	Example on the handscanning webpage interface . . . . .	38
2.5	Example of a reduced spectra of a type Ia supernova from the 2007 season of observations at the NTT. Overplotted is an example template spectra. . . . .	44
2.6	Example of a reduced spectra of a type Ia supernova from the 2007 season of observations at the WHT. Overplotted is an example template spectra. . . . .	46
2.7	Histogram of the number of epochs of photometry for the SDSS-II supernova survey’s first two years of observations. . . . .	48

2.8	Multi-colour ( <i>gri</i> ) light curves for three spectroscopically confirmed type Ia supernova, one at low redshift, one at intermediate redshift and one at high redshift. . . . .	49
2.9	Redshift histogram describing the distribution of objects for each of the three years of observations for the SDSS-II supernova survey. . . . .	51
2.10	The 327 spectroscopically confirmed type Ia events from the 2005 and 2006 seasons of the SDSS-II Supernova Survey. . . . .	52
3.1	The number of objects that have been spectroscopically confirmed as type Ia events, have a host galaxy redshift or have no spectral information as a function redshift for objects passing the criteria described in §3.2.4. . . .	69
3.2	The difference between the spectroscopic redshift for the 188 objects in the sample described above and the redshift obtained from the best-fit MLCS light-curve template as a function of redshift. Also shown are the 131 objects which are spectroscopically confirmed to be type Ia events. . .	71
3.3	A histogram of the difference between the spectroscopic redshift for the 188 objects and the redshift obtained from the best-fit MLCS light-curve template as a function of redshift. Also shown are the 131 objects which are spectroscopically confirmed to be type Ia events. . . . .	72
3.4	A representative light-curve of an object in the sample of 246 objects listed in Table G.1. This object has been spectroscopically confirmed as a type Ia event. The <i>gri</i> light-curves are shown along with the best-fit template from the MLCS2k2 light-curve fitter. . . . .	73
3.5	A representative light-curve of an object in the sample of 246 objects listed in Table G.1. This object has not been spectroscopically confirmed as a type Ia event. Instead this object has a light-curve that passes the cuts described in §3.2.4 and has a spectroscopic redshift for it's host galaxy candidate. The <i>gri</i> light-curves are shown along with the best-fit template from the MLCS2k2 light-curve fitter. . . . .	74
3.6	A representative light-curve of an object in the sample of 246 objects listed in Table G.1. This object has not been spectroscopically confirmed as a type Ia event. Instead this object has a light-curve that passes the cuts described in §3.2.4, but does not have a spectroscopic redshift for it's host galaxy. Thus the redshift described in Table G.1 is that determined from the shown fit. The <i>gri</i> light-curves are shown along with the best-fit template from the MLCS2k2 light-curve fitter. . . . .	75
3.7	The survey efficiency for the 2005 season. Plotted are the overall efficiency, the detection efficiency and the effect of the selection cuts described in §3.2 and §3.3. . . . .	81

3.8	The survey efficiency for the 2005 season. Plotted are the overall efficiency, the detection efficiency and the effect of the selection cuts described in §3.2 and §3.3. . . . .	82
3.9	The type Ia supernova volumetric rate as a function of redshift. . . . .	85
4.1	Example spectra of four different galaxy types from the PÉGASE.2 spectral library, as described in Table 4.1. Spectra of observed galaxies (Kennicutt (1992)) are overplotted. This figure is taken from Fioc & Rocca-Volmerange (1997). . . . .	92
4.2	The relationship between host galaxy stellar mass (as derived from the PÉGASE.2 SED's) and $r$ -band absolute magnitude. . . . .	94
4.3	Histogram showing the relationship between the $u - r$ absolute colour and the host galaxy star-formation rate as derived from the template fitting method described in §4.4.1. Galaxies with no ongoing star-formation activity are plotted in red, whilst those with current star-formation are plotted in blue (for highly star-forming objects) and green (for moderately star-forming objects). . . . .	96
4.4	The normalised distributions of best-fit PÉGASE.2 SEDs for the field sample in our redshift range of interest (plotted in blue) and host galaxy sample (plotted in red). . . . .	103
5.1	The distributions of objects used in this analysis in the stellar mass versus star-formation rate plane. Passive galaxies are plotted for effect. . . . .	108
5.2	Colour-magnitude diagram for host galaxies used in this analysis separated by host galaxy type, as defined in §5.2 . . . . .	110
5.3	Colour-magnitude diagram for host galaxies used in this analysis separated by host galaxy type, as defined in §5.2. Shown separately are objects with very low values of sSFR, which are not classified as passive in nature . . . . .	111
5.4	The star-formation rates of objects with very low sSFR as highlighted in §5.2 and §5.2.1. Also plotted are all objects with current star-formation activity . . . . .	112
5.5	The type Ia supernova rate per unit stellar mass per year as a function of sSFR . . . . .	114
5.6	The type Ia supernova rate per unit mass per year for 10,000 Bootstrap realisations of the SDSS-II sample described in §4.8 . . . . .	120
5.7	The type Ia supernova rate per galaxy year as a function of host galaxy mass. The host galaxy sample is split into the three galaxy types, as described in §5.2. . . . .	122

5.8	The value of $n_{\text{mass}}$ for passive galaxies for the sample used in this analysis when 10,000 bootstrap realisations of the data are made without splitting the sample in advance. A best-fit Gaussian function is overplotted. . . . .	129
5.9	The value of $n_{\text{mod}}$ for moderately star-forming galaxies for the sample used in this analysis when 10,000 bootstrap realisations of the data are made without splitting the sample in advance. A best-fit Gaussian function is overplotted. . . . .	130
5.10	The value of $n_{\text{high}}$ for highly star-forming galaxies for the sample used in this analysis when 10,000 Monte-Carlo realisations of the data are made by varying both the mass and star-formation rate of the host galaxy. A best-fit Gaussian function is overplotted. . . . .	131
5.11	The value of $\log A$ , as defined in Equation 5.3, in the case where $n_{\text{pass}}$ is not required to equal unity, when 10,000 bootstrap realisations of the data are made without splitting the sample in advance. A best-fit Gaussian function is overplotted. . . . .	132
5.12	The value of $\log A_0$ , as defined in Equation 5.3, in the case where $n_{\text{pass}}$ is forced to be unity, when 10,000 bootstrap realisations of the data are made without splitting the sample in advance. A best-fit Gaussian function is overplotted . . . . .	133
5.13	The type Ia supernova rate per galaxy year as a function of host galaxy mass. In this example, the host galaxy sample is split into two galaxy types, passive and star-forming. The best fit lines are overplotted along with the best fit line of gradient unity for the passive galaxy sample. . . .	134
5.14	An impression of the probability function, described in Equation 5.7, and the two components that it is modelled as. . . . .	137
5.15	The type Ia supernova rate as a function of ongoing star-formation activity within the host. This Figure shows the excess number of supernova events when the best-fit values from Equation 5.9 are assumed . . . . .	141
5.16	The type Ia supernova rate as a function of ongoing star-formation activity within the host. This figure shows the excess number of supernova events when the best-fit values from Equation 5.8, such that $n_{\text{mass}} = 1$ is enforced, are assumed . . . . .	142
5.17	The value of $n_{\text{star-forming}}$ from Equation 5.9, when a value of $n_{\text{mass}} = 1$ is enforced. 10,000 Monte-Carlo realisations of the data are made by varying both the mass and star-formation rate of the host galaxy. . . . .	148
5.18	The value of $\log B$ from Equation 5.9. 10,000 Monte-Carlo realisations of the data are made by varying both the mass and star-formation rate of the host galaxy. This analysis does not enforce a value of $n_{\text{SFR}} = 1$ . . . .	149

5.19	The value of $\log B$ from Equation 5.9, when a value of $n_{\text{mass}} = 1$ and $n_{\text{SFR}} = 1$ are enforced. 10,000 Monte-Carlo realisations of the data are made by varying both the mass and star-formation rate of the host galaxy.	150
6.1	The distribution of the MLCS2k2 $\Delta$ parameter for the three different galaxy populations.	160
6.2	The distribution of the SALT2 $x_1$ parameter for the three different galaxy populations.	165
6.3	The distribution of the SALT stretch parameter $s$ for the three different galaxy populations.	167
6.4	The low redshift approximation relating the SALT2 parameter $x_1$ to the MLCS2k2 parameter $\Delta$ .	168
6.5	The distribution of the SALT2 parameter $x_1$ as determined from the low redshift approximation (Figure 6.4) for the three different galaxy populations.	170
6.6	The distribution of the SALT stretch parameter $s$ as determined from the low redshift approximation (Figure 6.4) for the three different galaxy populations.	171
6.7	The distribution of the MLCS2k2 $A_V$ parameter for the three different galaxy populations when a standard $A_V$ prior is used.	174
6.8	The distribution of the SALT2 colour parameter $c$ for the three different galaxy populations.	176
6.9	The distribution of the MLCS2k2 $A_V$ parameter for the three different galaxy populations when a flat $A_V$ prior is used.	180
6.10	The distribution of the MLCS2k2 $\Delta$ parameter for the three different galaxy populations when a flat $A_V$ prior is used.	181
6.11	The distribution of the MLCS2k2 $A_V$ parameter for the three different galaxy populations when no $A_V$ prior is used.	184
6.12	The distribution of the MLCS2k2 $\Delta$ parameter for the three different galaxy populations when no $A_V$ prior is used.	185
6.13	This is figure 11b is re-printed from Sullivan et al. (2006b). It shows the "stretch" distribution for a set of low redshift SN Ia.	191
6.14	This is figure 11b is re-printed from Sullivan et al. (2006b). It shows the "stretch" distribution for objects in the SNLS complete SN Ia sample.	192
7.1	The Hubble diagram for the spectroscopically confirmed objects defined using a cosmological fit and the criteria described in S3.2.4 and §3.2.2 as a function of host galaxy type. Also shown are the residuals from this fit.	200

7.2	Residuals from the best-fit cosmology shown in Figure 7.1 as a function of host galaxy type. Also shown are the best-fitting Gaussian functions to each galaxy type. . . . .	201
7.3	The Hubble diagram for objects with a spectroscopic redshift (of any type) that have been fit using a cosmological fit and satisfy the selection criteria described in §3.2.4 and §3.2.2 as a function of host galaxy type. .	203
7.4	Residuals from the Hubble diagram shown in Figure 7.3 as a function of host galaxy type. Overplotted on each distribution are the best-fitting Gaussian functions. . . . .	203
7.5	The hubble diagram for objects where the $A_V$ distribution has been determined by either a standard $A_V$ prior for star-forming objects, or a steeper exponential decline for passive events. This figure includes all objects with a spectroscopic redshift. Also shown are the residuals from the fit as a function of redshift. . . . .	207
7.6	Residuals from the fit to the Hubble diagram (Figure 7.5) for objects where the $A_V$ distribution has been determined by either a standard $A_V$ prior for star-forming objects or a steeper exponential decline for passive events. This figure includes all objects with a spectroscopic redshift. Also shown are the residuals from the fit as a function of redshift. . . . .	208
7.7	The Hubble diagram for the spectroscopically confirmed objects defined using using the SALT2 light-curve fitter, as a function of host galaxy type. Also shown are the residuals from this fit. . . . .	213
7.8	The residuals from the best-fitting cosmology shown in Figure 7.7 as a function of host galaxy type. This analysis is for the SALT2 light-curve fitter. . . . .	214
7.9	The Hubble diagram for objects with a spectroscopic redshift (of any type) defined using using the SALT2 light-curve fitter, as a function of host galaxy type. . . . .	216
7.10	The residuals from the best-fitting cosmology shown in Figure 7.9 as a function of host galaxy type. This analysis is for the SALT2 light-curve fitter. . . . .	217
A.1	A comparison of the host galaxy photometric redshift estimates and the spectroscopic redshifts . . . . .	228
A.2	A histogram of the residuals between the host galaxy photometric redshift estimates and the spectroscopic redshift . . . . .	228
A.3	A comparison of the mass determined by a host galaxy photometric redshift and those estimated by a spectroscopic redshift . . . . .	230

A.4	A comparison of the star-formation rates determined by a host galaxy photometric redshift and those estimated by a spectroscopic redshift . . .	231
B.1	The mass as estimated from the PÉGASE.2 templates compared to the values determined by <a href="#">Kauffmann et al. (2003)</a> . . . . .	234
B.2	The difference between the mass as estimated from the PÉGASE.2 templates compared to the values determined by <a href="#">Kauffmann et al. (2003)</a> . . .	235
B.3	The star-formation rate as estimated from the PÉGASE.2 templates compared to the median value determined by <a href="#">Brinchmann et al. (2004)</a> . . . . .	237
B.4	The difference between the star-formation rates as estimated from the PÉGASE.2 templates compared to the median value determined by <a href="#">Brinchmann et al. (2004)</a> as a function of the redshift of each object. . . . .	239
C.1	The mass as estimated from the PÉGASE.2 templates for a sample of objects when the redshift is left as a free parameter compared to the case when the redshift is fixed to it's known value. . . . .	242
C.2	The mass differences between the estimates when the redshift is left as a free parameter and when when the redshift is fixed to it's known value as a function of the apparent <i>r</i> -band magnitude. . . . .	243
C.3	The difference between the estimated redshift from the PÉGASE.2 templates and the measured redshift as a function of the apparent <i>r</i> -band magnitude. . . . .	244
C.4	The difference between the estimated star-formation rate from the PÉGASE.2 templates when the redshift of each object is left as a free parameter and the case where the measured redshift is enforced as a function of the apparent <i>r</i> -band magnitude. . . . .	246
D.1	The difference between the mass as estimated when including GALEX data and only SDSS data as a function of apparent magnitude. . . . .	251
D.2	The difference between the star-formation rate as estimated when including GALEX data and when only using SDSS data as a function of apparent magnitude. . . . .	252
E.1	The differences between the photometric redshift from the Maraston models when compared to the spectroscopic redshift as a function of apparent magnitude for a set of bright galaxies. . . . .	256
E.2	The differences between the photometric redshift from the PÉGASE.2 models when compared to the spectroscopic redshift as a function of apparent magnitude for a set of bright galaxies. . . . .	257
E.3	The differences between the redshift from the PÉGASE.2 models and the Maraston models as a function of apparent magnitude. . . . .	259

# Chapter 1

## Introduction

The study of type Ia supernovae (SNe) has revolutionised the field of cosmology in the past decade. These events are the best probes of the expansion history of the Universe and have led to the detection that the Universe is currently experiencing a period of accelerated expansion, driven by a mysterious substance called “Dark Energy”. Cosmologists have little understanding of this phenomenon, and further to this, the probes on which its detection are based are also poorly understood. These supernovae can be standardised empirically through measurements of their light-curve properties, but a full understanding of their progenitor systems, and the diversity seen within the population, has not been explained.

In this chapter, I shall introduce the standard cosmological model, namely the Friedmann-Lemaître-Robertson-Walker cosmology. I shall then describe the classification of supernova events into different classes, including the type Ia SN events, and then explain how their light-curves allow cosmologists to use them as probes of the cosmic expansion history. I shall also discuss the physical interpretation of these events, and efforts undertaken in the astronomical community to detect and measure a large number of these objects to better understand “Dark Energy”.

### 1.1 The Standard Model of Cosmology

#### 1.1.1 The Cosmological Model and the Friedmann Equations

Cosmology is the study of the Universe through observations and theoretical predictions. The foundation of the current cosmological model comes from Einstein’s theory of General Relativity. The starting point for studies of the evolution of the Universe is the Cosmological Principle. This states that on sufficiently large scales the Universe is both

isotropic, at any given point, and homogeneous, at any given time. That is, there are no preferred places in the Universe (Misner et al. (1973), Milne (1933)). This has been verified through observations of the Cosmic Microwave Background (CMB), which have shown that the Universe appears to be isotropic on large scales to 1 part in  $10^5$  (Smoot et al. (1991)), and on scales of  $> 100\text{Mpc}$  from the large scale distribution of galaxies (Yadav et al. (2005)), once our dipole motion has been removed.

Using this principle and the added assumption that content of the Universe behaves as a perfect fluid, we can obtain the Friedmann equations (Friedmann (1924)),

$$H^2 = \left(\frac{\dot{a}}{a}\right)^2 = \frac{8\pi G\rho}{3} - \frac{\kappa}{a^2}, \quad (1.1)$$

which describes the acceleration of the Universe, and,

$$\frac{\ddot{a}}{a} = -\frac{4\pi G}{3}(\rho + 3p), \quad (1.2)$$

which describes the evolution of the Universe. In these equations,  $a(t)$  is the scale factor that describes the relative expansion of the Universe ( $a = 1$  today), and is dimensionless,  $\dot{a}$  is its derivative with respect to proper time,  $\rho$  and  $p$  are the density and pressure of the perfect fluid,  $G$  is Newton's gravitational constant, and  $\kappa$  describes the curvature of the Universe, which is governed by the amount of matter and energy inside it. Thus  $\kappa$  does not change with the expansion of the Universe, and can take three different values:

- $\kappa = +1$  for a geometrically elliptical Universe, with positive spatial curvature,
- $\kappa = 0$  for a Euclidean Universe which is geometrically flat and has zero spatial curvature, and
- $\kappa = -1$  for a geometrically hyperbolic Universe, with negative spatial curvature.

Hubble (1929) first measured the value of  $H$  today, denoted  $H_0$  when showing that the apparent recession velocity,  $v$  of distant galaxies is proportional to their physical distance or co-moving separation,  $r$ , such that,

$$v = Hr. \quad (1.3)$$

$H_0$  is commonly expressed with the dimensionless quantity,

$$h \equiv \frac{H_0}{100\text{km s}^{-1} \text{Mpc}^{-1}}, \quad (1.4)$$

---

<sup>1</sup>One parsec is defined to be the distance at which the parallax of an object is one arcsecond, and thus one Megaparsec is  $3.086 \times 10^{22}$  metres

and [Freedman et al. \(2001\)](#), using the Hubble Space Telescope determined that  $H_0 = 72 \pm 8 \text{ km s}^{-1} \text{ Mpc}^{-1}$  using Cepheid Variable measurements to 31 local galaxies. [Dunkley et al. \(2008\)](#) using 5-year data from the WMAP experiment alone found a value of  $71.9 \pm 2.6 \text{ km s}^{-1} \text{ Mpc}^{-1}$ , whilst [Komatsu et al. \(2009\)](#) determined a value of  $70.1 \pm 1.3 \text{ km s}^{-1} \text{ Mpc}^{-1}$  when the WMAP data is combined with other astronomical data such as Baryon Acoustic Oscillations and type Ia Supernova.

In cosmology, energy conservation is expressed in terms of the continuity equation ([Carroll \(2004\)](#)),

$$\dot{\rho} + 3H(\rho + p) = 0 \quad (1.5)$$

and tells us how the density of each component of the Universe expands. It is common practice in cosmology to consider the perfect fluid of the Universe to be governed with the following equation of state,

$$p = \omega \times \rho, \quad (1.6)$$

where in its simplest case,  $\omega$  can be treated as a constant, such that the density of the fluid evolves as,

$$\rho(t) \propto a^{-3(1+\omega)}. \quad (1.7)$$

### The Density Parameter

Before discussing the make-up of the Universe, I first introduce another parameter; the “critical density”,  $\rho_{\text{crit}}$ , which is defined as the density required for the geometry of the Universe to be flat, or,

$$\rho_{\text{crit}} = \frac{3H^2}{8\pi G}. \quad (1.8)$$

We can then define the density parameter as  $\Omega \equiv \rho/\rho_{\text{crit}}$ , i.e.

$$\Omega - 1 = \frac{\kappa}{a^2 H^2}. \quad (1.9)$$

Thus the Universe will have positive or negative curvature if the density of the Universe is bigger or smaller than the critical density respectively.

Current constraints, based on the first peak of the CMB angular power spectrum, from the WMAP survey are  $\Omega_{\text{tot}} = 1.02 \pm 0.02$  ([Spergel et al. \(2007\)](#)). Thus the geometry of the Universe is consistent with zero curvature, which we shall assume for the remainder of this thesis.

### 1.1.2 The Contents of the Universe

The analysis so far has presumed that the Universe is comprised of one perfect fluid. However, observations of the Universe suggest that it instead contains several independent components. We shall consider three components of the Universe, matter (comprising observable and Dark Matter), radiation and vacuum energy, such that

$$\rho = \sum_i \rho_i, \quad (1.10)$$

where  $\rho_i$  is the density of each individual component, and,

$$\Omega_{tot} = \Omega_m + \Omega_\gamma + \Omega_\Lambda, \quad (1.11)$$

where  $\Omega_m \equiv \rho_m/\rho_{crit}$  for the matter content of the Universe,  $\Omega_\gamma \equiv \rho_\gamma/\rho_{crit}$  for the radiation component, and  $\Omega_\Lambda \equiv \rho_\Lambda/\rho_{crit}$  for the vacuum energy. Observations indicate the presence of Dark Matter in the Universe alongside baryonic matter. These are both included in the matter term, such that,  $\Omega_m = \Omega_{baryons} + \Omega_{DM}$ .

I shall now describe how these three components of the Universe evolve with time and current constraints on their densities.

#### Matter

The matter content of the Universe is dominated by ‘‘Dark Matter’’ and not baryonic matter. ‘‘Dark Matter’’ does not interact electromagnetically and has only been detected from its gravitational effects. This was first inferred by [Zwicky \(1933\)](#) and later by [Rubin et al. \(1980\)](#), through the measurement of rotation curves of nearby galaxies. Recently, [Dunkley et al. \(2008\)](#) from the WMAP 5 year data release, found that,

$$\Omega_{DM} \simeq 0.214 \pm 0.027, \quad (1.12)$$

and, [Kirkman et al. \(2003\)](#) from the abundance of deuterium in high-redshift objects, showed that,

$$\Omega_{baryonic} h^2 \simeq 2.14 \pm 0.20 \times 10^{-2}. \quad (1.13)$$

Therefore, using the best-fit value of  $h = 0.72 \pm 0.08$ , found in [Freedman et al. \(2001\)](#), the total matter content of the Universe today is,  $\Omega_M \simeq 0.25 \pm 0.05$ .

This additional matter component is considered to be collisionless, (i.e. with zero pressure), and so its expansion is proportional to the physical volume of the Universe,

$$\rho_m \propto a^{-3}. \quad (1.14)$$

Hence, from the Friedmann Equation (1.1) we can write,

$$a \propto t^{2/3}. \quad (1.15)$$

### **Radiation**

This case is relevant for the early expansion of the Universe during the Hot Big Bang. For this component, the density and scale factor expand as,

$$\rho_\gamma \propto a^{-4}. \quad (1.16)$$

Thus, from Equation 1.1, we can write,

$$a \propto t^{1/2}. \quad (1.17)$$

Observations of the CMB, have accurately constrained the temperature, as  $T = 2.726 \pm 0.002K$  when it is assumed to be well represented by a black body spectrum. As,  $\rho_\gamma \propto T^4$ , we can that currently write,

$$\Omega_\gamma h^2 \simeq 2.47 \times 10^{-5}, \quad (1.18)$$

This is insignificant when compared to the matter content of the Universe, and thus is ignored for the remainder of this thesis.

### **Dark Energy**

As mentioned at the beginning of this thesis, current observations indicate that the Universe is experiencing a period of accelerated expansion, driven by a force termed ‘‘Dark Energy’’. This is often assumed to be a ‘‘Cosmological Constant’’, or *vacuum energy*, denoted by  $\Lambda$ .

This assumption leads to a component that mimics the dynamics of the Universe during periods of inflation (an accelerated expansion). A cosmological constant has constant

density, such that  $\rho_\Lambda = \rho_0$ , and an equation of state parameter  $\omega = -1$ . Thus in this case,  $p_\Lambda = -\rho_\Lambda$  and,

$$\Omega_\Lambda(z) = \Omega_\Lambda. \quad (1.19)$$

Thus, at early times, the energy density from  $\Lambda$  is much smaller than that of matter (which scales as  $\propto 1/a^3$ ) and radiation (which scales as  $\propto 1/a^4$ ), but comes to dominate at late times as the other components are diluted.

Using Equation 1.1 we see that,

$$a \propto e^{H_0 t} \quad (1.20)$$

and therefore, any epoch of the Universe that is dominated by a vacuum energy component will undergo an accelerated period of expansion.

Of course, a cosmological constant is not the only possibility for Dark Energy. A slightly more general Dark Energy parameterisation allows the equation of state,  $\omega_\Lambda$  to be a different value from  $-1$ . In this case the evolution is given by,

$$\Omega_\Lambda(z) = \frac{\Omega_\Lambda(z=0)}{a^{3(1+\omega_0)}} \quad (1.21)$$

where  $\omega_0$  is the equation of state. Alternate models allow the equation of state of Dark Energy to vary with time, with the equation of state parameterised as,

$$w(a) = w_0 + w_a(1 - a). \quad (1.22)$$

However, the current observational constraints on such parameterisations are weak. Current understanding of the physical interpretation of Dark Energy, beyond a vacuum energy, is weak, with many suggested possibilities, including scalar field models (such as quintessence), and models which modify the equations of gravity. We shall discuss observations that are used to determine the parameters of Dark Energy, and current constraints on the contents of the Universe in §1.4.

### 1.1.3 Distances in Cosmology

In our description of the cosmological model, the values of energy density and curvature parameter govern the geometry and expansion of the Universe. However, these parameters need to be measured observationally. To do this, distance estimates to astronomical objects are required. A common measure of distance is the Doppler shift of an objects

spectral features due to the expansion of the Universe, or its *redshift*,  $z$ , which is defined by,

$$1 + z = \frac{\lambda_{\text{observed}}}{\lambda_{\text{emitted}}} = a^{-1}. \quad (1.23)$$

However, this measure of distance is inferred from an objects recession velocity and thus not a measure of the absolute distance to the object. The *luminosity distance*,  $d_L$  represents the distance to an object with known luminosity, ( $L$ ) and flux, ( $F$ ) on a co-moving grid, by

$$F = \frac{L}{4\pi d_L^2}. \quad (1.24)$$

This  $d_L$  is dependent on the expansion history of the Universe, and is described through the metric and Friedmann equations.

This measure of distance is related to other distance measurements through the equation,

$$d_L = d_{PM} \times (1 + z) = d_A \times (1 + z)^2, \quad (1.25)$$

where  $d_{PM}$  is the proper motion distance, or co-ordinate distance, which tracks the evolution of the Universe, and  $d_A$  is the angular diameter distance, or the distance to an object of dimension,  $l$  subtending an angle  $\theta$ :  $d_A = l/\theta$ .

For a flat Universe, with negligible contribution from its radiation component, we derive that

$$d_L = (1 + z) \times \frac{c}{H_0} \int_0^z \frac{dz'}{[(1 + z')^3 \Omega_m + \Omega_\Lambda]^{1/2}}, \quad (1.26)$$

for a vacuum energy component,  $\Lambda$ , with constant equation of state (Peebles (1993)).  $d_L$  is traditionally measured in units of Megaparsecs.

One of the most common measurements in astronomy concerns an object's *magnitude*. This is a measure of an object's brightness. The *apparent magnitude*,  $m$ , of an object is a measurement of the brightness of an object as seen from the planet Earth assuming the absence of the atmosphere. For the magnitude system, brighter objects have lower values of their magnitude. The apparent magnitude,  $m_i$ , can be defined as,

$$m_i = -2.5 \log_{10}(b_i/b_i^0) \quad (1.27)$$

where  $b_i$  is the observed flux in the passband,  $i$ , and  $b_i^0$  is the flux of a reference object in the same band,  $i$ . Historically, the star Vega was used as a standard reference star, such that it had magnitude 0. In modern astronomy, several measurements of calculating

magnitudes are available. One such method, is the AB magnitude system, is calculated using the formula,

$$m_i = -2.5 \log_{10} f_i - 48.60 \quad (1.28)$$

where  $f_i$  is a flux density, measured in  $\text{erg sec}^{-1} \text{cm}^{-2} \text{Hz}^{-1}$  (Oke (1974)). The value of 48.60 is selected such that a source of  $F_\nu = 3631 \text{ Jy}$  has zero apparent magnitude.

Following this, an object's *absolute magnitude*,  $M$ , is defined to be the apparent magnitude it would have if it were at a distance of 10 parsecs.

The final measure of interest for this work, is the *distance modulus*. This is the relationship between the observed flux of an object (the apparent magnitude,  $m$ ), and the absolute magnitude ( $M$ ), defined to be the apparent magnitude an object at a distance of 10 parsecs from the observer. The difference between  $m$  and  $M$  is referred to as the distance modulus,  $\mu$ . The relationship between the distance modulus and luminosity distance is given by,

$$\mu(z) \equiv m(z) - M = 5 \log_{10}(d_L/10pc), \quad (1.29)$$

$$= 5 \log_{10} d_L + 25, \quad (1.30)$$

where  $d_L$  is a function of  $z, \Omega_m, \Omega_\Lambda, H_0$  as described in Equation 1.26 and is measured in Megaparsecs. For objects whose intrinsic luminosities are known, it is possible to constrain the cosmological parameters by comparing the distance estimates of  $\mu$  and  $z$ . These objects are known as “standard candles”.

## 1.2 Supernovae - Definitions and Classifications

Having introduced the cosmological model in §1.1, we now turn our attention to the focus of this thesis, and one of the most important cosmological probes, namely type Ia supernovae. These objects are used to measure distances in cosmology since they are observed to all have extremely similar absolute magnitudes, with only a small dispersion. They thus act as *Cosmic Light-Bulbs*.

Type Ia supernovae have proved to be an invaluable tool in probing the cosmic expansion history of the Universe. However, these objects are merely part of a family of cataclysmic events known as supernovae. These events have been well documented throughout history, including the events seen in the sky in years of 1006 and 1572, but they were not classified into sub-groups until they were first viewed by a spectrograph.

### 1.2.1 Spectral Classification of Supernovae

Originally supernovae were classified into two groups. This split was based purely on spectral observations and was independent of physical processes. Type “I” supernovae were defined to be objects that did not show any indication of hydrogen emission ( $H\alpha$  or  $H\beta$ ) in their spectra, whilst those that did, were classified as type “II” supernovae (Minkowski (1941), Popper (1937)). The type ‘I’ designation was later sub-divided into three sub-classes of supernovae; those displaying a deep absorption trough around  $6150\text{\AA}$ , produced by blueshifted silicon (SiII  $\lambda 6347, \lambda 6371$ ), were categorised as type “Ia” supernovae, whilst other events were designated as type “Ib” or type “Ic” supernovae. Type “Ib” supernovae are differentiated from type “Ic” events due to the fact that they lack the presence of helium  $\lambda 5876$  lines in their spectra (Wheeler & Harkness (1986), Harkness & Wheeler (1990)). The nomenclature of supernovae follow a specific routine; the name is formed by the year of discovery, immediately followed by a one- or two-letter designation. The first 26 supernovae of the year get an upper case letter from A to Z. Afterward, pairs of lower-case letters are used, starting with aa, ab, and so on.

Our understanding of these objects has improved dramatically since this first discovery. It is now known that type II, Ib and Ic supernovae are the result of a core collapse and explosion event at the conclusion of a massive star’s life. These events show great diversity within their light-curve profiles and spectral observations. However, type Ia supernova do not seem to be formed from the same mechanism, and further to this, are usually quite homogeneous within their light-curves and spectra. Our current physical understanding of the processes that cause a type Ia event are discussed in §1.3. These events are formed from the violent explosion of a white dwarf star that has accreted matter such that the total mass reaches the Chandrasekhar limit. Due to the common mass of each of these events, they produce peak luminosities and spectra that are remarkably homogeneous.

Figure 1.1 shows the spectra of three type Ia supernova events observed at maximum brightness in the  $B$ -band. These spectra are of three objects spanning the observed variety in type Ia peak luminosity, and are remarkably similar. These spectra all exhibit large absorption features from intermediate mass elements such as CaII, SiII, SII and MgII. Despite the homogeneity of these objects, differences amongst type Ia supernovae do exist. These differences are closely related to the peak brightness of the type Ia event. Spectroscopically similar events are commonly referred to as ‘Branch normal’ or ‘core normal’ supernovae (Branch et al. (2006)) and are spectroscopically similar to the event shown in Figure 1.2. Approximately 85% of spectroscopically confirmed type Ia supernova are contained in this category.

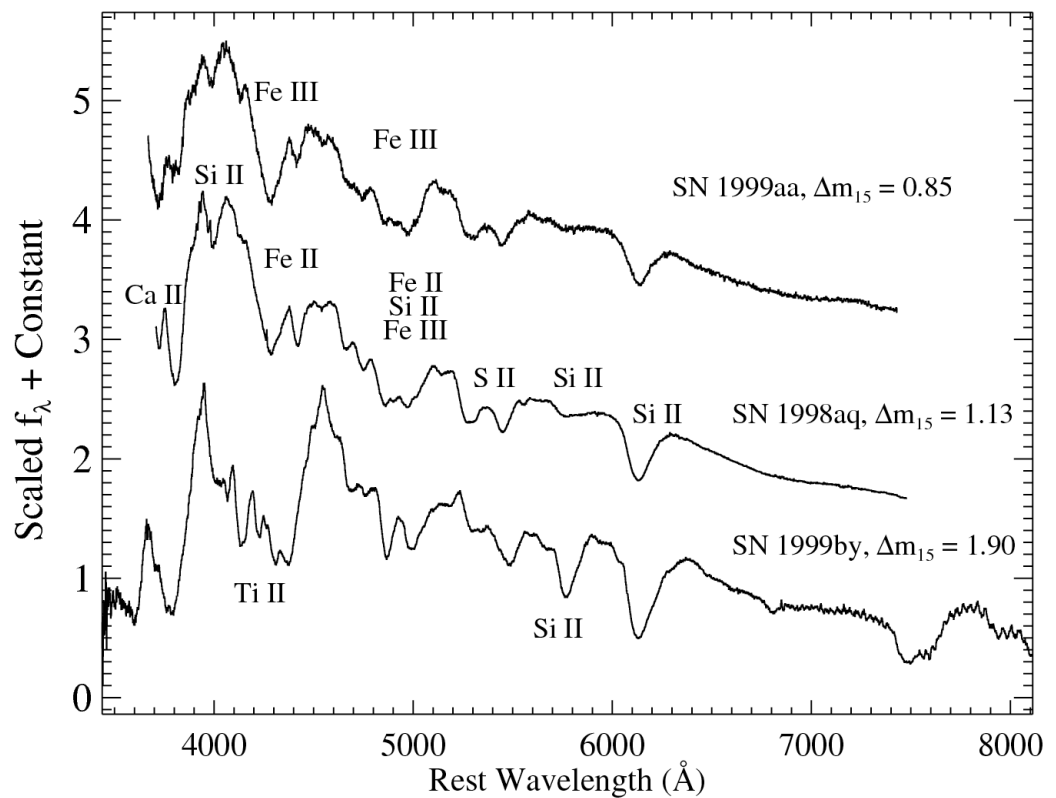


Figure 1.1: This figure shows the spectra of three type Ia supernova; 1998aq, 1999aa and 1999by at  $B$ -band maximum. The flux units for each object have been normalised and offsets for visual clarity have been applied. The major spectral features are labelled and an indication of the light-curve decline parameter,  $\Delta m_{15}$  is provided. This figure is taken from [Matheson et al. \(2008\)](#).

Overluminous supernovae are often categorised as 1991T-like events (Filippenko et al. (1992b), Phillips et al. (1992)). These objects show weak absorption of Silicon, Calcium and Sulphur at early epochs compared to “standard” Ia events, but closely resemble ‘core normal’ events at later epochs, suggesting that these events are not an entirely separate class to normal events.

Underluminous type Ia events are categorised as 1991bg-like events (Filippenko et al. (1992a), Leibundgut et al. (1993)). These are much fainter in the B and V bands than normal type Ia events, by up to 3 magnitudes, and redder in the B and V bands. These events generally have lower expansion velocities than typical events (Benetti et al. (2005)), indicating that this sub-class of objects is less energetic than the standard type Ia population. The spectra of these objects classically exhibit an enhanced Si II absorption at  $\lambda 5700$  and a trough of Ti II at  $\lambda 4100 - \lambda 4400$ .

Several other peculiar type Ia supernovae have been observed, such as 2002ic (Deng et al. (2004)), 2000cx (Li et al. (2001a)) and SNLS-03D3bb (Howell et al. (2006)), which further complicate the classification of type Ia events. However, these do not exhibit the highly useful property of type Ia supernovae, the fact that their light-curve shape correlates with their peak luminosity.

A full explanation of the spectral features and time evolution of supernovae is given in Filippenko et al. (1992a) and, more recently, Matheson et al. (2008).

## 1.2.2 The Light-Curves of Type Ia Events

In §1.1 we mentioned the use of “standard candles” to constrain cosmological parameters. Type Ia supernovae are the most prominently used of such events since their high absolute magnitudes allows them to be seen to large distances. In §1.2.1, we noted that the absolute brightness of these objects is highly uniform, especially in the ‘branch normal’ sub-class.

### Standardisable Candles

Unfortunately, whilst the peak brightness of type Ia supernovae are highly consistent, they are not perfect standard candles. These events have peak magnitudes of  $-18 \lesssim M_B \lesssim -19.5$  and thus are bright enough to be seen at large redshifts, however their absolute magnitudes contain an intrinsic scatter, which means that they are not standard for all events. This is seen in Figure 1.3 for a sample of nearby objects observed in the  $B$ ,  $V$  and  $R$  filters. As this figure clearly shows, there is an apparent relationship between the

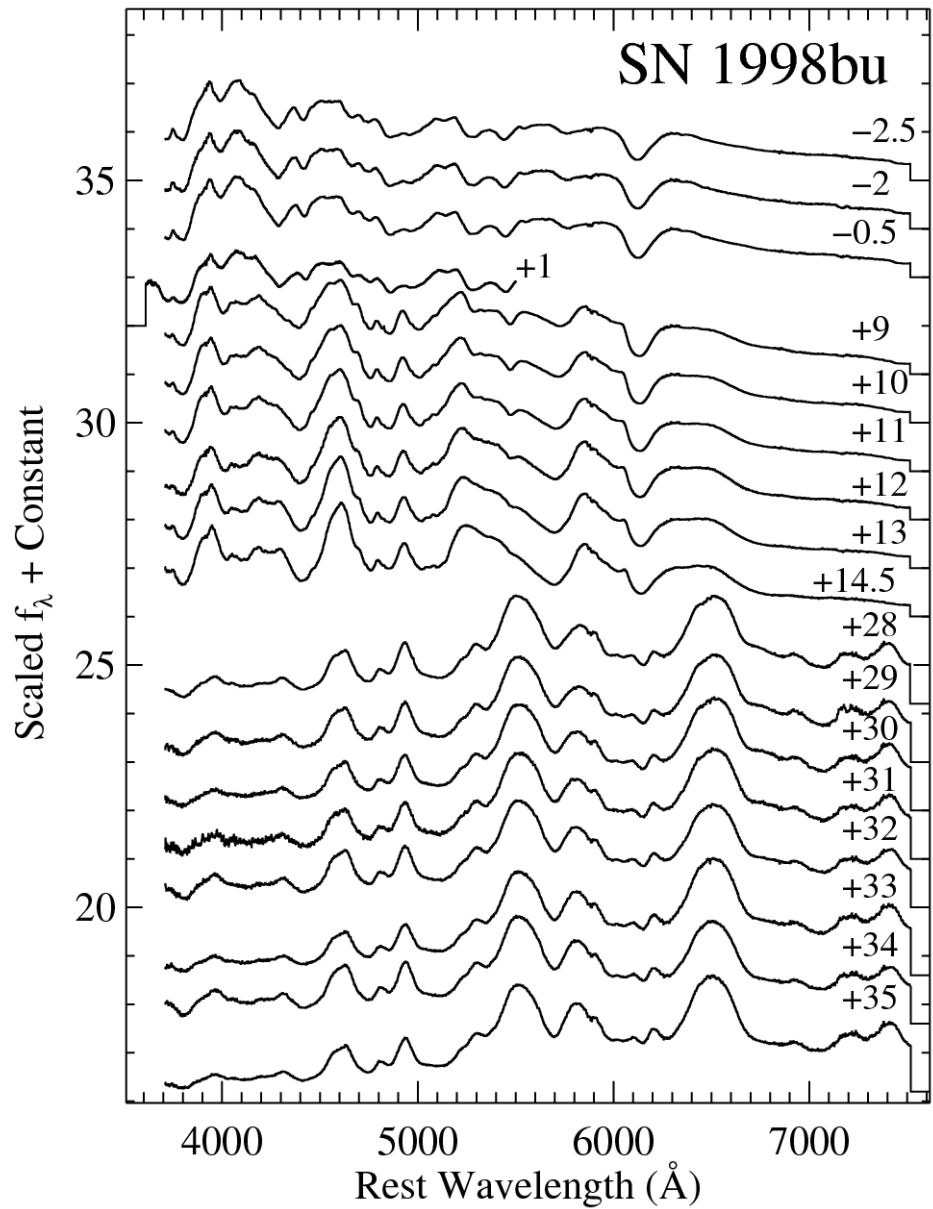


Figure 1.2: Spectra of the ‘branch normal’ type Ia supernovae, 1998bu. The figure shows the observed spectral evolution of this event from before maximum light until one month after maximum luminosity, and is taken from [Matheson et al. \(2008\)](#).

width of each light-curve and the associate peak-brightness. This relationship between absolute magnitude and light-curve width was first proposed in Pskovskii (1977), that the slope of the light-curve just after peak was related to the peak luminosity. Phillips (1993) statistically parameterised this relationship, by noting that the total decrease in magnitudes in the  $B$ -band, 15 days after maximum luminosity has a linear relationship to the peak magnitudes for type Ia events. This quantity,  $\Delta m_{15}$  is known as the ‘‘Phillips relation’’. This first order correction, normalises the maximum luminosity of these events, such that they can be used as cosmological probes. The dispersion of these peak magnitudes is drastically reduced, and thus they are considered ‘standardisable candles’.

In the last decade, this relationship has been parameterised in many different ways. The most prominent of these include the Multi Light-Curve Shape (MLCS) method (Riess et al. (1996)), the Spectral Adaptive Lightcurve Template (SALT and SALT2) method (Guy et al. (2007)), the timescale-stretch parameterisation (Goldhaber et al. (2001)) and an updated  $\Delta m_{15}$  method (Phillips et al. (1999)). For the stretch method, an empirically derived light-curve is stretched to match the observed event as a function of time, with the size of the stretch being proportional to the peak magnitude of the event. MLCS combines this technique with an additional colour relationship to determine the extinction for the observed event. However, all methods use a similar approach to decrease the observed scatter of the peak magnitudes of these events. This observed parameter decreases the intrinsic scatter (i.e. the scatter that cannot be removed) by a factor of  $\sim 2$ , such that  $\sigma_{M_{\text{peak}}} \sim 0.12$  instead of the observed value of  $\sigma_{M_{\text{peak}}} \sim 0.25$  (Phillips et al. (1999)). However, this scatter is not negligible, and thus presently, type Ia supernova are still not perfect ‘standardisable candles’. Several other parameters of type Ia supernovae have been suggested to further decrease this intrinsic scatter, such as spectral features (Benetti et al. (2005)), but none have been successful yet in achieving this.

The SALT and SALT2 methods are examples of *light-curve fitters*. These methods are primarily designed to determine the best-fitting light-curve template to the observed light-curves without necessarily using the output parameters to determine a distance to the supernova. A *distance estimator*, of which the MLCS method is an example, is solely interested in determining the distance to each object, instead of determining the best-fit to the data. Since type Ia supernovae are primarily used as distance indicators, this method is advantageous as it provides information that is comparable to other measurements. However, in the training of such methods a distance is required making the inclusion of both high and low redshift information difficult.

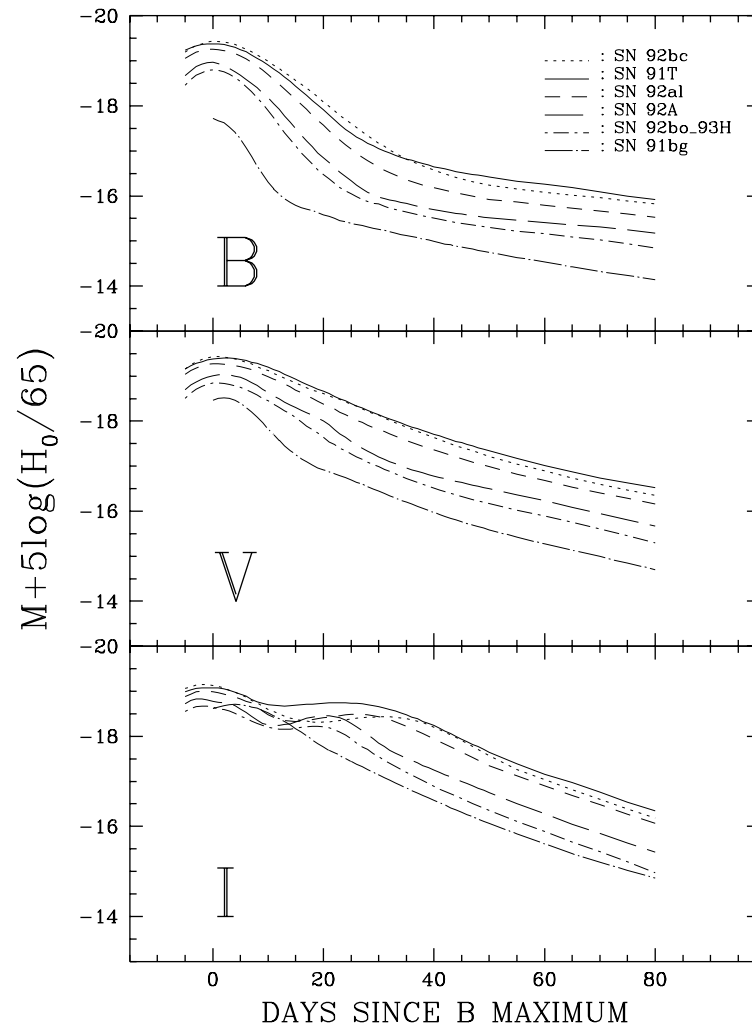


Figure 1.3: Uncorrected  $B$ ,  $V$ ,  $I$  type Ia light-curves for a sample of nearby events. These light-curves clearly show the intrinsic scatter between underluminous, ‘branch normal’ and overluminous events, with brighter events having broader light-curves than fainter events. The figure is taken from [Hamuy et al. \(1996d\)](#).

### 1.3 The Physics of Type Ia Supernovae

The current understanding of supernova physics is that type Ib, Ic and type II supernovae are the result of the collapse of a massive star's core. However, type Ia supernovae are considered to be entirely different. Astronomers are in general agreement that these events are the result of the explosion of a white dwarf star that has accreted matter from a companion star. Based upon spectra and light-curves, it is thought that these events are a white dwarf comprised of carbon and oxygen that reaches the Chandrasekhar mass limit ( $M_{CH} \sim 1.39M_{\odot}$ ) (Chandrasekhar (1931) and Branch et al. (1995)). This limit is the maximum non-rotating mass which can be supported against gravitational collapse by electron degeneracy pressure.

Even from this consistent set of initial conditions, it is still difficult to model the outcome of such an explosion. This is because the conditions of the ignition process and the level of rotation are impossible to predict, and thus there is some debate as to the dominating process that occurs in these stellar explosions. The actual explosion of the white dwarf only takes a few seconds, but prior to this, it is believed that there are several centuries of convection. This convective region grows to include most of the star and at some stage, ignition occurs. This deflagration causes a thermonuclear “flame” which is a runaway process, that spreads through the star's interior slower than the local speed of sound. The flame moves through the white dwarf, burning a significant proportion of the carbon and oxygen to heavier elements. The temperature of the white dwarf increases to  $9 \times 10^9 K$  in a only a few seconds. Once the process has started it will not stop until the star has been totally destroyed. However, the exact level of burning and the inferred luminosity is dependent on the initial position of the ignition. It is unclear if a single burning spot is formed, or whether ignition takes place throughout the central regions of the star. See Nomoto et al. (1997) and Woosley et al. (2007) for a review of these processes.

The thermonuclear “flame” engulfs the star from the inside out. In regions where the nuclear burning time-scales are shorter than the convective time-scale for expansion, the burning can continue to the formation of the stable element  $^{58}\text{Ni}$  and other iron-peak elements such as  $^{56}\text{Ni}$ . The optical and infra-red light-curves of these events are powered by the radioactive decay of  $^{56}\text{Ni} \rightarrow ^{56}\text{Co} \rightarrow ^{56}\text{Fe}$  (Colgate & McKee (1969)), with explosions which generate above average  $^{56}\text{Ni}$  levels producing brighter type Ia events. Large amounts of material does not reach this final stage and thus large amounts of intermediate mass elements, such as calcium, silicon and sulphur are produced (see Arnett (1996) for specifics).

Whilst this physical process is generally accepted as the power behind type Ia events, there is active debate about the details of this model. These include the stage of evolution of the binary companion, which may be a main sequence star, giant or sub-giant or another white dwarf, the location of the ignition point(s), the rotation of the white dwarf and the velocity of the burning front (see [Hillebrandt & Niemeyer \(2000\)](#) and [Röpke & Hillebrandt \(2006\)](#) and [Bravo & García-Senz \(2008\)](#) for information on different aspects of these models). These parameters will determine the amount of  $^{56}\text{Ni}$  produced by the event, and thus dictate both the luminosity and delay-time of each event.

## 1.4 Type Ia Supernova Surveys

In the previous sections, we have discussed the motivation behind efforts to discover and accurately measure a large number of type Ia supernova events, since these cosmological probes are able to determine the expansion rate of the Universe accurately.

Current supernova surveys include the Carnegie Supernova Project (CSP), the High-z Supernova Search Team (HzSST), the Supernova Cosmology Project (SCP), the SuperNova Legacy Survey (SNLS), the Equation of State: SupErNovae trace Cosmic Expansion (ESSENCE) project, the Nearby Supernova Factory, the Lick Observatory Supernova Search (LOSS) and the Sloan Digital Sky Survey II (SDSS-II) Supernova Survey. These projects span a wide range of redshift space and operate both with scheduled observations and year-round projects. The most recent surveys (SDSS, ESSENCE and SNLS), uses repeat images of fields with large CCDs, with the ambition of not only determining the cosmological parameters, but also to understand the diversity of the type Ia population.

Two of these surveys, SCP and HzSST were the first projects to identify a significant number of high redshift type Ia supernovae. [Riess et al. \(1998\)](#) used 16 events in the redshift range  $0.16 \leq z \leq 0.62$  and 32 local events and [Perlmutter et al. \(1999\)](#) with 42 supernovae in the redshift range  $0.18 \leq z \leq 0.83$ . These teams found that distant supernovae are  $\sim 0.25$  mag dimmer than they would be in a decelerating Universe, and thus provided the first evidence that the Universe is currently undergoing an accelerated period of expansion. The original Hubble diagram for the SCP and HzSST surveys combined is shown in [Figure 1.4](#).

### 1.4.1 Dark Energy

In [§1.1](#) we noted that for a flat Universe, as matched by CMB observations,  $\Omega_{tot} = 1$ . We also described how the total matter content of the Universe contributes approximately

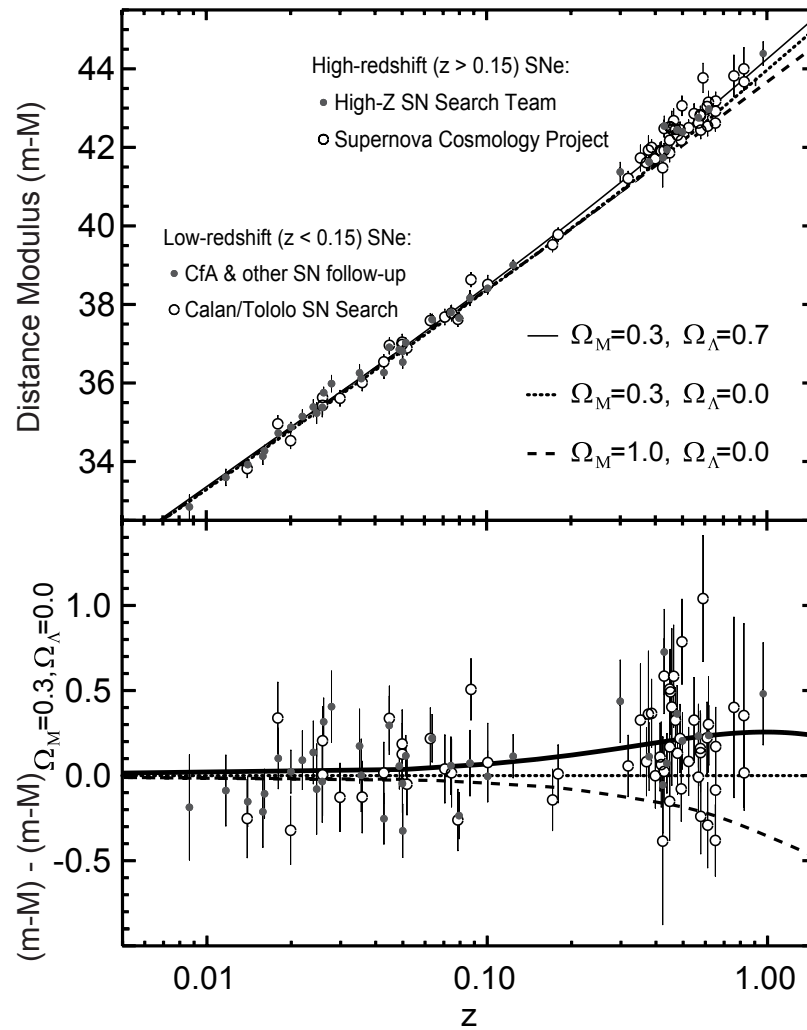


Figure 1.4: Hubble Diagram of type Ia supernovae as measured by the SCP and HzSST. The bottom panel shows the residuals from an open Universe with  $\Omega_M = 0.3$ . This figure is taken from [Frieman et al. \(2008b\)](#), who adapted figures from [Perlmutter et al. \(1999\)](#) and [Riess et al. \(1998\)](#)

25% of this, i.e.  $\Omega_m \simeq 0.25$ . Thus an additional component of the Universe is required. This component will have  $\Omega_X \simeq 0.75$ , and will be causing the expansion rate of the Universe to accelerate. This substance is called “Dark energy” (DE). As described in §1.1.2, a vacuum energy component of the Universe would cause an period of accelerated expansion.

The simplest current model to explain the observed phenomenon is called  $\Lambda$ CDM, where  $\Lambda$  is called the *Cosmological Constant*. This possible component is a vacuum energy component with constant equation of state parameter,  $\omega = -1$ . However, there are several problems with the Cosmological Constant. The most prominent of these, is the *Cosmological Constant Problem*. This problem states that whilst current observational evidence (from, for instance, type Ia Supernovae) suggests that any vacuum energy will have a very small value, most quantitative estimates, from effective field theories, predict a huge cosmological constant. For quantum field theory, the energy density of the vacuum is calculated to be of the order  $10^{91}$  grams per cubic centimetre, whilst the value based on cosmology and gravitation is of the order  $10^{-29}$  grams per cubic centimetre, and thus there is a difference of  $\sim 120$  orders of magnitude different from that observed.

A range of other DE models have been identified. These include scalar field theories, such as quintessence, and modified gravity models, including brane-world and  $f(R)$  theories. The aim of many current cosmological surveys is to determine the properties of this DE component and to determine if its properties are time varying. To do this, a DE component is included in the model and resulting predictions are compared to observations.

### Constraints on Dark Energy

Many different cosmological probes are used to constrain the parameter space of  $\Omega_\Lambda$  for a  $\Lambda$ CDM Universe, and  $\omega_{DE}(t)$  for a “Dark Energy” component. As noted earlier, observations of the CMB by the WMAP survey have constrained the level of curvature in the Universe, such that  $-0.251 < \Omega_\kappa < 0.0099$  (Dunkley et al. (2008)). Large Scale Structure observations, through probes such as Baryon Acoustic Observations (BAOs) have shown that  $\Omega_m = 0.273 \pm 0.025$  (Eisenstein et al. (2005), Percival et al. (2007)). Finally, observations of type Ia supernovae have constrained the current expansion rate of the Universe, and shown that it is undergoing an accelerated expansion. Recent results from the CSP (Knop et al. (2003)) and HsSST (Tonry et al. (2003)), and other independent teams (Wood-Vasey et al. (2007) for the ESSENCE team, and Astier et al. (2006) for the SNLS project), have spectroscopically determined hundreds of type Ia

supernovae to  $z \simeq 1$ . The latest Hubble diagram for these events is shown in Figure 1.5. Thus by combining these three probes, we find that  $\Omega_m = 0.29, \Omega_\Lambda = 0.71$  (Davis et al. (2007) and Kowalski et al. (2008)). When observations from the CMB, BAOs and type Ia supernovae are combined we are able to constrain the value of  $\omega_{DE}$  today. Figure 1.6 shows the current constraints from combined CMB, BAO and Supernova data on the equation of state of DE,  $\omega$ . Currently, if  $\omega$  is assumed to be constant, then  $\omega = -0.969 \pm 0.063(\text{stat}) \pm 0.066(\text{sys})$  (Kowalski et al. (2008)). Recent BAO measurements from Percival et al. (2007), using low redshift galaxy surveys, indicates that if a flat Universe is assumed with a constant Dark energy equation of state, then  $\omega < -1$  is favoured at the  $1.4\sigma$  level. However, when type Ia supernova data and CMB information is included, a value of  $\omega = -1.004 \pm 0.089$  is recovered. Other cosmological probes that can constrain cosmological parameters include weak lensing (Fu et al. (2008)) and the Integrated Sachs Wolfe (ISW) effect (Giannantonio et al. (2008)) This work is primarily concerned with data collected from the first two years of operation of the SDSS-II supernova survey. The aims and survey operations of this project are discussed in §2 as well as described in Frieman et al. (2008a). This project aims to discover, spectroscopically confirm and accurately measure the light-curves of a sample of  $\sim 500$  type Ia supernovae at intermediate redshift, where other supernova projects are unable to probe, due to the larger survey volume required for such a task (see for instance the redshift gap on Figure 1.5). One of the primary goals of the survey is to better understand the type Ia supernova population, thus reducing the uncertainty in the cosmological parameters derived from their measurements.

## 1.5 Measurements of Type Ia Supernova Diversity and the Supernova rate

The main focus of this thesis will be to look at the population of type Ia objects discovered at intermediate redshift and investigate the diversity of this population of objects through their photometric observations. We shall attempt to determine if their observed properties, and the rate in which they occur, is dependent on their environment, and more specifically the host galaxy in which they explode. These measurements will enable us to constrain the type Ia supernova progenitor system and investigate correlations that may allow the dispersion in the Hubble diagram (Figure 1.5) to be reduced, thus improving the constraints on cosmological parameter estimation, and the systematic uncertainty on their measurements.

There are several avenues that allow us to investigate type Ia diversity. This work shall

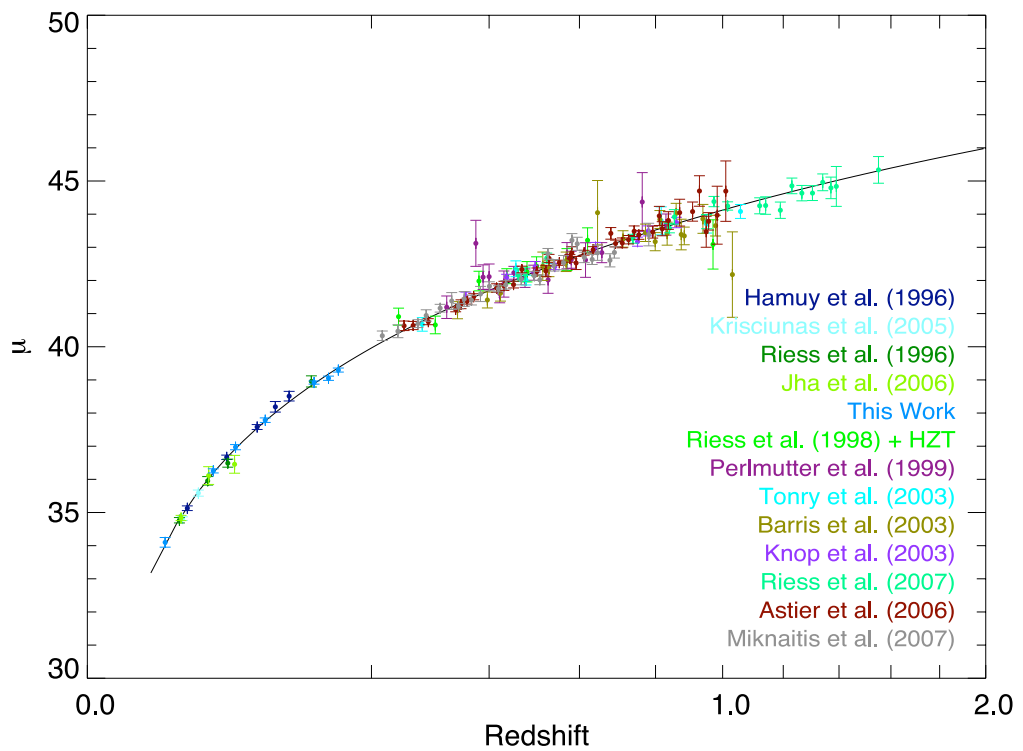


Figure 1.5: A Hubble diagram of type Ia supernovae, as published in [Kowalski et al. \(2008\)](#). This analysis combines data from a number of surveys spanning the last decade. This plot shows the distance modulus vs. redshift relation with the best-fitting flat cosmology of  $\Omega_m = 0.29, \Omega_\Lambda = 0.71$ )

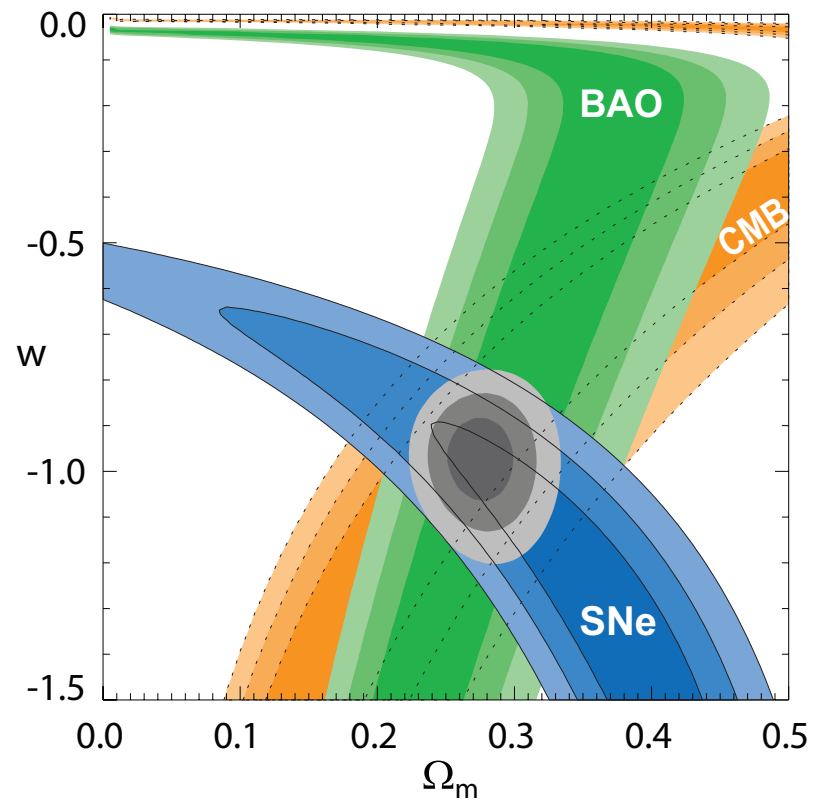


Figure 1.6: Current constraints of the cosmological parameters,  $\omega_{DE}$  and  $\Omega_M$ . This figure is taken from [Kowalski et al. \(2008\)](#). This analysis uses BAO, CMB and Supernova data. This figure requires that the overall energy content of the Universe has  $\Omega = 1$ , such that the Universe is spatially flat.

focus on the information about the type Ia population that can be inferred from their host galaxy population, but shall also briefly study the volumetric type Ia supernova rate.

### 1.5.1 The Type Ia Supernova Rate

The *volumetric rate* of type Ia supernovae has been carefully studied for the past decade; however, the uncertainty on these measurements is still high. At low redshifts ( $z \lesssim 0.1$ ), volumetric rate measurements have commonly suffered from small sample sizes (such as [Hardin et al. \(2000\)](#) with four events), or have been significantly affected by systematic errors due to biases in sample selection, such as targeting only luminous galaxies ([Blanc et al. \(2004\)](#)) or combining of various datasets ([Cappellaro et al. \(1999\)](#)). [Madgwick et al. \(2003\)](#) found type Ia supernovae in the spectra of galaxies observed as part of the SDSS-I survey. However, this measurement was dominated by uncertainties in the SDSS targeting system and aperture corrections. [Dilday et al. \(2008\)](#), using the first year results of the SDSS-II supernova survey, found that if only type Ia supernovae obeying the peak luminosity / decline-rate relationship described in §1.2.2 were considered, then the local type Ia supernova rate is  $r_V = [2.93_{-0.04}^{+0.17}(\text{systematic})_{-0.71}^{+0.90}(\text{statistical})] \times 10^{-5} \text{SNe Mpc}^{-3} h_{70}^3 \text{year}^{-1}$  when a constant rate is assumed. This is the best measured low redshift rate to date.

At higher redshift, determining the type Ia supernova rate is dominated by systematic uncertainties. Results indicate that type Ia supernova rate is higher at these redshift than that observed locally ([Barris & Tonry \(2006\)](#), [Neill et al. \(2006\)](#) and [Pain et al. \(2002\)](#) at  $0.3 < z < 0.8$ , and [Tonry et al. \(2003\)](#) and [Dahlen et al. \(2004\)](#) with  $z \sim 1$ , and [Strolger et al. \(2004\)](#) with  $z \sim 1.5$ ). These measurements have varying statistical and systematic uncertainties. [Neill et al. \(2006\)](#) considered the type Ia supernova rate to be related to the star-formation history of the Universe. [Dilday et al. \(2009\)](#) using the first two years of data from the SDSS-II supernova survey, showed that the type Ia supernova rate at intermediate redshifts,  $0.05 < z < 0.3$ , is higher than in the local Universe, and by splitting this measurement into redshift bins, and combining with the results of [Neill et al. \(2006\)](#), was able to show that the rate seems to be increasing out to  $z \simeq 0.5$ .

These volumetric rate measurements can be used to constrain the progenitor systems of these events. By observationally limiting the range of “delay-times” between the white-dwarf, and companion star binary forming, one can estimate the nature of this progenitor system. By convolving a delay-function with a cosmic star-formation history, a range of possible delay-times have been calculated, from  $\leq 1$  Gyr ([Barris & Tonry \(2006\)](#)), to  $\simeq 2 - 4$  Gyr ([Strolger et al. \(2004\)](#)), with [Maoz & Gal-Yam \(2003\)](#) finding  $\geq 2 \text{Gyr}$ .

Whilst the main focus of type Ia rate measurements has been to determine the volumetric rate, work carried out by [Oemler & Tinsley \(1979\)](#), [della Valle et al. \(1994\)](#) and later by [Mannucci et al. \(2005a\)](#) and [Sullivan et al. \(2006b\)](#), have attempted to determine the type Ia rate as a function of host galaxy mass and other properties. It has been shown that the type Ia supernova rate per unit mass is far higher in late-type galaxies than early-type galaxies ([van den Bergh et al. \(2005\)](#), [della Valle et al. \(1994\)](#)). In galaxies showing on-going star-formation activity, the type Ia supernova rate is higher in the spiral arms than the bulges of these objects ([Wang et al. \(1997\)](#)). Further to this, radio loud galaxies are seen to have higher type Ia supernova rate than those lacking radio emission ([Della Valle et al. \(2005\)](#)). These effects seem to suggest that the rate of type Ia events is not primarily dominated by the stellar mass of a galaxy, and some other process, possibly linked to the formation of new stars, is influencing the rate of these events. [Mannucci et al. \(2005a\)](#) (with a sample of local events), [Scannapieco & Bildsten \(2005\)](#) and later [Sullivan et al. \(2006b\)](#) (at higher redshifts) found evidence for a two component model for the type Ia supernova rate. This model, commonly known as the “A+B” model, suggested that the type Ia supernova rate is comprised of a component proportional to the stellar mass of the system, and another related to the formation of newly created stars. This model suggests the existence of two populations of type Ia supernova, one “prompt” component, with a short “delay-time” (caused by newly formed stars), and one “delayed” component, which is linked to the evolution of older, less massive systems. This relation with host morphology implies that despite the observed homogeneity of the type Ia supernova population, there is another undiscovered parameter that could be used to reduce the observed intrinsic scatter for hubble diagram measurements. Further to this, [Mannucci et al. \(2008\)](#) found that the type Ia supernova rate in highly overdense regions of the Universe, such as the centre of galaxy clusters, have far higher rates of supernova events than that of early-type galaxies in field environments per unit mass. Since this is not due to the mass distribution of these objects, it is found to be related to the morphology and activity of the parent galaxy. This results indicate that there is still some hidden parameter that determines the rate of these events, and thus affects their appearance.

## 1.5.2 The Type Ia Population

As noted above, the rate of type Ia supernovae seems to vary as a function of redshift, but more importantly, as a function of the properties of the environment that they are formed. However, in order to better understand these objects, and reduce their intrinsic scatter to better constrain cosmological models, an understanding of their diversity must be found, so that it can be used as another parameter in the modelling of type Ia

light-curves. This must be seen observationally. Thus there are two possible avenues to explore this possible variation; linking the observed environment of these events to their variation in light-curve shape, or doing the corresponding investigation with the spectra of these events. The work presented here will focus primarily on the environment of these events, and specifically typing their host galaxy properties with their observed light-curve distribution, but we shall outline the current understanding of supernova diversity in both fields.

### Diversity in Type Ia Spectra

The spectra of type Ia supernova reveal details about the chemical composition of these events, and with time sequenced observations, about the evolution of the explosion event. [Branch et al. \(1988\)](#), [Wells et al. \(1994\)](#) and [Fisher et al. \(1995\)](#) showed that the ejection velocities calculated from the absorption features of measured type Ia events appear to correlate with the peak luminosity of each event. These measurements study the chemical composition of the supernova explosion, and [Benetti et al. \(2005\)](#) used similar measurements of the spectral evolution of a set of low redshift supernova to split the type Ia supernova population into three groupings; faint objects (including 1991bg-like events), with low ejection velocities and rapid evolution of the SiIII absorption feature, normal objects with high velocity gradients but brighter absolute magnitudes, and larger expansion velocities than the faint objects, and a group of normal and 1991T-like events with a specific evolution of the SiIII feature, low velocity gradients and similar absolute magnitudes to the normal group. This empirical classification suggests that the explosion mechanism for each event is slightly variable and might explain the observed variability in peak magnitudes of the population. [Figure 1.7](#) shows the separation between these three groupings. [Hook et al. \(2005\)](#), with spectra from the SCP project, [Blondin et al. \(2006\)](#), using spectra from the ESSENCE project, and [Balland et al. \(2006\)](#) at intermediate redshifts, all independently showed that the spectra of type Ia supernovae are similar regardless of the redshift at which they are observed. The similarity of the supernova spectra imply that the chemical composition of such events is remarkably similar, and thus reduces the probability that this population of objects evolves with redshift. However, work carried out by [Foley et al. \(2008a\)](#) using spectra from the ESSENCE and KAIT surveys, found that whilst that the composite spectra appear very similar, the Fe III 5129Å line is weaker at higher redshift and in brighter supernova events, possibly suggesting that these events have lower temperatures and thus lower luminosities. However, it is unclear if these differences are due to a chemical evolution of the type Ia supernova event as a function of redshift or due to a difference in metallicity of the host galaxy, or just a selection effect.

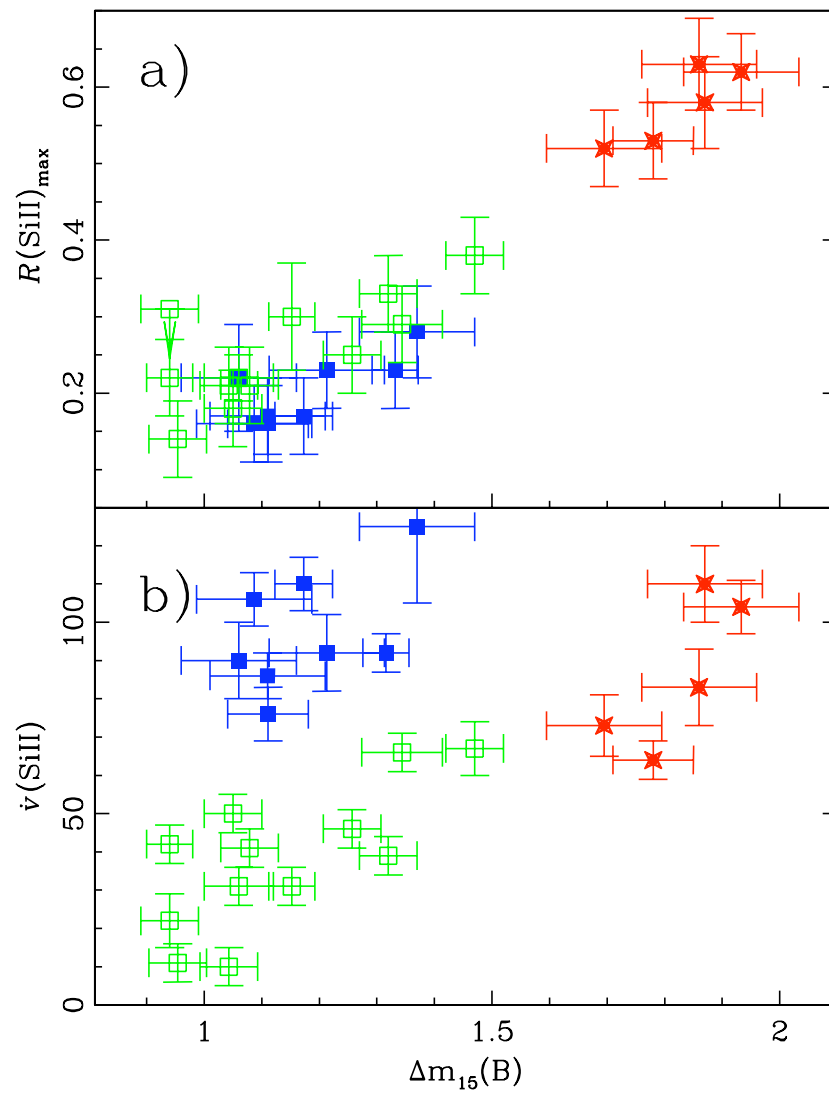


Figure 1.7: Comparing the velocity gradient and  $\mathcal{R}(\text{SiII})$  spectroscopic measurements to the photometric  $\Delta m_{15}$  parameter for a set of low redshift supernovae. The colours indicate the groupings of the supernova events. This figure is taken from [Benetti et al. \(2005\)](#).

Nugent et al. (1995b), showed that the depth of the SiII features in the wavelength range 5800Å to 6100Å may be correlated with the luminosity of the supernova event, and by comparing this to template models (Mazzali & Lucy (1993), Nugent et al. (1995a)), showed that this may be related to temperature differences in various burning stages. Other empirical correlations between the light-curves and spectra of type Ia supernovae have been found. Folatelli (2004), Garavini et al. (2007) and Hachinger et al. (2006), used equivalent width measurements to split the type Ia population into various sub-types whose photometry correlates with the measured peak brightness / light-curve decline rate relationship. All of these correlations are empirically determined and as yet no theoretical model has been found to account for the variability in spectral features of these objects, but these measurements indicate that the population of type Ia events, whilst being homogeneous with respect to the peak luminosity / light-curve decline rate relationship, still show levels of diversity.

### **Diversity in Host Galaxy Properties**

In §1.5.2, we looked at previous attempts to correlate the spectra and spectral evolution of type Ia supernovae with photometric properties and also to tie this to the variability of the chemical composition and temperature of such events. An alternative approach is to study the environment of the supernova event. Since these objects are observed in other galactic systems, it is common to link the properties of each supernova event to the overall stellar population of the host. Observationally, it has been seen that type Ia supernova occur primarily in late-type galaxies (Oemler & Tinsley (1979)), and as described in §1.5.1, the rate of type Ia supernovae seems to have a component dependent on the star-formation rate of the host galaxy. It has been shown that supernovae with brighter intrinsic peak luminosities are more commonly seen in late-type galaxies for a low redshift set of supernova (Gallagher et al. (2005), Hamuy et al. (2000), Riess et al. (1999), Hamuy et al. (1996d), Hamuy et al. (1995)). Sullivan et al. (2006b) showed that this relationship holds for a set of supernovae detected at high redshift, and matches that seen at low redshift, and extended this from a morphological separation to inferred galaxy properties, such as mass and star-formation rate. Thus, it has been at least partially shown that the observed differences in peak luminosity of type Ia events after they have been corrected for the observed decline-rate relationship, are correlated with the host galaxy type, and specifically the proportion of star-formation activity that is ongoing in the host galaxy.

There are two main differences between early-type and late-type galaxies; the population of stars that these dominate these galaxies and the level of dust that exists in these

different environments, with early-type galaxies believed to have little or no dust content. These differences mean that it may be possible that there are two different progenitor systems for creating a type Ia supernova event or that there is one progenitor system which is affected in different ways by the level of dust in its local environment. Models of two channels of producing type Ia's have been investigated by, for instance [Greggio & Renzini \(1983\)](#) and [Greggio et al. \(2008\)](#), who find that single degenerate or double degenerate channels are able to reproduce the observed type Ia supernova rate and associated distribution of delay times.

The main focus of type Ia supernova diversity studies is to better understand the systematic effects that this population may have on cosmological parameters, and methods to reduce the observed scatter of these events. [Sullivan et al. \(2003\)](#) showed that for a sample of morphologically classified type Ia events, the scatter observed on the Hubble diagram was reduced for a set of objects that occurred in early-type environments when compared to a dataset containing all objects. This may have a significant impact on future supernova surveys, such as DES ([The Dark Energy Survey Collaboration \(2005\)](#)), which aim to accurately constrain cosmological parameters, and thus may include a sample of events that are only seen in early-type galaxies.

### **Non-spectroscopically Confirmed Events**

Type Ia supernovae have been seen to consistently follow the peak-brightness / light-curve with relationship described in §1.2.2. Current large scale surveys spanning redshift space, use this relationship to prioritise spectroscopic follow-up observations. However, this relationship has not yet been used to create a sample of objects for determining cosmological parameters. [Wang et al. \(2007\)](#), [Wang \(2007\)](#), [Johnson & Crots \(2006\)](#) and [Sullivan et al. \(2006a\)](#) have introduced methods for accurately determining type Ia supernova event purely from their photometric properties. Such methods will be highly important for future surveys, which will cover large volumes to high redshifts, thus creating a large sample of probable type Ia events for cosmological analysis. With limited spectroscopic follow-up time, future Hubble diagrams may be dominated by events which are not spectroscopically confirmed, and whose redshift is estimated. In order to fully utilise these methods, the diversity of the type Ia population must be constrained, to ensure that these samples are not overly affected by contamination from non-Ia events, and that estimates of distance fully include all systematic uncertainties.

## 1.6 Description of this Work

This work is primarily concerned with data gathered as part of the first two years of the SDSS-II Supernova Survey. In §2, I will give a detailed description of this survey, and in particular the elements which are critical to determining a complete sample of objects. The primary aim of this analysis is to investigate the type Ia population. Thus we need a sample that is free from incompleteness, and any biases that may be introduced by the SDSS-II supernova survey. In §3, I shall describe efforts to create a sample that is free from biases and outline the method used to determine the efficiency of the SDSS-II survey. I shall also calculate the volumetric supernova rate in this sample. In §4, I shall describe how the host galaxies of each of the identified supernovae in §3 were determined, and how the derived properties of each of these galaxies was determined. In §5, I shall study the type Ia supernova rate, as a function of host galaxy properties, in an attempt to determine if the results from [Mannucci et al. \(2005a\)](#) and those from [Sullivan et al. \(2006b\)](#) are consistent with the sample outline in §4. In §6, I will look at the photometric properties of these events, specifically their light-curve decline rates and extinction estimates to discover if there exists a correlation similar to that seen in [Hamuy et al. \(2000\)](#) which have been split by galaxy type. In §7, I will discuss results concerning the residuals from the best-fit to the Hubble diagram for this sample, as a function of host galaxy type. Finally, I shall conclude in §8. Further to this, systematic tests of the results, specifically those in §5, are carried out in Appendices [A](#), [B](#), [C](#), [D](#), [E](#) and [F](#). Appendices [G](#) and [H](#) list the properties of the objects used in this analysis.

# Chapter 2

## The SDSS-II Supernova Survey

This Chapter describes the aims and search program for the Sloan Digital Sky Survey II (hence known as SDSS-II) Supernova Survey of which I am a collaborative member. This chapter references to work published in [Frieman et al. \(2008a\)](#), which provides an overview of the first year operations of the survey, [Sako et al. \(2008\)](#), which describes the search pipelines and operations, and [Dilday \(2008\)](#) which extends these analyses to include the second year of the survey. Other SDSS-II papers of interest include [Zheng et al. \(2008\)](#), which describes the SDSS-II spectral results, [Dilday et al. \(2008\)](#), which discusses the low- $z$  type Ia supernova rate and [Holtzman & SDSS-II Supernova Collaboration \(2006\)](#), which is primarily concerned with the photometric data reduction. The first year cosmological results will be presented in [Kessler et al. \(2009\)](#), whilst [Dilday et al. \(2009\)](#) and [Lampeitl et al. \(2009\)](#) are concerned with the high- $z$  type Ia rate and cosmological implications from the SDSS-II supernova survey alone, respectively. [Prieto et al. \(2007\)](#) and [Phillips et al. \(2007\)](#) study the peculiar SNe 2005gj and 2005hk, respectively.

### 2.1 Survey Aims and Description

In this section we discuss the goals of the SDSS-II supernova survey along with a description of its setup.

#### 2.1.1 Survey Aims

The SDSS-II Supernova Survey is one of three components of the SDSS-II project conceived with the aims of:

- Obtaining well measured multi-colour light-curves for several hundred type Ia SNe in the redshift range  $0.05 < z < 0.35$ , thus bridging the gap in published Hubble

diagrams in this redshift range, and constraining the cosmic expansion history of the Universe in this redshift range along with the properties of Dark Energy.

- Improving upon the systematic uncertainties in our understanding of SNe, by creating a complete SNe Ia sample in a redshift range which is completely in the Hubble flow and not dominated by noise in the light-curves or spectra. Other Supernova studies have reduced the statistical errors such that they are comparable with the systematic uncertainties. The photometric calibration errors of the SDSS survey are small especially over the well covered supernova survey area, see [Smith et al. \(2002a\)](#) and [Ivezić et al. \(2007\)](#).
- Anchoring the Hubble diagram for future supernova surveys and light curve training by providing a homogeneous sample which will be independent of large scale bulk flows. Recent work such as [Radburn-Smith et al. \(2004\)](#), [Hui & Greene \(2006\)](#), [Cooray et al. \(2006\)](#), [Cooray & Caldwell \(2006\)](#), have indicated that local effects such as peculiar velocities and phenomena such as the “Hubble bubble” ([Zehavi et al. \(1998\)](#), [Conley et al. \(2007\)](#) and [Neill et al. \(2007\)](#)) may be non-negligible sources of systematic uncertainty on cosmological measurements. The low-redshift part of the SDSS-II survey will be independent of these effects and be able to provide a full training set for the re-training of light-curve fitters.
- Studying SN rates, host galaxies and peculiar SNe discovered in this sample. The SDSS-II supernova survey will yield light-curves for a large number of unconfirmed type Ia events. With a well understood efficiency and selection process an accurate measurement of type Ia supernova rate will be possible ([Dilday et al. \(2008\)](#), [Dilday et al. \(2009\)](#)). With the well measured survey area, stellar populations and metallicities will enable important systematic uncertainties in the type Ia population to be uncovered ([Gallagher et al. \(2005\)](#)). These may be important in understanding biases when measurements of Dark Energy are made. Other peculiar Ia events ([Li et al. \(2001b\)](#), [Li et al. \(2003a\)](#), [Hamuy et al. \(2003b\)](#), [Li et al. \(2003a\)](#), [Aldering et al. \(2006\)](#)) will constrain the type Ia progenitor event and shed light on the diversity of these events. Further to this, future wide-field surveys, such as DES ([The Dark Energy Survey Collaboration \(2005\)](#)), PanSTARRS ([Kaiser et al. \(2002\)](#)) and LSST ([Tyson \(2002\)](#)) will measure optical multi-band light-curves for a large number of objects, with limited spectral confirmation only available for a small proportion of these. Thus these surveys will require the ability to photometrically confirm both object type and redshift. The SDSS-II survey’s well measured and well covered light-curves will provide an excellent test of this technique.

- Producing rest-frame UV light curve templates for High- $z$  surveys. Future high redshift surveys (with  $z \simeq 1$ ) will measure light-curves of type Ia supernovae in the rest-frame UV region. These light-curves will need to be matched with low-redshift templates. This part of the spectrum is difficult to measure locally, but with the redshift coverage of the SDSS-II survey, it is covered by the SDSS  $g$ -band thus improving upon rest-frame ultraviolet template data (Jha et al. (2006), Ellis et al. (2008)).

## 2.1.2 Technical Summary of the SDSS-II Survey

In order to achieve the goals described above, the SDSS-II Supernova Survey performed repeat imaging of the same 280 square degree area of the sky during the Autumn season (September - November) of 2005 to 2007 in five different filters to produce multi-colour light-curves of a large number of transient objects. The imaging survey was complemented by an extensive spectroscopic follow-up program to confirm supernova type and redshift.

This program exploited the capabilities of the SDSS 2.5m telescope (Gunn et al. (2006)) and its wide-field CCD imaging camera (Gunn et al. (1998)) at the Apache Point Observatory (APO) to survey a large volume of space at moderately high cadence at intermediate redshifts ( $0.05 < z < 0.4$ ). The wide field-of-view camera operates in time-delay-and-integrate (TDI, or drift scan) mode allowing for efficient detection of transient objects, with nearly simultaneous observations in the SDSS  $ugriz$  bands. This volume is not probed by other existing surveys, which instead either focus on a large proportion of the sky with a moderate sized telescope (such as the Katzman Automatic Imaging Telescope (KAIT) (Li et al. (2003b))) to probe local objects, or concentrate on deeply imaging several smaller sized fields with a larger instrument (such as the ESSENCE project (Smith et al. (2002b)) or the Supernova Legacy Survey (SNLS) (Pritchett & For The Snls Collaboration (2005))) to discover objects at high redshift. The SDSS has a well calibrated multi-band photometric system (Fukugita et al. (1996)) enabling precise measurements of supernova light curves with controlled systematics. Photometric calibration over the survey area is accurate to roughly 0.02 mag in the  $g$ ,  $r$  and  $i$  bands, and 0.03 mag in the  $u$  and  $z$  bands (Adelman-McCarthy et al. (2007)), with a factor of  $\sim 2$  improvement from the repeat imaging of the survey area (Ivezić et al. (2007)). The Supernova Survey scans at the normal (sidereal) SDSS survey rate, which yields 55-s integrated exposures in each passband, such that a 50% detection completeness rate for stellar sources is achieved for sources with  $u = 22.5, g = 23.2, r = 22.6, i = 21.9, z = 20.8$ . For comparison, the typical peak magnitude for a SN Ia with no extinction is  $r \simeq 19.3, 20.8$  and  $21.6$  mag for

$z = 0.1, 0.2$  and  $0.3$  respectively.

An overview of the original SDSS infrastructure is given in [York et al. \(2000\)](#), with various discussions on the pipelines, calibrations, target selection, data releases and value-added catalogues are given in [Lupton et al. \(2001\)](#), [Pier et al. \(2003\)](#), [Strauss et al. \(2002\)](#), [Stoughton et al. \(2002\)](#), [Abazajian et al. \(2003\)](#), [Adelman-McCarthy et al. \(2006\)](#) and [Blanton et al. \(2005\)](#). A full technical summary of the SDSS-II Supernova Survey is given in [Frieman et al. \(2008a\)](#). Figure 2.1 shows the measured filter curve for the SDSS filter set.

## 2.2 Survey Observations

Here we describe the region of the sky covered by the SDSS-II Supernova Survey, the SN search pipeline and algorithms, spectroscopic follow-up programs, final photometry reductions and light-curve fitting techniques used in the SDSS-II Supernova Survey.

### 2.2.1 Stripe 82

The SDSS-II Supernova Survey covered a region of the sky called “stripe-82”, centred on the celestial equator in the Southern Galactic hemisphere, bounded by  $-60^\circ < \alpha_{J2000} < 60^\circ$  (20 hrs to 4hrs in right-ascension,  $\alpha$ ) and  $-1.258^\circ < \delta_{J2000} < 1.258^\circ$  in declination,  $\delta$ . This stripe has been imaged multiple times in photometric conditions during the original SDSS-I survey and coadded images from those runs provided a deep template image for the supernova survey. This stripe is divided into northern (N) and southern (S) strips with a small overlap between them, such that the survey encompasses  $\sim 280$  square degrees. The SDSS imaging telescope is capable of scanning approximately one strip every night, such that, including breaks for full moon (the five brightest nights around full moon are used for telescope engineering), each part of the survey region is observed every four nights during an observing season, assuming good weather conditions. Figure 2.2 shows the sky coverage versus survey time for the 2006 observing season for the southern half of the survey area, whilst Figure 2.3 shows the number of imaging scans for both the northern and southern strips for both the 2005 and 2006 seasons.

As noted earlier this region of the sky has been well measured by the SDSS survey, with multiple images being coadded to produce a deep image of the sky ([Annis & Strauss \(2008\)](#)). This image is up to 1.75 magnitudes deeper than the single scan images, with a limiting magnitude of  $r = 23.95$ . This deep image not only allows accurate measurements of faint host galaxies but also provides an excellent galaxy sample for comparison

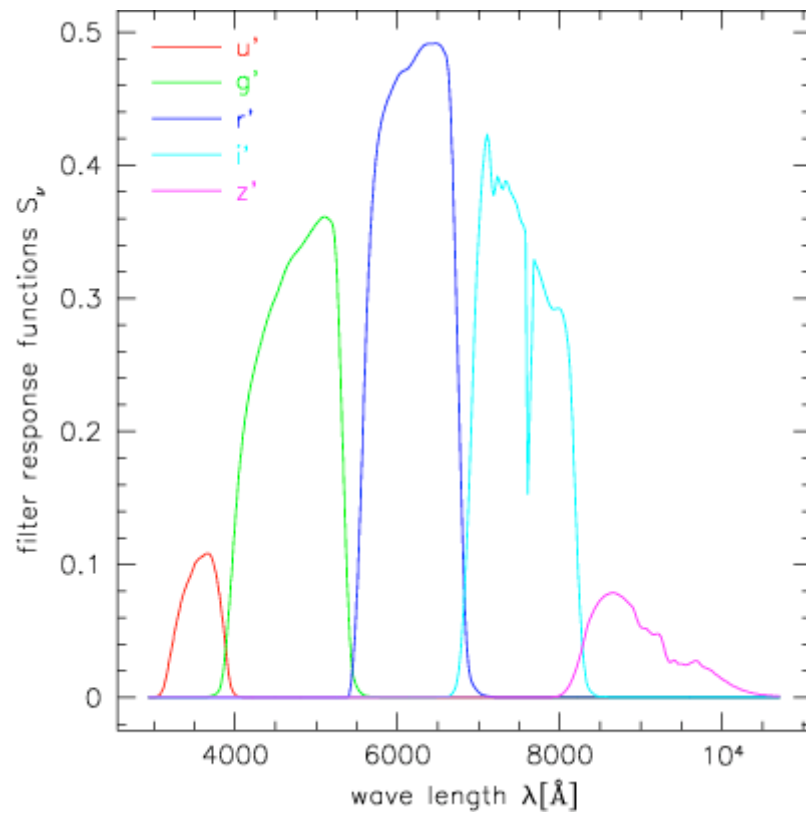


Figure 2.1: Figure showing the measured SDSS filter response functions. From left to right:  $u$ ,  $g$ ,  $r$ ,  $i$ , and  $z$ . These curves include the transmission of the atmosphere above the APO on a night of average humidity at airmass 1.3.

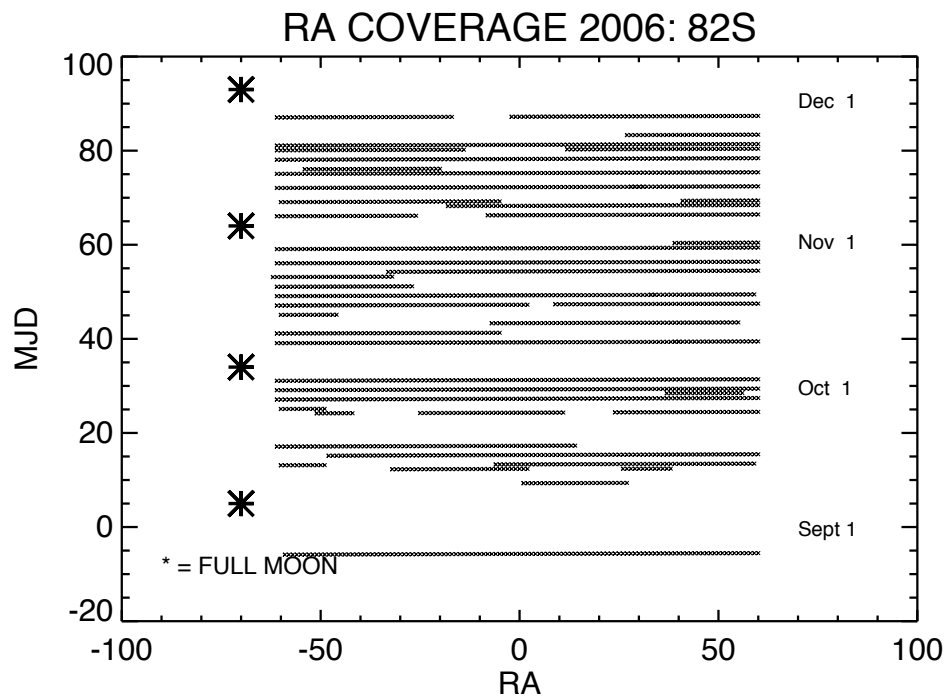


Figure 2.2: The right ascension (in degrees) range covered by the SDSS-II Supernova Survey imaging runs versus epoch (measured from the 1st September 2006, i.e.  $\text{MJD}=53980 = 0.$ ) for the southern strip during the 2006 observing season. The first scan was taken in late August to minimise survey edge effects. The first part of September suffered from poor observing conditions. The large asterisks denote gaps around full moon. This figure is re-printed from [Frieman et al. \(2008a\)](#).

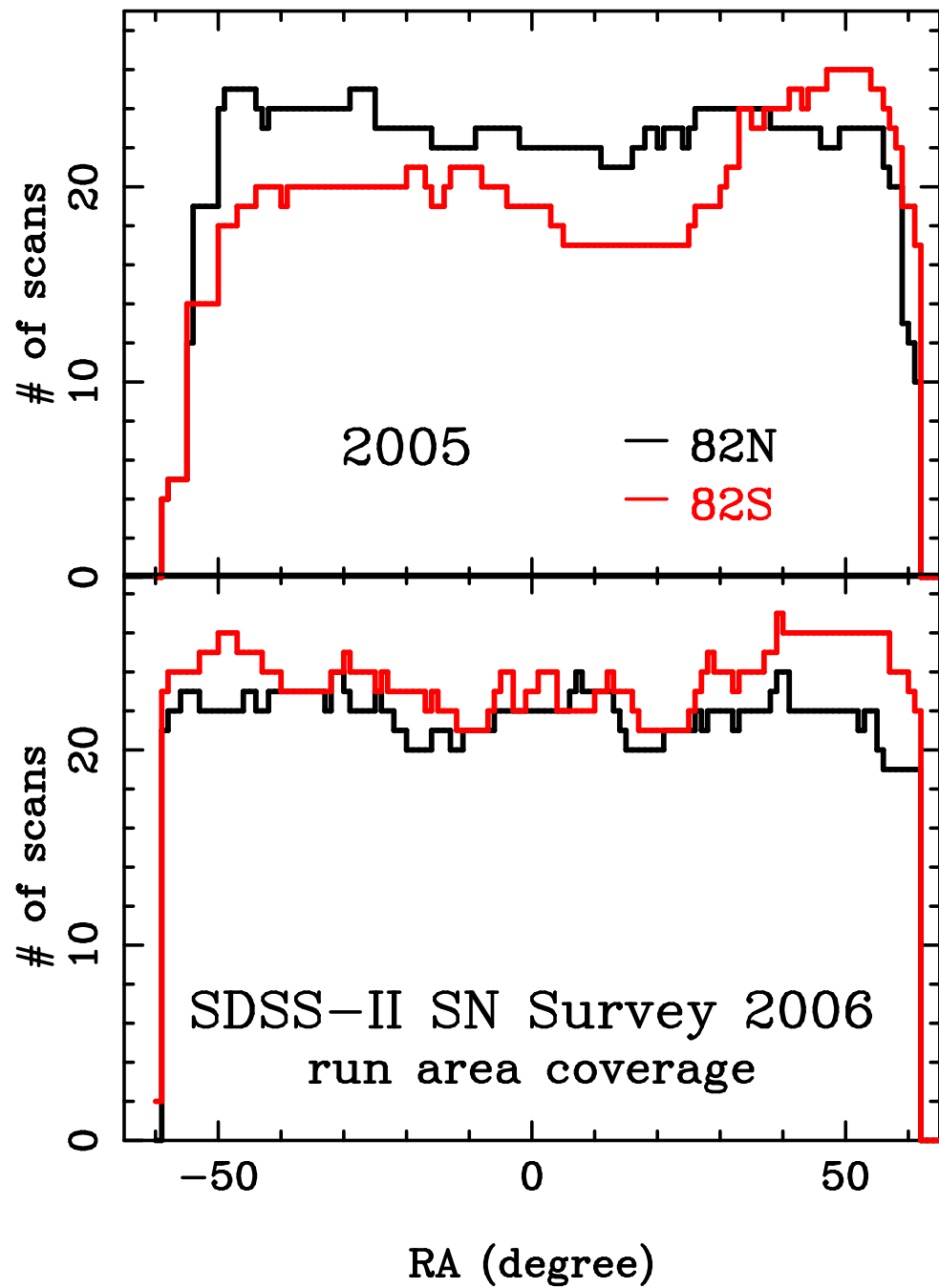


Figure 2.3: The number of imaging scans of the northern (black) and southern (red) strips for the 2005 (top) and 2006 (bottom) seasons of the SDSS-II Supernova Survey. The 2006 season is more evenly distributed between the northern and southern strips with little difference in right ascension coverage. This figure is re-printed from [Frieman et al. \(2008a\)](#).

(see §4.5). This area of the sky is easily accessible by telescopes in both the northern and southern hemispheres and thus has been covered in many wavelengths, including the Infrared by the UKIDSS survey (Lawrence et al. (2007)) providing a useful cross-check. Detailed information of the calibration of “stripe-82” can be found in Ivezić et al. (2007).

### 2.2.2 The Search Pipeline

There are five main parts to the supernova search pipeline: photometric reduction, image subtraction, automated object selection, visual inspection and light-curve fitting for spectroscopic target selection. We describe each briefly. The data is processed using a dedicated computer cluster at the APO to avoid a backlog of unprocessed data. For a full nights worth of imaging data, the entire pipeline runs for approximately 20 hours enabling the survey to keep up with the data flow for rapid spectroscopic selection.

In the first stage of the search pipeline, the imaging data was acquired from the camera and processed through the SDSS photometric reduction pipeline, known as PHOTO (Lupton et al. (2001)) to produce “corrected”, astrometrically calibrated (Pier et al. (2003)) images for the SN search data. In the second stage, the deeper coadded reference images (§2.2.1), comprising of data taken up to 2004, are convolved with a Point Spread Function (PSF) which matches the search images and subtracted, using a modified version of the PHOTPIPE software used in the ESSENCE survey (Miknaitis et al. (2007)). “Real-time” subtraction is limited to the *gri* bands, which are the bands of most interest for detecting supernovae in our redshift range. The subtracted images are then processed through an automated object detection algorithm (Schechter et al. (1993)), which also produces initial photometric measurements. The signal-to-noise threshold for object detection is  $g \simeq 23.2$ ,  $r \simeq 22.8$  and  $i \simeq 22.5$  for typical conditions.

In the third stage of the search pipeline objects of interest are selected from those detected in the difference images. Objects which are detected in at least two of the *gri* images with close positional matches (within  $0.8''$ ) and at least 2 contiguous pixels each above  $3.0\sigma$  that are not coincident with previously catalogued stars or variable objects and are not detected as moving during the  $\sim 5$  minute observing period during the *g* and *r* exposures are selected for further inspection. This removes cosmic rays, single-band spurious noise fluctuations, a large fraction of asteroids and rapidly moving objects and Active Galactic Nuclei (AGN), and other variable objects. The vetoed area of the survey accounts for  $\sim 1\%$  of the total survey area. Objects that pass these selection cuts include a variety of transient objects. Physical objects include slow moving asteroids that were not vetoed by the “moving” flag, non-catalogued AGNs and variable stars, high

proper-motion stars and supernovae. Non-physical objects include improperly masked diffraction spikes from bright stars and artifacts of improper image differencing (dipoles).

In the 2005 season, all new objects that pass the above cuts were visually inspected in the fourth stage of the search pipeline. This visual scanning is intended to reject artifacts and other objects that are clearly not supernovae. This *handscanning* process involved a webpage interface that displayed images of the object (in all 3 processed bands) along with information on the current detection and any coincident detection. An example of the webpage interface is shown in Figure 2.4. For each scanned object, a set of choices for the object's classification was available,

- **None**

The object does not appear to be an authentic astrophysical transient. This is often used for objects which are only marginally above the detection threshold and are indistinguishable from noise.

- **Artifact**

Artifacts of the subtraction process. These are generally diffraction spikes from bright stars that extend across two frames and thus have been improperly masked out.

- **Moving**

The object appears to be moving. There is an apparent offset between the detections in the *g* and *r* filters, which are the two most widely separated filters on the SDSS camera.

- **Saturated Star**

A bright star which did not subtract cleanly.

- **Dipole**

An object with adjacent regions of positive and negative subtraction residuals. These objects are generally in the core of bright galaxies or stars, where the PSF matching has not worked perfectly resulting in large differences in absolute magnitude.

- **Variable**

The object appears to be near the core of a star-like (as opposed to galaxy-like) object. This object may have detections that span a large period of time (including two different seasons) indicating that it is not supernova like.

- **Transient**

An object that is not obviously moving, but does not have a host galaxy. This object must be a single observation (i.e. cannot have previously coincident observations)

- **Cosmic Ray**

A sharply defined transient unresolved detection (i.e. less than two pixels). This category is almost never used, as the requirement that each object is detected in at least two filters removes these events.

Further to these non-supernova classifications there are four categories of supernova candidates. In all categories, a supernova classification implies that the object has the appearance of a supernova (i.e. a point source) and does not fall in to any of the categories listed above:

- **SN Gold**

The object is associated with, and is well separated from, a galaxy-like object. The object shown in Figure 2.4 is a typical example.

- **SN Silver**

This is an object with no host galaxy, but is not a transient object (i.e. has at least one instance of a previous detection). The object is also not moving.

- **SN Bronze**

This is an object associated with the centre of a galaxy-like object. Objects classified as SN Bronze usually include AGN-like events.

- **SN Other**

These are objects that have features inconsistent with a normal supernova, but are nevertheless an interesting astrophysical transient object. This category allows interesting events to be recorded, but are not necessarily high priority for spectroscopic follow-up.

With the selection criteria described above, an average of 3000 to 5000 objects were inspected each night by six scanners. This sample was overwhelmingly dominated by solar system objects. Thus, for the 2006 and 2007 seasons, the number of objects was reduced by only scanning bright objects ( $r < 21$ ) or objects with at least two epochs of observations. Further to this, for the 2006 and 2007 seasons, a new software filter, the “*autoscanner*”, was introduced. This software uses statistical classification techniques to identify and filter out first-epoch background non-SN objects, especially unmasked

**cutout frame**

**object frame**

**history frame**

**result frame**

Scanner	Richmond	No updates	All
Obj Id	492763		
srun	3607	sfield	136
trun	3659	ofield	109
rr	10	cc	1
ra	-9.402102	decl	-0.839913
gmag	21.730	g_delta	0.79
rmag	20.607	r_delta	0.79
imag		i_delta	
Flags			
TU	115		
Objects			
#	0		
Scanned			

Back to initialising page.

Obj Id	srun	trun	rr	cc	ra	decl	MJD	gmag	rmag	imag	Days Before
<a href="#">470312</a>	3597	3585	10	2	43.40515	0.83969	53625.2	21.84	20.69	20.88	1
<a href="#">501616</a>	3607	3585	10	2	43.40569		53627.2	0	20.73	20.6	1
<a href="#">513457</a>	3610	3659	10	1	43.40515	0.83979	53628.1	0	20.97	20.7	2

- None
- 1) Artifact
- 2) Moving
- 3) Sat. Star
- 4) Dipole
- 5) Variable
- 6) Transient
- 9) Cosine Ray
- 101) SN GOLD
- 102) SN SILVER
- 103) SN BRONZE
- 100) SN OI HbR
- Band Void

Figure 2.4: Example of the handscanning web interface. The top left panel (“cutout frame”) shows the search (left column), template (middle column) and difference (right column) images for the *g* (top row), *r* (middle row) and *i* (bottom row) filters. The bottom left panel (“history frame”) shows information on any previous detections of a transient object coincident with the current objects sky position (within 0.8”). The top right panel (“object frame”) displays summary information on the present detection of the object, whilst the bottom right panel (“result frame”) allows the human scanner to evaluate the objects classification.

diffraction spikes, artifacts of imperfect image registration (dipoles) and moving objects, by using the 2005 search data as a training set. This software is described fully in [Sako et al. \(2008\)](#). For bright objects, only  $\approx 0.7\%$  of objects are incorrectly tagged as moving, the main focus of the autoscanner. The autoscanner was found to be more reliable than human scanners in the classification of artifacts.

Objects that are visually classified into one of the four SN categories are denoted as *candidates*. These candidates are given a unique supernova identification (SN ID) number. A candidate will always remain a candidate unless it is manually vetoed by a scanner (this rarely happens). Once an object has been classified as a candidate, other appearances of an event at the same position (such as a later epoch on the light-curve of a supernova event) is never manually scanned again. Subsequent object detections in difference images at the same position are automatically associated with the same candidate.

In the 2005 season, this process took an average of 2-3 hours per scanner and resulted in an average of  $\sim 200$  new candidates per night. In the 2006 and 2007 seasons, with the new constraints and the introduction of the autoscanner software, this dropped significantly to approximately 10-20 minutes per session. In 2005, approximately 6,752 square degrees of imaging data was processed on the mountain: 190,020 objects were visually scanned, resulting in 11,385 unique SN candidates. In 2006, approximately 7,354 square degrees of data was processed, with only 14,441 objects being scanned, yielding 3,694 candidates.

The fifth and final stage of the supernova pipeline involves fitting model type Ia, type Ib/c and type II supernova light-curves to the *gri* data for each SN candidate. The non-Ia supernova models consist of template light curves constructed from photometric measurements of individual supernovae provided by the SUSPECT database ([Richardson et al. \(2001\)](#)), coupled with the corresponding SN spectral model provided by [Nugent et al. \(2002\)](#). The light-curves in the observed *ugriz* filters are calculated on a grid of four parameters,  $(z, A_V, T_{max}, [\Delta m_{15}(B), \text{template SN}])$ , where  $z$  is the redshift,  $A_V$  is the number of magnitudes of extinction in the V-band (assuming  $R_V = 3.1$ ), and  $T_{max}$  is the time of B-band maximum light. The last term corresponds to either the peak-luminosity / decline-rate parameter ([Hamuy et al. \(1996d\)](#)) for the Branch-normal Ia models, or the particular SN template for the peculiar Ia (1991T-like and 1991bg-like), and the core collapse models. An assumed cosmology of  $\Omega_m = 0.3$  and  $\Omega_\Lambda = 0.7$  is used to convert the redshift to luminosity distance. For the Ia templates, a fiducial peak B-band absolute magnitude of  $M_B = -19.0 + 5 \log(H_0/70)$  is assumed, where  $H_0$  is the Hubble constant in units of km/s/Mpc, for a standard type Ia with  $\Delta m_{15}(B) = 1.1$ .

The best-fit  $\chi^2$  is recorded for each of the three supernova types (Ia, Ib/c, II). In addition to identifying the supernova type with the lowest  $\chi^2$  value, we also searched for the nearest galaxy within  $10''$  from the supernova position in the SDSS galaxy catalog and refit, and retyped the light-curves using the best estimate of the galaxy redshift as a prior, using galaxy photometric redshifts from [Oyaizu et al. \(2007\)](#) and spectroscopic redshifts from the SDSS DR5 catalogue ([Adelman-McCarthy et al. \(2007\)](#)). For some candidates, additional difference imaging was carried out in the  $u$  and  $z$  bands, as type II supernovae are seen to be generally bluer ( $u - g \lesssim 0.5$ ) than type Ia events at early epochs.

In order to prioritise spectroscopic follow-up, all supernova Ia candidates found before peak with estimated current r-band magnitude  $\lesssim 20$  were placed upon the spectroscopic target list, so that our follow-up observations were nearly complete to that magnitude. The minimum value of the  $\chi^2$  statistic in both the cases with, and without the galaxy host redshift was also used to determine a candidate's viability for spectroscopic follow-up, as the scheduled spectroscopic time was far smaller than would have been needed to target every supernova event. Other factors, such as the galaxy brightness, and supernova-galaxy separation, were also used for prioritising the list of possible targets. This photometric pre-selection of type Ia supernovae proved very effective with approximately 90% of the candidates initially targeted as type Ia supernovae after two or more epochs of imaging data resulted in a spectroscopic confirmation. The full photometric classification and spectroscopic target selection for the SDSS-II Supernova Survey is discussed in detail in [Sako et al. \(2008\)](#).

### 2.2.3 Spectroscopic Follow-up

Here we discuss the spectroscopic observations of the SDSS-II Supernova Survey, with particular focus on activities at the ESO New Technology Telescope (NTT) and William Herschel Telescope (WHT) for which I carried out the spectroscopic follow-up.

The classification of type Ia supernovae (and all other supernova classes) are defined by their spectroscopic features. Spectra of these objects provides both accurate redshift information, and in most cases, information on the host galaxy, which may be used later for host galaxy subtraction purposes. Spectroscopy is primarily used to obtain redshifts and supernova typing, but also to measure other properties. Some of these include, multi-epoch spectroscopy of peculiar supernovae, supernovae in underluminous host galaxies, SN Ib/c and hypernova objects, detailed spectroscopic properties of supernova Ia hosts and multi-epoch studies of line features and their diversity in the type Ia population.

Where possible, a host galaxy redshift is used to more accurately determine the redshift of the supernova event, since the spectral features used to estimate the redshift from a galaxy spectrum are narrower than those used in supernova spectra, as the explosion mechanism causes a broadening of the spectral features. In the SDSS-II Supernova Survey, this was possible for approximately 66% of spectroscopically confirmed Ia's, yielding redshifts accurate to approximately  $\Delta z = 0.0005$ , whilst those of objects where only a supernova redshift is available are accurate to  $\Delta z = 0.005$ .

Spectroscopic follow-up in the SDSS-II supernova survey was carried out on a number of facilities. The primary telescopes used in the survey were the ARC 3.5m, NTT 3.6m, WHT 4.2m, MDM 2.4m, NOT 2.5m and KPNO 3.5m telescopes for low redshift objects, whilst the Subaru 8.2m, HET 9.2m, KECK 10m and SALT 11m telescopes were used for high redshift objects. In addition, several observatories were used to image SDSS supernovae to provide additional photometric data points on the light-curves, and extend them after the SDSS-II supernova survey had completed observations for the season. Telescopes used for this purpose include the University of Hawaii 2.2m, the Hiltner 2.4m at MDM, the New Mexico State University 1m at APO, the ARC 3.5m, the 1.8m Vatican Advanced Technology Telescope at Mt. Graham, the 3.5m WIYN telescope at Kitt Peak, the 1.5m optical telescope at Maidanak Observatory in Uzbekistan, and the 2.5m Isaac Newton Telescope at La Palma. In addition, the Carnegie Supernova Project (CSP; [Hamuy et al. \(2006\)](#)) obtained optical and near-infrared (NIR) imaging for many of the SDSS supernovae, and the SNFactory ([Aldering et al. \(2002\)](#)) obtained optical spectroscopy.

The spectra are analysed at the observatories to provide quick reductions confirming supernova type and provisional redshift information. All spectroscopically confirmed supernovae were announced in a timely manner through the Central Bureau for Electronic Telegrams (CBET). In addition, bright supernova candidates observed for at least two epochs and found on the rise were announced, often before spectroscopic confirmation. Moreover, for the 2006 and 2007 seasons, all candidates, with all relevant photometric information (based on the on-mountain reductions), were made available on the world-wide web as soon as they were identified<sup>1</sup>.

The fully reduced spectra are then analysed ([Zheng et al. \(2008\)](#)) to determine supernova type, redshift and host galaxy information, where available, such that the whole SDSS-II supernova sample is analysed in the same fashion. Only minor differences are

---

<sup>1</sup><http://sdssdp47.fnal.gov/sdsssn/sdsssn.html>.

found between the reductions produced at the observatories and in the complete sample, with the most prominent ones being more accurate typing for low signal-to-noise observations. This typing uses a standard cross-correlation technique (Tonry & Davis (1979)) to normal and peculiar Ia events from the work of Nugent et al. (2002), and to a public library of well measured supernova spectra (Matheson et al. (2005), Blondin & Tonry (2007)). There are two categories of type Ia supernova in the SDSS-II supernova survey; those that are considered to be secure Ia's, and those that are consistent with template Ia spectra but whose identification is not certain. These are referred to as "Ia?". The classification of objects as "Ia" and "Ia?" is somewhat subjective, but is based upon statistics of the cross-correlation analysis.

### **Spectroscopic Follow-up at the NTT**

Spectroscopic observations at the New Technology Telescope (NTT), La Silla, Chile, took place for the 2006 and 2007 seasons of the SDSS-II supernova survey. For each month of the survey, we were awarded 4 or 5 nights for each of September, October, November and December, with the December period used to spectroscopically confirm objects discovered late in the season, and to obtain accurate host redshifts of probable type Ia events that were not spectroscopically confirmed.

The 3.6m NTT telescope is altitude-azimuth mounted. That is the telescope is allowed to be moved in altitude and azimuth as separate motions. Thus for this mount the telescope field-of-view then rotates at a varying speed while the telescope tracks along the sky. The NTT has active, instead of adaptive, optics so that it corrects the defects and deformation of the telescope and mirror, but does not correct the turbulence, thus ensuring that the optics are always in perfect shape. The telescope has two Nasmyth platforms, so that two sets of instruments are mounted simultaneously. At the time of our observations, the available instrumentation consisted of EMMI, for optical imaging in blue and red, as well as low/medium/high resolution spectroscopy, and SUSI2 for high-resolution imaging, and a infrared instrument SOFI.

Our observations were carried out using EMMI (ESO Multi Mode Instrument). This instrument has since been decommissioned and replaced by EFOSC2. EMMI is a multi-purpose instrument allowing observations in the visible wavelengths, supporting wide-field imaging, low-resolution multi-object or long-slit grism spectroscopy, medium resolution long-slit grating spectroscopy and Echelle spectroscopy.

Our observations were carried out in "RILD" mode: Red Imaging and Low Dispersion

Spectroscopy. This produced low dispersion (0.28 nm / pix) spectra in the wavelength range  $\sim 4000\text{\AA}$  to  $8500\text{\AA}$ . The detector has two CCDs, which are mounted side-by-side, with an overscan gap in between. This set-up provides a large field of view ( $9.0' \times 9.9'$ ) meaning that the supernova candidate and host galaxy can be easily identified. Observations were carried using grism #2 and a  $1.0''$  or  $1.5''$  slit width depending on whether the object observed is a supernova candidate or host galaxy, and also depends on the seeing conditions. An order-sorting filter was used with the standard star calibration spectra so that second-order contamination (which can be seen at  $> 8200\text{\AA}$  can be later removed (Stanishev (2007))). For spectroscopic observations the slit was generally orientated at parallactic angle, to minimise photon loss, or was orientated to obtain spectra of both the supernova and potential host galaxy (when there is clear separation). Exposure times were chosen such that the resulting spectra had a signal-to-noise (S/N) of 10 per pixel, with is approximately 1800 seconds for faint objects ( $r \sim 21$ ) or between 900 ( $r \sim 20.5$ ) and 1200 seconds for the brighter objects ( $r \sim 20$ ). The median seeing at the La Silla site was  $0.9''$ .

Objects chosen for spectroscopic follow-up were usually required to have at least two epochs of photometry before targeting to guarantee that the source was not a solar system object. Objects at high redshift were prioritised according to their discovery time (early sources were prioritised over fading sources to ensure well sampled light curves) and distance from the host, with well separated objects favoured over potential AGN sources.

Reductions of the obtained spectra were produced at the telescope to provide quick and accurate determinations of supernova type and redshift. On several nights a variety of telescopes would be observing supernova candidates. These quick reductions allowed other observatories to monitor each others progress and ensure that time was not wasted by producing multiple spectra of the same candidate. The reductions were carried out using the reduction software IRAF (Tody (1986), Tody (1993)) and PYRAF (Greenfield & White (2000), de La Peña et al. (2001)), with scripts relevant to NTT reductions written for this purpose. The procedures laid out in Valdes (1986) and Valdes (1992), along with standard NTT procedure were followed. Bias frames, for removing extra signal in the spectra, and flat-field frames, for determining the relative response of the CCD and thus remove any wavelength dependent bias due to the instrumentation from the spectra, were taken during daylight. Helium and Argon lamps were used to produce arcs, which are later used to wavelength calibrate the spectra. During night-time observations a cosmic-ray rejection method, L. A. Cosmic (van Dokkum (2001)) was used to remove unwanted cosmic-rays. Telluric lines in the output spectra were removed manually. For

the 2007 season, the reduced spectra were compared to a set of template spectra, using the Supernova Identification (SNID) code (Blondin & Tonry (2007)) to produce accurate typing and redshift information. Figure 2.5 shows an example of a fully reduced flux-calibrated one-dimensional spectra from the 2007 season of the SDSS-II supernova survey as observed at the NTT. Overplotted is a template spectra using the SNID code.

### Spectroscopic Follow-up at the WHT

Observations at the William Herschel Telescope (WHT), La Palma, took place during the 2005 season of the SDSS-II supernova survey. The primary mirror on the WHT is 4.2 metres in diameter. Observations during this season took place over 12 nights in September, October and November 2005. This altitude-azimuth mounted observatory is equipped with several instruments. Our observations used the Intermediate dispersion Spectrograph and Imaging System (ISIS). ISIS is a high-efficiency, double-armed (red and blue), medium-resolution (8-120 Å/mm) spectrograph, allowing a combined wavelength coverage of 4000Å to 9000Å. The R300B and R316R gratings were used in the blue and red arms of the instrument, respectively, providing dispersions of 0.86Å and 0.93Å per mm, respectively. A standard 5300Å dichroic was used to split the light into the red and blue arms. Neon and Argon lamps were used to produce arcs for wavelength calibration. The median seeing at La Palma was 0.7", although the site occasionally suffers from large levels of dust. Similar to the NTT observations, exposure times were calculated so that our spectra possessed a signal-to-noise of 10 per pixel. That was approximately 1800 seconds for faint objects ( $r \sim 21$ ) and between 900 to 1200 seconds for bright objects ( $r \sim 20 - 21$ ).

Reductions at the WHT were carried out in a similar fashion to that on the NTT, with the exception that the WHT is a dual-arm spectrograph so the spectra from the blue and red arms were reduced separately, and then combined after all of the reduction stages. Since the SNID code was not publically available for the 2005 season, resultant spectra were compared to template spectra visually, with prominent features and host galaxy emission and absorption lines used to provide approximate redshift information. Figure 2.6 shows an example of a fully reduced, flux-calibrated, one-dimensional spectra, from the 2005 season of the SDSS-II supernova survey as observed at the WHT. A template type Ia spectrum is overplotted.

### 2.2.4 Final Photometry

To obtain more precise photometry than the on-mountain difference imaging pipeline, the imaging data in all five *ugriz* SDSS filters for all spectroscopically confirmed, and

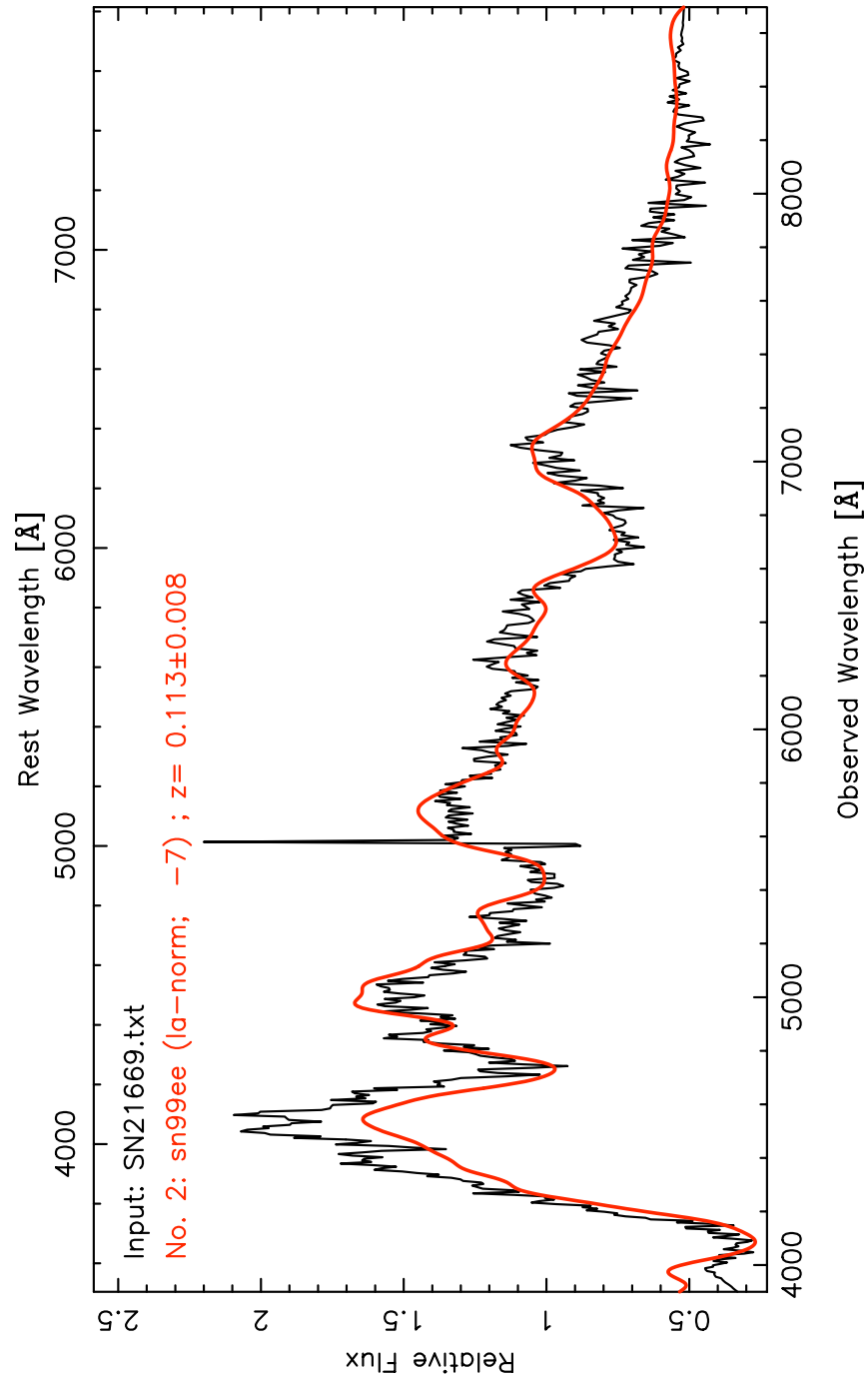


Figure 2.5: An example of a fully reduced, flux calibrated spectra of a type Ia supernova from the 2007 season of observations at the NTT. This object has been compared to a set of template spectra using the SNID code. An example of a template spectra is overplotted, showing that this object is a normal type Ia supernova at  $z = 0.113$  and is observed before peak brightness. No host galaxy subtraction has carried out on the observed spectra. This object has been given an IAU designation of 2007rs.

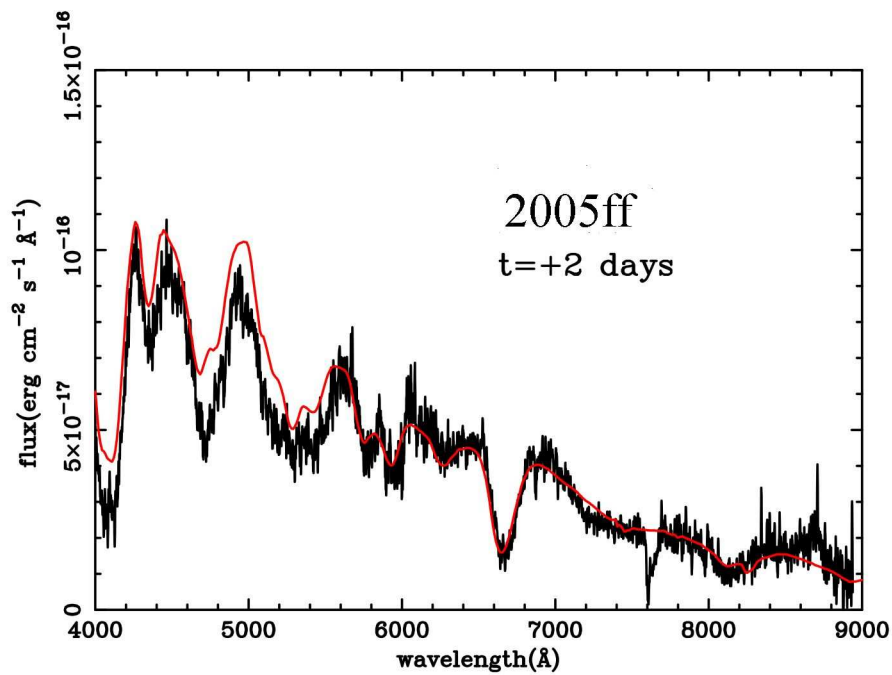


Figure 2.6: An example of a fully reduced, flux calibrated spectra of a type Ia supernova from the 2005 season of observations at the WHT. An example of a template spectra is overplotted, showing that this object is a normal type Ia supernova at  $z = 0.087$  and is observed before peak brightness. No host galaxy subtraction has carried out on the observed spectra. This object has been given an IAU designation of 2005ff.

other interesting supernova candidates (see §3) was re-processed through a final photometry pipeline (Holtzman & SDSS-II Supernova Collaboration (2006)). This “scene-modelling” code is developed for the SDSS-II supernova survey. In this “scene-modelling photometry” (SMP) pipeline the supernova and host galaxy (the *scene*) are modelled respectively as a time varying point-source and a background that is constant in time with a time-varying PSF. A set of well-measured stars around each supernova are used to produce frame scalings, and astrometric solutions, for each of the SN frames, as well as for frames before the supernova explosion, taken as part of either the SDSS-I survey or the supernova survey. Thus the error on each flux measurement can be accurately determined as there is no convolution of the images. Finally, the entire set of frames are simultaneously fit for a single supernova position, a fixed galaxy background in each filter and the brightness of the supernova in each frame.

The SMP pipeline often discovers photometric measurements at extra epochs when compared to the mountain-top image differencing pipeline. However, photometry is only detected in the  $u$  and  $z$  bands for low redshift objects, due to the low throughput in the  $z$  band, and relative lack of intensity of type Ia events in the  $u$  band.

Due to the computer intensive nature of the SMP process, where each candidate needs to be processed separately, it is not possible to produce “final” photometry for every available candidate in the SDSS-II supernova survey. The final analysis of supernova light-curves in the SDSS-II supernova survey uses SMP. In particular, selection cuts made in §3.2 use this photometry.

Figure 2.7 shows a histogram of the number of epochs of photometry for the spectroscopically confirmed supernovae and type Ia events for the first two years of the SDSS-II supernova survey. This figure is from Frieman et al. (2008a).

Light-curve fitting in the SDSS-II supernova survey is performed using the Multicolor Light-Curve Shapes method (MLCS, sometimes known as MLCS2k2; Jha et al. (2007)). Additional fitting is carried out using the Spectral Adaptive Lightcurve Template model (SALT; Guy et al. (2005) and SALT2; Guy et al. (2007)) to determine the consistency of the cosmological results, and to estimate the systematic uncertainty due to this effect. These two light-curve fitting methods are discussed fully in §3.2.3. Figure 2.8 shows three example light-curves from the the first year of observation of the SDSS-II supernova survey. For all three objects, the  $gri$  light-curves are shown along with overplotted the best-fit solution from MLCS.

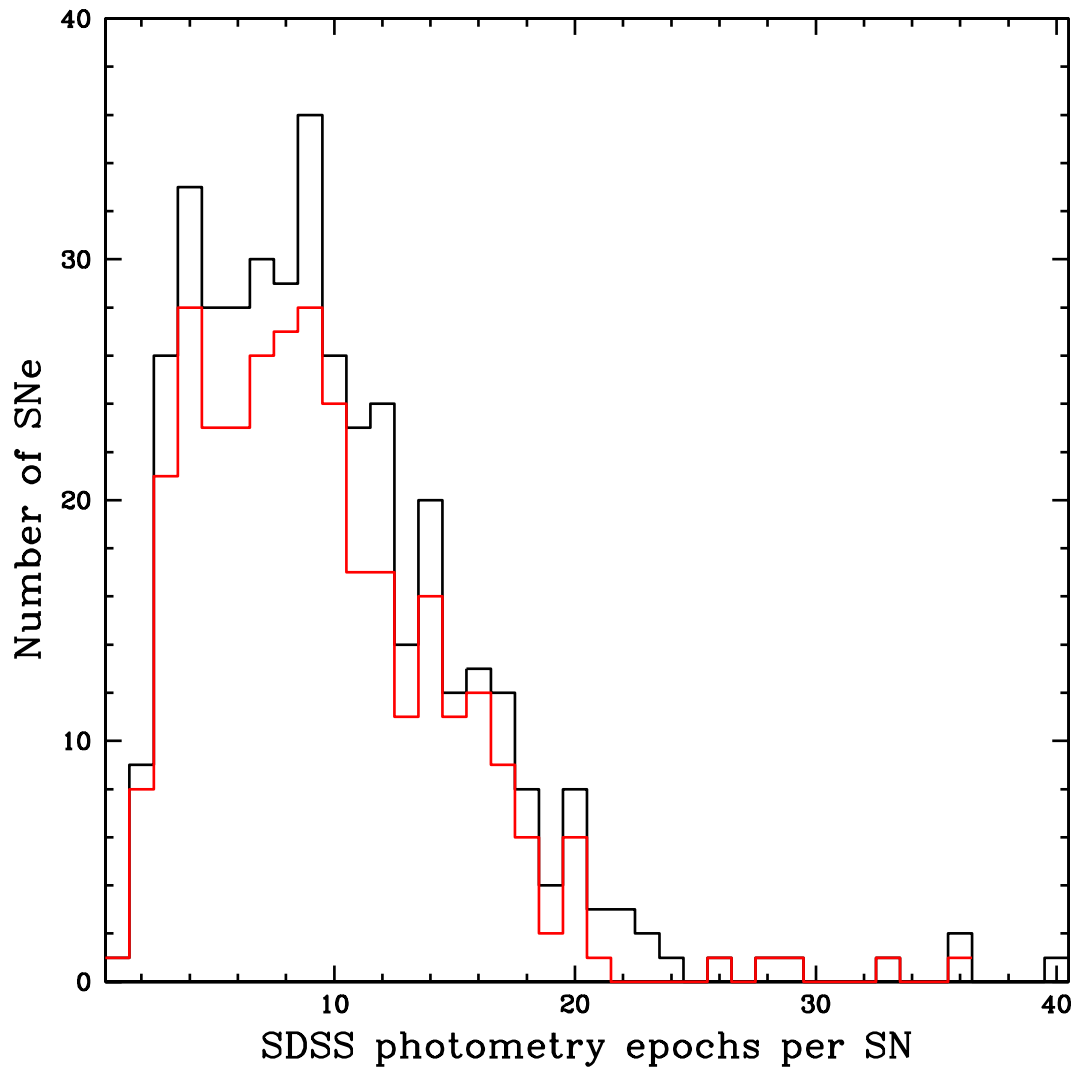


Figure 2.7: Histogram of the number of epochs of mountain-top photometry for the SDSS-II supernova survey's first two years of observations. Shown are the number of spectroscopically confirmed objects of all supernova types (black) and those for the type Ia sub-sample (red).

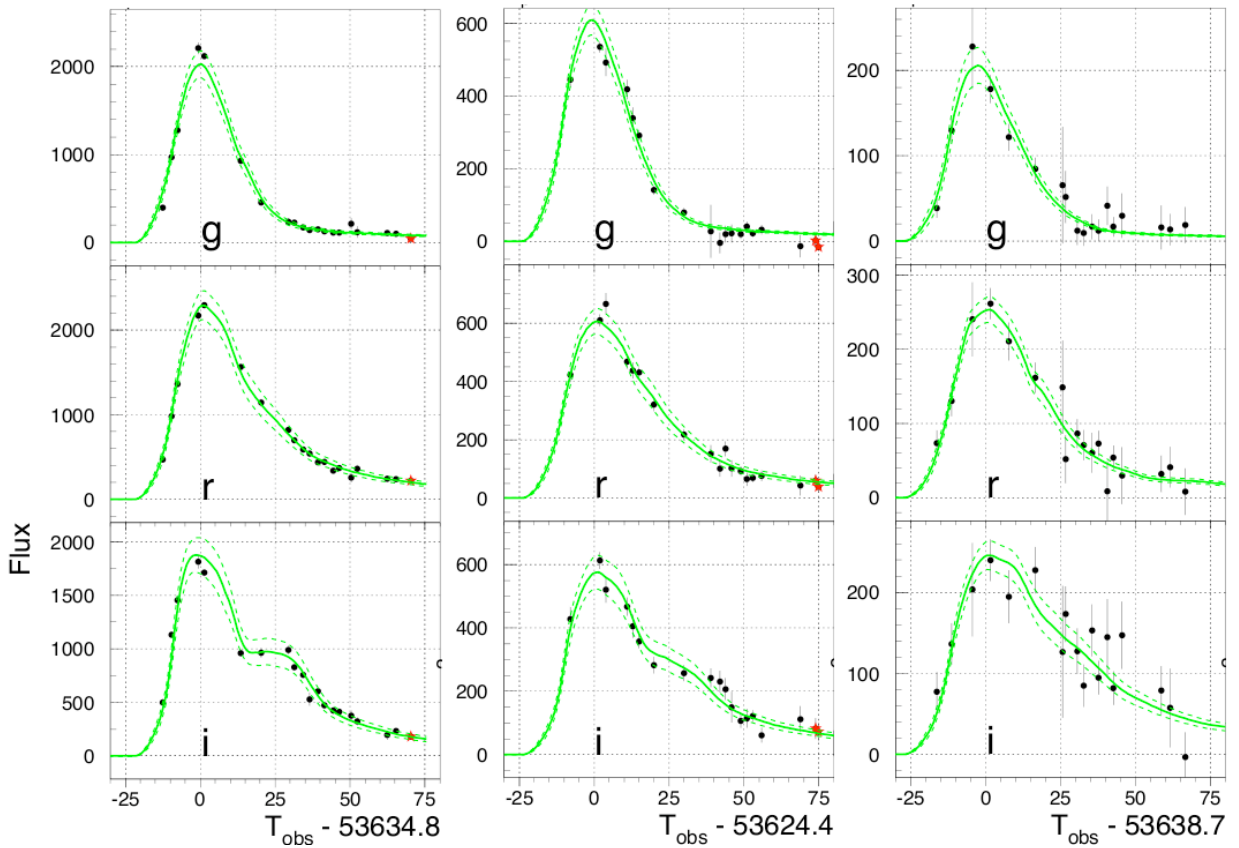


Figure 2.8: Multi-colour (*gri*) light curves for three spectroscopically confirmed type Ia supernovae in the SDSS-II supernova survey. One object (*left*) is at low redshift ( $z = 0.09$ ), one (*middle*) is at intermediate redshift ( $z = 0.19$ ) and one (*right*) is at high redshift ( $z = 0.36$ ). Overplotted in green on each is the best-fit solution from the MLCS light-curve fitter. Also shown, in dashed green, is an indication of the error values on the light-curve fit. Red points are those which have been discarded due to too low signal-to-noise. The three supernovae have  $\chi^2$  values of 31.5 (for 53 degrees of freedom), 34.3 (for 47 degrees of freedom) and 30.5 (for 50 degrees of freedom), respectively, indicating that they are excellent fits to the template light-curves, but that the error values may have been over-estimated.

## 2.3 Results from the SDSS-II Supernova Survey

In §2.2, we discussed the survey observations of the SDSS-II supernova survey. We outlined the methods used for each stage of the survey along with several important statistics. These observing strategies resulted in a very successful campaign for the SDSS-II supernova survey over all three years of observing. In total, the survey discovered and spectroscopically confirmed over 500 type Ia supernovae, including 498 type Ia events with a “Ia” designation, and 51 with a “Ia?” designation (see §2.2.3). It is possible that improved spectroscopic analysis techniques may change the spectroscopic designation of some “Ia?” events. The SDSS-II supernova survey also discovered 18 type Ib/c and 61 type II events. A redshift histogram of the distribution of objects for each of the three years is shown in Figure 2.9. The number of objects shown in this figure is lower than the 498 spectroscopically confirmed type Ia’s during the survey, as this number includes objects confirmed in the 2004 pre-SDSS-II run, which were primarily used to test the search pipelines and strategies. The major difference between the first year of the survey, and following seasons, is the increase in yield of spectroscopically confirmed type Ia events in the redshift range  $0.12 < z < 0.24$ . This is due to changes in the observing strategy and increase in spectroscopic resources, especially for 3m and 4m telescopes. For the third year of the survey, poor weather conditions at the beginning of the survey reduced the efficiency of the survey. The mean redshift for the three years is  $z = 0.22$ . To complement this dataset, another  $\sim 200$  host galaxy redshifts have been obtained to better constrain light-curves of non-spectroscopically confirmed objects. The spectroscopically confirmed type Ia supernovae from the SDSS-II supernova survey are listed in Dilday (2008).

An image gallery of the 327 spectroscopically confirmed type Ia events from the first two years of the SDSS-II supernova survey, with associated designations from the IAU, is shown in Figure 2.10. This figure is courtesy of Benjamin Dilday (University of Chicago for the SDSS-II Collaboration) (Dilday (2008)).

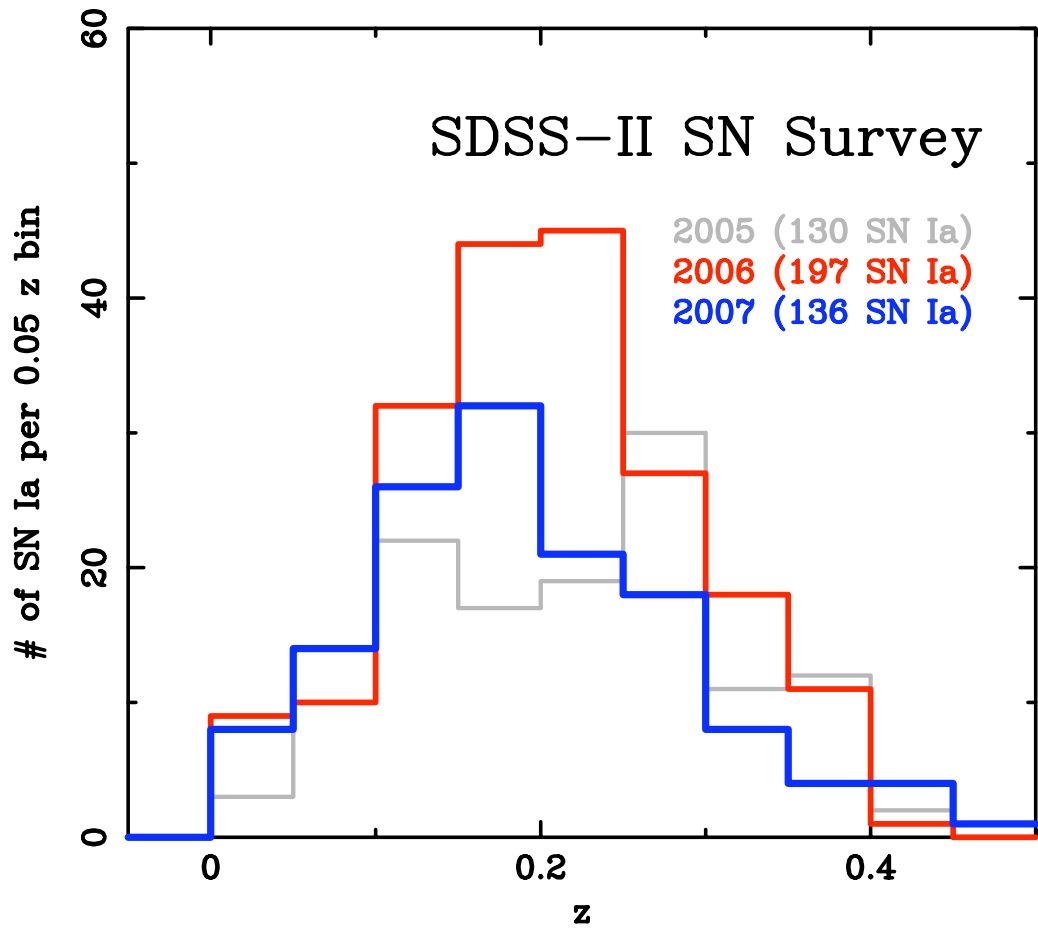


Figure 2.9: Redshift histogram describing the distribution of objects for each of the three years of observations. The third year of the survey saw a lower number of spectroscopic confirmations due to poor weather conditions at the beginning of the observation period.

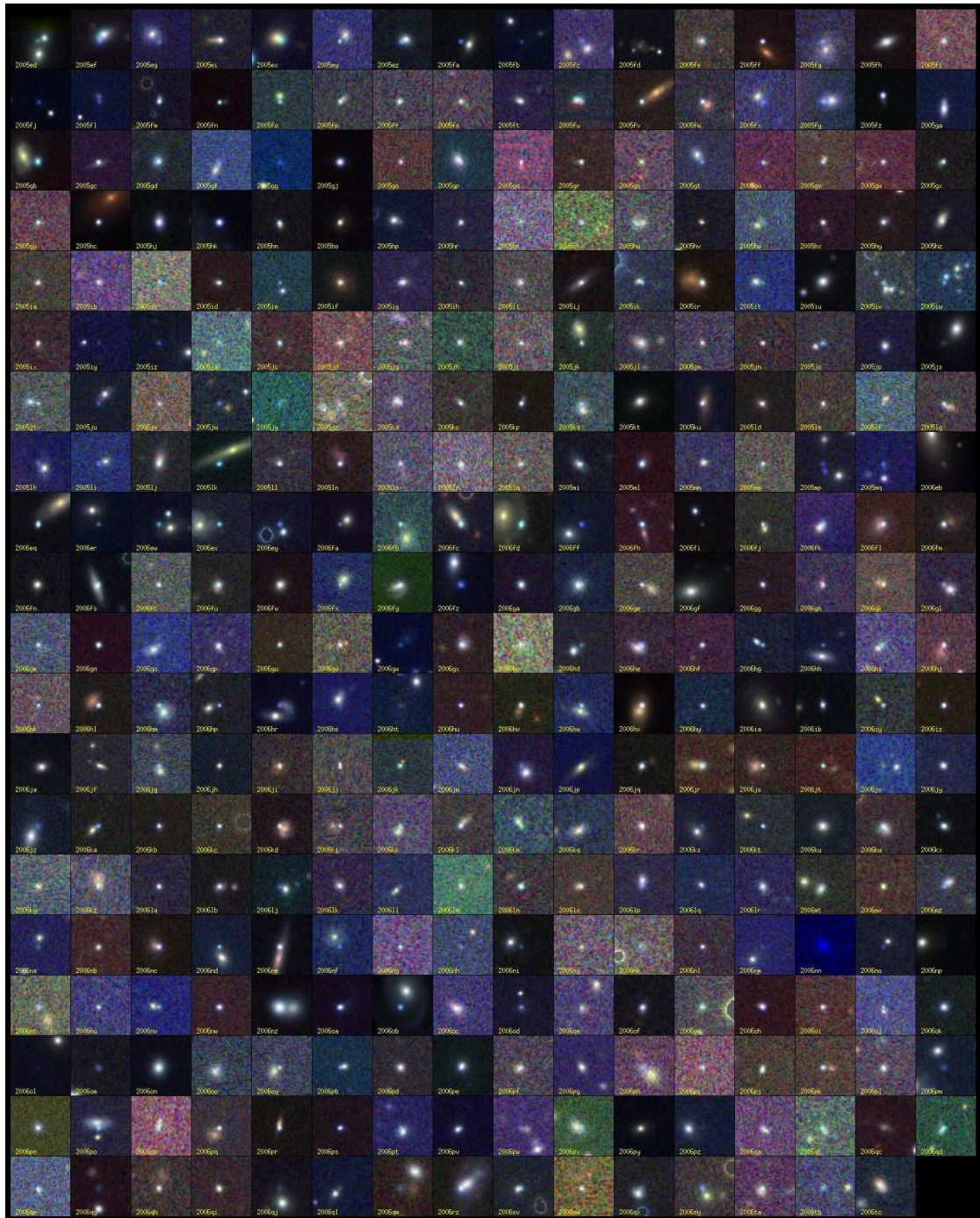


Figure 2.10: An image gallery of the 327 spectroscopically confirmed type Ia events from the first two years of the SDSS-II supernova survey, with associated designations from the International Astronomical Union (IAU). This figure is courtesy of Benjamin Dilday (University of Chicago for the SDSS-II Collaboration).

# Chapter 3

## The Complete SDSS-II Supernova Survey Sample

*This work is carried out in collaboration with Benjamin Dilday and represents a major part of the analysis of the SDSS-II supernova survey.*

*Specifically the work of §3.2 was carried out in conjunction with B. Dilday, whilst §3.3 is the primary work of B. Dilday's thesis and is published in [Dilday \(2008\)](#).*

### 3.1 Introduction

In this Chapter, I will discuss the methods used to correct for inefficiencies in the data from the first two years of the SDSS-II supernova survey. I will use these methods to define a “complete” sample of type Ia events that is not biased by spectroscopic or human influence. This sample will include both objects that have been spectroscopically confirmed to be type Ia, events and those which do not have a spectral confirmation, but do possess a light-curve that is well matched to a template Ia event. We will also look at estimating the efficiency of the SDSS-II supernova survey, due to effects such as weather conditions, a limited observing window (meaning that the object may be a Ia event but not meet the strict criteria used to pass the light-curve fitting stage) and inefficiencies within the search pipeline. Understanding this selection function, and correcting our sample for incompleteness will allow us to calculate the type Ia supernova rate as a function of volume, and will equip us with a sample that accurately describes the complete type Ia population.

As described in §2, the observing strategies of the SDSS-II supernova survey resulted in a very successful campaign for discovering and spectroscopically confirming a large number of type Ia supernovae. During the complete three years of the SDSS-II survey,

nearly 500 type Ia supernovae were spectroscopically confirmed. The analysis presented in the remainder of this thesis is concerned with results from the first two years (2005-2006) of the survey. In this period, the survey spectroscopically confirmed 327 unique type Ia supernovae out to a redshift of  $z = 0.4$ . However, this sample does not represent a complete sample of type Ia events in this redshift range ( $0 < z < 0.4$ ), due to a variety of factors, the most prominent of which is the lack of spectroscopic time available to follow them all up. To investigate the type Ia population as a whole, this needs to be corrected for.

The purpose of this chapter is to define a sample that is suitable for analysing the type Ia population. In doing this, there are two approaches available. We have the option to either include all Ia events, including those that are peculiar, either spectroscopically or photometrically, or exclude them from the analysis. These peculiar events include objects resembling 1991T and 1991bg, which are highly over-luminous and under-luminous events respectively. These objects still seem to follow the relation between peak luminosity and decline-rate, and are now generally considered to be extreme members of the normal type Ia population (Nugent et al. (1995b)). Other unusual objects include 2002ic (Hamuy et al. (2003a), Wood-Vasey et al. (2004)) and 2002cx (Li et al. (2003a), Branch et al. (2004)), which are far more strange and do not fit the light-curve decline rate relationship, but are spectroscopically classified as Ia events. In the first two years of the SDSS-II supernova survey, two further peculiar events were discovered, 2005hk and 2005gj. These events, along with those described above, are all type Ia supernovae, almost certainly following the same evolutionary path, but are not well described by the usual template light-curves. Thus the sample defined in this analysis only includes objects that obey the standard light-curve relationship for type Ia events. More specifically, we only consider objects that are well fit by the model light-curves in the MLCS light-curve fitter (Riess et al. (1996), Jha et al. (2007)), see §3.2.3. Branch et al. (1993) found that  $\sim 83 - 89\%$  of type Ia supernovae can be classified as “normal”. Since “peculiar” type Ia supernovae represent a small proportion of the overall type Ia group, this means that our sample includes the vast majority of available type Ia supernovae. These peculiar objects are rejected primarily because there is no secure method to determine the efficiency for detecting them without introducing a large level of contamination from other events. From observations they seem to represent a small fraction of the type Ia population. However, the existence of these type Ia supernovae does indicate the diversity of the type Ia population is not fully understood.

In §3.2, we shall introduce the problem of incompleteness into our sample, and attempt to produce a sample which solves this issue. In §3.3, we shall discuss the efficiency of

the SDSS-II supernova survey to detect these events, without necessarily following them up. These two factors will enable us to produce a “complete” sample of type Ia events in our redshift range of interest along with a weighting function to describe our efficiency to detect them. These are then used in §3.4 to calculate the type Ia supernova rate in the sample and compare it to previous measurements. We can also discuss the influence on the sample by objects which have not been spectroscopically confirmed as type Ia events (§3.2.5). Using this “complete” sample we will then be able to look at the type Ia population, and specifically determine its relationship to their host galaxies (§4, §5, §6).

## 3.2 Correcting for Incompleteness

The type Ia sample used to look at their properties, especially their host properties, needs to include all objects in our redshift range of interest. This means we need to include any objects that were missed by the survey, either due to inefficiencies in the search pipeline or because they are lacking a spectroscopic observation. These objects may have been missed completely by the search pipeline or may not have been spectroscopically confirmed, as they may be too difficult to observe, due to, for instance, large levels of host galaxy contamination, a lack of spectroscopic follow-up resources during the necessary observing period (due to either poor observing conditions or no available facilities), targeting errors or because the time of sufficient brightness fell during bright time (close to full moon).

In order to correct for this, the two sources of incompleteness, detectability and spectroscopic incompleteness are treated separately. The detectability of objects, the survey efficiency, is discussed in §3.3. This source of incompleteness can be estimated as a selection function, as it is independent of human and natural (such as weather) influence. However, the most difficult source of incompleteness to solve is spectroscopic incompleteness. The survey area of the SDSS-II supernova survey is unbiased (the survey is purely magnitude limited, without galaxy bias), however this sample is not complete.

This source of incompleteness involves trying to get a handle on the proportion of type Ia events that have been detected but were never spectroscopically observed. This is influenced by a variety of factors. As described in §2.2.2, once an object has been detected it is treated in the same manner. A light-curve is produced from the mountain-top photometry in 3 bands (*gri*). These light-curves are then compared to a set of template light-curves, using a bayesian light-curve fitting method (Sako et al. (2008)), to determine an estimate of the event being a type Ia supernova. However, at this stage, a variety of factors are

introduced, that influence whether the candidate will obtain a spectroscopic observation. The probability that an object will be promoted to receive a spectroscopic follow-up is determined by a variety of factors (as discussed in §2.2.2 and §2.2.3), including a human judgement element, that cannot be modelled as a selection function. This selection criteria is dependent on telescope availability, weather conditions, light-curve coverage and other factors, and thus is not dependent on one parameter. So the selection of type Ia events that are followed-up may well introduce a bias in to the sample of events. Thus to correct for this we need to include Ia events that did not receive a confirmation spectrum. To do this, we can use the Bayesian light-curve fitter.

### 3.2.1 The Bayesian Light-Curve Fitter

As discussed in §2.2.2, light-curves obtained from mountain-top photometry were fit to models of type Ia, type Ib/c and type II supernova. The technique used was to define a Bayesian probability for each individual object to be a supernova event of a particular type. To do this, the fit parameters are marginalised over to obtain the Bayesian evidence and the sum of the evidences is required to equal one; thus each object has three probabilities,  $p_{Ia}$ ,  $p_{Ib/c}$  and  $p_{II}$ . These probabilities are bounded such that  $0 < p_T < 1$ , where  $T$  is the class to which the object belongs such that  $\sum_T p_T = 1$ . However, the implicit assumption in this analysis is that the object of investigation is a supernova event, and thus does not allow for another class of object, such as an AGN or variable star event, which are possible identifications for a large number of candidates in our sample. Nevertheless, these probabilities are useful statistics for analysing the search photometry light-curves of candidates. This method is motivated and modelled after those discussed in [Kuznetsova & Connolly \(2007\)](#) and [Poznanski et al. \(2007\)](#).

### 3.2.2 The Search Photometry Criteria

As discussed in §2.2.2 over 15,000 candidates were identified in the first two seasons of the SDSS-II supernova survey. However, as discussed in §2.2.4, the final analysis of supernova light-curves for the survey was carried out using the scene-modelling photometry (SMP) ([Holtzman & SDSS-II Supernova Collaboration \(2006\)](#)). To limit the number of candidates that are processed through this software pipeline the Bayesian light-curve fits (described above) are used to define a selection criteria for our sample. Specifically, we require that,

- $P_{Ia} > 0.45$ ,
- At least three search discovery epochs,

- Should the candidate have more than five search photometry epochs, then the best fit Ia template is not that of 2005gj (Prieto et al. (2007)).

These selection cuts were determined by using a set of  $\sim 1000$  objects from the 2005 season of the SDSS-II supernova survey of which  $\sim 700$  were selected at random and combined with  $\sim 300$  objects, which had been either spectroscopically confirmed, or had search photometry light-curves that resemble a type Ia event. The selection cuts were chosen to produce a sample that is virtually complete, with respect to known Ia events, but is not dominated by high levels of contamination.

These three criteria were found to be the most useful for this purpose, and no significant improvement was found when additional criteria, such as the value of the reduced  $\chi^2$  statistic were included. At least three epochs are required, so that our sample is not dominated by asteroid events, which are highly prevalent in the first season candidate list (§2.2.2). Additionally, the cuts used to define the “final” sample (§3.2.3) will require at least five epochs of observations in the final photometry, and no objects in the first year analysis were found to increase from two epochs of observations in the search photometry to five epoch in the SMP. The peculiar type Ia supernova, 2005gj, is included as part of the type Ia models used in the Bayesian light-curve fitter (§3.2.1). This object has a flat, AGN-like light-curve post maximum (Prieto et al. (2007)), and therefore will not be included in our final sample, as it does not follow the standard peak-luminosity / decline-rate relationship. This cut is used to remove AGN-like events that are not included in the veto catalogue used in the search pipeline. The final selection criteria,  $p_{Ia} > 0.45$  is used such that the samples are limited to  $\sim 600$  supernova per year, and other supernova types are not dominant contaminants in the final sample. This is a reasonable number to process through the final photometry pipeline. These selection criteria can be modelled as a selection function, since they do not require any subjectivity, and thus can be included in the overall detection efficiency of the SDSS-II supernova survey. This is discussed in §3.3. Dilday (2008) has shown that the cuts described above do not significantly bias the resultant sample towards any particular type Ia event.

As discussed in §2.2.2, for several objects (especially spectroscopically confirmed type Ia’s) extra epochs are available beyond the usual search photometry, since when computing facilities are available, the positions of these objects are processed through the difference imaging at all epochs. These “forced photometry” epochs would better constrain the light-curves of these objects. However, these extra epochs are not included, as the selection criteria used to select them biases towards objects that have been spectroscopically followed-up, or are likely Ia events, and thus it is impossible to model this

into the survey efficiency selection function (§3.3). Also, as described in §2.2.2, it is possible for the Bayesian light-curve fitter to be recalculated using the best estimate of its redshift (either photometric or spectroscopic) as a prior. Since this judgement is subjective and related to host galaxy magnitude (bright host galaxies will preferentially have spectroscopic redshifts) this function is not included in the criteria described above.

### The Effect of the Search Photometry Criteria

In the first two years of the SDSS-II survey, 16413 supernova candidates were identified from the software pipeline and human scanning. Due to improvements in the scanning routine for the second season of the survey (such as the *autoscanner*) 12021 of these are from the first year alone, mostly consisting of asteroids or single epoch objects. Of these objects, 327 were spectroscopically confirmed as type Ia supernovae.

The cuts described in §3.2.2 reduce the number of candidates to 1175, of which 281 are spectroscopically confirmed to be SN Ia's and only 6 are shown to be other supernova events. From this analysis, 46 confirmed type Ia events have been lost due to the search photometry selection criteria. Of these, 10 have been lost due to not having enough epochs, 34 do not have a high enough probability to pass the likelihood of being a SN Ia event, and 2 (including 2005gj itself) fail as their decline rate is too long. The 1175 events that pass these criteria are then processed through the SMP pipeline to obtain final photometry light-curves for analysis.

This selection criteria produces a sample of likely Ia events. However, as shown in [Dilday et al. \(2009\)](#) and [Dilday \(2008\)](#), there is considerable scatter when the search photometry light-curves are compared to those produced for the SMP pipeline. The light-curves produced from the SMP pipeline are far more accurate than those from the search photometry. Further to this, the light-curve fitter used for these cuts, is used under the assumption that each candidate is a supernova event of some variety. This is clearly not an accurate assumption. Thus another light-curve fitter is required. The light-curve fitter of choice for the SDSS-II supernova survey is the MLCS light-curve fitter, and is discussed below. Several other methods are available, such as SALT and SALT2, and are discussed in §6

### 3.2.3 MLCS

In §3.2.2 we described a set of criteria to define a sample of 1175 objects for which “final” photometry was obtained. This SMP photometry produces the most accurate light-curves for each of our objects with small, well-understood uncertainties. There are several methods to analyse these light-curves. In this section, we describe the method used to analyse

these light-curves.

There are plenty of light-curve fitting techniques available. The analysis for this work primarily uses the `MLCS2k2` light-curve fitter, with the criteria described in §3.2.4. Some of the analysis in §6 uses the `SALT2` light-curve fitter. These two methods reflect different assumptions about the nature of the colour variations in type Ia events and are described in this section. We also discuss our choice of prior information in the fitting process.

### MLCS2k2

The Multicolor Light-Curve Shape, known as `MLCS2k2` in its current incarnation (Jha et al. (2007)), is an improved version of the the `MLCS` method (Riess et al. (1996), and updated in Riess et al. (1998) to include a quadratic term), which was first described as the `LCS` method in Riess et al. (1995). This was used by the High- $z$  Supernova Team (Filippenko & Riess (1998)) in the discovery of cosmic acceleration (Riess et al. (1998)). Throughout this work, we shall consider `MLCS` and `MLCS2k2` to be the method as described in Jha et al. (2007).

This method is a linear estimation algorithm that uses the shapes of the  $B - V$ ,  $V - R$  and  $V - I$  colour curves for a set of type Ia supernovae to improve the precision of the distance measurements. These colour curves provide information on the relationship between the absolute magnitude and intrinsic colour of type Ia events. This intrinsic colour can be used to measure the extinction of the supernova. Thus the luminosity, extinction and extinction corrected distance (and associated errors) to the type Ia event is measured. One key assumption in the `MLCS` light-curve fitting technique, is that the colour variation in type Ia supernova can be entirely explained by the amount of line of sight extinction after the correction for light-curve shape. Conley et al. (2008) have shown that the addition of the quadratic term, like the one in `MLCS2k2`, does little to address intrinsic versus extrinsic colour.

For `MLCS2k2`, the light-curve model magnitude is given by

$$m_{\text{model}}^{e,f} = M^{e,f'} + p^{e,f'} \Delta + q^{e,f'} + \Delta^2 + X_{\text{host}}^{e,f'} + K_{ff'}^e + \mu + X_{MW}^{e,f}, \quad (3.1)$$

where  $e$  is the epoch index that runs over the observations,  $f$  and  $f'$  are the observer and rest frame filter indices ( $f = ugriz$ ,  $f' = UBVRI$ ),  $\Delta$  is the `MLCS2k2` shape-luminosity parameter that accounts for the correlation between peak luminosity and the light-curve decline rate,  $X_{\text{host}}$  is the host galaxy extinction,  $X_{MW}$  is the Milky Way extinction,  $K_{ff'}$  is the K-correction between rest-frame and observer-frame filters, and  $\mu$

is the distance modulus, defined as  $\mu = 5 \log_{10}(d_L/10pc)$ , where  $d_L$  is the luminosity distance, defined in §1.

The parameters  $M^{e,f'}$ ,  $p^{e,f'}$  and  $q^{e,f'}$  are model vectors that have been determined using a well-observed low-redshift supernova training set. This “training” set consists of type Ia supernovae as measured in the U, B, V, R and I bands, compiled from large homogenous sets, such as Hamuy et al. (1996a), Riess et al. (1999) and Jha et al. (2006), with known relative distances and creates a continuum of template light-curves.  $M$  is the mean magnitude at 10 parsecs for a type Ia supernova with  $\Delta = 0$ , no extinction and assuming a Hubble parameter  $h = H_0/100\text{km/sec/Mpc} = 0.65$ . The  $p$  and  $q$  vectors translate the shape-luminosity parameter  $\Delta$  into a change in the type Ia absolute magnitude. Vectors from Jha et al. (2007) are used, but with adjustments to each passband that are independent of epoch. This is done to provide better agreement with the observed colours of low redshift events.

In the MLCS2k2 model, observed supernova colour variations are assumed to be primarily due to the extinction by dust of the host galaxy. This is assumed to behave in a fashion similar to dust in the Milky way, with some colour smearing. The host galaxy extinction,  $X_{\text{host}}^{e,f'}$ , is determined by  $A_V$ ,  $R_V$ , the time dependent spectral energy distribution (SED) of the supernova event and the rest-frame passband  $f'$ , where  $A_V$  is the extinction in magnitudes at the central wavelength of  $V$ -band; the extinction in other bands is described by the parameterisation introduced by Cardelli et al. (1989) (CCM law) and is determined by the parameter,  $R_V$ , which is the ratio of the  $V$ -band extinction to colour excess, such that  $R_V = A_V/E(B - V)$ . This one parameter relationship was found by Cardelli et al. (1989) in the  $3.5\mu\text{m} \geq \lambda \geq 0.125\mu\text{m}$  range, using data from Fitzpatrick & Massa (1988), which was applicable to both diffuse and dense regions of the interstellar medium. The Cardelli et al. (1989) model closely resembles those of Seaton (1979) and Savage & Mathis (1979) when  $R_V$  is close to 3.1. Geminal & Popowski (2005) found that the majority of extinction curves are able to be well-fit by a CCM law. For the Milky way, the value of  $R_V$  varies from  $\sim 2.0$  to  $\sim 5.5$ , with an average value of  $R_V = 3.1$ . This has been used in previous supernova analyses, however recent studies (Nobili & Goobar (2008), Wang (2005)) have indicated that a global value may be lower than this, possibly due to the variation of galaxy types, with different extinction profiles in the Universe. We adopt a value of  $R_V = 1.9$ , which has been derived from the first year results of the SDSS-II supernova survey (Kessler et al. (2009)). A discussion of the  $A_V$  prior and prior assumptions on  $\Delta$  is given in §3.2.3. Should a value of  $R_V = 1.9$  not be correct, then our sample will be biased against objects with large variations in their extinction profile.

K-corrections are computed using the method described in [Nugent et al. \(2002\)](#). This uses an average, epoch-dependent type Ia spectral template (SED) from [Hsiao et al. \(2007\)](#) and then “warping” the SED so that the synthetic colours of the warped template match the MLCS2k2 model colours at each rest-frame epoch. The K-correction depends strongly on the “warping” of the SED, whilst the value of  $X_{\text{host}}$  is only weakly dependent and so can be determined from the unwarped SED using the values of  $A_V$  and  $R_V$ . Template fitting is carried out using calibrated flux instead of magnitudes since the majority of observations for the SDSS-II supernova survey result in low signal-to-noise ratios, which are ill defined when magnitude space.

Having described the method used to calculate the parameters,  $\mu$ ,  $A_V$  and  $\Delta$  for each supernova light-curve, we now describe the priors used in the fitting process for the MLCS2k2 light-curve fitter.

### Priors used in the Fitting Process

The MLCS2k2 light-curve fitter has two parameters that affect the light-curve shape,  $A_V$  and  $\Delta$ . In the case of the  $A_V$  parameter, which is physically motivated and always positive, a Bayesian prior is used that requires the resultant values of  $A_V$  to be positive and contains information regarding the distribution of extinction in type Ia supernova host galaxies. This has been determined for the SDSS-II supernova surveys first year results in conjunction with predictions from a Monte-Carlo simulation, to be well described by an exponential function,

$$P(A_V) = \exp(-A_V/\tau_V), \quad (3.2)$$

with,  $\tau_V = 0.35$ . This prior functional form of the  $A_V$  distribution is used in the fitting process, with an additional Gaussian smearing of 0.005. It is also possible to assume no prior knowledge of the distribution of the value of  $A_V$ , except for the requirement for it be positive. The effect of using this prior, and the case where no prior information is known is discussed in §6.4.

The other MLCS parameter that can be influenced by prior knowledge is the  $\Delta$  parameter. For this we assume a uniform prior that spans the range  $-0.3 \leq \Delta \leq 1.6$ . This matches the values used in [Jha et al. \(2007\)](#), and matches the values seen in the low redshift training set.

Note that the MLCS light-curve fitter attempts to model the colour variation of the supernova through a universal extinction law which is independent of time. Our analysis

contains an implicit assumption that the amount of dust in a supernova explosion is positive, and thus should variations in colour for type Ia supernova not be entirely fit by such a law, and in fact have different colours, then our results will be biased against these objects. However, analysis by [Kessler et al. \(2009\)](#) using a Monte-Carlo technique, has shown that the distribution of  $A_V$  in the SDSS-II Supernova Survey sample is well described by the  $A_V$  prior described above.

Finally, the updated version of the MLCS2k2 model allows for the light-curve fit to be carried out to obtain the redshift of the supernova event. This is done by using a cosmology prior to set the distance modulus relationship. For this we use a spatially flat Universe with  $\Omega_M = 0.3$ ,  $\Omega_\Lambda = 0.7$  and  $w = -1$ . It is possible for the analysis to be carried out in several ways. Firstly, we could decide to fit each object with a known spectral redshift of some form (either from the supernova event itself, or the host redshift) with a cosmological fit and then fit all other objects with a photometric fit. This is the method used in [Dilday et al. \(2009\)](#) and has the advantage that the uncertainty on light-curve fitting is reduced when with prior information on the redshift is considered. Alternatively all objects could be fit for the photometric redshift. This is the method used for this analysis. It is chosen primarily because it allows all objects to be treated identically, independent of whether they have been spectroscopically observed or not. As described above, without prior information on the redshift of each object there is considerable spread in the fitting parameters. It is also possible to use the host galaxy redshift (either spectroscopic or photometric) as a prior on the fitting process. This is not used in this work since the host galaxy redshift and determination is not uniform for all objects. Large discrepancies are possible for photometric redshifts and host galaxy identification as the nearest object (the method used by the light-curve fitter) is dependent on redshift, such that local objects are more probable to have incorrectly determined hosts, and thus poor redshift priors. The choice of prior information described above allows us to analyse a dataset without introducing biased information into the fitting process.

We have now described how the “final” light-curves produced by the SMP pipeline are analysed, both for the SDSS-II supernova survey, and for this analysis. We shall now briefly discuss the SALT2 light-curve fitting process which is used in §6.

## SALT2

The SALT2 light-curve fitting method ([Guy et al. \(2007\)](#)) is a newly released version of the Spectral Adaptive Light-Curve Template method (SALT), [Guy et al. \(2005\)](#), that has been developed by the Supernova Legacy Survey (SNLS) collaboration. This model is a

two-dimensional surface in time and wavelength that describes the temporal evolution of the rest-frame spectral energy distribution (SED) for type Ia supernovae. This model has a resolution of 1-day and has a wavelength resolution of  $\sim 100\text{\AA}$ , thus allowing for model fluxes to be compared to observed data. This surface has been made through the combination of light-curves of hundreds of type Ia spectra, both at low redshift (such as Hamuy et al. (1996a), Riess et al. (1999) and Jha et al. (2006)) and high redshift (such as Astier et al. (2006) and Howell et al. (2005)). The surface span a range of  $2000\text{\AA} - 9200\text{\AA}$  in rest wavelength and -20 to +50 days relative to maximum light in rest-frame times. This modelling of the supernova in spectroscopic space ensures that K-corrections are treated consistently and that errors can be correctly propagated throughout the model. The distances to the supernova in the “training set” are not required since the flux normalisation is a free parameter in the fit.

In the SALT2 model, the rest-frame flux at wavelength  $\lambda$  and time  $t$  (such that  $t = 0$  at  $B$ -band maximum), is given by the formula,

$$F(t, \lambda) = x_0 \times [M_0(t, \lambda) + x_1 M_1(t, \lambda) + \dots] \times \exp[c \times CL(\lambda)], \quad (3.3)$$

where  $M_0(t, \lambda)$  is the average spectral sequence, whilst  $M_1(t, \lambda)$  and higher order terms, are components that intend to describe the observed variability of type Ia supernova. This model has a time independent variation with colour (something that distinguishes it from the MLCS2k2 model), which is determined by the term  $CL(\lambda)$ , the average colour correction term. These three parameters are all determined by a training process, using the supernova events mentioned above. Thus the free parameters that are determined from the fitting process are  $x_0, x_1$  (only two terms are generally considered) and  $c$ . Unlike the MLCS2k2 model, the extraction of the distance to the supernova event is part of a global fit that includes cosmological parameters. The SALT2 output can be used to produce a corrected distance, using the expression,

$$\mu_i = m_{Bi}^* - M + \alpha \times x_{1,i} - \beta \times c_i \quad (3.4)$$

where the index  $i$  denotes the parameters  $(m_B^*, x_1, c)$  that have been determined for each supernova fit, and  $M, \alpha$  and  $\beta$  are global parameters that describe type Ia supernova in general. For cosmological analyses, a  $\chi^2$  minimisation is carried out to calculate the values of  $M, \alpha, \beta$  and the cosmological parameters, such as  $\Omega_M, \Omega_\Lambda$  and  $w$ , with various priors.

For each individual light-curve fit, the optical depth is treated as a colour offset relative to the average value at the time of maximum brightness in the  $B$ -band. That is  $c = (B - V)_{\text{MAX}} - \langle B - V \rangle$ . Thus the  $c$  parameter models the colour variation that is independent of epoch (i.e. constant with time), whilst other variations in the colour of the supernova event are included in the  $x_1$  (and possibly other) terms.

As shown in [Guy et al. \(2007\)](#), most of the variability in type Ia events can be described by stretching the light-curves. Thus the  $x_1$  parameter can be converted into a stretch parameter, such as the one used in the SALT model,  $s$ , using the transformation,

$$s(\text{SALT}) = 0.98 + 0.091x_1 + 0.003x_1^2 - 0.00075x_1^3. \quad (3.5)$$

Transformation to other systems is also possible. The mean colour correction term,  $CL(\lambda)$  can be well approximated by the extinction law given in [Cardelli et al. \(1989\)](#), over much (but not all) of the optical spectrum.

For the analysis carried out in §6, we use the publicly available version of the SALT2 light-curve fitter ([Guy et al. \(2007\)](#)). Several minor changes have been included to the version used by the SDSS-II supernova survey, but are not used in this analysis, since its primary function is to confirm the results found with the MLCS2k2 light-curve model, and to compare with results published in [Sullivan et al. \(2006b\)](#).

Several other light-curve fitting techniques are available, such as SiFTO ([Conley et al. \(2008\)](#)), which uses a generalisation of the “stretch” method. This differentiates itself from the SALT2 light-curve fitter by not enforcing a colour model during the light-curve fitting, but instead adjusts the template to match the observed colours. Other methods include the  $B$ -band light-curve template, “Parab-18” ([Goldhaber et al. \(2001\)](#)) and the Color-Magnitude Intercept Calibrations (CMAGIC) method ([Wang et al. \(2002\)](#)), but we shall not consider them or SiFTO for this analysis. Having described the two techniques that are used in this work, we can now describe the final selection criteria that was used to determine our “final” data-set.

### 3.2.4 The SMP Selection Criteria

For the determination of a “incompleteness corrected” sample of type Ia events, we impose several criteria based upon the SMP light-curves. These criteria are based upon the MLCS light-curve fitter (§3.2.3). The criteria are identical for objects that have been spectroscopically confirmed as for those which are photometrically determined. The

original cuts used to determine the sample of 1175 objects are discussed in §3.2.2. The additional selection cuts are as follows,

- $-51^\circ < \alpha_{J2000} < 57^\circ$ ,

Although, as discussed in §2.2.1, the SDSS-II supernova survey covers the right ascension range of  $-60^\circ < \alpha_{J2000} < 60^\circ$ , the early part of the 2005 season of the survey did not have complete reference images in the regions,  $\alpha_{J2000} < -51^\circ$  and  $\alpha_{J2000} > 57^\circ$ , thus these regions were not used at the beginning of the survey. These regions could be included in the “incompleteness corrected” sample, by including these differences in the efficiency calculation (§3.3) as a time varying search area, but for efficiency they are discarded. Further to this, the calibration star catalogue used for the SMP pipeline (Ivezić et al. (2007)) does not extend below  $\alpha_{J2000} < -51^\circ$ , and thus no final photometry in this range is presently available. This reduces the overall search area of the survey to 280 square degrees.

- There must be photometric observations on at least five separate epochs between -20 days and +60 days relative to maximum light (in the B-band) in the supernova rest-frame.

The time of peak light in the supernova rest frame is calculated using the best fit light-curve template from the MLCS2k2 light-curve model (§3.2.3). This requires that the light-curve be reasonably well-sampled so that an accurate fit probability can be determined. A photometric observation simply means that the survey observed the region of sky where the object is situated and the SMP reported a supernova flux measurement. This does not need to be significant or even positive, but does require that no error flags (see Holtzman & SDSS-II Supernova Collaboration (2006)) are set. At least one of the three *gri* passbands are required for an epoch to be counted.

- At least one epoch (see above) must have a signal-to-noise ratio of  $S/N > 5$  in each of *g*, *r* and *i*. The same epoch is not required for each passband.

This cut requires that there are well-measured points on the candidate’s light-curve, and thus, removes low S/N events from the sample.

- At least one photometric observation is required at least two days before peak light in the supernova rest frame and at least one photometric observation is required at least ten days after peak light in the supernova rest frame.

These two cuts require that the light-curve is sampled both before and after peak. Thus the time of peak can be measured accurately. Non-type Ia events are removed

by this selection criteria, since it requires that the light-curve follow the basic peak luminosity / decline-rate relationship of a type Ia supernova. This cut also guarantees that the peak magnitude of the supernova event occurs in the observing season of the SDSS-II supernova survey, and thus a specific time frame for the rate measurements presented in §3.4 and §5.3 is determined. These are the main cuts that will contribute to the inefficiency of the SDSS-II survey (§3.3).

- MLCS2k2 light-curve fit probability  $> 0.01$

The MLCS2k2 light-curve fitter (§3.2.3) finds the likelihood as a function of the four parameters,  $\mu$  (the distance modulus),  $A_V$  (the extinction parameter), the time of peak light in the B-band,  $t_{max}$ , and the light-curve shape parameter,  $\Delta$ . The MLCS fit probability is defined by evaluating the usual  $\chi^2$  statistic for the data and the best fitting model, and assuming that the statistic obeys the  $\chi_{n-4}^2$  probability distribution, where  $n$  is the number of photometric data points. The model parameters of the best fitting MLCS model are defined as the mean probability distribution for each corresponding parameter. Thus, this cut removes objects with peculiar light-curves relative to the expected type Ia supernova light-curve. A probability of 0.01 is chosen since it encapsulates the vast majority of spectroscopically confirmed Ia events (which primarily have  $fitprob > 0.1$ ). This cut is explained fully in [Dilday et al. \(2008\)](#).

- MLCS2k2 light-curve fit parameter,  $\Delta > -0.4$

As described in §3.2.3, the parameter  $\Delta$  is the MLCS parameter that is used to describe the peak luminosity / decline rate relationship seen in type Ia events. It is a measure of the light-curve shape, such that large values of  $\Delta$  correspond to fainter and faster declining events, and small values of  $\Delta$  are seen in objects which are intrinsically brighter and decline more slowly. This matches the type Ia supernova population seen at low redshift, that train the MLCS light-curve fitter.

The selection cuts described above, match those used in the first year cosmology analysis from the SDSS-II supernova survey ([Kessler et al. \(2009\)](#)), and those used in calculating the low redshift type Ia supernova rate ([Dilday et al. \(2008\)](#)) and corresponding high redshift rate ([Dilday et al. \(2009\)](#)) for the SDSS-II supernova survey. It is possible to remove further contamination from the final sample of objects that pass this criteria (e.g. from objects such as type Ib/c events which have similar light-curves to type Ia supernovae), that a photometric observation could be required at +20 days after peak light. However, this cut would remove a large number of confirmed type Ia events which do not have a long enough light-curve coverage, and analysis carried out in [Dilday \(2008\)](#) has shown that it does not dramatically effect the photometrically confirmed objects in our sample.

### 3.2.5 The “Complete” Sample

As described in §3.2.2, the SMP light-curves of 1175 objects from the first two seasons of the SDSS-II supernova survey, were obtained, such that a “final incompleteness corrected” sample of type Ia events could be found. This sample will represent an unbiased sample, with a measurable selection function, which is independent of whether the object has been spectroscopically confirmed.

In §3.2.4, we described the selection criteria used for determining whether an object can be considered to be a type Ia event or not. This uses the MLCS light-curve fitter (§3.2.3). These selection cuts result in 559 of the 1175 candidates passing the criteria in §3.2.4. Of these objects, 196 have been spectroscopically confirmed as SN Ia’s, with a further 3 having spectra that are classified as “probable SN Ia events”, or “Ia?” (Zheng et al. (2008), §2.2.3). A further 305 have host galaxy redshifts. One object, 2005jr, is a spectroscopically type II supernova at  $z = 0.2944$ , thus showing that the selection criteria have not ensured that the sample is free of contamination, although this object is at high redshift and thus is a low signal-to-noise object.

For the type Ia events lacking a spectroscopic redshift (i.e. are not spectroscopically confirmed or do not have a host galaxy spectroscopic redshift), we take the redshift of the candidate to be the photometric redshift from the best-fit light-curve of MLCS2k2, since the photometric redshift option is used in the fitter (as described in §3.2.3). These redshifts are based on an assumed cosmology ( $\Omega_M = 0.3, \Omega_\Lambda = 0.7, \Omega_{total} = 1, w = -1$ ), but are not highly sensitive to the values of these parameters, especially at these intermediate redshifts. A description of the accuracy of these redshifts can be found in Dilday et al. (2009), who find that accounting for the intrinsic scatter in the peak brightness of type Ia events, these redshifts are accurate to  $\sim 0.02$ . For objects with a spectroscopic redshift, the observed redshift is used.

For the analysis used in this study, we are interested in type Ia events within a redshift range of  $0.05 < z \leq 0.25$ . This redshift range is chosen since it is a range where our survey efficiency is high (§3.3), and where our sample is still dominated by objects which have a spectroscopic redshift, or spectroscopic confirmation spectra, thus ensuring that our sample is relatively free of contamination which are expected to dominate at higher redshifts (the full SDSS-II supernova sample contains objects out to a redshift of  $z > 0.4$ ). The low redshift cut is due to poor efficiency in this range and due to the fact that host galaxies (as described in §4) are not volume limited in this range.

Of the 559 type Ia candidates described above, 246 of them satisfy this redshift condition, and thus make up our final “incompleteness corrected” type Ia supernova sample. Of these, 128 have been spectroscopically confirmed as type Ia events, with a further 3 designated as “Ia?”. A further 57 of these objects have a spectroscopic redshift of the supernova’s host galaxy. The remaining 58 objects have photometric redshifts determined from the light-curve fitter. No spectroscopically confirmed type II and type Ib/c supernovae are contained in this sample.

Table 3.1 expresses the number of candidates that are involved in each of the stages described in this chapter. Alongside this, the number of objects which have been spectroscopically confirmed as type Ia events is included. This gives an indication of the number of events that are not included in the “final” sample. The primary source of loss for these objects is a lack of light-curve coverage caused by the observing period of the SDSS-II supernova survey. Figure 3.1 shows how the sample of 559 objects passing the criteria described in §3.2.4 are distributed as a function of redshift. The sample has been split in to three distinct groups, spectroscopically confirmed objects (plotted in red), objects with no spectroscopic confirmation, but possessing a host galaxy redshift (plotted in green) and objects with no spectroscopic information (plotted in blue). As described in Table 3.1 there are a combined 246 objects with  $0 < z < 0.25$ . This figure shows that the level of non-confirmed objects is low for  $z \lesssim 0.12$  (as would be expected from the analysis of Dilday et al. (2008)), and increases with redshift. Objects with  $z \lesssim 0.20$  are dominated by events with some spectral information (either from the host galaxy or supernova event), whilst for  $z \gtrsim 0.3$ , objects with no spectral information dominate the sample. Table G.1 gives a list of the 246 objects from §3.2.5 that pass the selection criteria described in §3.2.2 and §3.2.4. Also given are the output  $\Delta$  and  $A_V$  values from the MLCS2k2 light-curve fitter, the redshift of each object and its origin. Also shown is the fit probability that is used in the selection criteria described in §3.2.4. This sample represents the incompleteness corrected SDSS-II supernova sample from the first two seasons of the SDSS-II supernova survey. This sample is free of bias from spectroscopic follow-up prioritisation, and forms the sample that will be used to look at the host properties and light-curve properties of this population, in §5 and §6, respectively. The sample given in Table G.1 contains objects that are not spectroscopically confirmed. A discussion of the effect of these non-spectroscopically confirmed objects on our final results can be found in each chapter of this work. It should be noted, that while there is no guarantee that our final sample contains only Ia events, with no contamination issues, each of the objects has had to pass two separate light curve fitters, one to remove non-Ia events (such as type IIs) and one to assess the likelihood of Ia activity. This and the stringent light curve restrictions, means that our contamination from other transient events should be

Stage of Analysis <sup>a</sup>	# candidates	# confirmed <sup>b</sup>	% confirmed events
Candidate in database <sup>c</sup>	16413	327	1.99
After Search Photometry Criteria <sup>d</sup>	1175	281	23.91
After SMP / MLCS Criteria <sup>e</sup>	559	199	33.22
Redshift in range $0.05 < z < 0.25$	246	131	53.25

<sup>a</sup>These are described fully in §3.2

<sup>b</sup>Includes objects classed as probable Ia's

<sup>c</sup>As described in §2.2.2

<sup>d</sup>As described in §3.2.2

<sup>e</sup>As described in §3.2.4

Table 3.1: Table showing the number of candidates that pass each of the stages as described in §2.2.2, §3.2.2 and §3.2.4, along with the number of objects that have a spectroscopic confirmation, and thus give an indication of the completeness as it is affected by the cuts.

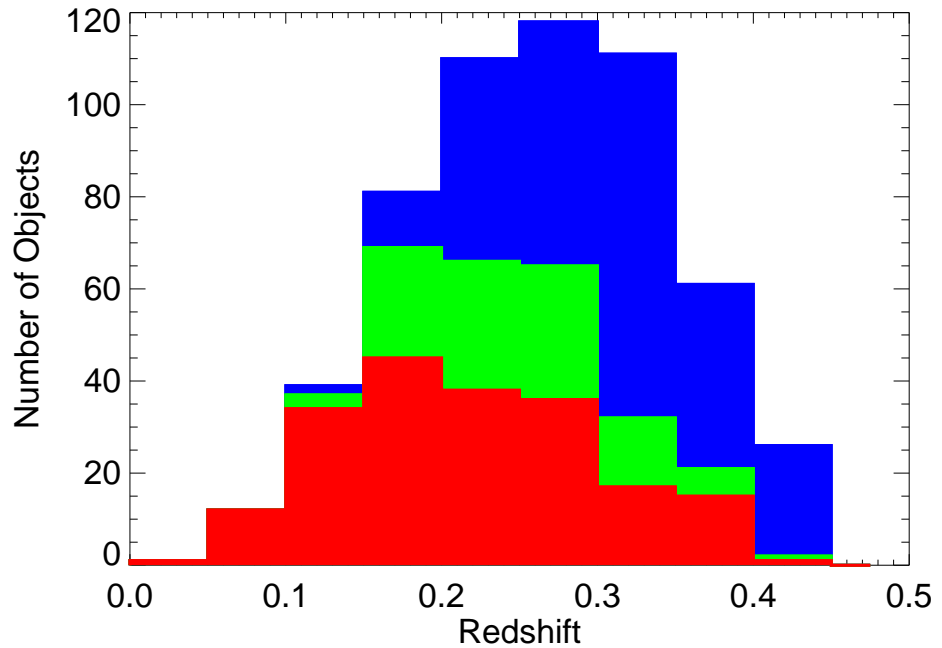


Figure 3.1: This figure describes the number of supernova that pass the criteria described in §3.2.4 as a function of redshift. The sample has been split in to three distinct groups. Those plotted in red are spectroscopically confirmed as type Ia events. Objects in green (plotted such that the histogram shows the combined red and green values) have a spectroscopic host redshift. Objects in blue (similarly plotted so that they are valued as the sum of the red, green and blue objects) lack any spectroscopic redshift information, and the redshift of these objects is determined from the best-fit MLCS model. As described in Table 3.1 there are a combined 246 objects with  $0 < z < 0.25$ .

low. Analysis carried out in [Dilday \(2008\)](#) has shown that the level of contamination from non-type Ia events should conservatively be  $\sim 3\%$ . A full analysis of the contamination within this sample is given in [Dilday \(2008\)](#) and [Dilday et al. \(2009\)](#), who also determine that the photometric redshifts determined from the supernova light-curves using the MLCS2k2 light-curve fitter are unbiased with respect to redshift and signal-to-noise of the observed object. For this sample, this is best described in [Figure 3.2](#), which shows the differences between the spectroscopic and photometric redshifts for objects in our sample which have a spectroscopic redshift of some kind. Two datasets are shown, those which are spectroscopically confirmed as type Ia events, and those which have a spectroscopic redshift of some kind. The median values for the differences between the spectroscopic redshift and photometric redshift are statistically insignificant, with a value of 0.0002 for the occasion where only known Ia events are considered, and -0.0001 when both confirmed objects and objects with a spectroscopic host redshift are considered. The median differences are 0.002 for both samples. This is below the accuracy limit for the photometric redshift estimates. The scatter between the two measurements is shown in [Figure 3.3](#), which is a histogram showing the differences between the two measurements. Several objects show considerable scatter, but this represents a negligible proportion of the final sample. Removing objects with large disagreements between the spectroscopic and photometric redshifts was considered, but dismissed since it would not significantly affect the sample size, and would introduce a bias between the objects that have a spectroscopic redshift and those that do not.

[Figures 3.4, 3.5 and 3.6](#) show the SMP photometry for three representative objects from the sample described in this section and listed in [Table G.1](#). These objects consist of one ([Figure 3.4](#)) that is spectroscopically confirmed as a type Ia event and two ([Figures 3.5 and 3.6](#)) which are not confirmed as type Ia supernova, but all three have light-curves that pass the criteria described in [§3.2.2](#) and [§3.2.4](#). Of the two objects that have not been spectroscopically confirmed, one ([Figure 3.5](#)) has a spectroscopic host redshift and one ([Figure 3.6](#)) does not. Also plotted are the best fit light-curves from the MLCS2k2 light-curve model and the residuals from this fit. Several points have been removed from the fitting process as they do not satisfy the criteria described in [§3.2.4](#). Also shown are the output MLCS2k2 parameters  $A_V$  and  $\Delta$  from the fitting process.

The sample described in this section is partially dependent on the set of priors used in the MLCS2k2 set-up. Especially important are the priors of the  $A_V$  distribution of the sample and the decision to impose a photometric fit for all objects, independent of whether they have a spectroscopic redshift or confirmation. The effect of these priors on the sample size, make-up and results found in this analysis are discussed in [§6.4](#) and [§7](#).

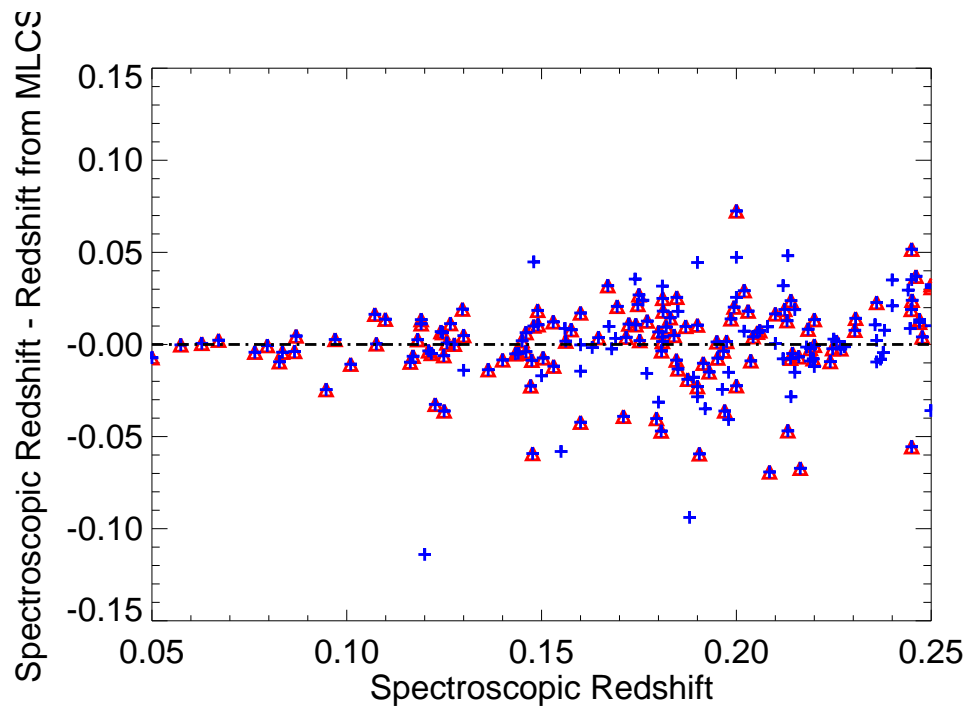


Figure 3.2: Describing the difference between the spectroscopic and photometric redshifts (as obtained using the MLCS2k2 light-curve fitter (§3.2.3)) for objects that pass the criteria described in §3.2.4. Plotted are objects which are spectroscopically confirmed as type Ia events (red triangles) and those which have a spectroscopic redshift of some kind, such as a host galaxy redshift (blue crosses). Plotted as a reference is the line describing no difference between these two measurements.

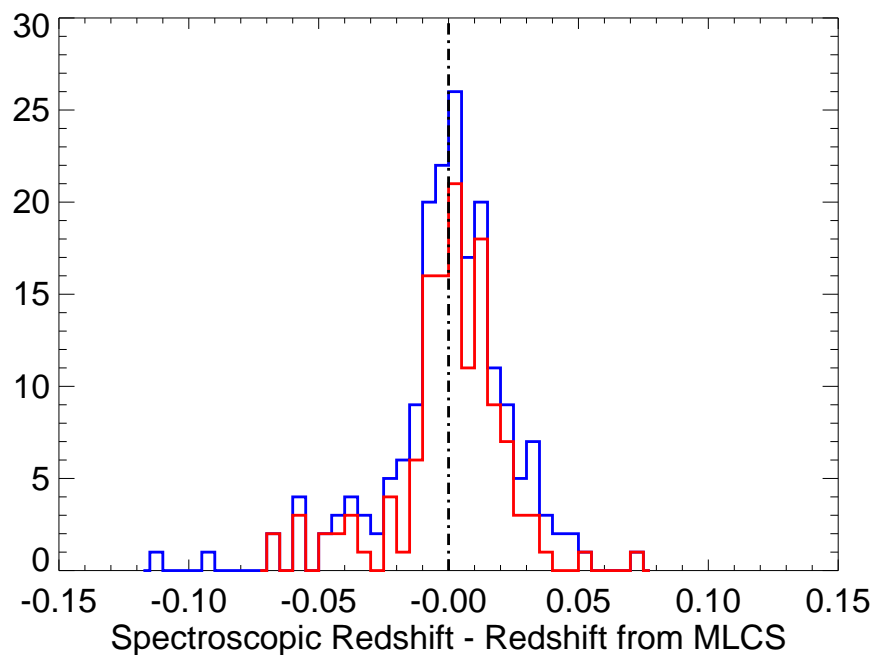


Figure 3.3: This figure consists of two histograms showing describes the difference between the spectroscopic and photometric redshifts (as obtained using the MLCS2k2 light-curve fitter (§3.2.3)) for objects that pass the criteria described in §3.2.4. Plotted are objects which are spectroscopically confirmed as type Ia events (red) and those which have a spectroscopic redshift of some kind, such as a host galaxy redshift (blue). Plotted as a reference is the line describing no difference between these two measurements.

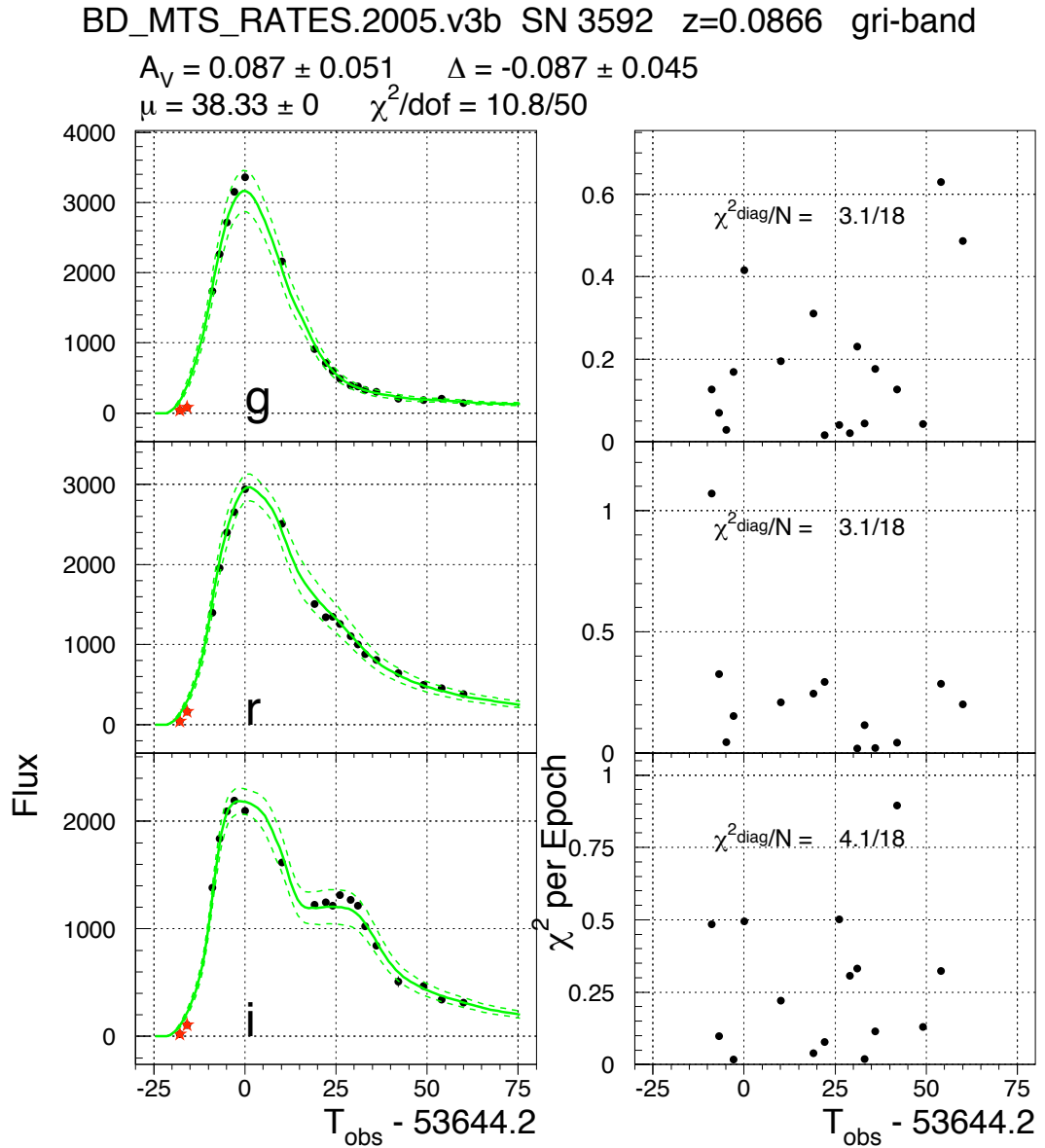


Figure 3.4: A representative light-curve of an object in the sample of 246 objects listed in Table G.1. This object has been spectroscopically confirmed as a type Ia event. The *gri* light-curves are shown along with the best-fit template from the MLCS2k2 light-curve fitter. Also shown are the residuals from this fit, and the resultant  $\chi^2$  statistic for each filter. The best-fit values for the MLCS2k2 parameters  $A_V$  and  $\Delta$  are shown. This fit is carried out to determine the photometric redshift of the object, and thus a cosmology has been assumed. Points highlighted in red have been removed from the fit due to failing at least one of the criteria described in §3.2.4.

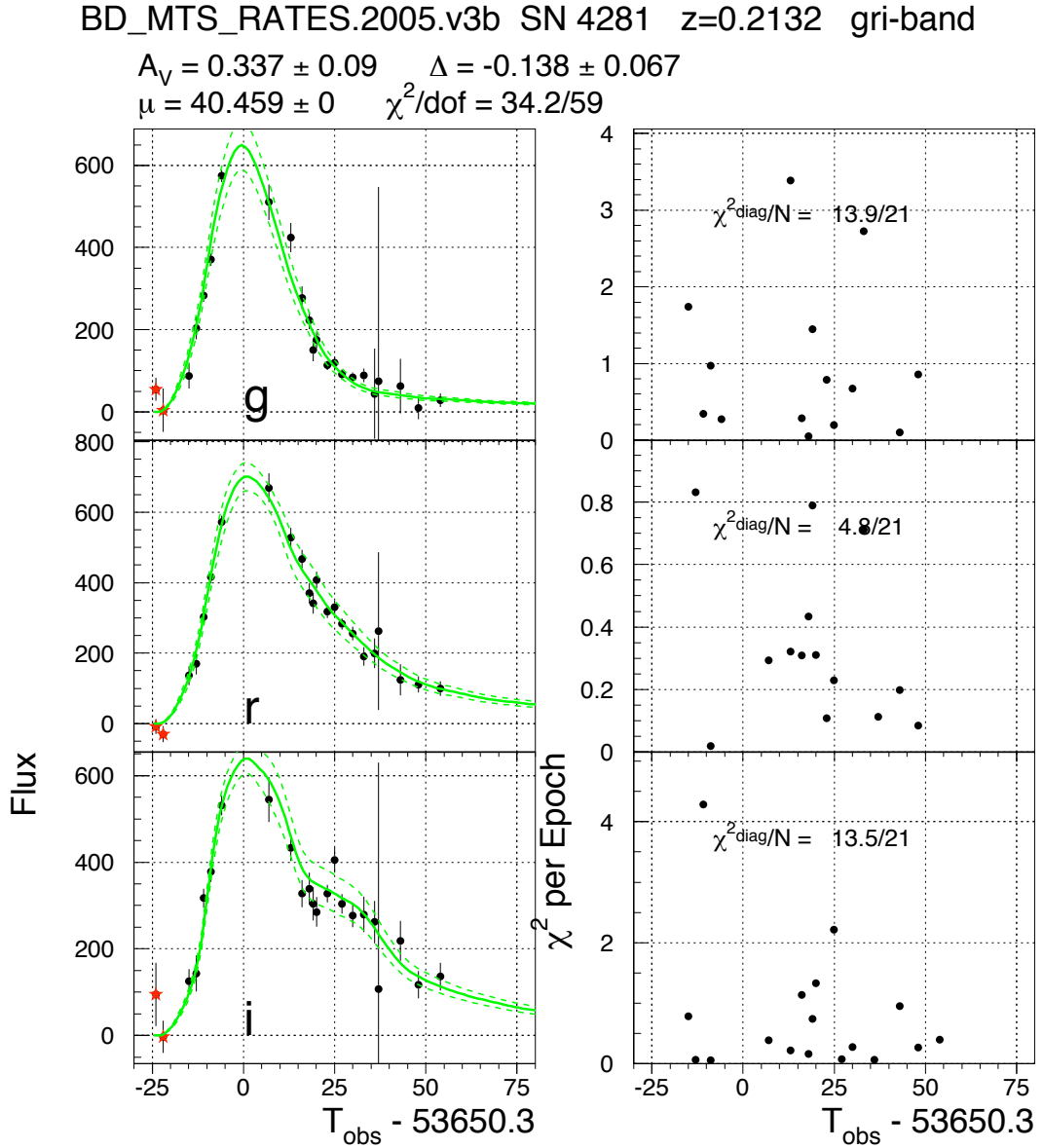


Figure 3.5: A representative light-curve of an object in the sample of 246 objects listed in Table G.1. This object has not been spectroscopically confirmed as a type Ia event. Instead this object has a light-curve that passes the cuts described in §3.2.4 and has a spectroscopic redshift for its host galaxy candidate. The *gri* light-curves are shown along with the best-fit template from the MLCS2k2 light-curve fitter. Also shown are the residuals from this fit, and the resultant  $\chi^2$  statistic for each filter. The best-fit values for the MLCS2k2 parameters  $A_V$  and  $\Delta$  are shown. This fit is carried out to determine the photometric redshift of the object, and thus a cosmology has been assumed. Points highlighted in red have been removed from the fit due to failing at least one of the criteria described in §3.2.4.

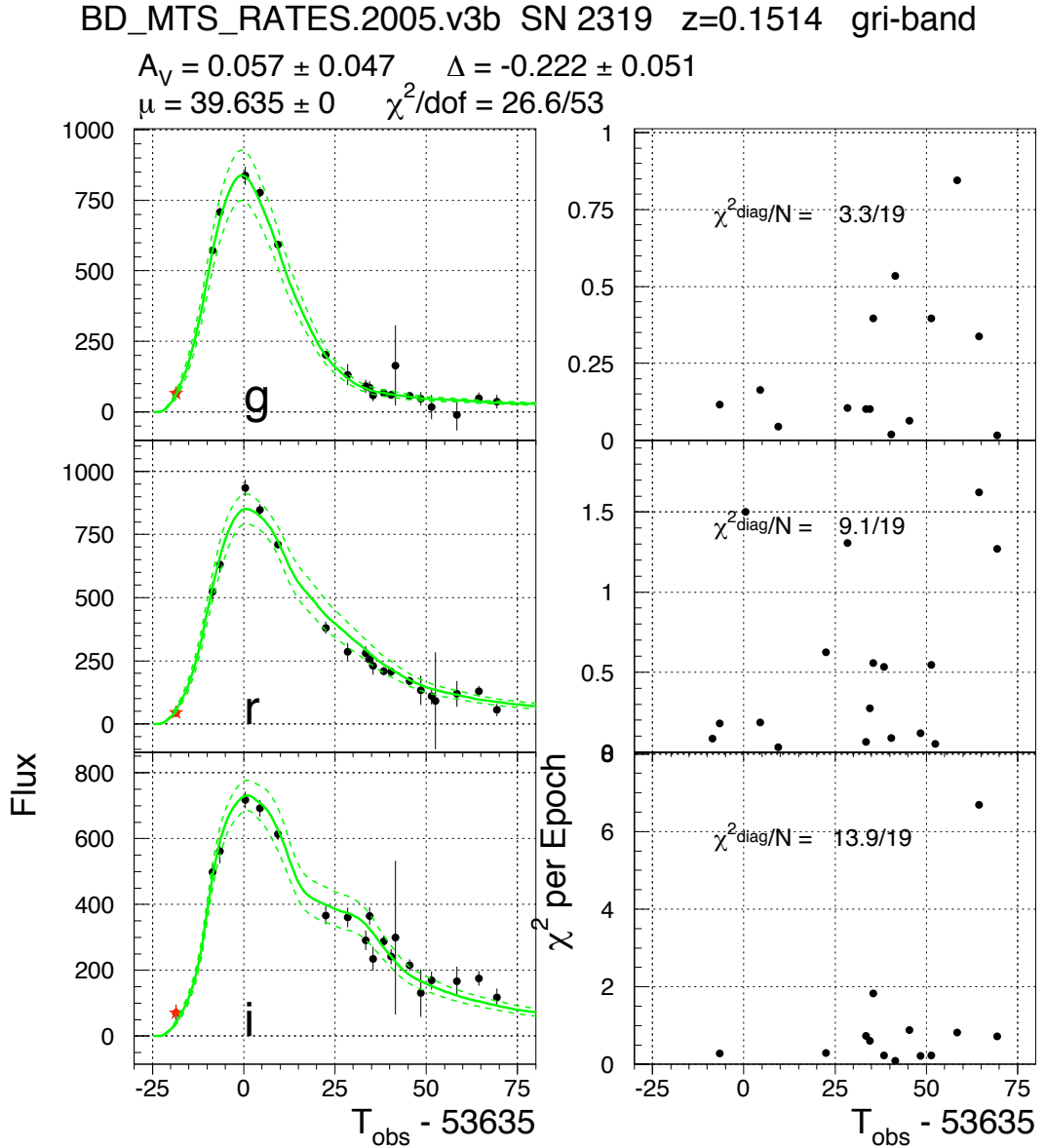


Figure 3.6: A representative light-curve of an object in the sample of 246 objects listed in Table G.1. This object has not been spectroscopically confirmed as a type Ia event. Instead this object has a light-curve that passes the cuts described in §3.2.4, but does not have a spectroscopic redshift for its host galaxy. Thus the redshift described in Table G.1 is that determined from the shown fit. The *gri* light-curves are shown along with the best-fit template from the MLCS2k2 light-curve fitter. Also shown are the residuals from this fit, and the resultant  $\chi^2$  statistic for each filter. The best-fit values for the MLCS2k2 parameters  $A_V$  and  $\Delta$  are shown. This fit is carried out to determine the photometric redshift of the object, and thus a cosmology has been assumed. Points highlighted in red have been removed from the fit due to failing at least one of the criteria described in §3.2.4.

Having produced a sample that is free of spectroscopic prioritisation, and thus “complete” with respect to human judgement we can now look at the overall efficiency of the SDSS-II supernova survey. With this we shall be able to estimate the number of objects that we have lost due to the search pipeline and the selection criteria described above, and thus estimate the type Ia supernova rate in the redshift range of the SDSS-II supernova survey.

### 3.3 Estimating Survey Efficiency

In §3.2.5 we used the selection criteria described in §3.2.4 and §3.2.2, to define a sample of 246 candidates that is free of bias from human influence or spectroscopic inefficiencies. However, this will have an effect of the detection efficiency of the survey, since known type Ia supernova have been rejected.

To determine how many supernova there are in the observing period of the SDSS-II survey we need to determine how many objects have been missed. Objects may not have made it through to the final sample for a number of reasons. The inefficiencies in our search pipeline, including the additional step described in §3.2.2, which are not used for the cosmological analysis need to be estimated. To correct for these effects, we use the scheme described in Dilday et al. (2008) and Dilday (2008), who calculated the efficiency of the SDSS-II supernova survey to a redshift limit of  $z = 0.12$  and later to a limit of  $z = 0.25$  and above. This analysis uses two methods, one where artificial supernova are entered into the data stream using the observing season and Monte-Carlo simulations.

*This section is completed in collaboration with Benjamin Dilday. However, this work comprises the primary result from his PhD thesis.*

#### 3.3.1 Artificial Images

As part of normal survey operations, artificial type Ia supernovae (also known as *fakes*) were inserted directly into the corrected survey images after being processed through the photometric reduction pipeline, PHOTO, but before the difference imaging (see §2.2.2). This allows real-time monitoring of the performance of the software pipeline and of the human scanning operation, *handscanning*.

The fakes are a pixel level simulation of a point source with a light-curve chosen to closely represent that of a real type Ia supernova. At each epoch that the fake has a

chance of being detected, the calculated flux signal for the fake is added to the survey image. A library of fake objects with varying position, redshift, date of maximum light (in the V-band) and intrinsic magnitude dispersion was generated for this purpose, with  $\sim 1,000$  objects in the 2005 season and  $\sim 2,000$  objects in the 2006 and 2007 observing periods, resulting in 7,800 epochs of observation in the 2005 season, and 25,000 epochs for 2006. The redshift distribution of these objects is generated such that the number of objects is approximately proportional to the volume of the Universe at that epoch. Each fake is placed near a galaxy selected from the photometric redshift catalogue (Oyaizu et al. (2007)) for SDSS imaging on Stripe 82. The host galaxy is selected at random such that the redshift of the host is within  $\sim 0.01$  of the simulated fake.

The light-curves of these fakes are generated in the *ugriz* filters using the Bayesian light-curve fitter described in §3.2.1, but with the light-curve parameters chosen from an input probability distribution. To generate the image for each observation, the PSF from the PHOTO pipeline was estimated and the fake photometry was scaled to match the observation, with noise fluctuations added to each pixel. The fake observations were left in the survey pipeline and not revealed to the human scanners during scanning to enable the efficiency of the scanners to be analysed. These fakes are also processed through the automated light-curve fitter to determine the accuracy of this tool in classifying objects after just a few epochs of photometry.

These fakes are used to measure the object detection efficiency as a function of signal-to-noise ratio (SNR) in the *g*, *r* and *i* bands. This detection efficiency is not sensitive to observing conditions (seeing, clouds, moon), as it would be if it was a function of magnitude or redshift. With this detection efficiency known, the type Ia discovery efficiency, as a function of redshift, for all choices of light-curve model parameters and observing conditions can be estimated. These efficiency functions are used in the Monte-Carlo simulations.

These fakes also provide information on the efficiency of the human scanning part of the search pipeline with 95% of all fakes tagged as supernova candidates at least once in their observing period. The 5% that are never identified are only detected at a single epoch by the search pipeline, due to either being at high redshift or because they obtained maximum light well before or after the observing period. All fakes with two or more epochs were flagged at least once by human scanners. A full discussion of these artificial images can be found in Dilday et al. (2008) and Dilday (2008).

### 3.3.2 Monte-Carlo Simulations

Having determined the survey efficiency as a function of signal-to-noise, we are now able to estimate the efficiency as a function of several different variables. This is done using a Monte-Carlo (MC) light-curve simulator. This simulates individual light-curve points based on real observing statistics, but without having to add fake images to the observations. This is possible since the artificial images have shown the *handscanning* to be virtually 100% efficient at detecting supernova events. The MC technique uses the MLCS2k2 light-curve model (§3.2.3) to generate simulated light-curves instead of the Bayesian light-curve model (§3.2.1). For each simulation, the following parameters are drawn randomly:

- *Redshift.*  
This is drawn from a parent distribution that is proportional to the comoving volume element, thus assuming that the type Ia supernova rate is constant with redshift. However, this should not be an issue as the statistics for the dataset make this effect negligible.
- *Host galaxy extinction,  $A_V$ .*  
This is drawn from the same distribution as discussed in §3.2.3, with  $P(A_V) \propto e^{-A_V/\tau}$ , with  $\tau = 0.35$ .  $R_V = 3.1$ , the Cardelli et al. (1989) reddening law is assumed to extrapolate the extinction to other wavelengths. The values of  $R_V$  and  $\tau$  are chosen to be consistent with the inferred extinction distribution for spectroscopically confirmed type Ia in the SDSS supernova sample, and as discussed in §3.2.3 have now changed slightly. However, as discussed in Dilday et al. (2008), these values make no practical difference to the results.
- *MLCS2k2 light curve shape/luminosity parameter,  $\Delta$ .*  
This is drawn from a bimodal Gaussian with a standard deviation of 0.26 for  $\Delta < 0$  and 0.12 for  $\Delta > 0$  (to match the first year results from the SDSS-II supernova survey) and truncated to lie within the valid range of the MLCS2k2 model,  $-0.35 < \Delta < 1.8$ .
- *Time of peak light in rest-frame B-band.*  
This is drawn to be in the observing period of the SDSS-II supernova survey, September - December 2005 / 2006 (for this analysis).
- *Sky Position.*  
This is chosen to be in the survey area, as described in §2.2.1.

- *Location within the host galaxy.*

This is chosen from a distribution that is proportional to the host galaxy surface brightness and is used only to determine galaxy background light. The host galaxy is selected from the SDSS galaxy photometric redshift catalogue (Oyaizu et al. (2007)), such that it has a photometric redshift within  $\sim 0.01$  of the simulated supernova event.

The simulated photometry is generated for each supernova in the rest-frame *UBVRI* magnitudes from the MLCS2k2 light-curve model at epochs for which the survey obtained imaging data at the sky location of the object. Thus the differences in efficiency between areas with differing coverage is automatically accounted for. The magnitudes are corrected for host galaxy and Milky Way extinction, and K-corrected to the observed *gri* passbands (Blanton & Roweis (2007)). Using the zero-points from the SDSS-II supernova survey, these magnitudes are converted to flux values that would have been measured by the SDSS 2.5m telescope. Additional noise is added to each measurement based on observing conditions at the sky location in each filter for the particular epoch by using the PSF of the survey image. Noise from the host galaxy is estimated by fitting an exponential profile (Freeman (1970)) to the galaxy light profile in the *r*-band, which acts as a probability distribution from which the supernova position within the galaxy is drawn, thus the type Ia supernova rate is considered to be proportional to the *r*-band stellar luminosity of a galaxy. The PSF of the survey image is used to convolve the galaxy image and thus estimate the noise contribution from the galaxy.

A set of distributions are compared to observations from the first year of the survey, and confirm that these simulated supernova events are consistent with observations, see Dilday et al. (2008). Since the MC method produces results that are comparable to observed events, 17,000 supernovae were simulated in 17 narrowly defined redshift bins, resulting in  $\sim 1000$  objects per bin, in the redshift range  $0.025 < z < 0.4$ . The efficiency as a function of signal-to-noise, as determined by the artificial images (§3.3.1), were then applied to the simulated MC photometry. As in the search pipeline, a detection in at least two of the *gri* filters is required for the observation to be considered detected and thus to be included in the fit.

As an extension to the work shown in Dilday et al. (2008), the simulated search photometry was then fit with the Bayesian light-curve fitter, as described in §3.2.1, and the cuts as outlined in §3.2.2 were applied. This means that the simulated objects will include the additional cuts used in this work. As shown in §3.3.1, the *handscanning* pipeline causes no obvious loss of candidates. The efficiency is thus the number of simulated

type Ia events that are detected by the pipeline, pass the selection criteria described in §3.2.2, and satisfy the requirements given in §3.2.2, when compared to the total number of objects that reach peak brightness during the survey observation period. Since the observing strategy and weather condition differ between the 2005 and 2006 seasons of the SDSS-II supernova survey, the efficiencies for these two years will differ. The resulting efficiencies for these two seasons are shown in Figures 3.7 and 3.8, where the overall efficiency, the detection efficiency and the efficiency of the cuts described in §3.2.2 are shown. The cuts of §3.2.2 result in the loss of efficiency at low redshift, where the survey had previously been  $\sim 100\%$  efficient (Dilday et al. (2008)). As mentioned in §3.2.2, the Bayesian light-curve fitter can include extra epochs and host galaxy redshift information as priors on the fitting process. These are not used in the method described above, since we require that the method matches that described in §3.2.2.

In §3.2.5, we defined a “incompleteness corrected” sample for the 2005 and 2006 seasons of the SDSS-II supernova survey with the additional constraint that the supernova event lies in the redshift range,  $0.05 < z \leq 0.25$ . The redshift range was chosen primarily because the resultant sample is not dominated by non-spectroscopically confirmed objects, but also because, as shown in Figures 3.7 and 3.8, the SDSS-II survey is not dominated by efficiency corrections over this redshift range. However, a lower redshift cut, whilst ensuring that the survey is highly efficient, would remove a significant fraction of the sample defined in Figures 3.7 and 3.8, and leave any results dominated by statistical and systematic (due to contamination) effects. All of the results given in §5, §6 and §3.4 are also shown with various differences in redshift limits.

Thus, in §3.2.5, we have provided a sample that is free of spectroscopic incompleteness in the redshift range  $0.05 < z \leq 0.25$ , and we have now described the selection function that is the efficiency of the SDSS-II supernova survey. With these two pieces of information, we are able to investigate this population of objects as a function of volume, host galaxy information and their observed properties.

### 3.4 The Volumetric Type Ia Supernova Rate

The primary focus of this analysis is to investigate the properties of the type Ia supernova population with respect to their host galaxy properties and supernova properties. In §3.2 we defined a sample of objects from the first two years of the SDSS-II supernova survey that is free of bias due to spectroscopic incompleteness in the redshift range

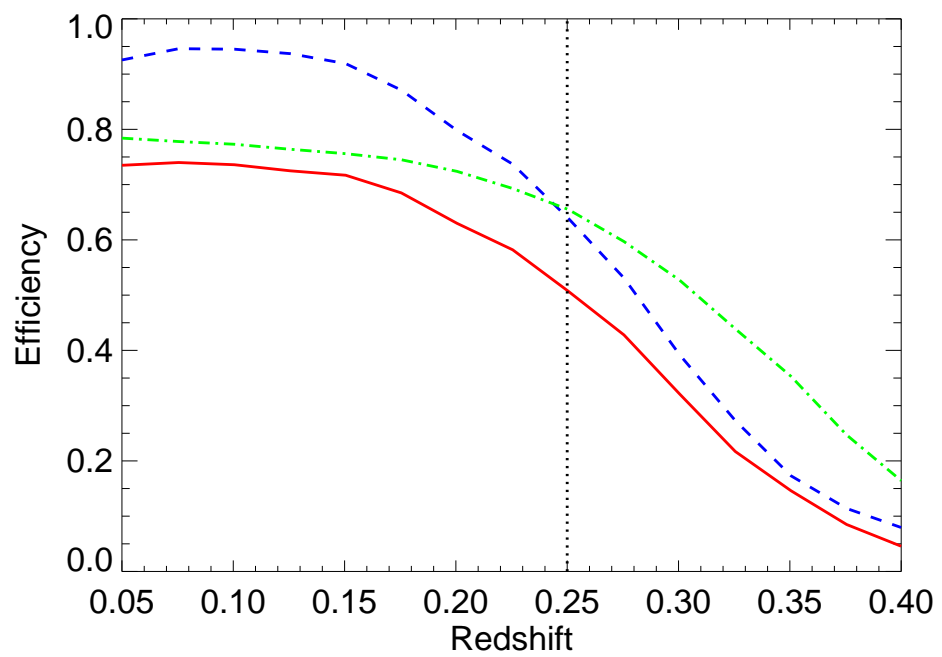


Figure 3.7: Shows the survey efficiency for the 2005 season of the SDSS-II supernova survey. Plotted are the overall efficiency (red solid line), the detection efficiency (green dashed and dotted line) and the effect of the selection cuts (blue dashed line) described in §3.2 and §3.3.

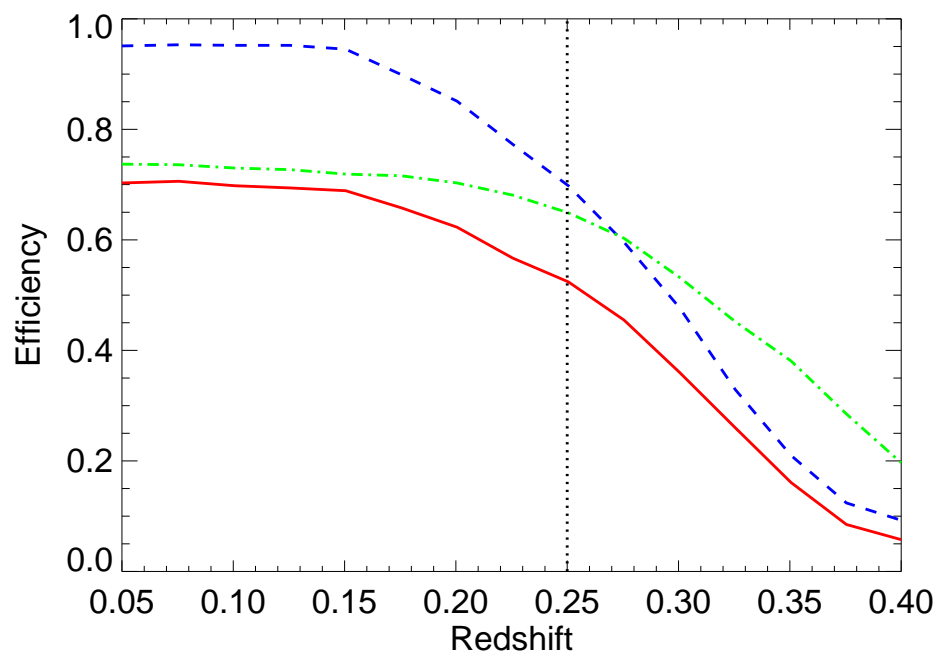


Figure 3.8: Shows the survey efficiency for the 2005 season of the SDSS-II supernova survey. Plotted are the overall efficiency (red solid line), the detection efficiency (green dashed and dotted line) and the effect of the selection cuts (blue dashed line) described in §3.2 and §3.3.

$0.05 < z < 0.25$  and in §3.3 we calculated the efficiency of the survey given the constraints used in §3.2. Using these we can look at the type Ia population. However, this data can also be used to calculate the volumetric type Ia supernova rate. Here we assume a constant rate model.

To do this, we assume a cosmological model, such that  $\Omega_M = 0.3, \Omega_\Lambda = 0.7, \Omega_{total} = 1$  and dark energy equation of state parameter,  $w = p/\rho = -1$ . The observed volumetric type Ia supernova rate,  $r_V$ , is defined as,

$$r_V = \frac{N}{\widetilde{VT}\epsilon}, \quad (3.6)$$

where  $N$  is the number of objects in the sample, and  $\widetilde{VT}\epsilon$  is the multiple of the survey volume,  $V$ , the observer-frame survey duration,  $T$ , and the SN discovery efficiency,  $\epsilon(z)$ , such that,

$$\widetilde{VT}\epsilon = (\Theta T) \int_{z_{min}}^{z_{max}} dz \epsilon(z) u^2(z) \frac{du}{dz} \frac{1}{(1+z)}, \quad (3.7)$$

where  $\Theta$  is the solid angle covered by the survey and  $u(z)$  is the comoving distance in the Friedmann-Robertson-Walker metric, given by,

$$u(z) = \int_0^z dz' \frac{c}{H(z')} = \frac{c}{H_0} \int_0^z \frac{dz'}{\sqrt{\Omega_m(1+z')^3 + \Omega_\Lambda}}. \quad (3.8)$$

If the survey efficiency is independent of redshift, as in our case, such that the redshift range of interest is small, then,

$$\widetilde{VT}\epsilon \sim (VT\epsilon)/(1 + \langle z \rangle), \quad (3.9)$$

where  $V$  is the survey volume and  $\langle z \rangle$  is the volume-weighted mean redshift of the survey.

For the SDSS-II supernova survey, we have  $T = 89$  days ( $= 0.244$  years) for the 2005 season, and  $T = 90$  days ( $= 0.247$  years) for the 2006 season. The solid angle covered by the survey is  $\Theta = 0.08277 \times 0.98$  steradians, which is 98% of the actual sky area of the covered by the survey, due to the masking of bright stars and variable sources. For the sample described in §3.2.5, we have 246 objects (or  $N = 246$ ), for our redshift range of interest,  $0.05 < z < 0.25$ . The efficiency  $\epsilon(z)$  is given in §3.3 for the 2005 and 2006 seasons.

The values of the volumetric type Ia supernova rate for this sample are given in Table

3.2. The rate is calculated in a set of running bins of size  $\Delta z = 0.05$  and are calculated by assuming that the rate in each bin is constant, a good approximation considering the size of each bin. These values are plotted in Figure 3.9 for a set of bins of width  $\Delta z = 0.025$ . Also plotted in Figure 3.9, and given in Table 3.2, are the Poisson error values for each measurement. Dilday (2008) has shown that the systematic uncertainties on these measurements, due to the supernova extinction distribution, and estimated contamination, dominates over the statistical uncertainties only for  $z \gtrsim 0.2$ .

We note that the value for a redshift cut-off of  $z = 0.12$  is  $2.24 \pm 0.49 \times 10^{-5} \text{ SNe yr}^{-1} \text{ Mpc}^{-3} h_{70}^3$ . This is lower than that derived for the first year data-set of the SDSS-II supernova survey (Dilday et al. (2008)) of  $r_V = 2.93 \pm 0.90(\text{statistical}) \pm (\text{systematic})$ , but comparable to the result found in Dilday (2008). For the 2006 season of the SDSS-II supernova survey, 11 type Ia supernovae with  $z \leq 0.12$  were spectroscopically confirmed and peaked during the survey observing period, compared to 19 events in the 2005 season. Thus the supernova yields from the 2005 and 2006 seasons differ by a factor of  $\sim 1\sigma$ . With this redshift range being virtually complete in terms of spectroscopic follow-up, this is the cause of the difference in type Ia rates in this redshift range. As the redshift limits are increased, the type Ia supernova rate in the 2005 and 2006 seasons, when treated separately, are seen to converge. A detailed study of the systematic uncertainties on these measurements can be found in Dilday (2008).

As shown in Figure 3.9 and Table 3.2, the type Ia supernova rate at  $z = 0.1$  and  $z = 0.2$  differ by  $\sim 2.5 - \sigma$  (when an estimate of the systematic uncertainty from Dilday (2008) is included, these values differ by  $\sim 1.9 - \sigma$ ). A fit to these rate values to a linear model of rate versus redshift gives a slope of  $1.63 \pm 0.76 \times 10^{-4} \text{ SNe yr}^{-1} \text{ Mpc}^{-3} h_{70}^3$ . Thus a constant supernova rate is ruled out with  $\sim 2.1 - \sigma$  (excluding systematic uncertainties).

Redshift Limit	Type Ia Supernova Rate <sup>a</sup>
0.10	$2.16 \pm 0.64 \times 10^{-5}$
0.15	$3.05 \pm 0.48 \times 10^{-5}$
0.20	$3.79 \pm 0.41 \times 10^{-5}$
0.25	$3.94 \pm 0.37 \times 10^{-5}$
0.30	$4.16 \pm 0.37 \times 10^{-5}$

<sup>a</sup>measured in  $\text{SNe yr}^{-1} \text{ Mpc}^{-3} h_{70}^3$

Table 3.2: Values of the volumetric type Ia supernova rate for different values of the maximum redshifts considered. The sample described in §3.2.5 is used along with the efficiency calculated in §3.3

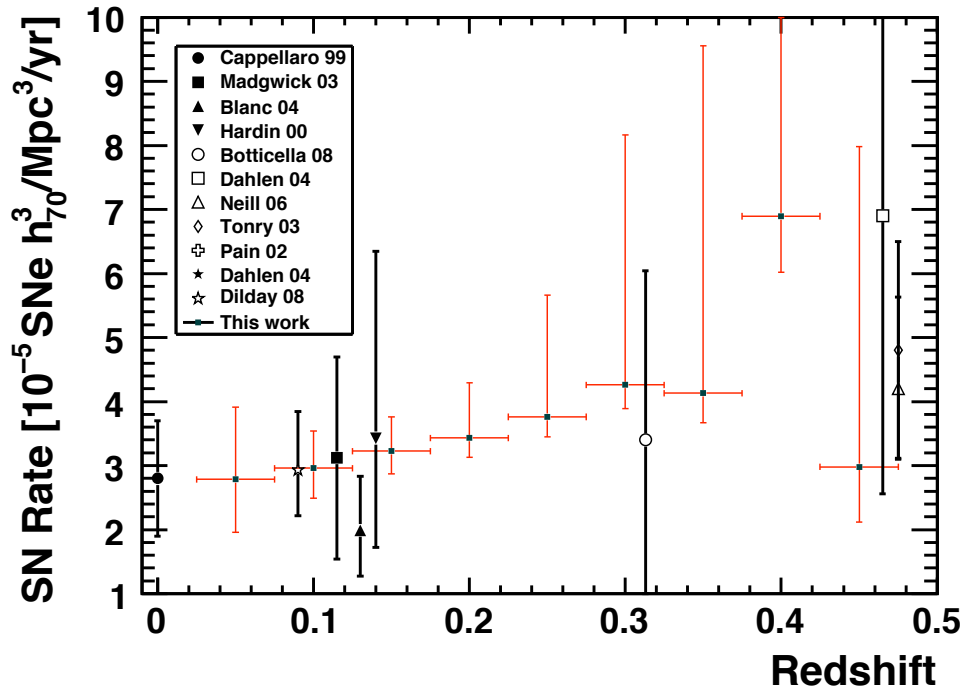


Figure 3.9: Shows the type Ia supernova volumetric supernova rate as a redshift for the SDSS-II Supernova Survey and a selection of measurements from the literature. The redshift is the median redshift of running bins of width  $\Delta z = 0.05$ , assuming a constant rate within the bin. This figure is taken from [Dilday et al. \(2009\)](#), who calculated the supernova rate in the SDSS-II Supernova Survey, with particular attention to the systematic errors, which are shown in red on the plot. Any difference in values to those quoted in Table 3.2 can be accounted for by the different redshift bins, and the fact that the value is calculated as the median in each bin. This analysis has slightly increased the redshift range considered above.

### 3.5 Summary

In this chapter we have described a sample of type Ia supernova events from the first two years of the SDSS-II supernova sample that is complete in the redshift range of  $0.05 < z < 0.25$ . We have also calculated the efficiency of the survey in this redshift range for each of the first two years. Using these, we have been able to calculate the type Ia supernova volumetric rate in this redshift range, and shown that the results are consistent with those derived in [Dilday et al. \(2008\)](#). We have also found that the type Ia supernova rate is increasing in this redshift range. This is consistent with results found at higher redshift, such as those of [Neill et al. \(2006\)](#). We shall now use this sample to investigate the type Ia supernova population with respect to their host galaxies.

# Chapter 4

## Derived Properties of the Complete Supernova Sample

### 4.1 Introduction

In §3, and in detail in §3.2.5, we introduced a “incompleteness” corrected sample of supernovae from the first two years of the SDSS-II supernova survey. This sample, along with the efficiency of the survey (§3.3), is free of bias due to spectroscopic targeting and resources, and thus provides us with the best dataset to investigate the properties of these events. In §3.4, we calculated the volumetric supernova rate of these objects. The main focus of this work is to look at how these supernovae are distributed with respect to their host galaxies and observed properties. Work carried out by [Sullivan et al. \(2006b\)](#) and [Mannucci et al. \(2005a\)](#) has indicated that rate of these supernovae depends on the galaxies they inhabit, primarily that star-forming galaxies host the majority of type Ia supernova (relative to their overall mass). Also the observed properties of these supernovae, such as their light-curve decline rate (parameterised as the MLCS2k2 parameter,  $\Delta$ , or SALT2 parameter,  $x_1$ ) are dependent on the galaxy type. Specifically, [Sullivan et al. \(2006b\)](#) determined that type Ia supernovae occurring in star-forming galaxies are intrinsically brighter than their counterparts in passively evolving galaxies. The intention of this work is to use the well-understood SDSS-II dataset to verify these results in a redshift range where it has not previously been tested. In our redshift range, the host galaxies of these supernovae are free from peculiar velocities, but are not too distant to be dominated by statistical noise.

In order to do this, we need to determine the host galaxy of each supernova. Further to this, we need to obtain a large, comparison sample of galaxies that can be used as an

indicator of the overall population of galaxies. This can be used to compare the distribution of galaxies that host type Ia events with the average galaxy in our redshift range of interest.

In §4.2, we shall introduce the images used to determine the host galaxies of our supernovae. In §4.3, we shall explain how the particular host of each supernovae is determined, and in §4.4, we shall discuss the methods used to convert the observed properties of the host galaxies into physically meaningful characteristics that can be used in our analysis. In §4.5 and §4.6, we shall describe the sample of objects that we are using for the comparison field sample, and the methods used to correct for incompleteness. In §4.7, we will discuss systematic uncertainties in these measurements and the methods used to obtain them. These will be primarily discussed in Appendices §A, §B, §C, §D, §E and §F. Finally in §4.8, we will list the characteristics of the sample and discuss them.

## 4.2 Galaxy Data

In §2.2.1, we introduced the SDSS-II supernova survey region, i.e.  $\sim 300$  square degrees, located on the celestial equator, which has already been imaged multiple times in photometric conditions by the SDSS-I survey (Adelman-McCarthy et al. (2007)). These images were taken before the SDSS-II supernova survey, and thus contain no supernova in our sample. These images have been combined to produce a deep optical stack (Annis & Strauss (2008)) which we will use to identify the host galaxy of each supernova in our final sample. Each single epoch image has a limiting magnitude of  $r = 22.2$ , but the coadded images probe significantly fainter objects with a limiting magnitude of  $r = 23.95$  (calculated from the  $r$ -band number counts of the entire field). A modified version of the PHOTO pipeline (Lupton et al. (2001)) has been used to identify objects in the field in the SDSS  $r$  filter (consistent with the procedures of the SDSS-I survey). Each identified object is then measured in the other four band passes, resulting in a dataset of objects that is complete to the limiting magnitude given above. Photometric zero points of the image are determined from observations of standard stars in the field (Ivezić et al. (2007)).

A variety of magnitude estimates are available for these objects. For this analysis, we use the SDSS `model` magnitudes, which are preferred for faint galaxies. Two models of a galaxy are fit to the two-dimensional image of the object in each band to produce

optimal measures of the fluxes of a galaxy. A pure deVaucouleurs profile, [de Vaucouleurs \(1948\)](#), with surface brightness profile of

$$I(r) = I_e \exp \left( -7.67 \left( \frac{R}{R_e} \right)^{1/4} \right), \quad (4.1)$$

where  $R_e$  is the radius containing half the total luminosity, and  $I_e$  is the surface brightness at  $R_e$ , such that it is truncated beyond  $7R_e$  to smoothly go to zero at  $8R_e$ , and with some softening within  $R = R_e/50$ , is fit to the galaxies light profile, along with a pure exponential profile ([Freeman \(1970\)](#)), with surface brightness profile,

$$I(r) = I_e \exp \left( -1.68 \left( \frac{R}{R_e} \right) \right), \quad (4.2)$$

such that it is truncated beyond  $3R_e$  to smoothly go to zero at  $4R_e$ .

The deVaucouleurs profile provides a good estimation of the light profile of elliptical galaxies and bulges within spiral galaxies, whilst an exponential profile is a reasonable approximation to the disks in late-type galaxies. The best fitting model is returned as the model magnitude. Other magnitude estimates (such as the Petrosian magnitude and aperture magnitudes) are available, but model magnitudes are recommended since they are calculated using a fixed aperture, calculated in the  $r$ -band and applied to each band.

### 4.3 Determining the Supernova Host Galaxies

Having described the images that are available for investigating the host galaxies of the supernovae in our sample, we now turn to the task of determining which of the objects in the deep images are the host galaxies of the 246 candidates listed in [Table G.1](#).

To determine the host galaxy for each supernova event a simple algorithm is used to determine the nearest primary photometric object to the supernova event. The pointing of the SDSS-II survey is exceptional ([Gunn et al. \(2006\)](#), [Pier et al. \(2003\)](#)), meaning that the exact position of the SN Ia event is well known, with the average measured position used for the analysis. These observations are then visually inspected. As all of our objects have  $z \leq 0.25$ , many of them are extended, and thus trivial to identify. In the vast majority of cases ( $\sim 90\%$ ) the determination of the host galaxy is clearly correct. However in a small number of cases ( $\sim 7\%$ ), especially at low redshift, the host galaxy is extended such that another primary object (such as a faint background galaxy or HII region in the spiral arms of the host galaxy) is closer. In this case, the host galaxy is

determined visually. In a minority of cases ( $\sim 3\%$ ), the host galaxy is ambiguous, either because it is too faint to be seen in the coadded stacks, or because it lies in an interacting galaxy pair. In this case, the nearest photometric object is taken to be the host galaxy. For each of these photometric objects, measured model magnitudes and associated errors are obtained in all five *ugriz* filters.

The coadded stack has small gaps in the coverage ( $\sim 15\%$ ), due the masking of bright stars and variable seeing conditions in the single scan images. In the event that a host falls in a gap of the coadd ( $\sim 11\%$  of the time), we use the single scan measurements (York et al. (2000)). Analysis carried out in Annis & Strauss (2008) has shown that there is no systematic difference between these two observations, only larger errors on the obtained magnitudes, and less depth on the coverage.

## 4.4 Determining the Properties of the Host Galaxies

In this section, we determine the properties of each of the host galaxies. In §4.3, we determined the host galaxy of each of the type Ia supernova events described in §3.2.5. The magnitudes and associated error values for each host galaxy was obtained in the *ugriz* bands. However, the colour of a galaxy is not a meaningful physical quantity. Previous studies of galaxies have used their colours to infer physical characteristics such as position on the Hubble sequence. In order to accurately determine the processes occurring within a galaxy, a spectrum is required. This allows observers to calculate the levels of star-formation activity and other factors, such as metallicity, accurately. However, for a large set of objects, including faint sources, such as those in the sample described in §4.3, it is not possible to obtain a complete set of spectra. Thus, these properties need to be calculated in an alternative manner. The most common method for doing this involves fitting Spectra Energy Distributions (SEDs) to the observed colours of the host galaxies.

### 4.4.1 Fitting Spectral Energy Distributions to Galaxy Data

SEDs are template spectra that have been computed for a variety of galaxy evolutionary tracks. These model spectra can be obtained from stellar population models, and stellar evolution theory, such as Bruzual & Charlot (2003) and Maraston (2005). These model spectra are based on simple stellar populations (SSPs), consisting of chemically homogeneous and concurrent stars of various stellar masses according to an initial mass function (IMF), such as Salpeter (1955), Scalo (1986) and Kroupa (2001).

The template stellar population models can be compared to observed quantities (e.g.

fluxes or magnitudes) of the galaxies to obtain the best fit template and thus determine the likely physical properties of the host galaxy. To do this, the input SEDs are convolved with a given filter set and the resultant magnitudes are compared to the observed values. A  $\chi^2$  minimisation, is then used to find the best fit. i.e.

$$\chi^2 = \sum_{i=1}^N \left( \frac{F_i^{obs} - b \times F_i^{synth}}{\sigma_i} \right)^2 \quad (4.3)$$

where  $N$  is the number of filters used,  $F_i^{obs}$  is the observed flux in each filter  $i$ ,  $F_i^{synth}$  is the template flux in each filter,  $\sigma_i$  is the errors on the observed flux in each band, and  $b$  being the normalisation factor between the template and the observation.

The best-fit template can be used to estimate the photometric redshift of the galaxy, the age of the dominant stellar population and other physical properties. Alternatively, if the redshift of the input galaxy is known, then it can be used to reduce the uncertainty on the best fit template and thus improve the accuracy of the derived properties.

In this work we shall consider the PÉGASE SED's. Whilst there are many available template SED's, this choice enables us to produce a result which is directly comparable to that of [Sullivan et al. \(2006b\)](#), who used the same templates.

### The PÉGASE Models

In this analysis, we shall use the PÉGASE.2 (Projet d'Étude des GALaxies par Synthèse Évolutive) galaxy spectral evolution code ([Fioc & Rocca-Volmerange \(1997\)](#), [Le Borgne & Rocca-Volmerange \(2002\)](#) and [Le Borgne et al. \(2004\)](#)) and associated SEDs. This code consists of nine evolutionary scenarios, of which we consider eight (to match the analysis of [Sullivan et al. \(2006b\)](#)), which are defined by various star-formation parameters. K+e-corrections are computed so that the model is able to predict redshifted SEDs, and thus compare it to our galaxies throughout redshift space.

The PÉGASE.2 models are an example of an ‘‘Isochrone Synthesis’’ approach to galaxy modelling. For these models, the monochromatic flux of the galaxy at age  $t$  and wavelength  $\lambda$  can be written as,

$$F_\lambda(t) = \int_0^t \int_{m_1}^{m_u} \tau(t - \theta) \phi(m) f_\lambda(m, \theta) dm d\theta, \quad (4.4)$$

where  $\tau(t - \theta)$  is the star-formation rate at time  $(t - \theta)$  in  $M_\odot$  per time and mass units,  $\phi(m)$  is the IMF in the interval  $[m_1, m_u]$ , normalised to  $1M_\odot$ , and  $f_\lambda(m, \theta)$  is the monochromatic flux of a star with initial mass  $m$  at wavelength  $\lambda$  and at age  $\theta$  (Fioc & Rocca-Volmerange (1997)). In this method, the integral over time is discrete, such that

$$F_\lambda(t) = \sum_{i=1}^{p-1} \tau(t - \theta_i)(\theta_{i+1} - \theta_i) \int_{m_1}^{m_u} \phi(m) f_\lambda(m, \theta_i) dm, \quad (4.5)$$

where  $\theta_1 = 0$  and  $\theta_p = t$ , and  $(\theta_{i+1} - \theta_i)$  is small such that  $\int_{m_1}^{m_u} \phi(m) f_\lambda(m, \theta_i) dm$  has not significantly evolved between isochrones. The tracks used in this analysis are discussed fully in Fioc & Rocca-Volmerange (1997).

To carry out this process, we use the public tool Z-PEG which is primarily used to estimate redshifts of objects, but in our case, with the redshift of our galaxies known, is used to determine the physical parameters. The method assumes that distant galaxies are similar to local galaxies, but just look younger at high redshift. The eight spectral types used in this analysis are shown in Table 4.1, with the star-formation rates being proportional to the gas density (except for one exception), with the conversion rate,  $\nu$ , increasing with galaxy type through the Hubble sequence. Infall is used to simulate the growth of mass, whilst and galactic winds are used to prevent further star-formation activity (by subtracting the level of gas). These scenarios match the observations of galaxies at  $z \simeq 0$  (Le Borgne et al. (2004)). Figure 4.1 shows a comparison of four synthetic spectra at  $z = 0$  as described in Table 4.1 to observed galaxy spectra from Fioc & Rocca-Volmerange (1997). In this Figure, emission lines have been removed from the observed spectra (Galaz & de Lapparent (1998)). Here the prominent absorption features of the observed spectra are well re-produced.

For our analysis, we use a Kroupa (2001) IMF. This is represented by a two part power law,  $\xi(m) \propto m^{-\alpha_i}$ , with  $\alpha_1 = 1.3$  for  $m < 0.5M_\odot$  and  $\alpha_2 \simeq 2.2$  for  $m > 0.5M_\odot$ . This has been shown to resemble observations better than the commonly used Salpeter IMF (Salpeter (1955)), which is a single power-law with slope (parameter  $\alpha$  from above) of 1.35. Analysis carried out in Le Borgne & Rocca-Volmerange (2002) and Giallongo et al. (1998) has shown that the choice of IMF does not significantly influence the resulting template fits for a set of high signal-to-noise objects.

In PÉGASE.2, there are two available dust profiles. For passive galaxies (Elliptical and S0 galaxies), the dust distribution is modelled using a King profile (King (1980)), whilst for star-forming galaxies (Sa, Sb, Sbc, Sc, Sd, Irr), the dust is distributed along a uniform

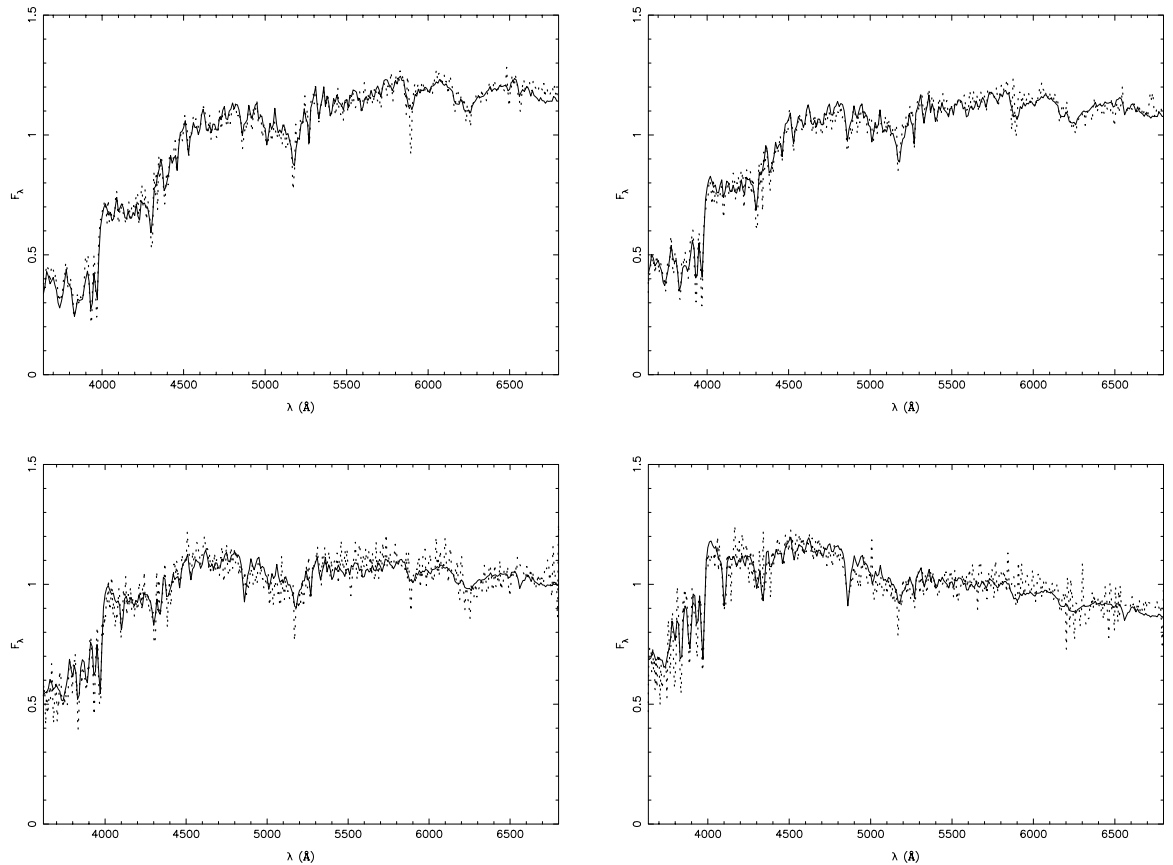


Figure 4.1: Example spectra of four different galaxy types from the PÉGASE.2 spectral library, as described in Table 4.1. Spectra of observed galaxies (Kennicutt (1992)) are overplotted. The synthetic spectra are shown at  $z = 0$ . This figure is taken from Fioç & Rocca-Volmerange (1997). Top left: synthetic elliptical vs. NGC 3379. Top right: synthetic Sa vs. NGC 3368. Bottom left: synthetic Sbc vs. NGC 3147. Bottom right: synthetic Sd vs. NGC6643.

plane-parallel slab and mixed with gas. The amount of dust in the host galaxy is such that it evolves in parallel with the amount of gas present in the galaxy. No additional dust is added in the fitting process, since this would lead to additional freedom in the template spectra, which especially in regards to the field sample, would be difficult to constrain, possibly leading to a systematic bias in the determined derived properties.

To fit the template SEDs to the observed fluxes, we use a spatially flat cosmology with  $\Omega_M = 0.3$ ,  $\Omega_\Lambda = 0.7$  and  $H_0 = 70 \text{ km s}^{-1} \text{ Mpc}^{-1}$ . For the host galaxy sample, all of the redshifts are known, either from the spectra of the supernova or host galaxy, or from the photometric redshift from MLCS2k2. All of the template SEDs are computed at 69 time-steps, so with 8 scenarios, we have a total of 552 template SEDs. For the objects in our host sample, we convert the magnitudes to fluxes, along with their associated error values, and fit the template SEDs. Each of the five SDSS filter bands is used in the template fitting process. Having discussed the set-up used for the SED fitting, we now move on to a discussion of the important parameters that are output from this process.

#### 4.4.2 Derived Properties

For this study two parameters dominate a galaxy evolutionary path; the galaxy mass and star-formation rate.

##### Host Galaxy Mass

The total stellar mass of a galaxy is the current mass of all stars in the galaxy. This is calculated by integrating the total star formation history (SFH) of the best fit template up to the best-fit age of the galaxy and subtracting the mass of stars that have died out. This is calculated using the normalisation factor determined from Equation 4.3. Since the PÉGASE.2 templates are normalised to  $1M_\odot$ , it is trivial to calculate the stellar mass.

Alternative methods to using SED template fitting for deriving the mass of a galaxy include using the absolute magnitude of the host object as a proxy for its stellar mass. Most commonly used is the  $r$ -band magnitude, or specifically red bandpasses, since the stellar mass of an object is dominated by older and further evolved stellar objects. This is principally due to the fact that low mass stars live much longer than high mass stars. Figure 4.2 shows the relationship between host galaxy mass, as derived from the PÉGASE.2 templates and the  $r$ -band absolute magnitude of each object. The host galaxy of each object described in §4.3 is plotted along with associated error bars for each object. The best-fitting line is also plotted which has a gradient of  $0.49 \pm 0.01$ , showing that for the

objects described in §3.2.5, the host galaxy mass is well correlated with the magnitude of the object.

### Host Galaxy Star-Formation Rate

The second parameter of interest is the star-formation rate within the host galaxy. This is difficult to determine accurately since the instantaneous star-formation rate of an object is best determined from the nebular emission lines from the host (Kennicutt (1998)). These are only accurately measured from observed spectra of the host galaxies, for which we have a very limited and non-homogeneous sample. Template fitting methods are unable to determine the instantaneous star-formation accurately, since our best fit scenario is determined using broad-band filters. As an alternative method, we follow the process of Sullivan et al. (2006b) and estimate the “mean” star-formation rate over an extended period. These can be determined from our best fit template by averaging the star-formation rate over an extended period. Sullivan et al. (2006b) determined that a period of 0.5 Gyr was sufficient to estimate star-formation rates without large systematic uncertainties. We adopt this time period in this analysis. We also require that the best-fit template has an age that is younger than the age of the Universe at the redshift of the galaxy.

An alternative method to estimate the proportion of star-formation activity that is ongoing in the host galaxy, relative to the mass of the host is to consider the colour of each object. Galaxies which are passively evolving are primarily seen to be red in colour, whilst galaxies with ongoing star-formation activity, are blue. To probe this, Figure 4.3 shows the  $u - r$  absolute magnitude colour for the galaxies in our sample. These galaxies have been corrected for Milky-Way extinction. The plot shows how objects which are considered to have no ongoing star-formation (from the best fit PÉGASE.2 templates) are plotted in red, whilst those with determined star-formation rates are plotted in green (for moderate levels of star-formation) and blue (for high levels of new stars being formed). This figure shows that galaxy colours are in good agreement with our determination of star-formation, but that galaxies with high or moderate levels of star-formation activity cannot be determined purely based on their colour information, and that the luminosity of the object is also required. This is due to a degeneracy between the age of a galaxy and its metallicity, and the fact that young galaxies can be red in colour when they are dominated by stars in the TP-AGB phase of their evolution (see §E for more detail).

Another possible approach to determine the star-formation rates of our host objects is to consider the ultra-violet (UV) luminosity, and use a method similar to that described

Type	$\nu$	Infall	gal. winds	age at $z = 0$
E	3.33	300	1 Gyr	$> 13Gyr$
S0	2	100	5 Gyr	$> 13Gyr$
Sa	0.71	2800		$> 13Gyr$
Sb	0.4	3500		$> 13Gyr$
Sbc	0.175	6000		$> 13Gyr$
Sc	0.1	8000		$> 13Gyr$
Sd	0.07	8000		$> 13Gyr$
Irr	0.065 <sup>a</sup>	8000		$> 9Gyr$

<sup>a</sup>For this scenario we have  $SFR = \nu \times M_{gas}^{1.5}$

Table 4.1: The eight PÉGASE scenarios used for our SED fitting process. This table is based on information in Table 1 of [Le Borgne & Rocca-Volmerange \(2002\)](#). Here  $SFR = \nu \times M_{gas}$ , except for irregular galaxies, for which  $SFR = \nu \times M_{gas}^{1.5}$ .  $\nu$  is in units of  $Gyr^{-1}$  and  $M_{gas}$  is the gas density. Infall time-scales are in Myrs. For all scenarios, the age of the Universe acts as an upper limit for the age of the galaxy. The dust distribution is fitted on a King profile for E and S0 galaxies, whilst an inclination-averaged disk distribution is used for spiral and irregular galaxies.

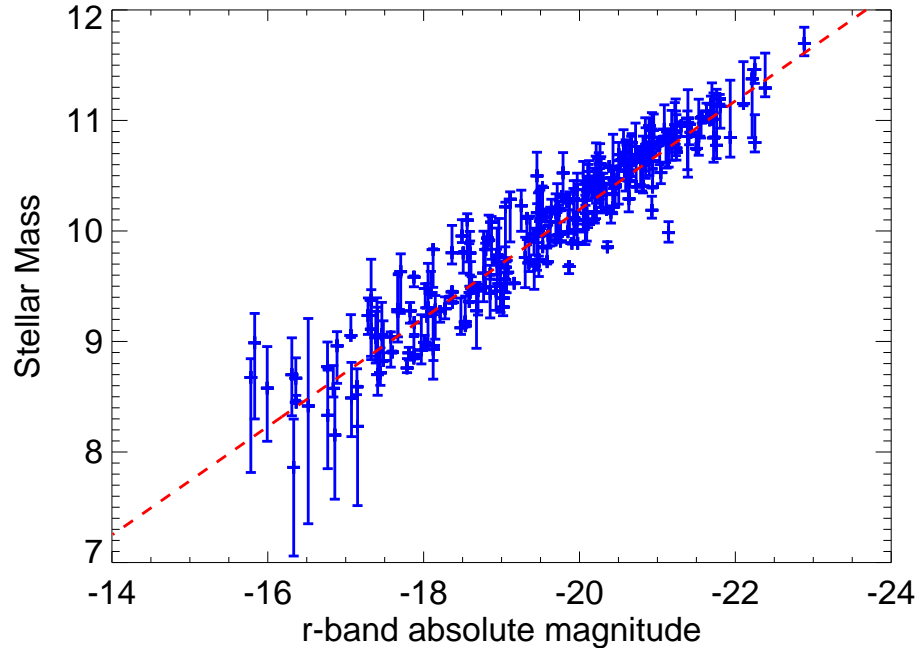


Figure 4.2: Showing the relationship between host galaxy mass (as derived from the PÉGASE.2 model templates using the ZPEG code) and  $r$ -band absolute magnitude. The host galaxy stellar mass is plotted in logarithmic units, with error bars as estimated from the PÉGASE.2 templates. The best-fitting line is overplotted in blue, with a gradient of  $0.49 \pm 0.01$ .

in [Donas et al. \(1987\)](#). There are two issues with this method. This method tends to overestimate the star-formation rate in old stellar systems, due to contamination of evolved systems, and the ultra-violet filter used in this analysis (*u*-band) has a poor response function, resulting in large error values on these measurements.

We have now determined the derived parameters that are important for our analysis. Several other mechanisms are important when looking at the evolution of a galaxy, such as metallicity and age of the object. However, there is a degeneracy between the age of a galaxy and its metallicity, meaning that there are significant systematic uncertainties on these measurements, and thus they are not considered here. Statistical uncertainties, due to errors in the magnitudes of our objects, in the resultant derived parameters are determined using a  $\chi^2$  statistic and considering all of the 552 templates available in the fitting process, such that a likelihood surface in mass and star-formation rate is produced. This surface can then be used to produce the associated error values on the best-fit solution. In the event of two minima in the  $\chi^2$  statistic, the best-fit solution is considered. This is only appropriate in the case where the redshift of the object is not known, since in this case there is a degeneracy between galaxy properties and redshift.

## 4.5 The Comparison Field Sample

In order to investigate the type Ia supernova host galaxy population, we also require a large (and preferentially deep) sample of galaxies that will form a representative galaxy sample in our redshift range. In §4.3 and §4.4, we both determined the host galaxies of each supernova in our sample (§3.2.5) and obtained their derived properties. For our comparison field sample we shall use the galaxy data for “stripe-82”. This sample consists of greater than 10 million objects which are considered galaxies by the SDSS pipeline PHOTO; 9 million of these have magnitudes above the limiting magnitude of the coadded image.

### 4.5.1 Derived Properties of the Comparison Field Sample

In order to investigate the differences between this sample, and that of the host galaxies (which shall form part of the analysis of §5), we need to determine the derived properties of the field sample. Further to this, the redshift of each object in the field sample is unknown, and thus to determine the distribution of galaxies in our redshift range of interest,  $0.05 < z < 0.25$ , we need to determine the redshift of each object.

The method used to determine all of these properties is similar to that discussed in §4.4,

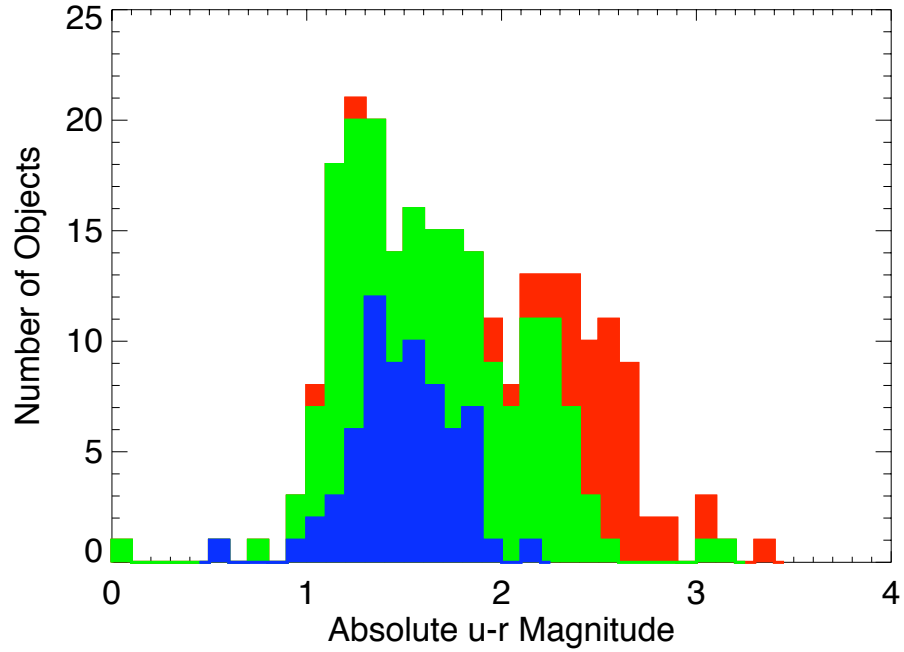


Figure 4.3: Cumulative histogram showing the distribution of objects in the sample described in §3.2.5 as a function of  $u - r$  absolute colour. Objects with current levels of star-formation activity are plotted in blue (for highly star-forming objects (defined, here, as  $SFR > 0.5$ )) and green (for moderately star-forming objects (defined here, as  $SFR < 0.5$ )) and those with no current star-formation activity are shown in red. The plot shows that passively forming galaxies are primarily red in absolute colour. However, objects with current star-formation activity are widely spread in  $u - r$  colour. No observable trend between levels of ongoing star-formation activity and  $u - r$  colour is seen, since highly and moderately star-forming galaxies are seen to have similar colours in  $u - r$  space. This is due to the degeneracy between age and metallicity, and the fact that young galaxies can be red in colour when they are dominated by stars in the TP-AGB phase of their evolution (see §E for more detail).

with the exception that in this case, the redshift of the best-fit template is left as a free parameter. For this, we enforce a redshift range of  $0 < z < 2$  for the template fitting process, with redshift steps of  $dz = 0.01$ . This method will produce photometric redshifts with errors larger than this value. We also use the same fiducial cosmological model as described in §4.4.1, and again fit in flux-space, having removed the contribution from Milky-Way dust. The same templates to those described in §4.4 are used. The resultant derived parameters, and associated error values, are the same as described in §4.4. In the case where two or more minima are found to be viable solutions the best-fit template is considered. This is only prominent for objects with low signal-to-noise ratios. Only objects with magnitudes greater than the limiting magnitude of the coadded image are considered. In total, only 1.5 million objects are found to be in our redshift range of interest. Our redshift range of interest contains a low redshift cut-off of  $z = 0.05$ . This is implemented to ensure that objects that are determined to be stellar objects by the best-fit PÉGASE templates are not included in any analysis.

An alternative approach to this would be to consider using measured mass and luminosity functions from other galaxy samples, such as those of [Baldry et al. \(2006\)](#) and [Cresswell & Percival \(2008\)](#). However, whilst it is possible to determine the mass distribution of objects in our redshift range of interest, no such information on the star-formation rate of these objects and their relationship to stellar mass exists, without a conversion to galaxy colour. A large sample of galaxies have had their masses and star-formation rates determined spectroscopically ([Kauffmann et al. \(2003\)](#) and [Brinchmann et al. \(2004\)](#)), but these samples are limited to low-redshift and high signal-to-noise observations, and thus is biased towards high mass systems. An analysis of the differences between these determinations of star-formation rates and masses, when compared to those from the PÉGASE.2 templates, is given in §B.

## 4.6 Incompleteness of the Field Sample

In §3, we discuss the methods used to correct the sample of supernova events as detected and confirmed by the SDSS-II supernova sample for incompleteness. Incompleteness will also affect our field galaxy sample. Since our sample of field galaxies is magnitude limited, galaxies with different absolute magnitudes will pass the magnitude limit of the coadded image at different redshifts. This is dependent on both galaxy type and absolute magnitude for each object, and needs to be corrected for.

The maximum redshift that we consider for our analysis is  $z = 0.25$ . Thus objects

that can be seen past this redshift limit will not be affected by incompleteness. However, for objects which cannot be seen to this limit, we need to correct for the fact that they will be under-represented at large redshifts. To do this, we adopt the  $V_{\max}$  method (Schmidt (1968), Felten (1976)).

For each object in the comparison field sample the maximum redshift at which it would still be included in our sample is calculated. This is determined to be either the redshift in which the object would exceed the limiting magnitude of our coadded image (in the  $r$ -band) or the maximum redshift considered for this study ( $z = 0.25$ ). Using this redshift, the corresponding co-moving volume is calculated. Each galaxy is then weighted by a factor of  $V_{\text{survey}}/V_{\max}$ , where  $V_{\text{survey}}$  is defined as the co-moving volume of the SDSS-II supernova survey considered, or in this case, the total volume enclosed by  $0.05 < z < 0.25$ .

Using this method, objects which can be seen throughout the survey volume will have a  $V_{\max}$  correction of one, whilst objects which cannot be seen to all redshifts will be weighted by a factor greater than one. This method assumes that the luminosity functions of passive and star-forming galaxies will follow the same path, after the turn-over magnitudes are reached. Recent work, such as Salimbeni et al. (2007) and Cresswell & Percival (2008), have indicated that these two galaxy populations do not perfectly follow a Schechter function (Schechter (1976)) and instead are differently distributed in low mass systems, with the number density of passive galaxies dropping off for low mass systems, and the opposite effect seen for star-forming objects. Despite this, the  $V_{\text{survey}}/V_{\max}$  correction is useful for correcting for incompleteness, and with the depth of our coadded image, the value of  $V_{\text{survey}}/V_{\max}$  does not significantly affect any of our results in §5 and §6.

Therefore we have defined a sample of objects that represents the overall population of galaxies in our redshift range of interest and described a method for correcting this for incompleteness due to our sample being magnitude limited.

## 4.7 Systematic Uncertainties

In §4.4, we described how the statistical uncertainties due to errors in the magnitude measurements of our host galaxy and field galaxy samples are included in the errors of our template fitting process. However, it is possible that there will also be systematic errors in our determination of the masses and star-formation rates of our objects.

There are many obvious sources of systematic uncertainty in our measurements. These include the wavelength coverage of our filter selection, the choice of SED templates used and the effect of knowing (and thus forcing) the redshift of our host galaxies, especially when compared to those in our comparison field sample, which are fitted without redshift information. Several of these are discussed in the various appendices at the end of this work. Other possibilities, such as our choice of IMF are considered in other published work.

We summarise some of these errors below.

- The potential of a bias in the use of spectroscopic redshifts for the host galaxy sample, when compared to the photometric redshifts used for the comparison field sample.

This is considered in Appendix [A](#). This issue mainly concerns our comparison field sample. Here we look for differences between the spectroscopic redshifts of the host galaxies in our sample and the photometric redshifts that are obtained when these objects are fitted without prior knowledge of their spectroscopic redshift. We find that the photometric redshifts produced by the PÉGASE.2 templates differ from the spectroscopic redshifts with a mean difference of  $0.044 \pm 0.0022$ , with photo- $z$ 's being smaller than spectroscopic redshifts. The corresponding mass distribution is found to differ with a mean value of  $0.11 \pm 0.0055$ . In Appendix [E](#) we use the Maraston SEDs to show that it is reasonable to expect this offset in redshift between the true redshift and that predicted by PÉGASE is constant with apparent  $r$ -band magnitude for the entirety of our field sample. There is considerable scatter between the star-formation rates determined by fixing the redshift compared to leaving it free, although this is expected by the extra freedom in the template fitting.

The effect of this systematic is difficult to quantify, since it primarily concerns the comparison field sample. However, any increase in galaxies in our redshift range of interest can be reasonably expected to be offset by the corresponding decrease in mass. The scatter in the star-formation rate plane indicates that this bias should not affect specific galaxy types. In Appendix [F](#), we attempt to quantify the effect of this observed offset. We find that if the redshift of each galaxy in the field sample is corrected in both mass and redshift, using the values calculated above, then the results found in Chapter [5](#) are not affected. This makes the assumption that there is no overall bias with respect to galaxy type.

- The wavelength coverage of the SDSS survey.

This is discussed in Appendix [D](#). Here we investigate the effect on the derived properties by the wavelength covered by the SDSS filters, to ensure that our derived properties are directly comparable to those of [Sullivan et al. \(2006b\)](#) at high redshift. We find no systematic offset in the derived parameters when different filter sets (including GALEX) are used in the template fitting.

- The accuracy of the derived properties

This is discussed in Appendix [B](#). We compare the results of the PÉGASE.2 fitting to a set of galaxies whose mass and star-formation has been estimated from their spectra. We find no evidence of a systematic bias in the estimated mass and star-formation rates from the PÉGASE.2 templates. However, it should be noted that the estimates of mass and star-formation rate derived from the spectra are calculated using the SED's of [Bruzual & Charlot \(2003\)](#), which use the same underlying physics as the PÉGASE models, and also omit the TP-AGB phase of evolution. The spectral features used to determine these quantities are broad, and thus the estimates are somewhat uncertain. A discussion of these effects is given in Appendix [B](#).

- The accuracy of the redshift and derived properties of the field sample.

This is investigated in Appendix [C](#). We use a large sample of galaxies with a spectroscopic redshift to quantify the results found in Appendix [A](#). A small offset in redshift is seen, but this affect on the final results discussed in [§5](#) is offset by a corresponding change in mass.

- The effect of using the PÉGASE.2 templates.

Other template fitting methods are available, such as [Bruzual & Charlot \(2003\)](#) and [Maraston \(2005\)](#). Analysis of the various available templates have shown that the main systematic difference between them involves the estimated age of a galaxy. However, there is limited data to suggest that these different models produce significantly differing redshift estimates. The ZPEG code used in this analysis is the only publicly available method for determining both the redshift, mass and star-formation rate of a host galaxy using colour information alone.

- The effect of dust on the stellar mass estimates.

This systematic was discussed in [Sullivan et al. \(2006b\)](#) and investigated fully in [Le Borgne & Rocca-Volmerange \(2002\)](#). Dust is already included in each of the scenarios of [Table 4.1](#), but purely as an average correction. The analysis of [Sullivan et al. \(2006b\)](#) showed that the inclusion of additional dust using a [Calzetti et al.](#)

(2000) extinction law lead to a systematic under-estimation of the determined star-formation rate, but did not affect the stellar mass estimates.

These systematic tests described above show the scatter that can be introduced by varying some of the parameter choices described previously in this analysis. However, importantly no trend is seen with redshift (for the comparison field sample) or host galaxy mass and star-formation rate for either of the two samples. Thus, within the framework of the PÉGASE models, we should not have a bias towards a particular galaxy type. Therefore, we can proceed with the belief that the analysis described in this chapter will not introduce a galaxy dependent bias into our results.

There are other possible sources of systematic uncertainty in our method of obtaining the derived properties of objects in our sample, but these are expected to be sub-dominant to those discussed above.

## 4.8 Details of the Galaxies in our Sample

In this chapter, we have taken the sample of supernovae described in §3.2.5 and determined the host galaxy of each. Having determined this host galaxy we have described the method used to calculate the derived properties, and in particular the host galaxy mass and ongoing star-formation rate. Thus we have a sample of 246 galaxies, each with a value their mass and star-formation activity. We have also described a comparison field sample which is complete to  $r = 23.95$ . This sample of galaxies will be used in later work as a representative sample of galaxies in our redshift range of interest. We have also explained a method for correcting this sample for incompleteness.

In §4.5, we explained that only objects with  $r < 23.95$  are included in our final comparison field sample. In a similar manner, two objects from the host galaxy sample are excluded from later stages of the analysis since they do not satisfy this criteria. These are candidates 12978 and 13038 from Table G.1. One of these objects is a spectroscopically confirmed object with  $z = 0.101$ , whilst the other is an object whose redshift of  $z = 0.166$  has been determined from the MLCS2k2 light-curve fitter. Thus we have 244 objects that shall be used in the analyses of §5 and §6. The lose of these two objects does not affect the results from these chapters.

Table H.1 lists the determined host galaxy properties of the 244 objects that comprise our final sample. Listed in the table are the redshift of each object, its host galaxy mass (in logarithmic units) and estimated mean star-formation rate (also in logarithmic units).

Galaxies with no star-formation activity are denoted as  $-99$ . Also listed is the specific star-formation rate (§5.2,  $sSFR$ ) which is defined as,

$$sSFR = SFR/Mass, \quad (4.6)$$

or,

$$\log(sSFR) = \log(SFR) - \log(Mass). \quad (4.7)$$

For galaxies with no mean star-formation rate, the value of the specific star-formation rate is undefined, and thus they are denoted with the value of  $-99$  in Table H.1. Also shown in this table are the best-fitting templates as determined by ZPEG. Figure 4.4 shows a histogram of the best-fit templates for both the host galaxy sample (plotted in red) and the comparison field sample (shown in blue). This Figure has been normalised such that both distributions contain the same area. On this Figure, 1 represents the Elliptical template (described Table 4.1), whilst 2=S0 galaxies, 3=Sa, 4=Sb, 5=Sbc, 6=Sc, 7=Sd, 8=Irr galaxies respectively. The field sample has not been corrected for incompleteness. The key difference between the two samples involves the percentage of objects that are classified as Elliptical and S0 respectively, with the host galaxy sample finding a larger percentage of objects that are S0 in nature. This difference between the two samples is discussed further in §5.2.1.

Thus we have described, and in Table H.1 listed, the host galaxy properties of the 244 objects in our final sample of supernova events (as listed on Table G.1). Two objects have been lost due to having particularly faint hosts. Using this sample, and the correction for efficiency described in §3.3, we can thus describe the population of type Ia supernova hosts from the first two years of the SDSS-II supernova survey. We have also defined a comparison field sample, and associated correction for incompleteness, which can be used to describe representative objects in our redshift range of interest. Using these two components we can thus move forward to describe how the type Ia supernova rate, and the properties of their light-curves are related to the host galaxy in which they occur. This is investigated in §5 and §6.

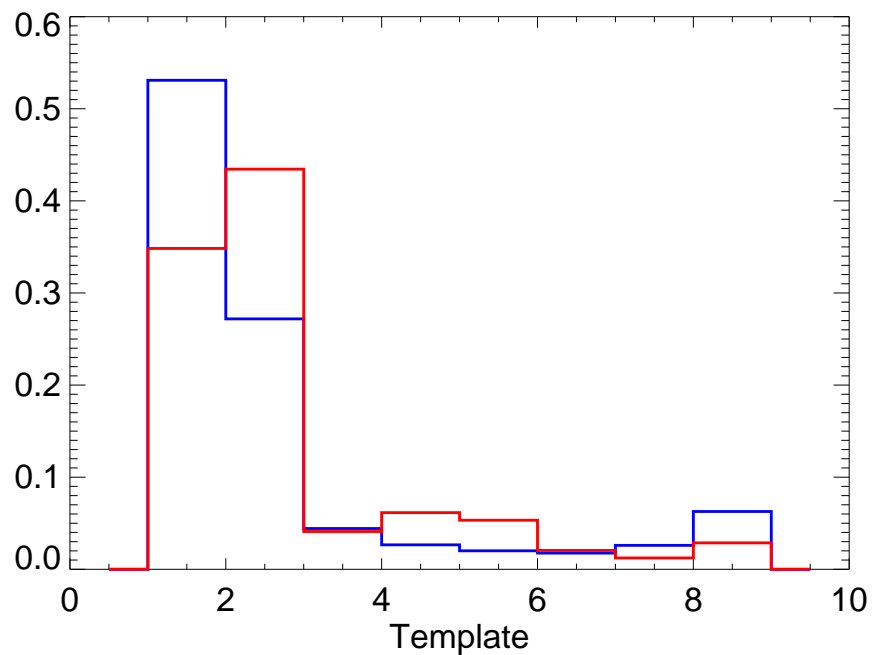


Figure 4.4: The normalised distributions of best-fitting PÉGASE.2 SEDs for the field sample in our redshift range of interest (plotted in blue) and host galaxy sample (plotted in red). For this figure we have normalised the two histograms to have the same area. The values stand for the following templates: 1=Elliptical, 2=S0, 3=Sa, 4=Sb, 5=Sbc, 6=Sc, 7=Sd, 8=Irr respectively. The field sample has not been corrected for incompleteness. The main difference between the two populations concerns the percentage of Elliptical and S0 objects.

# Chapter 5

## Host Properties of Type Ia Supernovae

### 5.1 Introduction

Previous studies of the type Ia supernova population has primarily involved the type Ia supernova volumetric rate, which has been seen to be increasing as a function of redshift, at least until a redshift of  $z \sim 1$ . However, several recent studies ([Mannucci et al. \(2005a\)](#) and [Sullivan et al. \(2006b\)](#)) have attempted to investigate the type Ia supernova rate as a function of the host galaxy in which the supernova occurs. Both of these studies have found that for early-type or passive galaxies, the type Ia supernova rate is dependent on the mass of the host galaxy, with a linear dependence found. However, this parameterisation of the type Ia supernova rate is not found to be consistent for galaxies with recent star-formation activity, and another parameter is required. These observations have been used to introduce a “two-component” model of the type Ia supernova population ([Mannucci et al. \(2005a\)](#) and later [Scannapieco & Bildsten \(2005\)](#)), which states that the type Ia supernova rate is a function of both the mass and recent star-formation rate of the host galaxy. This model, commonly described as the “A+B” model has been shown to fit the data at low redshift ([Mannucci et al. \(2005a\)](#)) and high redshift with a sample of supernovae from the SNLS survey ([Sullivan et al. \(2006b\)](#)).

The aim of this work is to determine if this parameterisation of the type Ia supernova rate accurately resembles the observations of supernovae from the first two years of the SDSS-II supernova survey. Thus, using the sample described in §3.2.5, which has been corrected for incompleteness, and the host galaxies and their derived properties determined in §4, we are able to quantify the type Ia supernova rate as a function of the host properties in which it is found. The dataset described in §4, has been defined to match the observations of [Sullivan et al. \(2006b\)](#), such that the results produced in this analysis will be directly comparable to those determined at high redshift. The analysis of [Mannucci](#)

[et al. \(2005a\)](#) uses a set of morphologically classified objects and thus differs from the analysis given here.

In §5.2 we shall introduce the sample of objects used in this analysis and define the method used to split them into passive and star-forming events. Further to this, we shall discuss the colour-magnitude distribution of our events. In §5.3 we shall quantify the type Ia supernova rate as a function of specific star-formation rate, and in §5.4 we shall test if a type Ia supernova rate with one component purely dependent on the mass of the host is a viable parameterisation. In §5.5 we shall introduce the “A+B” model. In §5.6 we shall consider the star-formation rate of the host galaxy in the type Ia supernova rate, and in §5.7 we shall perform a two-component fit to the data.

## 5.2 The Mass and Star-Formation Rate Distribution of Supernova Ia Hosts

In §4.8 we gave the derived properties for each of the 244 objects in the sample described in §3.2, with two objects discarded since their host galaxies were not detected in the coadded image used. In this Chapter we are interested in determining if the rate of type Ia supernovae is determined by the characteristics of the galaxy in which the event takes place. We shall start off by looking at how the SN Ia rate is affected by the relative star-formation rate within the host galaxy. This is generally characterised by the Specific Star Formation Rate (sSFR) ([Brinchmann & Ellis \(2000\)](#)). This is defined to be the current star formation rate within the galaxy divided by the total mass of the galaxy.

To look at this we split our set of host galaxies into three datasets. The first group is that of passive galaxies. These have no star formation activity within the galaxy, and thus zero sSFR ( $\log sSFR$  is undefined). These objects are likely to be older, massive galaxies, whose mass is predominantly contained in low mass stars. The second group, contains galaxies with moderate signs of star formation rate relative to the size of their host galaxy. These moderately star-forming galaxies have  $-12.0 \leq \log(sSFR) \leq -9.5$ , and are thus likely to contain a large proportion of their mass in the form of evolved stars with longer lifetimes. The final group of galaxies have high sSFR’s. This group of highly star-forming galaxies have  $-9.5 \leq \log(sSFR)$ . These galaxies are likely to be undergoing a large recent burst of star formation, which is consuming a significant amount of the gas in the galaxy. These galaxies will contain a significant fraction of their mass in the form of massive young stars with shorter timescales. The division between these groups is shown in Figure 5.1, with the passive galaxies plotted with random levels

of star-formation, between  $-4 < \log SFR < -3$ , for effect, since these objects have  $\log SFR$  as being undefined. The boundary between objects with high levels of sSFR and those with moderate values of sSFR match that of the analysis of [Sullivan et al. \(2006b\)](#).

To investigate our sample further, Table 5.1 shows how the objects in our sample are distributed amongst the three groupings described above. For this sample  $\sim 20\%$  of the objects are found to be passive in nature. Interpretations of observations suggest that the most massive galaxies are also the most passive in nature ([Bender et al. \(1996\)](#), [Bell et al. \(2004\)](#), [Thomas et al. \(2005\)](#), [Stanford et al. \(1998\)](#), [Poggianti et al. \(2001\)](#)). This is seen in our sample, with the most massive galaxies being designated as passive, and with the average mass of the passive galaxies being greater than that of galaxies with  $SFR \neq 0$ . Conversely, objects with high levels of sSFR, who are currently producing high levels of new stars relative to their overall mass are shown to have the lowest mass. The vast majority of objects in our sample are seen to exhibit some level of star-formation activity. Another prominent feature of Figure 5.1, is that there exists a population of objects with very low levels of sSFR. These 30 objects lie on the boundary between passive galaxies and moderately star-forming objects. To further study these galaxies, we investigate the colour-magnitude distribution of the objects in our sample.

### 5.2.1 The Colour-Magnitude Distribution of Type Ia Hosts

Observed galaxy bimodality has been well studied ([Chester & Roberts \(1964\)](#), [Cole et al. \(2000\)](#), [Kauffmann et al. \(2003\)](#) [Baldry et al. \(2006\)](#)). These observations have shown that galaxies in the local Universe appear to exist in two broad populations. The first, “red sequence”, marked by appearing red in colour, are the most luminous objects and are generally found in over-dense regions. This population of galaxies shows a tight relationship in colour space. Furthermore, objects in these environments are seen to be old systems, and thus have lower star-formation rates ([Taylor et al. \(2008\)](#)). These objects

	Passive	Moderately Star-Forming	Highly Star-Forming
Range of Specific SFR	$sSFR \leq -12.5$	$-12.5 < sSFR \leq -9.5$	$sSFR > -9.5$
Number of Galaxies	48	106	92
Percentage of Sample	19.5	43.1	37.4
Mean Mass	$6.30 \times 10^{10}$	$3.76 \times 10^{10}$	$6.29 \times 10^9$

Table 5.1: Shows how the hosts described in §3.2 and §4.8 and split by Specific Star-Formation Rate (§5.2) are distributed. The number of elements in each set and mean mass of each sample is given.

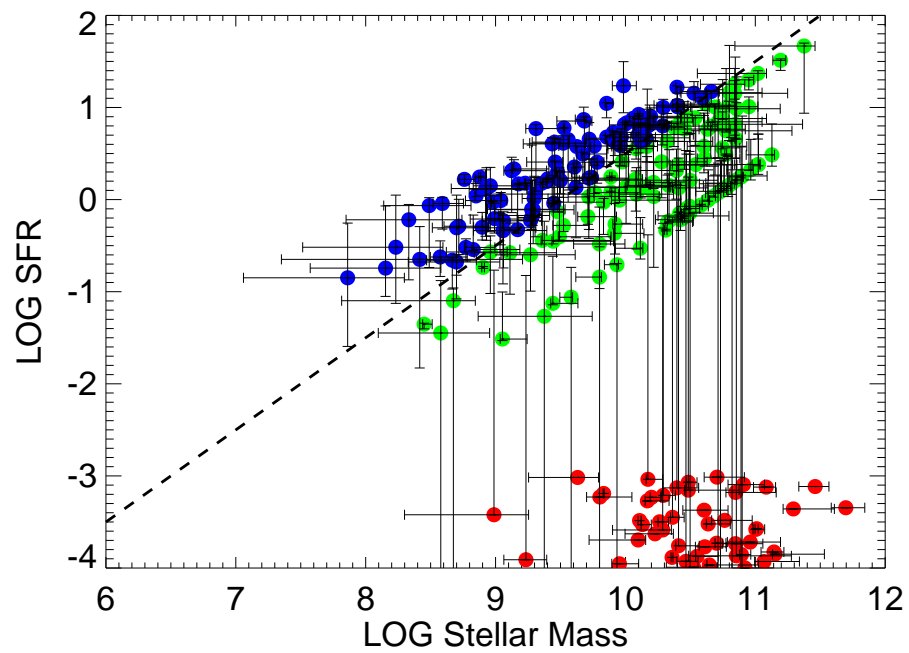


Figure 5.1: Shows the distribution of the hosts galaxy in the sample used in this paper, in the Mass / Star Formation plane. Passive galaxies are shown on the plot in red, for effect. The line used to differentiate between moderately star forming and highly star forming galaxies is shown, with the two distributions plotted in green (for moderately star forming) and blue (for highly star forming). The error bars for each galaxy are those obtained from the PEGASE.2 template fitting method. A population of objects is seen with low specific star formation rate that are not considered to be passive galaxies. These objects are discussed further in §5.2.1

are passive in nature. The second, “blue cloud”, consists of blue objects. Studies of the local Universe has shown that the smallest galaxies are found in this “blue cloud”, and that these objects are located in low density environments, such as voids and filaments. These are well described as star-forming in nature.

Figures 5.3 and 5.2 show how the objects in our sample are distributed in colour-magnitude space. We have plotted the results for both extinction corrected apparent magnitude and absolute model magnitude. The choice of  $u - r$  for the colour used allows a maximum split between the red and blue populations (Rice (1980)).

Figures 5.3 and 5.2 confirm that objects described as passive by the PEGASE SEDs (§4.4) are the most luminous and reddest objects in our sample. We can also see that the “blue cloud” is occupied with objects determined to have current star-formation activity, and that increasing levels of star-formation relative to the size of the host (sSFR) is associated with bluer objects. Interestingly, the objects shown in orange in Figures 5.2 and 5.3, those with very low levels of sSFR, are found between the “red sequence” and “blue cloud”, indicating that they may be in the process of moving between the two. In models of galaxy evolution, such as Bower et al. (2006) and De Lucia & Blaizot (2007), objects are thought to evolve towards the “red sequence”, and thus these objects in our sample may have recently stopped star-forming. Of the 30 objects in our sample which are in this category, through visual inspection we see that none exhibit recent merger activity, and only 1 has a nearby companion. This indicates that any recent change in the star-formation rates of these objects has not been caused by interactions. One of these objects appears as a spiral galaxy, whilst only a further 3 show signs of spiral arms. This, along with the red colour of the objects, indicate that any ongoing star-formation activity is small in these objects, although non-negligible. Figure 5.4 shows a histogram of the star-formation rates for the 30 objects which lie at the edge of the sSFR distribution (plotted in red) when compared to those in the overall sample of 244 objects. These objects have lower star-formation rates than average galaxies, as would be expected, but do not solely occupy the tails of the distribution, with some objects showing moderate levels of star-formation activity. Thus these galaxies can clearly not be classified as purely passive objects.

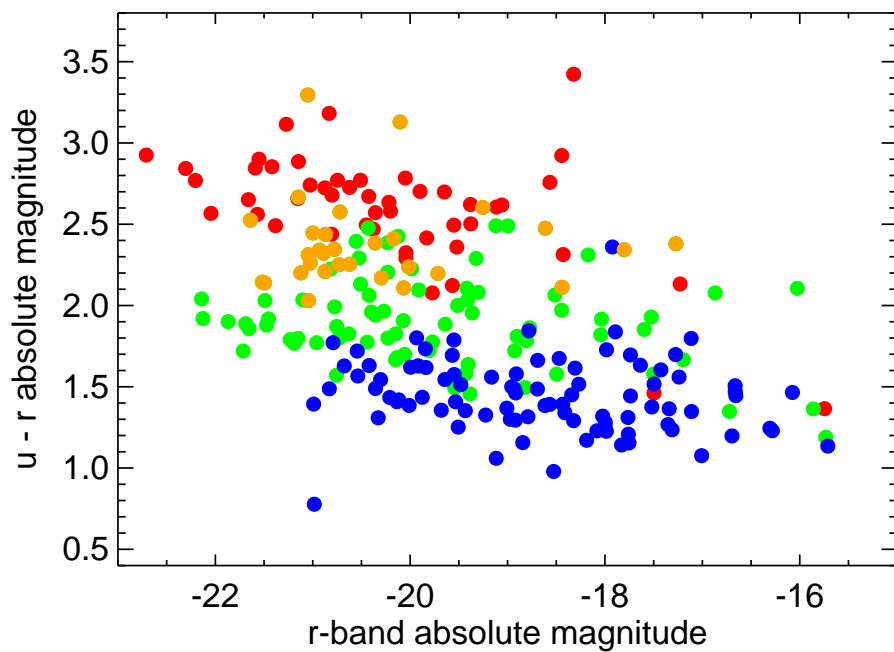


Figure 5.2: Shows the colour-magnitude distribution for host galaxies in the sample used in this paper. The absolute magnitude of objects is used. In this Figure, galaxies described as passive (§5.2) are shown in red, whilst moderately star-forming and highly star-forming galaxies are given in green and blue respectively. Further to this, objects with very low levels of specific star-formation are shown in orange (these are also part of the moderately star-forming population).

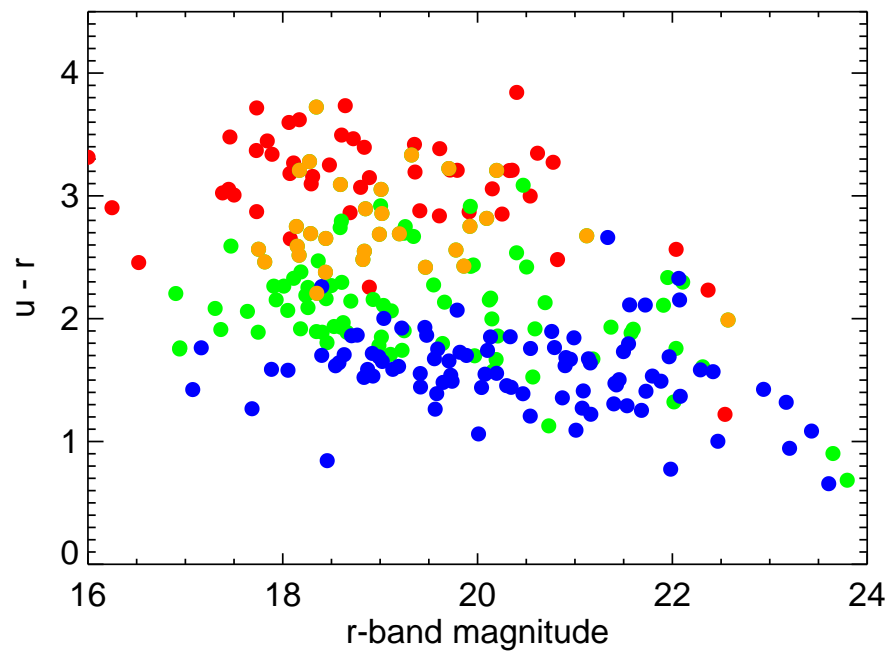


Figure 5.3: Shows the colour-magnitude distribution for host galaxies in the sample used in this paper. The extinction corrected apparent magnitude of objects is used for both the colour and magnitude. In this Figure, galaxies described as passive (§5.2) are shown in red, whilst moderately star-forming and highly star-forming galaxies are given in green and blue respectively. Further to this, objects with very low levels of specific star-formation are shown in orange (these are also part of the moderately star-forming population).

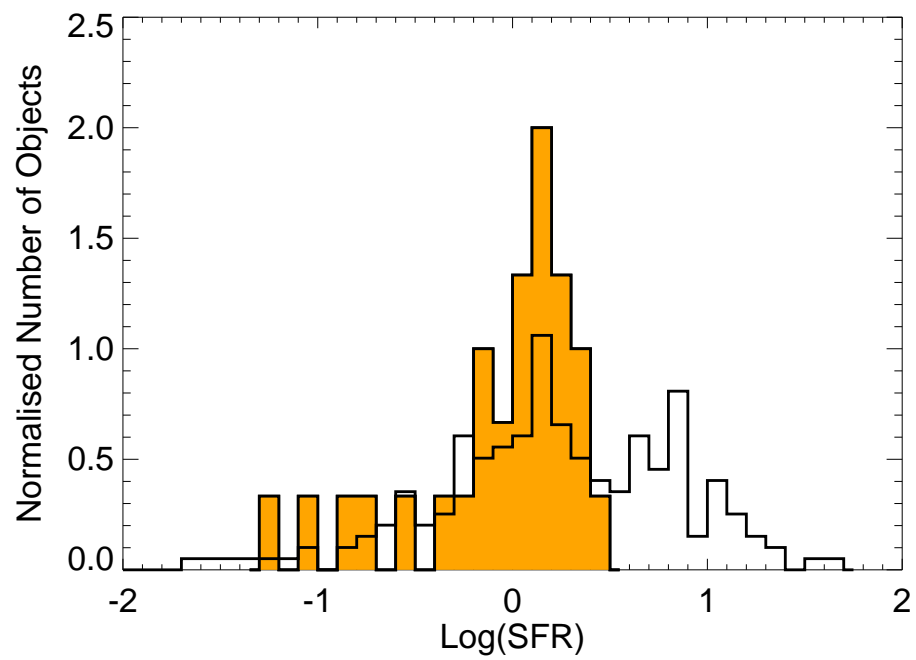


Figure 5.4: Shows the SFR's of objects which lie at the lower boundary of the sSFR distribution. These 30 objects are plotted in orange. Also plotted on the graph is a histogram showing the corresponding figure for all objects in the sample of 244 objects (only those with star-formation activity are plotted). The histograms have been normalised so that they have equal areas.

### 5.3 The Type Ia Supernova Rate as a Function of Galaxy Type

In §5.2 we took the hosts described in §3.2 and split them by sSFR. Thus we are now able to determine how the type Ia Supernova rate is related to sSFR. In §4.5 we described a comparison field sample which is representative and corrected for incompleteness within our redshift range. We bin these galaxies similarly to that described in §5.2. Using the  $1/V_{max}$  correction, as described in §4.6, we can thus calculate the total mass of field galaxies within each bin of sSFR. Having applied the correction for the efficiency of the survey (§3.3) to the host galaxy sample, we can then calculate the SN Ia rate per unit stellar mass per year as a function of host galaxy sSFR.

Previous attempts to measure the type Ia supernova rate as a function of host galaxy properties have found indications of a linear relationship between the Ia rate and the sSFR of the host galaxy, with the rate in passive galaxies being far lower than that of star-forming objects (Sullivan et al. (2006b) and Mannucci et al. (2005b), whose hosts classified by morphology). Figure 5.5 shows the type Ia supernova rate per unit mass per unit time as a function of sSFR for objects in our sample. These measurements are shown on Figure 5.5, with the values from Mannucci et al. (2005b), positioned on the graph along with those from Sullivan et al. (2006b).

From Figure 5.5 it is clear that galaxies in our sample do not match the measurements made from other type Ia supernova samples. The sample created from the incompleteness corrected first two years of the SDSS-II Supernova sample shows a far lower rate per unit mass in passive galaxies than is seen in both the Sullivan et al. (2006b) and Mannucci et al. (2005b) analyses, with differences of  $2.2\sigma$  between our result and that seen in Sullivan et al. (2006b) and  $1.6\sigma$  between ours and Mannucci et al. (2005b). Further to this, the sample used in this analysis shows a “step function” between the rate in passive galaxies and that of star-forming galaxies; there is no evidence of a linear relation as a function of sSFR. These differences can only be partially explained by the elements noted in §5.2.1, since the addition of these objects to the passive population would result in a rate of  $2.02 \times 10^{-14}$  per unit mass per year, still  $1.4\sigma$  different from that of Sullivan et al. (2006b).

However, Figure 5.5 clearly shows a difference in the type Ia supernova rate per unit mass per year between passive and star-forming galaxies, with the rate in star-forming galaxies being virtually flat with sSFR. This difference in the SN Ia rate per unit mass

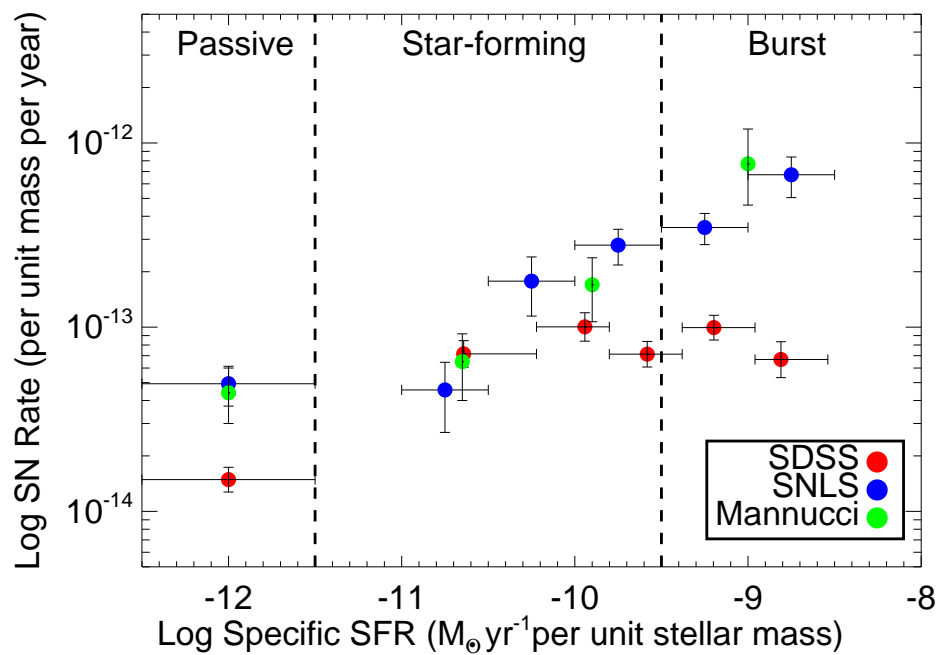


Figure 5.5: This Figure describes the number of type Ia events per unit stellar mass per year as a function of the specific star formation rate per solar mass per year within the host galaxy. The rate in passive galaxies is shown on the plot for effect as they have zero sSFR. The corresponding points from [Sullivan et al. \(2006b\)](#) and [Mannucci et al. \(2005b\)](#) are also shown on the plot. The error values for these points represent statistical Poisson error estimates.

between different galaxy types, indicates that a SN Ia rate based purely on the stellar mass of a host galaxy is ruled out and that a further parameter is required, in agreement with [Sullivan et al. \(2006b\)](#) and [Mannucci et al. \(2005b\)](#).

Table 5.2 shows the values for the passive rates for all three samples, as plotted in Figure 5.5, with associated error bars. All of these error values are purely statistical.

However, as stated in §4.8 the sample used in this work is comprised of objects that have been spectroscopically confirmed combined with objects with only a spectroscopic host redshift and objects with no spectral information. Thus it is useful to determine if our result is dependent on these extra objects, and if some possible bias within the sample has lead to the discrepancy between the result found above, and those of [Mannucci et al. \(2005a\)](#) and especially [Sullivan et al. \(2006b\)](#), whose methodology is similar to ours.

### 5.3.1 The Effect of Our Selection Criteria and Various Cuts on the Passive Rate

In Table 5.3 we show the effect of various cuts to the sample described in §4.8 on the passive rate calculated in §5.3. Several different sample selection criteria are discussed.

- Rows 2 and 3 of Table 5.3 show the values discussed in §5.3 in the cases where only supernovae that have been spectroscopically confirmed are considered or in the case where only supernovae with a spectroscopic redshift of some form are used. These samples have therefore not entirely been corrected for incompleteness. Thus they are far smaller than that given in §4.8. In these two cases, the comparison field sample is identical to that for Table 5.3, and thus the values given are smaller in both cases. In both these systematic tests there is a difference between the rate in passive galaxies and that of star-forming objects. However, neither of these values are comparable to those found in [Mannucci et al. \(2005a\)](#) and [Sullivan et al.](#)

Sample	Passive Rate per unit mass per year and associated $1\sigma$ error value
SDSS-II	$1.49 \pm 0.25 \times 10^{-14}$
<a href="#">Mannucci et al. (2005a)</a>	$3.83 \pm 1.4 \times 10^{-14}$
<a href="#">Sullivan et al. (2006b)</a>	$4.93 \pm 1.20 \times 10^{-14}$

Table 5.2: Table showing how the type Ia rate per unit mass per year, and associated  $1\sigma$  error value, in passive galaxies varies for the 3 different samples mentioned (where the value for the [Mannucci et al. \(2005b\)](#) sample corresponds to their value for “Elliptical Galaxies”)

(2006b), and no linear relationship between sSFR and the type Ia supernova rate is seen.

- Rows 4, 5 and 6 of Table 5.3 show the values of the rate of type Ia supernovae per unit mass in passive galaxies when different redshift limits are used. As discussed in §3 the sample used principally for this work has a redshift cut-off of  $z = 0.25$ . However, it is possible that the correction for incompleteness (by including non-spectroscopically confirmed objects) is not complete in this range. A detailed description of the spectroscopic completeness of this sample as a function of redshift is given in §3.2.5. Here, we consider the redshift limits,  $z = 0.20$ ,  $z = 0.16$  and  $z = 0.12$ . As discussed in Dilday et al. (2008), the SDSS-II supernova survey is virtually complete at a redshift of  $z = 0.12$ . In each of the three cases, the comparison field sample is cut to match the redshift range of the supernova sample. Thus any deviation from the result found in §5.3 may indicate a problem with our incompleteness correction. In all cases, the rate in passive galaxies is consistent with the result of §5.3 and does not match that found in Mannucci et al. (2005a) and Sullivan et al. (2006b). There is a change in the rate in the highest bin of sSFR, but this is partially explained by a change in the width of this bin, as the sample size decreases. In all three examples there is a difference between the rate in passive galaxies and that of star-forming objects, but no linear relationship is seen.
- Rows 7 and 8 of Table 5.3 show the values of the passive rate per unit mass when both the first year and second year of the SDSS-II supernova survey are considered separately. As shown in §3.3, both observing seasons have differing efficiency functions as a function of redshift, and thus are different in size, with the second season of the survey being far more efficient. When these two samples are treated separately the observed rate in passive galaxies is statistically unchanged from that of the overall measurement as shown in Table 5.3. Again these results are not consistent with those found by other surveys. A difference in the rate per unit mass in passive and star-forming galaxies is again noted, with no observed difference in the Ia rate per unit mass as a function of sSFR for star-forming galaxies.
- Rows 9 and 10 of Table 5.3 show the effect of the measurements discussed in §5.3 when different areas of the sky are used. The SDSS-II survey observes each strip of “stripe-82” (§2.2.1) every other night, each section of the stripe can be considered separately, and will have a different level of spectroscopic completeness (§3.3). Since the comparison field sample covers the same region of sky as the supernova survey it is possible to look at the SN Ia as a function of sky coverage. The two

cases shown, split the sample by declination (as the two strips of “stripe-82” converge at zero declination). Any differences between the photometry on the two halves of the survey area will be highlighted by this selection cut, as the two strips are processed separately. There is a small difference between the number of elements in each sample, probably due to the survey covering the edges of the strip differently and due to small gaps in the comparison field sample, but in both cases the rate per unit mass in passive galaxies matches that found in §5.3, and are statistically different to the values found by other surveys. Again a difference in the rates for star-forming objects differs from that of passive galaxies, but no relation as a function of sSFR is seen.

- The final major source of systematic uncertainty is the comparison field sample. In the analysis of Mannucci et al. (2005a), a spectroscopic sample of galaxies was used, whilst the analysis of Sullivan et al. (2006b) used a similar technique to this analysis with a faint magnitude limit ( $i = 26$ ). However, this analysis is completed at higher redshift ( $0.2 < z < 0.75$ ) and thus the galaxy populations and magnitude limits are not comparable. A full analysis of the differences between the sample criteria for the comparison field samples of this analysis and that of Sullivan et al. (2006b) and Mannucci et al. (2005a) is given in Appendices B, C and D along with their consequence on the final results.

### 5.3.2 The Effect of SED errors on the Passive Rate

The errors on the calculations in §5.3 are purely statistical. However, to determine whether our results are indeed inconsistent with those of Mannucci et al. (2005a) and Sullivan et al. (2006b) we need to investigate sources of systematic uncertainty further. Several sources of these were discussed in §5.3.1. The analysis of §5.3 only considers the best fit SED values produced by the PEGASE templates. With the galaxy magnitudes as measured by SDSS-II along with the large number of templates available in the SED fitting process these derived quantities (stellar mass, star-formation rate and sSFR) have associated errors which have not been considered in the analysis of §5.3 and §5.3.1. For each object in the sample, errors are available for both the mass and star-formation rate measurements. These errors are not necessarily symmetric, but are considered to be Gaussian in the mass determination, and Gaussian with a cut off of  $\log(SFR) = \log_{10}(5) - 4$  at low star-formation rates where appropriate. That is, for objects with star-formation rate errors which include zero star-formation activity, or anything below  $\log(SFR) = \log_{10}(5) - 4$  is considered to be passive. For the host galaxy sample the redshifts are known, and so their errors are negligible, and for the correction

Cuts / Selection Criteria	# Objects	# Passive	Passive Rate <sup>a</sup>	1 $\sigma$ error <sup>b</sup>	Rate at high sSFR <sup>c</sup>
No cuts	244	48	1.49	0.25	6.68
Confirmed Objects	120	15	0.43	0.14	4.54
Minimum spectral redshift	187	35	1.05	0.21	4.82
Redshift limit = 0.2	134	28	1.14	0.26	6.45
Redshift limit = 0.16	66	13	0.84	0.30	3.68
Redshift limit = 0.12	21	7	0.95	0.51	2.00
First Year only	104	21	1.22	0.33	8.09
Second Year Only	140	27	1.76	0.41	5.27
Objects at high dec.	120	20	1.21	0.34	8.16
Objects at low dec.	124	28	1.77	0.40	6.72
<a href="#">Mannucci et al. (2005a)</a>		21	4.4	1.3	77
<a href="#">Sullivan et al. (2006b)</a>			4.93	1.20	67.2

<sup>a</sup>in units of  $\times 10^{-14}$

<sup>b</sup>on passive rate, in units of  $\times 10^{-14}$

<sup>c</sup>in units of  $\times 10^{-14}$

Table 5.3: Table showing how passive rate measurement described in §5.3 varies with various cuts and systematic tests. The number of objects in the sample described in §3 after the applied cuts is given, along with the Passive Rate per Unit Mass and corresponding 1- $\sigma$  error value and the value of the SN Ia rate in the bin with the largest value of sSFR. Also, for comparison, the values stated in the work of [Mannucci et al. \(2005a\)](#) and [Sullivan et al. \(2006b\)](#) are given. The precise nature of each cut is given in §5.3.1

for efficiency (§3.3), the errors are not considered large enough to be statistically important.

To account for these uncertainties, we perform both a Monte-Carlo and Bootstrap (B-S) analysis of the errors. These provide a more accurate determination of the statistical errors on the measurement calculated above. Four different sample of the incompleteness corrected SDSS-II supernova sample, described in §4.8, were produced, each with 10,000 realisations.

- Firstly, for each point in the sample used for this analysis, a point was drawn from both the mass and star-formation rate distributions. These values were then used to determine a new value of sSFR (since  $\log sSFR = \log Mass - \log SFR$ ). This was repeated for each of the 10,000 realisations.
- Secondly, the same analysis as above was carried out, this time with only the mass of each host being drawn from the probability distribution of the host. This approach resembles the analysis carried out in Sullivan et al. (2006b). In this case, with the minimum value of sSFR in the observed sample being  $sSFR = -10.642$ , but with a limit of  $sSFR = -12.5$  between passive and moderately star-forming objects, a significant change in mass is required to allow one object to move from a star-forming galaxy to a passive galaxy, when only the mass of the host is varied. Thus, any variation in the passive rate per unit mass is due primarily to any changes in the masses of the observationally determined passive galaxies. With a redshift being used to constrain these objects, the possible differences in mass for each host galaxy are small, and thus this systematic test is not likely to produce large error values.
- A bootstrap selection was carried out without first splitting the host galaxy sample by host galaxy type. That is, for the 244 galaxies in the host galaxy sample, 244 galaxies with replacement were selected in such a way that no prior knowledge of the split in galaxy type was used. This approach meant that the ratio of passive to star-forming objects is allowed to vary. This was repeated for each of the 10,000 realisations.
- Finally the same analysis as above was carried out with the exception that the host galaxy population was first split in to the three galaxy types as defined in §5.2. In this scenario the same number of galaxies will appear in each galaxy set (passive, moderately star-forming and highly star-forming) for each realisation, with the only difference in the supernova rate per unit mass being due to the altered mass distribution of the sample.

Having carried out these four tests we are able to better determine the true statistical error on the values produced in §5.3. Previously we have seen that the statistical error on the type Ia supernova rate per unit mass per year produces a value of  $1.49 \pm 0.25 \times 10^{-14}$ . A non-linear least-squares fit to a Gaussian function with three parameters of the form,

$$f(x) = A_0 \exp\left(-\frac{z^2}{2}\right), \quad (5.1)$$

where  $z = \frac{x-A_1}{A_2}$ , and  $A_0$  is the height of the Gaussian,  $A_1$  is the centre and  $A_2$  is the width (standard deviation), is performed for each of the four tests described above. The standard deviation of this Gaussian fit provides an estimate of the overall error on the value given above. The Gaussian mean and standard deviation in each of the four cases above is given in Table 5.4. For each of the four cases, we see that the Gaussian mean value is consistent with the observed value of  $1.49 \times 10^{-14}$  per unit stellar mass per year. The standard deviations of these Gaussian distributions provides an indication of the overall error on the passive rate per unit mass.

Figure 5.6 shows the histogram of values for the type Ia supernova rate per unit mass per year in passive galaxies for the third of the systematic tests carried out in Table 5.4, which carries out a Bootstrap analysis of the sample without splitting the sample in advance. The best-fit Gaussian function is overplotted. For all four of the systematic tests described above we find that the Gaussian mean value is not statistically different from the observed value of  $1.49 \times 10^{-14}$  type Ia supernova per unit mass per year. In all four cases the derived error on our measurement is smaller than the statistically poisson measurement error.

The four systematic tests described above, and whose results are contained in Table 5.4 all give indications of the systematic error for the type Ia supernova rate per unit mass per year in passive galaxies. These results indicate that the measurement provided is statistics limited, since the estimate of the systematic error is dominated by the statistical error value. Using the largest of these systematic estimates and including the statistical error, we find that a value of  $1.49 \pm 0.25(\text{statistical}) \pm 0.20(\text{systematic}) \times 10^{-14}$  is preferred. Comparing this value to that given in the Mannucci et al. (2005a) and Sullivan et al. (2006b) analyses (as shown in Table 5.2), we see that they are statistically incompatible. Further, we see that including this conservative value for the error leads us to the conclusion that the Ia rate per unit mass is different in galaxies with no signs of current star-formation activity when compared to those that exhibit recent star-burst events (Table 5.3). Since this measurement is independent of mass we can conclude that the rate

Systematic Test	Gaussian Mean	Standard Deviation <sup>a</sup>
Observed results for passive rate	$1.49 \times 10^{-14}$	0.25
MC, variable mass and SFR <sup>b</sup>	$1.40 \times 10^{-14}$	0.065
M-C, variable mass <sup>c</sup>	$1.49 \times 10^{-14}$	0.003
B-S, no prior split <sup>d</sup>	$1.48 \times 10^{-14}$	0.20
B-S, with prior split <sup>e</sup>	$1.48 \times 10^{-14}$	0.20

<sup>a</sup>in units of  $\times 10^{-14}$

<sup>b</sup>Monte-Carlo with variable mass and star-formation rate

<sup>c</sup>Monte-Carlo with variable mass

<sup>d</sup>Bootstrap with no prior split on the sample

<sup>e</sup>Bootstrap with the host sample first split by galaxy type

Table 5.4: Table showing the Gaussian standard deviation from the Gaussian fit for the two Monte-Carlo systematic tests and two Bootstrap tests described in §5.3.2 to determine the systematic error on the type Ia supernova rate per unit mass per year in passive galaxies, as described in §5.3. Also shown are the observed values and statistical error values for the sample used.

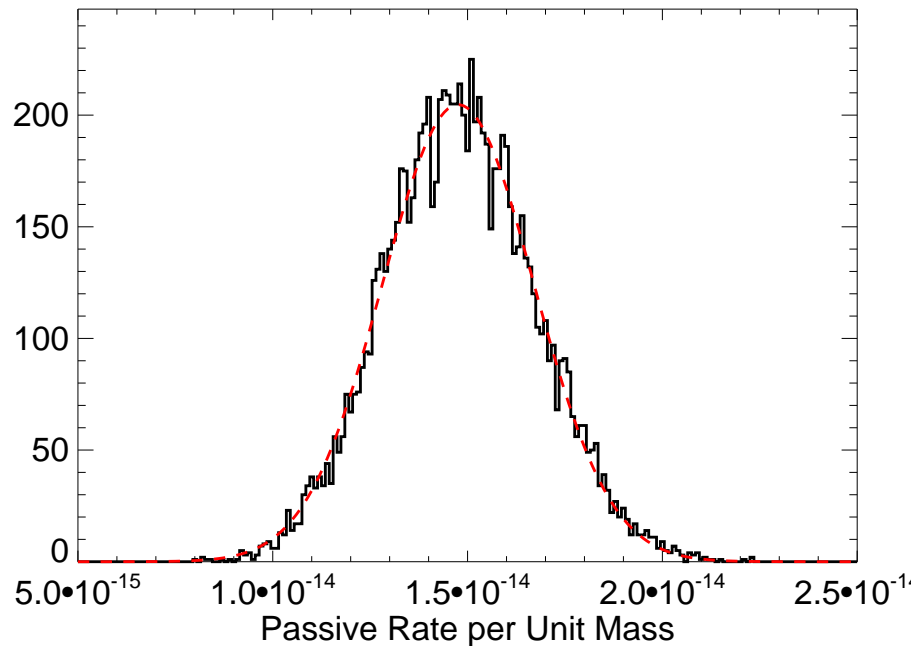


Figure 5.6: This figure shows the values of the rate of type Ia supernova rate per unit mass per year in passive galaxies for the incompleteness corrected SDSS-II supernova survey sample (described in §4.8) when 10,000 Bootstrap realisations of the data are produced. In this example, the sample has not been split in advance of the bootstrap analysis. That is, that the number of objects of each galaxy type are allowed to vary. A Gaussian function has been fitted to the histogram shown to determine the standard deviation of the Gaussian distribution. This is given in Table 5.4.

of type Ia supernova cannot be purely dependent on the mass of its host galaxy, and that another influence is required.

## 5.4 The Supernova Ia Rate as a Function of Host Galaxy Mass

In §5.3, we showed how the type Ia supernova rate per unit mass varies as a function of sSFR, or the relative amount of star-formation activity that is occurring within the host. We showed that the rate is different between passive and star-forming galaxies, but for the SDSS-II sample, no difference is seen between star-forming galaxies with differing levels of sSFR. Thus we have showed that the type Ia supernova rate in a galaxy cannot be purely dependent on the mass of the host. However, there is still significant reason to believe that the type Ia supernova rate is at least partially dependent on the mass of the host galaxy (Wang et al. (1997), Madau et al. (1998)). Thus, we now move on to study the rate as a function of host galaxy mass.

To do this we split the host galaxy sample and comparison field samples into the three components as described in §5.2. The SN Ia events in each component are then binned by host galaxy stellar mass and corrected for the efficiency of the survey (§3.3). The passive galaxies in the field sample are similarly determined, binned and corrected for incompleteness (§4.6).

By dividing the number of elements in the binned host sample by the corresponding number of field sample galaxies we are able to calculate how the SN Ia rate per galaxy per year is related to the mass of the host galaxy. This is shown in Figure 5.7. This plot shows the dependence on mass for the passive galaxies in our incompleteness corrected sample, and similarly for the two populations of galaxies with ongoing star formation.

Passive galaxies are primarily comprised of old stellar populations with little or no gas to propel star-formation activity. Thus, these objects are relatively simple compared to star-forming objects, as the primary influence on their evolution is the mass of the galaxy (other parameters such as metallicity may play a role, but are likely to be sub-dominant). Therefore, if the supernova rate is related to any factor within these objects it will be their mass. Other galaxies with ongoing star-formation activity are likely to have a star-formation component related to their mass, but may also be affected by other factors.

From Figure 5.7, we are able to determine how the rate of type Ia supernova is related

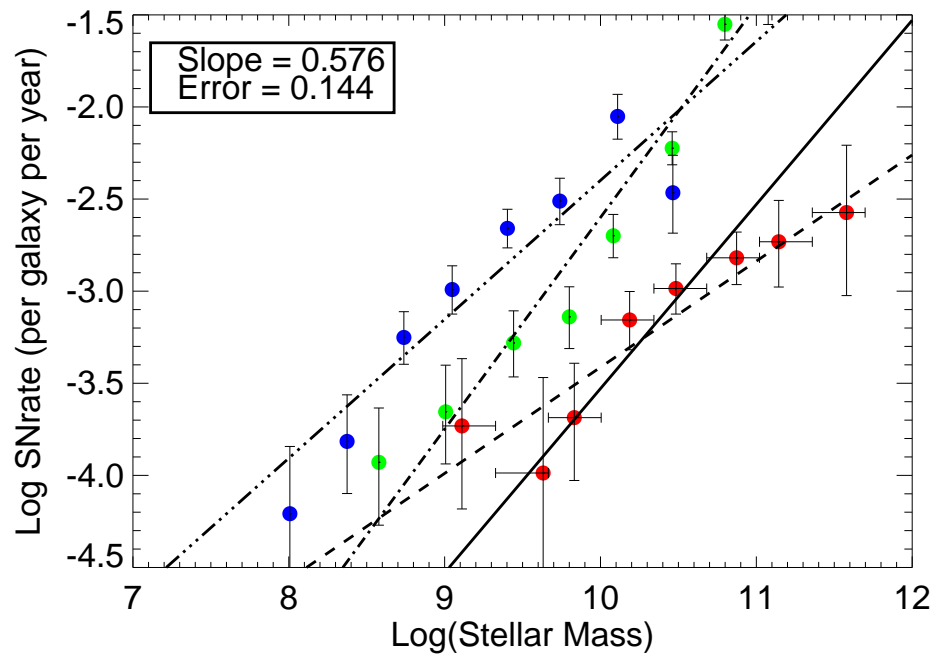


Figure 5.7: This Figure describes the number of SN Ia events per host galaxy per year as a function of the stellar mass of the host galaxy. The three colours are used to distinguish between different galaxy types. The red circles indicate the passive galaxies, green circles are used to mark the galaxies with intermediate values of specific star formation rate and the blue points used for galaxies which are showing signs of recent strong star formation activity. The lines of best fit are overplotted, with the dashed line for passive galaxies, dot-dashed for moderately star-forming and multiple dotted / dashed for highly star-forming. A further line, indicating the line of best fit of unit gradient for the passive galaxies is also shown as a solid line. The passive gradient and associated error is also given.

to the mass of a galaxy. From the passive galaxies, we can see that the mass of the host galaxy clearly influences the number of type Ia events that occur within it. The type Ia supernova rate (per galaxy per year) is highest in high mass systems for all types of host galaxies, including those with recent star-formation activity, indicating that the mass of these galaxies still plays a part in the type Ia supernova rate for these objects. Using purely statistical error bars (as shown on the Figure) to produce a best-fit relation, we see that for passive galaxies, the relationship is best described with the equation,

$$\log(\text{SNR}_{\text{Ia}}) = 0.58 \pm 0.14 \times \log(M_{\text{stellar}}) - 9.18, \quad (5.2)$$

and thus for passive galaxies in the SDSS-II sample, if we model Equation 5.2 such that it becomes,

$$\text{SNR}_{\text{Ia}} = A \times M_{\text{stellar}}^{n_{\text{mass}}}, \quad (5.3)$$

we find that  $n_{\text{mass}} = 0.58 \pm 0.14$  and  $\log A = -9.18 \log \text{SNe yr}^{-1} M_{\odot}^{-1}$ , a constant, respectively.

A linear fit ( $n_{\text{mass}} = 1$ ) is shown on the Figure and is clearly not a good fit to the passive data points and is not favoured from the fit parameters. Thus it is clear that for passive galaxies, the type Ia supernova rate is proportional to the mass of the host, but probably has the form of  $\text{SNR}_{\text{Ia}} \simeq A \times M_{\text{stellar}}^{\frac{1}{2}}$ . If a value of  $n_{\text{mass}} = 1$  is enforced, such that,

$$\text{SNR}_{\text{Ia}} = A \times M_{\text{stellar}}, \quad (5.4)$$

then for passive galaxies, a value of  $\log A = -13.53$  is determined. For comparison, the best-fitting model, as given in Equation 5.2 has a  $\chi^2$  statistic value of 8.4 for 6 degrees of freedom, whilst that when a value of  $n_{\text{mass}} = 1$  is enforced provides a  $\chi^2$  value of 15.4 for 7 degrees of freedom. This gives us a value of  $P(\chi^2) = 0.213$  for the model described in Equation 5.2 compared to a value of  $P(\chi^2) = 0.0313$  of the model where  $n_{\text{mass}} = 1$  is enforced. This indicates that the extra degree of freedom allowed by varying the  $n_{\text{mass}}$  parameter is favoured over the case where it is fixed.

The relationship found above provides a good fit for the SN Ia rate in passive galaxies, but clearly does not hold for galaxies with recent indications of star formation activity, as shown in the form of green and blue circles in Figure 5.7 (their lines of best fit are also plotted). The two populations (as split in §5.2) have best fit slopes of  $1.15 \pm 0.07$  for those with moderate levels of star formation, and  $0.75 \pm 0.15$  for those with high star formation levels. These two values cannot be simultaneously reconciled with the value found for passive galaxies. Thus it is clear that if, as seems logical, the SN Ia rate for passive

galaxies can be described in terms of the mass of the galaxy alone, then for galaxies with ongoing star-formation activity, the SN Ia rate cannot be described by the mass of the host galaxy alone, as then the three data-sets would follow the same relation. Thus the rate of type Ia supernova in a galaxy must consist of at least two components according to the SDSS-II dataset. This matches the result found in §5.3. The value of the star-forming gradient when the two populations are combined is discussed in §5.4.2.

### 5.4.1 The Effect of Our Selection Criteria and Various Cuts on these Results

In the previous section we have investigated how the mass of a galaxy is related to the type Ia supernova rate. We have shown that objects with greater masses produce greater numbers of type Ia supernovae per year, and that for passive galaxies this relation is not linear in nature, but instead seems to favour a relation closer to  $\text{SNR}_{\text{Ia}} \simeq A \times M_{\text{stellar}}^{\frac{1}{2}}$ . We have also shown that for each different galaxy type a different relationship holds, and thus it is clear that another factor, apart from the host galaxy mass, is related to the type Ia supernova rate.

However, the sample used to calculate this contains a mixture of objects that are spectroscopically confirmed to be type Ia events and objects with light-curves that mimic a type Ia supernova light-curve. Thus it is possible that the result discussed in §5.4 is partially explained by a bias in the sample that have been added during the correction for incompleteness. To investigate this further, Table 5.5 shows the effect of various cuts to the sample described in §4.8 on the measurements calculated in §5.4, with the number of objects in the sample, the values of  $n_{\text{mass}}$  for the three samples (now called  $n_{\text{pass}}$ ,  $n_{\text{mod}}$  and  $n_{\text{high}}$  for the three samples of galaxies), the value of  $A$  in Equation 5.3 for passive galaxies, and the value of  $A$  in Equation 5.3 when we force  $n_{\text{mass}} = 1$  (this is called  $A_0$  in the table) given in all of the cases. The various tests carried out are discussed fully §5.3.1. The observed values are also given.

In the cuts considered, there is no statistical difference between the observed results, and those produced when either the incompleteness correction is removed, the redshift limit is changed or the sample is split by year / declination. The most significant differences between the results occurs for the parameters,  $n_{\text{pass}}$  and  $\log A$ , in the case where  $n_{\text{pass}}$  is not required to equal unity. Both of these results are connected, as the value of  $\log A$  is the value of the intercept of the fitted line whose gradient is  $n_{\text{pass}}$ . This scatter is not statistically important, as in all cases the stated values are consistent within  $1\sigma$  to the observed values. It is useful to note that in all cases considered, the value of  $n_{\text{mass}}$  is

inconsistent with  $n_{\text{mass}} = 1$ , except in the case where only the first year data is considered. In all other cases, it is apparent that  $n_{\text{mass}} = 1$  is not compatible with the observed results. For the other galaxy types, we also see that the values of  $n_{\text{mod}}$  and  $n_{\text{high}}$  differ from that of  $n_{\text{mod}}$  and in all cases are greater than the value of  $n_{\text{mod}}$ . This confirms the result that if the rate in passive galaxies is purely dependent on host galaxy mass, then the rate in other galaxy types cannot be purely dependent on this and another quantity is required.

## 5.4.2 Estimating the Errors on these Measurements

In the previous section, we have discussed how the mass of a galaxy is related to the type Ia supernova rate. However until now these measurements are only concerned with statistical error measurements, and do not take in to account any systematic uncertainties.

In §5.3.2, we introduced the concept of using a Monte-Carlo and bootstrap approach to investigate the effect of the SED template errors on the type Ia supernova rate per unit mass per year in passive galaxies. This allowed us to determine the effect that the errors on the derived mass and star-formation rates had on our result. Here we replicate this approach to determine the effect these errors have on how the type Ia supernova rate depends on stellar mass.

As before, we carry out our four tests to see how the results from §5.4 vary due to the errors on the derived quantities for each of our host galaxies. This mimics the technique used in Sullivan et al. (2006b), with the difference that here we use 10,000 realisations of each sample, with the parameters described above calculated in each case, whilst in Sullivan et al. (2006b), 5,000 realisations are used to determine one overall value. As described in 5.3.2, for each object the errors on the derived parameters of mass and star-formation rate are not necessarily symmetric, but are considered to to be Gaussianly distributed in the mass determination, and Gaussianly distributed with a cut off of  $\log(SFR) = \log_{10}(5) - 4$  at low star-formation rates where appropriate. That is, for objects with star-formation rate errors which include zero star-formation activity, or an undefined level in  $\log(SFR)$ , anything below  $\log(SFR) = \log_{10}(5) - 4$  is considered to be passive. For the host galaxy sample the redshifts are known, and so their errors are negligible, and for the correction for efficiency (§3.3) the errors are not considered large enough to be statistically important.

Again, both a Monte-Carlo and bootstrap analysis of the errors are calculated. For the Monte-Carlo analysis, for each host galaxy, a point was drawn from both the mass

and star-formation rate distributions, or purely from the mass distribution (to match the method used in Sullivan et al. (2006b)). A new value of sSFR is then determined and the analysis described in §5.4 is repeated. This allows an object to move from one classification (passive / moderately star-forming / highly star-forming) to another. For the bootstrap analysis, 244 galaxies with replacement (such that a galaxy may be selected on multiple occasions) were selected (to match the number of galaxies in the host sample), either before the sample was split by galaxy type (as described in §5.2) or afterwards. In the first case the number of galaxies in each category is allowed to vary, whilst it remains constant in the second case. To understand the errors given from this method, a non-linear least-squares fit to a Gaussian function with three parameters is performed for each of the four tests described. The standard deviation of this Gaussian fit provides an estimate of the overall error on the value given above.

Having carried out this four tests we are able to better determine the systematic error on the values produced in §5.4. From this section, there are five parameters of interest. These are the values of  $n_{\text{mass}}$  for the three samples (now called  $n_{\text{pass}}$ ,  $n_{\text{mod}}$  and  $n_{\text{high}}$  for the three samples), the value of  $\log A$  in Equation 5.3 for passive galaxies and the value of  $\log A$  in Equation 5.3 when  $n_{\text{mass}}$  is forced to be unity (this shall be known as  $\log A_0$ ). This is the case of Equation 5.4. The best-fit values for these quantities were discussed in §5.4. The Gaussian means and standard deviation for each of these parameters, including the observed case (with Poisson error estimates), are shown in Table 5.6. This provides an indication of the overall error on value of  $n_{\text{mass}}$  for the 3 different galaxy types. For each parameter investigated the Gaussian centre found is not statistically different from the observed value for all four systematic tests.

Figures 5.8, 5.9, 5.10, 5.11 and 5.12 show histograms of the various parameters discussed in §5.4 for the most important systematic tests discussed in Table 5.6. Figures 5.8, 5.9, 5.11 and 5.12 show the effect of 10,000 bootstrap realisations of the sample used on these parameters, whilst Figure 5.10 shows the effect of 10,000 Monte-Carlo's on the sample, when both the mass and star-formation rates of the host galaxies are varied. In all cases the best fit Gaussian function is overplotted.

- For the parameter  $n_{\text{pass}}$ , we find that the statistical error value is larger than the error estimate produced by all four of the systematic tests. Thus taking the most conservative approach, we find that for the sample described in §4.8,  $n_{\text{mass}} = 0.58 \pm 0.14$ . This value is  $3\sigma$  different from a value of  $n_{\text{mass}} = 1$ , or a 0.135% of being the same.

Selection Criteria	# Objects	$n_{\text{pass}}^a$	$n_{\text{mod}}^b$	$n_{\text{high}}^c$	$\log A^d$	$\log A_0^e$
No cuts	244	$0.58 \pm 0.14$	$1.15 \pm 0.07$	$0.75 \pm 0.15$	$-9.18 \pm 1.13$	$-13.529 \pm 0.20$
Confirmed only	120	$0.24 \pm 0.34$	$1.09 \pm 0.17$	$0.79 \pm 0.21$	$-5.91 \pm 1.36$	$-13.84 \pm 0.24$
SNe with a spec-z	187	$0.55 \pm 0.19$	$1.18 \pm 0.11$	$0.81 \pm 0.19$	$-8.97 \pm 1.22$	$-13.66 \pm 0.21$
z limit = 0.2	134	$0.35 \pm 0.16$	$1.05 \pm 0.11$	$0.62 \pm 0.17$	$-6.83 \pm 1.19$	$-13.63 \pm 0.21$
z limit = 0.16	66	$0.39 \pm 0.15$	$0.88 \pm 0.08$	$0.83 \pm 0.28$	$-7.30 \pm 1.17$	$-13.56 \pm 0.23$
z limit = 0.12	21	$0.34 \pm 0.31$	$0.69 \pm 0.42$	$1.01 \pm 0.29$	$-6.47 \pm 1.31$	$-13.11 \pm 0.27$
First Year	104	$0.79 \pm 0.22$	$0.91 \pm 0.03$	$0.56 \pm 0.12$	$-11.33 \pm 1.25$	$-13.59 \pm 0.22$
Second Year	140	$0.44 \pm 0.26$	$1.11 \pm 0.07$	$0.74 \pm 0.19$	$-7.50 \pm 1.28$	$-13.29 \pm 0.24$
High dec.	120	$0.60 \pm 0.09$	$1.22 \pm 0.10$	$0.63 \pm 0.16$	$-9.41 \pm 1.12$	$-13.51 \pm 0.20$
Low dec.	124	$0.68 \pm 0.28$	$1.14 \pm 0.02$	$0.75 \pm 0.13$	$-10.03 \pm 1.29$	$-13.36 \pm 0.22$
SNLS <sup>f</sup>		$1.10 \pm 0.12$	$0.66 \pm 0.08$	$0.77 \pm 0.08$		$-13.29 \pm 0.12$

<sup>a</sup>The value of  $n_{\text{mass}}$  for the passive galaxy sample

<sup>b</sup>The value of  $n_{\text{mass}}$  for the moderately star-forming galaxy sample

<sup>c</sup>The value of  $n_{\text{mass}}$  for the highly star-forming galaxy sample

<sup>d</sup>In the case where  $n_{\text{pass}}$  is not required to equal unity

<sup>e</sup>When  $n_{\text{pass}}$  is unity

<sup>f</sup>Sullivan et al. (2006b)

Table 5.5: Shows how the value of the parameters,  $n_{\text{pass}}$ ,  $n_{\text{mod}}$ ,  $n_{\text{high}}$ ,  $A$  and  $A_0$  described in §5.4 vary with various cuts and systematic tests. Also given are the associated Poisson error values.

Systematic Test	$n_{\text{pass}}^a$	$n_{\text{mod}}^b$	$n_{\text{high}}^c$	$\log A^d$	$\log A_0^e$
Observed values	$0.576 \pm 0.144$	$1.149 \pm 0.070$	$0.754 \pm 0.154$	$-9.176 \pm 1.133$	$-13.529 \pm 0.196$
M-C mass and SFR <sup>f</sup>	$0.638 \pm 0.087$	$1.054 \pm 0.078$	$0.752 \pm 0.113$	$-9.836 \pm 0.902$	$-13.555 \pm 0.072$
M-C mass <sup>g</sup>	$0.630 \pm 0.080$	$1.111 \pm 0.085$	$0.815 \pm 0.084$	$-9.747 \pm 0.836$	$-13.494 \pm 0.059$
B-S no split <sup>h</sup>	$0.531 \pm 0.139$	$1.121 \pm 0.108$	$0.722 \pm 0.097$	$-8.696 \pm 1.444$	$-13.522 \pm 0.088$
B-S split <sup>i</sup>	$0.533 \pm 0.138$	$1.120 \pm 0.106$	$0.720 \pm 0.096$	$-8.707 \pm 1.440$	$-13.524 \pm 0.070$

<sup>a</sup>The value of  $n_{\text{mass}}$  for the passive galaxy sample

<sup>b</sup>The value of  $n_{\text{mass}}$  for the moderately star-forming galaxy sample

<sup>c</sup>The value of  $n_{\text{mass}}$  for the highly star-forming galaxy sample

<sup>d</sup>In the case where  $n_{\text{pass}}$  is not required to equal unity

<sup>e</sup>When  $n_{\text{pass}}$  is unity

<sup>f</sup>Monte-Carlo with variable mass and SFR

<sup>g</sup>Monte-Carlo with variable mass

<sup>h</sup>Bootstrap with no prior split of the sample

<sup>i</sup>Bootstrap with the sample first split by galaxy type

Table 5.6: Shows the Gaussian centres and standard deviations from the Gaussian fits for the two Monte-Carlo systematic tests and two bootstrap tests described in §5.4.2 to determine the systematic error. Also shown are the observed results for the sample used in this analysis, along with the associated Poisson errors.

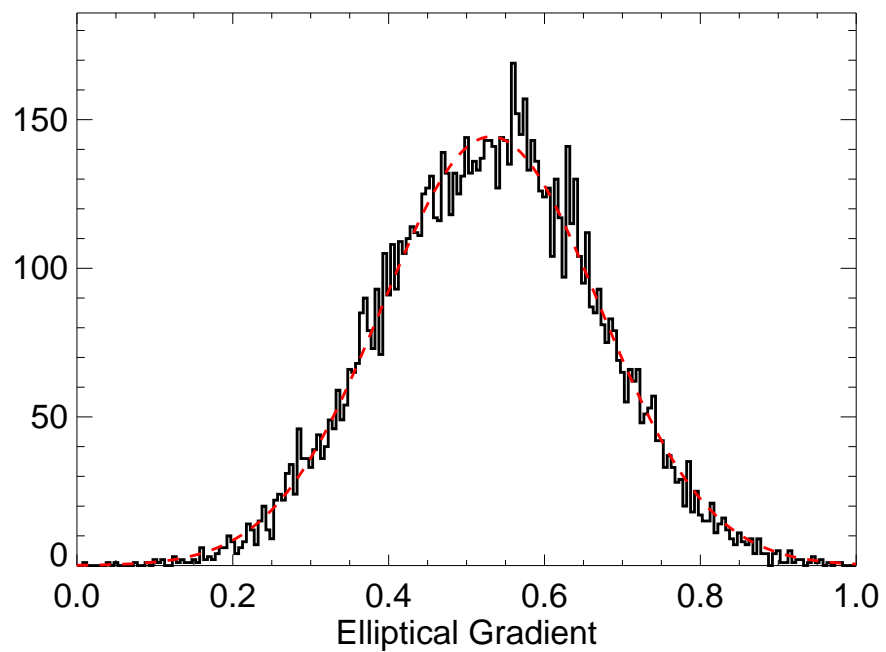


Figure 5.8: Shows the value of  $n_{\text{mass}}$  for passive galaxies (also called  $n_{\text{pass}}$ ), as defined in Equation 5.3 for the incompleteness corrected SDSS-II supernova survey sample when 10,000 bootstrap realisations of the data are produced without splitting the galaxy sample in advance. A Gaussian function has been fitted to the histogram shown to determine the standard deviation of the Gaussian distribution. The mean value and standard deviation of this Gaussian function is given in Table 5.6.

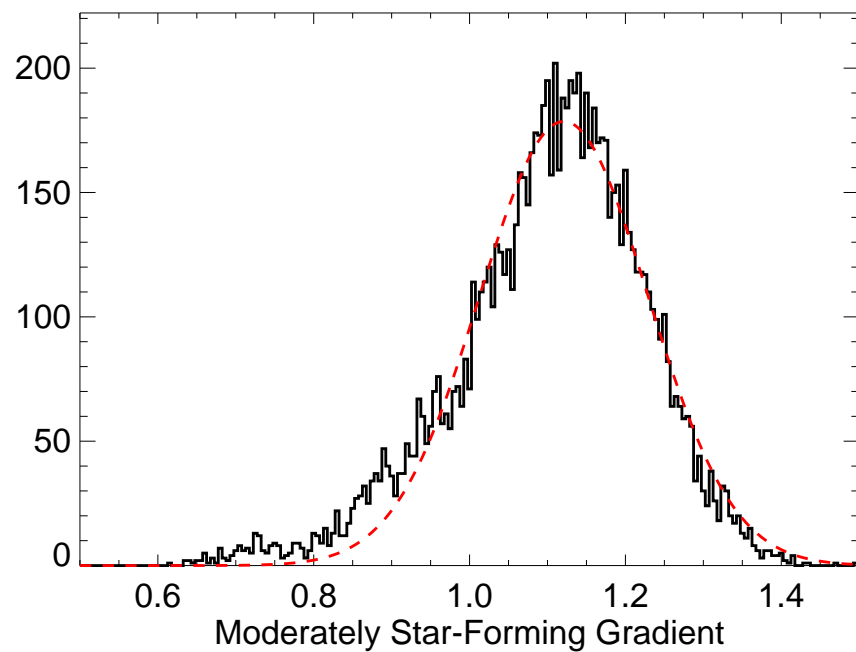


Figure 5.9: Shows the value of  $n_{\text{mod}}$ , as defined in Equation 5.3 for moderately star-forming galaxies in the incompleteness corrected SDSS-II supernova survey sample when 10,000 bootstrap realisations of the data are produced without splitting the galaxy sample in advance. A Gaussian function has been fitted to the histogram shown to determine the standard deviation of the Gaussian distribution. The mean value and standard deviation of this Gaussian function is given in Table 5.6.

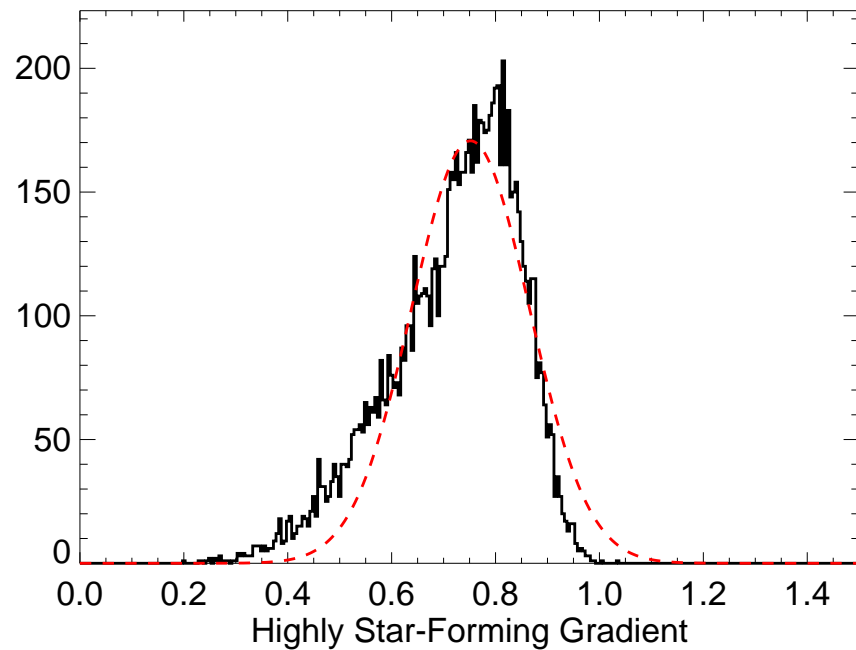


Figure 5.10: Shows the value of  $n_{\text{high}}$ , as defined in Equation 5.3 for highly star-forming galaxies in the incompleteness corrected SDSS-II supernova survey sample when 10,000 Monte-Carlo realisations of the data are produced such that the mass and star-formation rates of each of the host galaxies are varied. A Gaussian function has been fitted to the histogram shown to determine the standard deviation of the Gaussian distribution. The mean value and standard deviation of this Gaussian function is given in Table 5.6. This fit is clearly not a great estimator if the error on  $n_{\text{high}}$ , since it is clearly not symmetric.

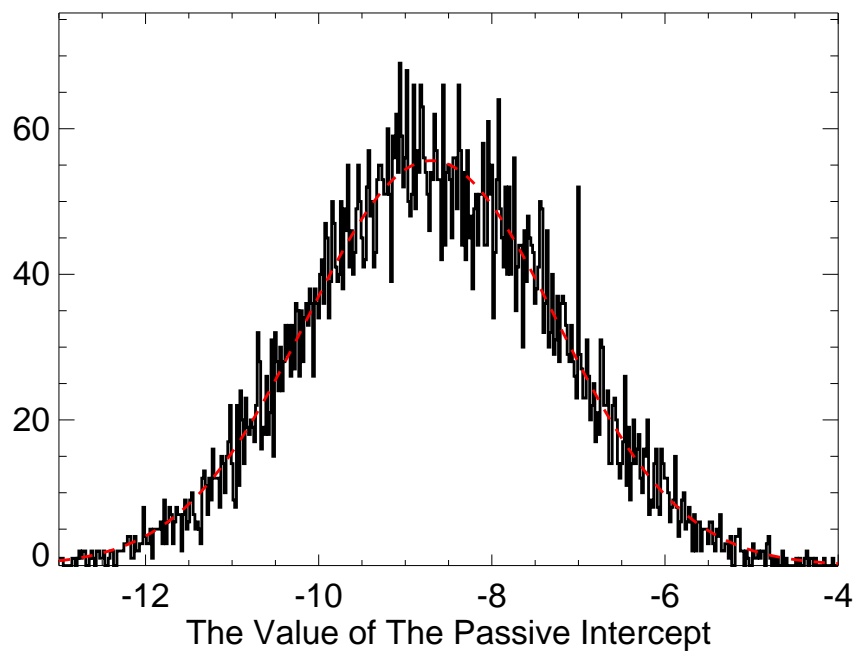


Figure 5.11: Shows the value of  $\log A$ , as defined in Equation 5.3, in the case where  $n_{\text{pass}}$  is not required to equal unity, for the incompleteness corrected SDSS-II supernova survey sample when 10,000 bootstrap realisations of the data are produced without splitting the galaxy sample in advance. A Gaussian function has been fitted to the histogram shown to determine the standard deviation of the Gaussian distribution. The mean value and standard deviation of this Gaussian function is given in Table 5.6.

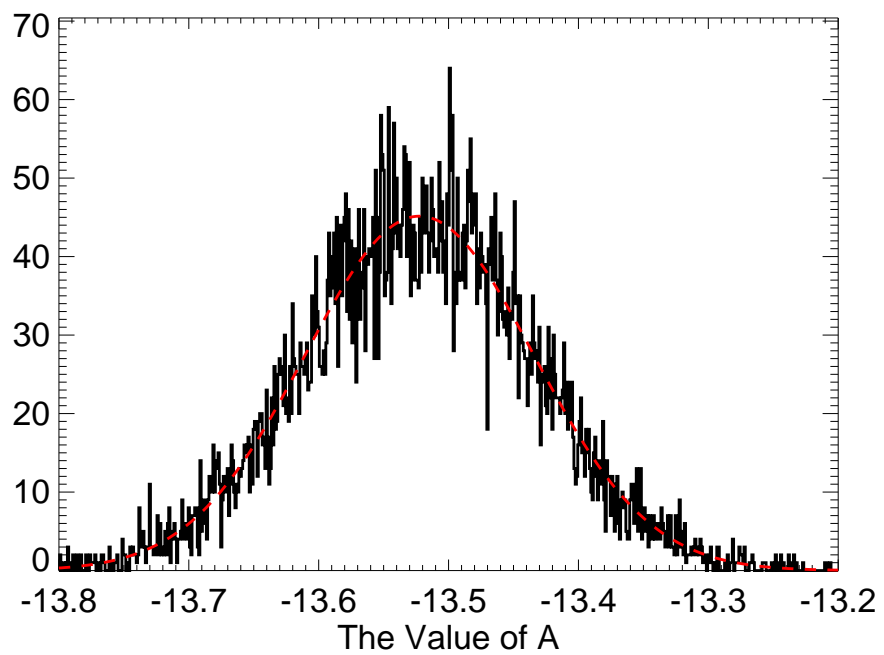


Figure 5.12: Shows the value of  $\log A_0$ , as defined in Equation 5.3, in the case where  $n_{\text{pass}}$  is forced to be unity, for the incompleteness corrected SDSS-II supernova survey sample when 10,000 bootstrap realisations of the data are produced without splitting the galaxy sample in advance. A Gaussian function has been fitted to the histogram shown to determine the standard deviation of the Gaussian distribution. The mean value and standard deviation of this Gaussian function is given in Table 5.6.

- For the parameters  $n_{\text{mod}}$  and  $n_{\text{high}}$  we find that the greatest source of error is best probed by the bootstrap analysis when the sample is not split first for the  $n_{\text{mod}}$  sample and by the statistical Poisson error value for  $n_{\text{high}}$ . Thus, taking the most stringent value for both, we find that  $n_{\text{mod}} = 1.15 \pm 0.11$  and  $n_{\text{high}} = 0.75 \pm 0.15$ . Whilst the value of  $n_{\text{high}}$  is not statistically different from that of  $n_{\text{pass}}$ , the value of  $n_{\text{mod}}$  is significantly different. Thus for these objects we are unable to reconcile a type Ia supernova rate which is purely dependent on mass, which will satisfy both passive and moderately star-forming objects.
- Figure 5.13 shows the type Ia supernova rate as a function on host galaxy type. This Figure is analogous to Figure 5.7, with the exception that in this plot both of the star-forming sub-samples have been combined in to one category, containing all galaxies with ongoing star-formation activity. The best fit value for the gradient of this combined star-forming category (or  $n_{\text{star-forming}}$ ), using similar notation to that used previously) is  $n_{\text{star-forming}} = 0.85 \pm 0.06$ . This is statistically different from the value for  $n_{\text{pass}}$  described earlier. Thus if all galaxies exhibiting signs of recent star-formation activity are merged, then it is difficult to describe a type Ia supernova rate that is dependent purely on the mass of the host galaxy, which fits both passive and star-forming galaxies. It should be noted that the rate in star-forming galaxies is higher than that seen in passive objects, and thus any extra component to the type Ia supernova rate should be dependent on factors occurring within this galaxy type.
- For the value of  $\log A$ , in the case where  $n_{\text{pass}}$  is not required to equal unity, such that  $\log A$  represents the gradient of the fitted line for the passive galaxies, the greatest source of error comes from the bootstrap analysis when the sample is not first split by galaxy type. Thus we can say that  $A = 10^{-9.17 \pm 1.44} \text{SNe yr}^{-1} M_{\odot}^{-1}$  in the case where  $n_{\text{pass}}$  is not constrained.
- Finally for the value of  $\log A$  when  $n_{\text{pass}}$  is forced to be unity, we find that the Poisson error is a larger form of uncertainty that any systematic test provides. Thus we have that, for Equation 5.4, a best fit value of  $\log A = -13.53 \pm 0.20 \log \text{SNe yr}^{-1} M_{\odot}^{-1}$ , or  $A = 2.95 \pm 1.73 \times 10^{-14} \text{SNe yr}^{-1} M_{\odot}^{-1}$  is preferred.

To summarise, for passive galaxies, we find that if the type Ia supernova rate is purely dependent on the mass of the host, then Equation 5.3 is best fit by values of  $n_{\text{mass}} = 0.58 \pm 0.14$  and  $A = 10^{-9.18 \pm 1.44} \text{SNe yr}^{-1} M_{\odot}^{-1}$ . In this case, we cannot reconcile the type Ia supernova rate in star-forming galaxies to be purely dependent of the mass of the host, since a value of  $n_{\text{mass}} = 0.85 \pm 0.06$  is preferred, and thus another parameter is required to satisfy the type Ia rate in these galaxy types.

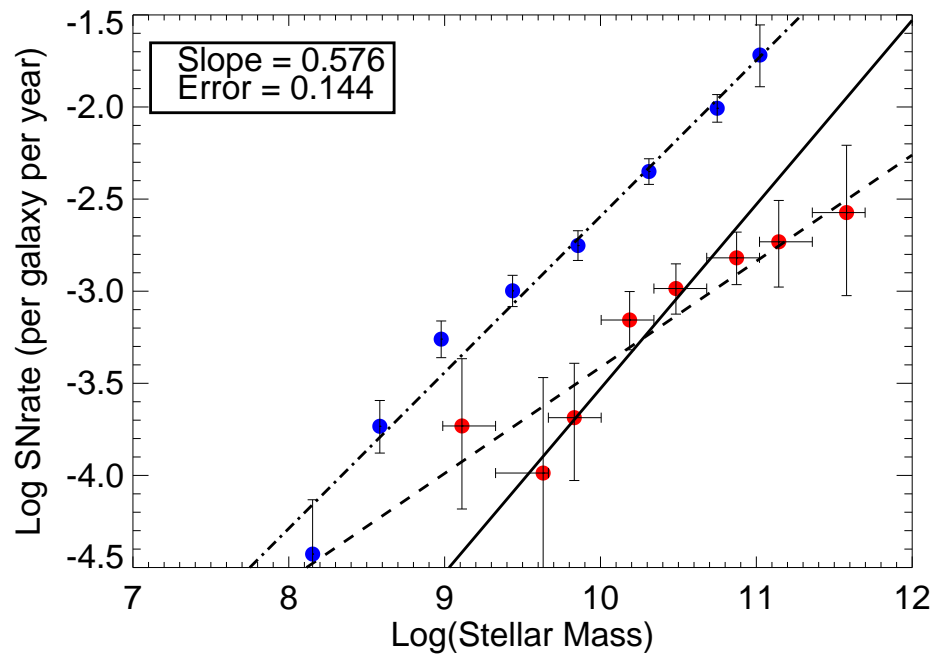


Figure 5.13: Showing the number of SN Ia events per host galaxy per year as a function of the stellar mass of the host galaxy. The sample described in §4.8 has been split into two distinct sub-samples, one for passive galaxies (plotted in red), and one for objects displaying signs of recent star-formation activity (plotted in blue). The lines of best fit are overplotted, with the passive galaxies as a dashed line and star-forming objects as a dashed-dotted line. The line of best fit of gradient unity for the passive galaxies is also shown as a solid line.

## 5.5 The “A+B” Model

In §5.3 and §5.4, we discussed how the type Ia supernova rate per unit mass per year varied as a function of sSFR, and how the type Ia supernova rate varied as a function of host galaxy mass (with specific attention given to passive galaxies). We managed to show that for passive galaxies, the type Ia supernova rate can be explained using the relation,

$$\log(\text{SNR}_{\text{Ia}}) = 0.58 \pm 0.14 \times \log(M_{\text{stellar}}) - 9.18 \pm 1.44. \quad (5.5)$$

Further to this, the rate in star-forming galaxies is incompatible with this relation, and thus another parameter is required. In this section we shall discuss a potential model for explaining how the type Ia supernova rate can be dependent on host galaxy characteristics, and how it compares to this sample. It is known as the “A+B” model.

Wang et al. (1997) and Branch et al. (1995) showed that type Ia supernovae primarily occur in active galaxies with ongoing star-formation activity. Further to this Hamuy et al. (1996d), Howell (2001) and van den Bergh et al. (2005) showed that the brightest supernova Ia events (such as 1991T (Li et al. (2003a))) only occur in active galaxies, and conversely underluminous events (such as 1991bg (Leibundgut et al. (1993))) are seen primarily in passive galaxies. This is discussed further in §6. These characteristics indicate the possibility that type Ia supernova can occur from a variety of evolutionary paths, and thus a single “delay-time” (for example, Madau et al. (1998)) is improbable. Instead it indicates the existence of at least two distinct evolutionary paths with different observables. One “prompt” path, which tracks the current SFR of the host galaxy, and another “delayed” component, that is affected by the stellar mass of the host.

Scannapieco & Bildsten (2005) first introduced the concept of this “two-component” model, parameterising the type Ia supernova rate ( $\text{SNR}_{\text{Ia}}$ ) as,

$$\frac{\text{SNR}_{\text{Ia}}}{(100\text{yr})^{-1}} = A \left[ \frac{M_{\star}(t)}{10^{10}M_{\odot}} \right] + B \left[ \frac{\dot{M}_{\star}(t)}{10^{10}M_{\odot}\text{Gyr}^{-1}} \right], \quad (5.6)$$

where A and B are dimensionless constants. In this case, the first term is dominant in older stellar populations, such as passive galaxies, whilst the second term is primarily concerned with younger more active objects, such as star-burst galaxies. Scannapieco & Bildsten (2005) measured the values of A and B using the results from Mannucci et al. (2005a) to determine  $A = 4.4_{-1.4}^{+1.6} \times 10^{-2}$  and  $B = 2.6 \pm 1.1$ .

This approach was expanded upon by Sullivan et al. (2006b) looking at the first two

years of the SNLS sample set, who generalised the  $\text{SNR}_{\text{Ia}}$  to be a probability function, where the probability of getting a type Ia event from a stellar population at time,  $t$ , is thus,

$$\text{SNR}_{\text{Ia}}(t) = \int_0^t \dot{M}_{\text{new}}(t')P(t-t')dt'. \quad (5.7)$$

where  $\dot{M}_{\text{new}}$  is the rate of new stars in a galaxy, and  $P$  is the probability function described above. This is primarily considered to take the form of an exponential decay.

The probability function is then modelled as two distinct components, one in the form of a delta function at time  $t = 0$  and another which is constant with time. An impression of this modelling is shown in Figure 5.14. Here, the shape of the overall probability function is shown (in black), whilst the two components are shown in red (for the component constant with time) and blue (for the delta function - plotted here offset from zero for effect).

Thus this short ‘‘prompt’’ component represents short delay-time events, whilst the constant, or ‘‘delayed’’ component, is used to describe events with long delay times. This model simplifies to the assumption that any recent star-formation activity in a galaxy will likely produce a white dwarf population in a short period of time, with a range of masses. Those white dwarfs with masses close to the Chandrasekhar mass limit are likely to explode in a short period of time, representing a ‘‘prompt’’ component, whilst those white dwarf’s with low masses, will take a significant time to accrete enough mass to become a type Ia SNe, and form part of the ‘‘delayed’’ component (constant with time). By attaching the high probability that a recently formed white dwarf is related to any recent star formation activity, and that any white dwarfs that have existed for a significant fraction of the lifetime of the host galaxy are associated with the mass of the host. From Equation 5.7, if the probability function shown in Figure 5.14 is generalised in to the two components described above, one with constant probability,  $P = A$ , with time, and a delta function at time,  $t = 0$  with probability  $P = B$ , Equation 5.7 becomes,

$$\text{SNR}_{\text{Ia}}(t) = A \times M_{\text{tot}}(t) + B \times \dot{M}(t), \quad (5.8)$$

where  $\dot{M}$  is the current star formation rate of the host galaxy.

For simplicity,  $A$  and  $B$  are generally considered to be constants which relate the stellar mass and star formation rate of the host galaxy to the  $\text{SNR}_{\text{Ia}}$  of the galaxy. In effect,  $A$  is the  $\text{SNR}_{\text{Ia}}$  per unit stellar mass for the old component (where the mass of the host galaxy is expected to dominate) and  $B$  is the  $\text{SNR}_{\text{Ia}}$  per unit SFR for the prompt component (which is driven by recent bursts of star formation in the galaxy).

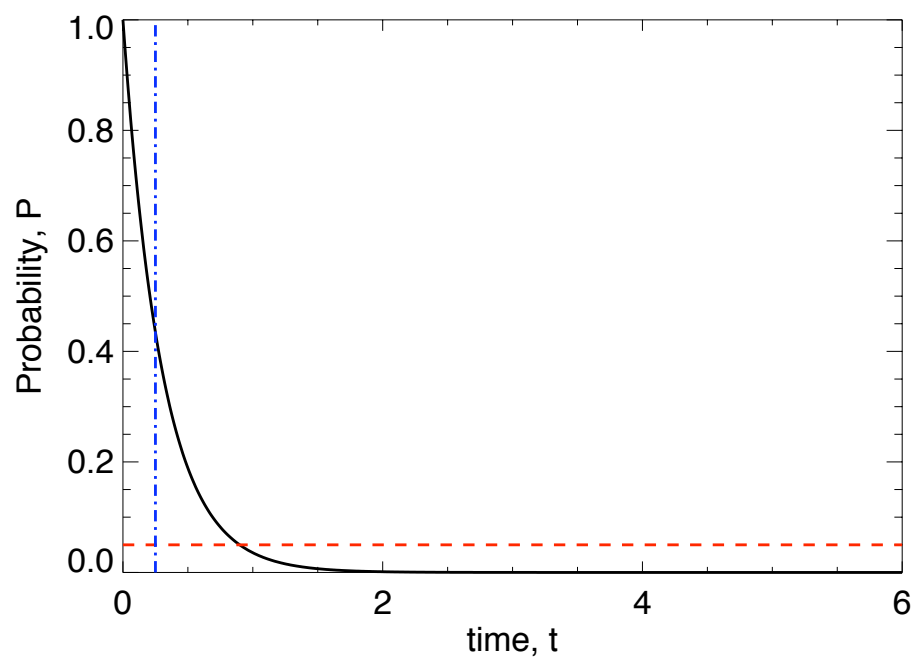


Figure 5.14: An impression of the probability function, described in Equation 5.7, and the two components that it is modelled as. Here the probability function is shown as an exponential decline, whilst the two components that model it are shown in red (for the component that is constant with time) and blue (for the delta function - shown here offset from zero for effect).

The analysis of [Sullivan et al. \(2006b\)](#), using the SNLS sample, found best fit values of  $A = 5.1 \pm 1.2 \times 10^{-14} \text{SNe yr}^{-1} M_{\odot}^{-1}$  and  $B = 4.1 \pm 0.7 \times 10^{-4} \text{SNe yr}^{-1} (M_{\odot} \text{yr}^{-1})^{-1}$ .

Equation 5.8 is not necessarily linear in mass and star-formation rate, and equation 5.8 can be further generalised to,

$$\text{SNR}_{\text{Ia}}(t) = A \times M_{\text{tot}}^{n_{\text{mass}}} + B \times \text{SFR}^{n_{\text{star-forming}}}, \quad (5.9)$$

where  $n_{\text{mass}}$  and  $n_{\text{SFR}}$  are additional constants to be determined, partially representing the probability distribution of a recently created white dwarf exploding to a Ia event. For the analysis of [Sullivan et al. \(2006b\)](#), best fit values of  $n_{\text{mass}} = 1.10 \pm 0.12$  and  $n_{\text{star-forming}} = 0.84 \pm 0.06$  are found, indicating that Equation 5.9 can indeed be generalised to Equation 5.8.

The model described above, and formulated in Equation 5.8, is a generalisation of the physics involved. For the ‘‘prompt’’ component as zero delay time is assumed, whilst in reality some non-zero delay-time due to the accretion on to the progenitor star is clearly required. The ‘‘delayed’’ component is assumed to be constant with time, whilst a more general Gaussian probability would probably be a better fit, as with time the stellar population of the host galaxy will vary, and the number of available white-dwarfs to act as progenitor stars will decrease. However, [Sullivan et al. \(2006b\)](#) and [Mannucci et al. \(2006\)](#) show the type Ia supernova delay-time distribution is well modelled by a ‘‘prompt’’ component centred at  $t = 50 \text{Myr}$  combined with a component with exponential decay of  $t = 3 \text{Gyr}$ , which can be approximated to a delta function at  $t = 0$  combined with a constant probability, as described above.

This model may also explain the observed variations within SN Ia decline rate and host galaxy. It is been well measured that SN Ia events in older systems are seen to have slower decline rates than their counterparts in younger systems, showing signs of star-formation activity ([Hamuy et al. \(1995\)](#), [Hamuy et al. \(1996d\)](#), [Gallagher et al. \(2005\)](#)). This effect implies a correlation between the delay time of a SN Ia event and its host galaxy, and thus the SN Ia rate, as expected within the ‘‘A+B’’ model.

In §5.4, we looked at how the type Ia supernova rate per galaxy per year varied as a function of host galaxy mass. For passive galaxies, with no ongoing star-formation activity, Equations 5.8 and 5.9 are simplified to,

$$\text{SNR}_{\text{Ia}}(t) = A \times M_{\text{tot}}(t), \quad (5.10)$$

and

$$\text{SNR}_{\text{Ia}}(t) = A \times M_{\text{tot}}(t)^{n_{\text{mass}}}, \quad (5.11)$$

which are analogous to Equations 5.4 and 5.3. Thus for the dataset used in this analysis we find that for Equation 5.11, the best-fit values are  $n_{\text{mass}} = 0.57 \pm 0.14$  and  $A = 10^{-9.18 \pm 1.44} \text{SNe yr}^{-1} M_{\odot}^{-1}$ , whilst for Equation 5.10, the best-fit value is  $A = 10^{-13.53 \pm 0.20} \text{SNe yr}^{-1} M_{\odot}^{-1}$ , or  $A = 2.96 \pm 1.69 \times 10^{-14} \text{SNe yr}^{-1} M_{\odot}^{-1}$ .

As discussed in §5.4, the best fit values for Equation 5.11 strongly indicate that the simplified ‘‘A+B’’ model, as described in Equation 5.8 is not favoured for the dataset used in this analysis. However, this result possibly indicates a preferred relation of,

$$\text{SNR}_{\text{Ia}}(t) = A \times M_{\text{tot}}^{\frac{1}{2}} + B \times \text{SFR}^{\text{star-forming}}, \quad (5.12)$$

since the result found in §5.4 for passive galaxies is well described by this. In this case, the best-fitting values of A as derived from §5.4 are  $A = 10^{-6.464 \pm 0.196} \text{SNe yr}^{-1} M_{\odot}^{-1}$ . In order to determine whether the type Ia supernova rate in star-forming galaxies is well described by Equations 5.12 or 5.12, §5.6 investigates how the type Ia supernova rate is related to the star-formation rate of star-forming galaxies.

## 5.6 The Supernova Ia Rate as a Function of Host Galaxy Star Formation Rate

In §5.4, we showed how the type Ia supernova rate per year is related to host galaxy mass. We showed that for passive galaxies, the type Ia supernova rate is approximately proportional to  $M_{\text{stellar}}^{\frac{1}{2}}$ , but that this result is not consistent to the rate in star-forming galaxies. In §5.5, we introduced the ‘‘A+B’’ model which attempts to model the type Ia supernova rate as a function of both the host galaxy mass and ongoing star-formation activity within the host. Here we shall look at how the star-formation activity within the host galaxy is related to the type Ia supernova rate, and hence constrain the parameters in Equations 5.8, 5.9 and 5.12.

To do this, we split the galaxy sample by galaxy type, and as we are only concerned with galaxies with ongoing star-formation activity, we only consider those with non-zero star-formation rates. The host galaxies are then binned by star-formation rate and corrected for the efficiency of the survey (§3.3). Star-forming galaxies in the comparison field sample are similarly binned and corrected for incompleteness (§4.6).

We first need to correct for the expected rate from the “delayed” component (as described in §5.5). Using Equation 5.8, and the best fit values in Equation 5.9 for  $n_{\text{pass}}$  and  $A$ , we are able to determine what this “delayed” component is, and estimate the expected number of supernova from this old component as a function of ongoing star-formation activity. This value can be subtracted from the observed value to provide us with an indication of the excess of type Ia supernova above the predicted amount just from the stellar mass of the host galaxy. This is shown in Figure 5.15 for the best-fit values from Equation 5.9, and Figure 5.16 for the best-fit values from Equation 5.8, where a value of  $n_{\text{mass}} = 1$  is enforced, which from §5.4 is not a good fit to the data.

From Figure 5.15 and 5.16, it is clear that another component is required to describe the type Ia supernova rate apart from the stellar mass. It is also clear that any additional component is well described by the star-formation activity with each host galaxy, regardless of the values of  $n_{\text{mass}}$  from Equation 5.9. We find that the best-fit gradient,  $n_{\text{star-forming}}$ , in Equation 5.9, is  $n_{\text{star-forming}} = 0.67 \pm 0.08$  and  $B = 10^{-2.99 \pm 0.07} \text{SNe yr}^{-1} (\text{M}_{\odot} \text{yr}^{-1})^{-1}$ , and  $n_{\text{star-forming}} = 0.92 \pm 0.10$  (or  $B = 10^{-2.99 \pm 0.02} \text{SNe yr}^{-1} (\text{M}_{\odot} \text{yr}^{-1})^{-1}$  when  $n_{\text{mass}} = 1$  is assumed in Equation 5.9). When a value of  $n_{\text{mass}} = 0.5$  is assumed, we find that  $n_{\text{star-forming}} = 0.78 \pm 0.23$  and  $B = 10^{-3.073 \pm 0.08} \text{SNe yr}^{-1} (\text{M}_{\odot} \text{yr}^{-1})^{-1}$  respectively. Finally, when  $n_{\text{mass}} = 1$  and  $n_{\text{star-forming}} = 1$  in Equation 5.9 is assumed, such that Equation 5.8 holds, then we get  $B = 10^{-2.982 \pm 0.173} \text{SNe yr}^{-1} (\text{M}_{\odot} \text{yr}^{-1})^{-1}$ . The values given here are the  $1\sigma$  Poisson error values. Thus we find that the best fit for Equation 5.9 give,

$$\text{SNR}_{\text{Ia}}(t) = (2.96 \pm 1.69 \times 10^{-14}) * M_{\text{tot}}^{0.58 \pm 0.14} \quad (5.13)$$

$$+ (1.02 \pm 0.17 \times 10^{-3}) * \text{SFR}^{0.67 \pm 0.08}, \quad (5.14)$$

and by enforcing a linear relationship, we find that  $B = 1.04 \pm 0.51 \times 10^{-3} \text{SNe yr}^{-1} (\text{M}_{\odot} \text{yr}^{-1})^{-1}$ .

The result from Equation 5.13 provided a good fit to the data since it agrees with the values found in §5.4 for passively evolving galaxies, and above for star-forming objects. However, from §5.4, we see that by enforcing a linear relationship for  $n_{\text{mass}}$  in Equation 5.9, it does not provide a good fit to the data. Finally, we find that the output parameters for the case where  $n_{\text{mass}} = 0.5$ , as in Equation 5.12, are consistent for those where no linear relationship is enforced, and thus

$$\text{SNR}_{\text{Ia}}(t) = A * M_{\text{tot}}^{\frac{1}{2}} + B * \text{SFR}, \quad (5.15)$$

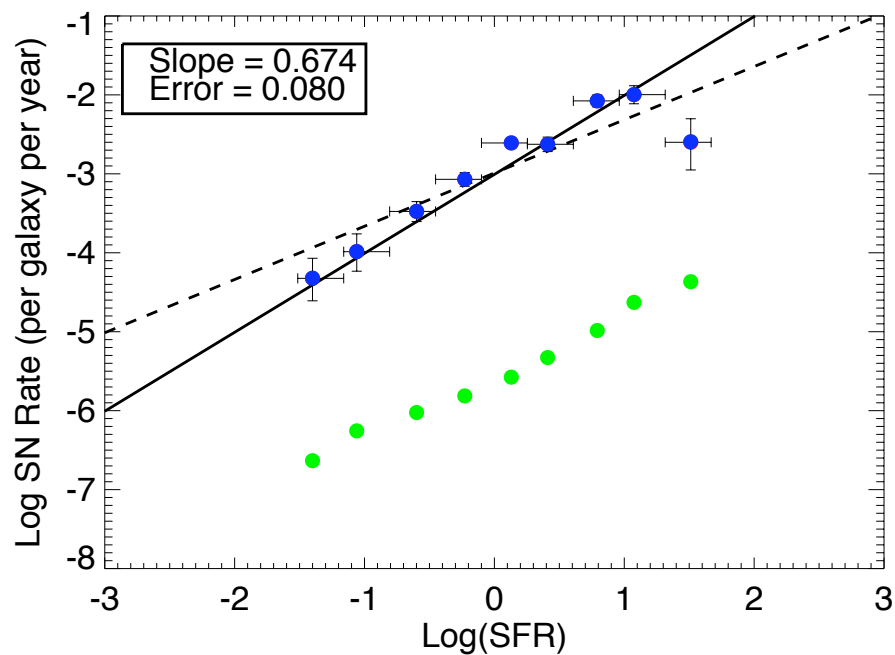


Figure 5.15: Shows the number of type Ia's per host galaxy per year as a function of host galaxy star formation rate. The blue circles show the observed rate in galaxies with active star formation. The green circles show the expected component based on the galaxy mass alone, given the best fit in §5.4. The red circles show the corrected number per galaxy after this expected component has been subtracted from the observed rate (note, this may not be visible below the blue points). The line of best fit is shown as a dashed line (with value shown), whilst the line of best fit with gradient unity is also shown as a solid line.

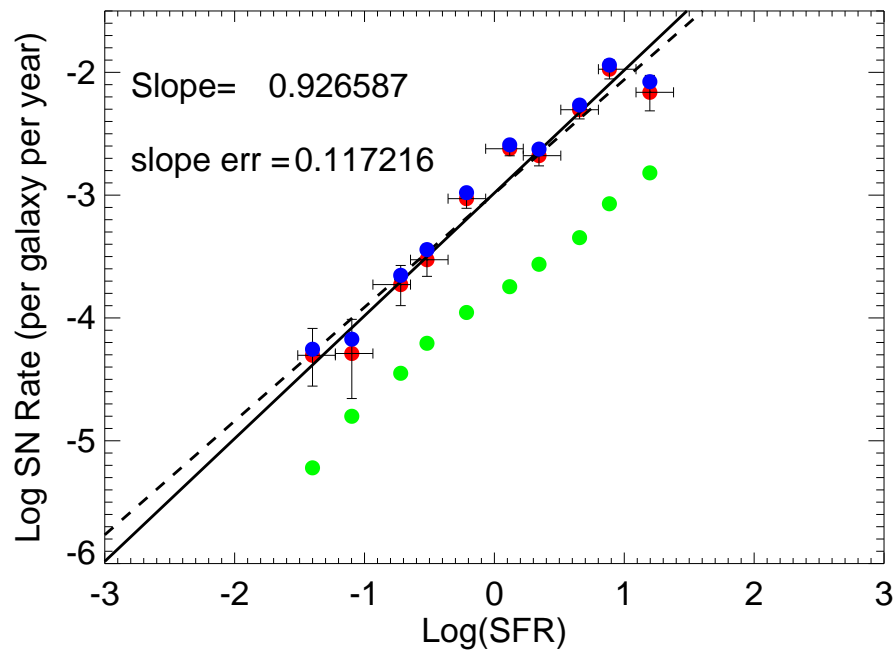


Figure 5.16: Shows the number of SN Ia per host galaxy per year as a function of host galaxy star formation rate. The blue circles show the observed rate in galaxies with active star formation. The green circles are used to show the expected component derived from the galaxy mass alone, whilst assuming the original “A+B” model (i.e. that the  $\text{SNR}_{\text{Ia}}$  in passive galaxies is proportional to the galaxy mass). The red circles show the corrected number per galaxy after the expected component has been subtracted. The line of best fit is shown as a dashed line, whilst the line of best fit with unit gradient is also shown as a solid line.

provides an adequate fit to the data. Thus, we find that for our sample of type Ia supernova rate that is proportional to the square-root of the host galaxy mass and proportional to the ongoing star-formation activity of the galaxy, provides a good relationship to the data. It should however, be noted that there is considerable scatter in these results. This is primarily due to a lack of highly star-forming objects in our sample. Visually, we see that a linear relationship proportional to the star-formation rate of the host galaxy is an excellent fit to the data for galaxies with low or moderate levels of ongoing star-formation activity. However, for objects with rates above  $\log_{10} \text{SFR} = 2M_{\odot}$  per year, we see that this relationship does not hold. Thus, the derived values for the gradient in this correlation, or the value of  $n_{\text{star-forming}}$  are lower than would be expected. This may be because galaxies that have been previously considered as Active Galactic Nuclei (AGN) are vetoed from the targeting selection of the SDSS-II supernova survey, since they are variable objects and thus difficult to distinguish from supernova events. Thus, the sample described in §3.2.5 contains no (or at least a minimal number) of supernovae in AGN hosts, which can have high levels of star-formation activity. These hosts are not removed from the sample of galaxies in the field sample, and thus the proportion of objects that are highly star-forming may be under-represented.

However, it is clear that a type Ia supernova rate that is proportional purely on the stellar mass of the system is not well represented by this dataset. This agrees with the results found in §5.3 and §5.4.

### 5.6.1 The Effect of Our Selection Criteria and Various Cuts on these Results

As discussed previously, this sample of supernovae contains a variety of events, including supernovae which are spectroscopically confirmed, ones with light-curves that follow the peak-luminosity / decline rate relationship and have a spectroscopic host galaxy redshift, and those that have type Ia-like light-curves, but only a photo-z. Thus, it is possible that this result is dependent on the objects that have been added due to the incompleteness correction. To investigate this further, Table 5.7 shows the values of the parameters described above when various cuts are made to the sample. The number of galaxies, the value of  $n_{\text{star-forming}}$  (when the best-fit  $n_{\text{mass}}$  come from Equation 5.9) and the value of  $n_{\text{star-forming}}$  (when  $n_{\text{mass}} = 1$ ) is used. Also shown are the values of the constant associated with the star-forming component when various considerations to the values of  $n_{\text{mass}}$ ,  $A$  and  $n_{\text{SFR}}$  are made. The various tests carried out are discussed fully §5.3.1. Also shown is the effect on the values when only galaxies classified as moderately star-forming (§5.2) or highly star-forming are considered.

The results in Table 5.7 show variation from the observed results, though no statistical difference is found from the best fit values found in §5.6. Some variation is seen when value of  $n_{\text{mass}} = 1$  is required, although this may partially be related to the loss of objects that are considered to be forming large numbers of new stellar systems. From Equation 5.9, it is clear that the values of  $n_{\text{star-forming}}$  and  $B$  are correlated. The best-fit values for the star-forming gradient from the first year data is the most inconsistent value to those observed above. However, this is primarily due to a lack of highly star-forming objects in this sample, with objects at low star-formation rates finding a positive correlation between the excess supernova rate and the star-formation rate. In all cases, the value of  $n_{\text{star-forming}}$  is positive, and in the case where the redshift limit is varied, the star-forming gradients are all consistent, implying that this result has no redshift dependence. Importantly, we have also shown that the relationship described above is valid for both moderately star-forming objects and highly star-forming objects, respectively.

## 5.6.2 Estimating Errors

We now attempt to quantify the systematic uncertainty in our result. In §5.3.2, we introduced the concept of using a Monte-Carlo and bootstrap approach to investigate the effect of the SED template errors on the type Ia supernova rate per unit mass per year in passive galaxies. These techniques allow us to quantify the possible effect caused by the errors on the derived mass and star-formation rates. We now repeat these methods to determine the systematic uncertainty on our measurements, in particular with respect to how the derived star-formation rates affect the type Ia supernova rate.

Similar to §5.3.2, we carry our four tests to see how the results from §5.6 vary due to errors on the derived quantities for each of our host galaxies. As described in 5.3.2, for each object, the errors on the derived parameters of mass and star-formation rate are not necessarily symmetric, but are considered to be Gaussian in the mass determination, and Gaussian with a cut off at  $\log(SFR) = \log_{10}(5) - 4$  for low star-formation rates where appropriate. That is, for objects with star-formation rate errors which enclose zero star-formation activity, or have anything below  $\log(SFR) = \log(5) - 4$  are considered to be passive. For the host galaxy sample the redshifts are known, and so their errors are negligible, and for the correction for efficiency (§3.3) the errors are not considered large enough to be important.

For the Monte-Carlo analysis, a point was drawn from both the mass and star-formation rate distributions, or purely from the mass distribution. A new value of sSFR is then

Cuts / Selection Criteria <sup>a</sup>	# Objects	$n_{\text{SFR}}^b$	$n_{\text{SFR}}^c$	$\log B^d$	$\log B_0^e$	$\log B_0^f$
No cuts	196	0.674	0.924	-2.990	-2.987	-2.982
Confirmed Objects only	105	0.853	0.855	-3.193	-3.263	-3.256
Objects with a spectral redshift	152	0.893	0.873	-3.088	-3.147	-3.161
Redshift limit = 0.2	106	0.664	0.603	-3.033	-3.149	-3.162
Redshift limit = 0.16	53	0.666	0.526	-3.156	-3.374	-3.427
Redshift limit = 0.12	14	0.637	0.682	-2.948	-2.966	-3.057
Only moderately star-forming objects	106	0.791	0.612	-2.681	-2.817	-2.803
Only highly star-forming objects	90	0.973	0.886	-2.999	-2.997	-3.021
First Year only	83	0.513	0.208	-3.042	-3.163	-3.277
Second Year Only	113	0.842	0.827	-2.854	-2.975	-2.973
Objects at high dec.	100	1.017	0.944	-2.913	-2.911	-2.920
Objects at low dec.	96	0.651	0.409	-2.932	-3.061	-3.132
<a href="#">Sullivan et al. (2006b)</a>	-	0.84	-	-	-	-3.387

<sup>a</sup>The best-fit values for  $n_{\text{pass}}$ ,  $A$  and  $A_0$  from Table 5.5 are used for each selection criteria

<sup>b</sup>When  $n_{\text{pass}}$  in Equation 5.9 is not enforced

<sup>c</sup>When a value of  $n_{\text{pass}}$  in Equation 5.9 is chosen to be  $n_{\text{pass}} = 1$

<sup>d</sup>When  $n_{\text{pass}}$  in Equation 5.9 is not enforced

<sup>e</sup>When  $n_{\text{pass}} = 1$  and  $n_{\text{SFR}}$  is not constrained

<sup>f</sup>when  $n_{\text{pass}} = 1$  and  $n_{\text{SFR}} = 1$

Table 5.7: Shows how the parameters described in §5.6 change when different values of  $n_{\text{mass}}$  are considered.

determined and the analysis described in §5.6 is repeated. This allows galaxies to move from one classification to another. For the bootstrap analysis, for the 244 galaxies in the sample, 244 galaxies are selected with replacement (such that an object may be selected on multiple occasions). This is done either before the sample was split by galaxy type (as described in §5.2) or afterwards. In the first case, the number of galaxies in each category is allowed to vary, whilst in the second case it remains constant. To understand the errors given from this method, a non-linear least-squares fit to a Gaussian with three parameters is performed for each of the four tests described above. The standard deviations of these Gaussians are provided as an estimate of the overall error.

Having carried out these four tests we are able to better determine the systematic error on the values produced in §5.6. There are several parameters of interest in this section. Here, we consider the values of two parameters. For the parameter  $n_{\text{star-forming}}$  we consider the case where the best fit values for  $n_{\text{pass}}$  and  $A$  from §5.4 are considered, and the case where  $n_{\text{pass}} = 1$  from §5.4 is enforced. For the parameter,  $B$  we consider the cases discussed for  $n_{\text{star-forming}}$ , with the additional case when the values of  $n_{\text{pass}} = 1$  and  $n_{\text{SFR}} = 1$  in Equation 5.9 are enforced. The best-fit values for these parameters were discussed in §5.4. For each of the four systematic tests, a Gaussian was fit to the resultant distribution. The Gaussian means and standard deviation, are shown in Table 5.8. This provides an indication of the overall error on the values of  $n_{\text{star-forming}}$  and  $B$  in the different scenarios. For each parameter investigated the Gaussian mean was found to be statistically similar to the observed value.

Figures 5.17, 5.18 and 5.19 show histograms for three of the parameters discussed in §5.4 for the most important systematic tests discussed in Table 5.8. In these three cases, the largest systematic test is the Monte-Carlo estimate when the mass and star-formation rates of the host galaxies have both been varied, such that each galaxy is allowed to move from one sample into another. In all cases, the best fit Gaussian is plotted.

- For each of the parameters considered in Table 5.8, we find that the biggest source of error, including the statistical uncertainty, is quantified from the Monte-Carlo test, where the mass and star-formation rates of each galaxy have been varied. These errors are comparable to the Poisson error.
- We find that for the sample defined in §3.2.5,  $n_{\text{star-forming}} = 0.67 \pm 0.08$  (statistical)  $\pm 0.24$  (systematic). This value is  $1.1\sigma$  different from a value of  $n_{\text{star-forming}} = 1$ , and thus not significant. In this case, we find that the constant associated with this value is  $\log(B) = -2.99 \pm 0.07$  (stat)  $\pm 0.09$  (sys)  $\log \text{SNe yr}^{-1} (M_{\odot} \text{yr}^{-1})^{-1}$  or  $B = 1.02 \pm 0.17$  (statistical)  $\pm 0.23$  (systematic)  $\times 10^{-3} \text{SNe yr}^{-1} (M_{\odot} \text{yr}^{-1})^{-1}$ .

Cuts / Selection Criteria <sup>a</sup>	$n_{\text{SFR}}^b$	$n_{\text{SFR}}^c$	$\log B^d$	$\log B_0^e$	$\log B_0^f$
Observed values	$0.674 \pm 0.080$	$0.924 \pm 0.101$	$-2.990 \pm 0.065$	$-2.987 \pm 0.020$	$-2.982 \pm 0.173$
M-C mass and SFR <sup>g</sup>	$0.490 \pm 0.242$	$0.776 \pm 0.217$	$-3.044 \pm 0.087$	$-3.102 \pm 0.071$	$-3.240 \pm 0.185$
M-C mass <sup>h</sup>	$0.696 \pm 0.017$	$0.967 \pm 0.023$	$-3.034 \pm 0.017$	$-3.048 \pm 0.018$	$-3.064 \pm 0.020$
B-S no split <sup>i</sup>	$0.697 \pm 0.107$	$0.810 \pm 0.193$	$-2.979 \pm 0.040$	$-3.030 \pm 0.061$	$-3.004 \pm 0.054$
B-S split <sup>j</sup>	$0.698 \pm 0.109$	$0.817 \pm 0.193$	$-2.977 \pm 0.040$	$-3.031 \pm 0.059$	$-3.002 \pm 0.055$

<sup>a</sup>the best-fit values for  $n_{\text{pass}}$ ,  $A$  and  $A_0$  from Table 5.5 are used for each selection criteria

<sup>b</sup>when  $n_{\text{pass}}$  in Equation 5.9 is not enforced

<sup>c</sup>when a value of  $n_{\text{pass}}$  in Equation 5.9 is chosen such that  $n_{\text{pass}} = 1$

<sup>d</sup>when  $n_{\text{pass}}$  in Equation 5.9 is not enforced

<sup>e</sup>when  $n_{\text{pass}} = 1$  and  $n_{\text{SFR}}$  is not constrained

<sup>f</sup>when  $n_{\text{pass}} = 1$  and  $n_{\text{SFR}} = 1$

<sup>g</sup>Monte-Carlo with galaxy mass and star-formation rate allowed to vary

<sup>h</sup>Monte-Carlo with galaxy mass allowed to vary

<sup>i</sup>Bootstrap with no prior split of the sample

<sup>j</sup>Bootstrap with the sample first split by galaxy type

Table 5.8: Table showing the Gaussian centres from the Gaussian fits for the two Monte-Carlo systematic tests and two bootstrap tests described in §5.6.2 to determine the systematic error on the parameters described in §5.6. Also shown are the observed results for the sample used in this analysis.

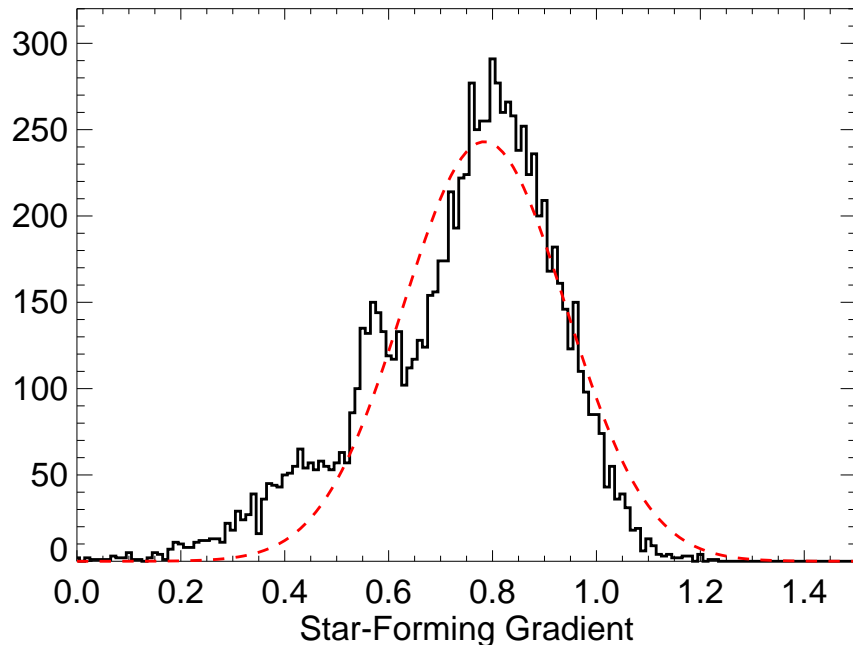


Figure 5.17: Shows the value of  $n_{\text{star-forming}}$  from Equation 5.9, when a value of  $n_{\text{mass}} = 1$  is enforced. 10,000 Monte-Carlo realisations of the data are made by varying both the mass and star-formation rate of the host galaxy. A Gaussian function has been fitted and the mean value and standard deviation of this are given in Table 5.8.

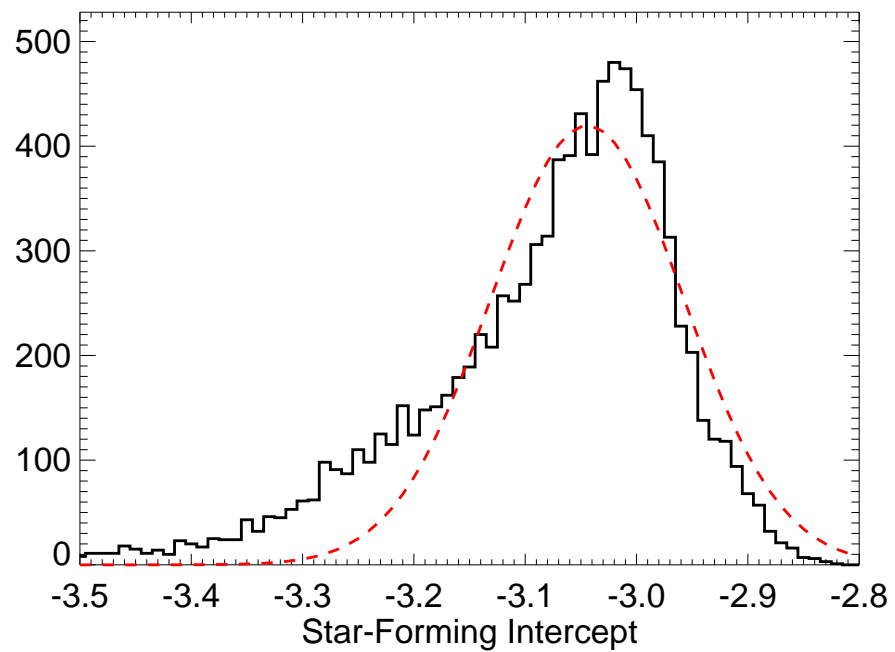


Figure 5.18: Shows the value of  $\log B$  from Equation 5.9, when the best-fit values for  $n_{\text{mass}}$  and  $A$  as derived in §5.4 are used. 10,000 Monte-Carlo realisations of the data are made by varying both the mass and star-formation rate of the host galaxy. This analysis does not enforce a value of  $n_{\text{SFR}} = 1$ . A Gaussian function has been fitted and the mean value and standard deviation of this Gaussian function is given in Table 5.8.

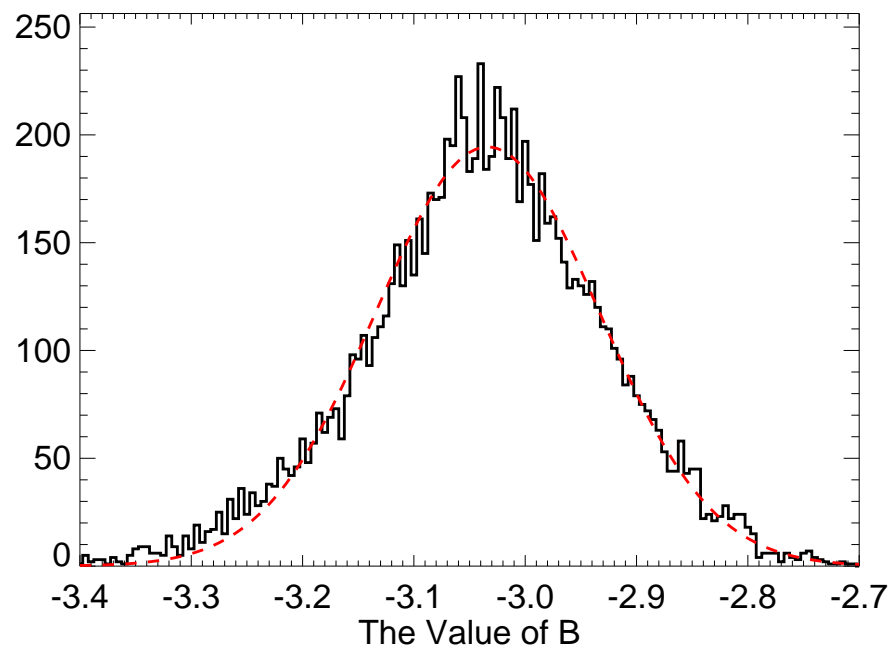


Figure 5.19: Shows the value of  $\log B$  from Equation 5.9, when a value of  $n_{\text{mass}} = 1$  and  $n_{\text{SFR}} = 1$  are enforced. 10,000 Monte-Carlo realisations of the data are made by varying both the mass and star-formation rate of the host galaxy. A Gaussian function and the mean value and standard deviation of this Gaussian function is given in Table 5.8.

- In the case where the value of  $n_{\text{pass}} = 1$  in Equation 5.9 is enforced, we find that the best-fit value is  $n_{\text{star-forming}} = 0.92 \pm 0.10(\text{stat}) \pm 0.22(\text{sys})$ . This value is not significantly different from a value of  $n_{\text{star-forming}} = 1$ . Here, the value for  $B$ , is  $\log(B) = -2.99 \pm 0.02(\text{stat}) \pm 0.07(\text{sys}) \log \text{SNe yr}^{-1} (M_{\odot} \text{yr}^{-1})^{-1}$ , or  $B = 1.03 \pm 0.05(\text{stat}) \pm 0.18(\text{sys}) \times 10^{-3} \text{ SNe yr}^{-1} (M_{\odot} \text{yr}^{-1})^{-1}$ .
- Finally, for the case where we enforce  $n_{\text{pass}} = 1$  and  $n_{\text{star-forming}} = 1$ , we find  $\log(B) = 2.98 \pm 0.17(\text{stat}) \pm 0.185(\text{sys}) \log \text{SNe yr}^{-1} (M_{\odot} \text{yr}^{-1})^{-1}$ , or  $B = 1.04 \pm 0.51(\text{stat}) \pm 0.55(\text{sys}) \times 10^{-3} \text{ SNe yr}^{-1} (M_{\odot} \text{yr}^{-1})^{-1}$ .

To summarise, we have investigated the ‘‘A+B’’ model described in §5.5. From §5.4, it was clear that the basic ‘‘A+B’’ model is not a good fit to the data. However, it appears from both §5.4 and §5.6 that a modified version of this model where the type Ia supernova rate is proportional to the square-root of the mass of the host galaxy, and linearly proportional to the star-formation rate of the galaxy, is a good fit to the data, with  $\log A = -6.46 \pm 0.20 \log \text{SNe yr}^{-1} M_{\odot}^{-1}$  and  $\log B = 3.10 \pm 0.18 \log \text{SNe yr}^{-1} (M_{\odot} \text{yr}^{-1})^{-1}$ . In the next section we shall discuss the possibility of determining the values of  $n_{\text{mass}}$  and  $n_{\text{SFR}}$  at the same time with a bivariate fit.

## 5.7 Bivariate Fit

A bivariate fit to Equations 5.8 and 5.9 would provide a more accurate and robust method for determining the parameters described previously. We can perform a least squares fit to the joint mass and star formation rate plane and determine the goodness of fit and the effect of any correlations between the two functions.

To achieve this, the 2-D mass and star-formation rate planes (as shown in Figure 5.1) are binned for both the host galaxy and field galaxy population. Having corrected for incompleteness and inefficiency effects (§3.3 and §4.6), we are able to calculate the type Ia supernova rate in each bin, by dividing the number of SN Ia hosts in each bin by the corresponding number of field galaxies.

We then fit several equations to this probability distribution. Firstly, we consider the form of the type Ia supernova rate which is purely dependent on the stellar mass of the host galaxy, i.e.

$$\text{SNR}_{\text{Ia}} = A \times M^{\text{mass}}, \quad (5.16)$$

such that the component dependent on the star-formation rate is zero.

The best fit values for this functional form of the supernova rate are  $A = 6.89 \pm 10.23 \times 10^9 \text{ SNe yr}^{-1} M_{\odot}^{-1}$  and  $n_{\text{mass}} = 0.47 \pm 0.06$ , with a  $\chi^2$  of 134 with 39 degrees of freedom (d.o.f.). The stated errors are statistical only. The value of  $n_{\text{mass}}$  found is similar to that in §5.4.

Next we consider,

$$\text{SNR}_{\text{Ia}} = A \times M^{0.5} + B \times \text{SFR}^{\text{n}_{\text{star-forming}}}, \quad (5.17)$$

and,

$$\text{SNR}_{\text{Ia}} = A \times M + B \times \text{SFR}, \quad (5.18)$$

For Equation 5.17, we find that  $A = 1.60 \pm 0.23 \times 10^{-11} \text{ SNe yr}^{-1} M_{\odot}^{-1}$  and  $B = 5.95 \pm 0.07 \times 10^{-4} \text{ SNe yr}^{-1} (M_{\odot} \text{ yr}^{-1})^{-1}$  and  $n_{\text{star-forming}} = 0.98 \pm 0.07$  with a  $\chi^2$  value of 99 for 38 d.o.f. For Equation 5.18, we find  $A = 1.18 \pm 0.18 \times 10^{-14} \text{ SNe yr}^{-1} M_{\odot}^{-1}$  and  $B = 5.51 \pm 0.52 \times 10^{-4} \text{ SNe yr}^{-1} (M_{\odot} \text{ yr}^{-1})^{-1}$ , with  $\chi^2 = 56$  for 39 d.o.f.

The values of the  $\chi^2$  statistic can be converted into a probability that the data is in agreement with the proposed model. We are able to rule out the case of a supernova rate that is solely dependent on the mass of the host galaxy, since a  $\chi^2$  of 134 with 39 degrees of freedom has a zero probability of being the correct distribution. For the case of Equation 5.17 we find a probability of  $2.4 \times 10^{-7}$  that this is the correct model, so this is strongly disfavoured. For Equation 5.18 we find  $P(\chi^2) = 0.038$ , the best-fitting model so far. This provides significant evidence that the additional parameter, concerning the star-formation rate of the host galaxy, is required to improve the overall parameterisation.

We can now generalise the equation to,

$$\text{SNR}_{\text{Ia}} = A \times M^{n_{\text{mass}}} + B \times \text{SFR}^{\text{n}_{\text{star-forming}}}. \quad (5.19)$$

For this equation, we find  $A = 4.35 \pm 0.31 \times 10^{-11} \text{ SNe yr}^{-1} M_{\odot}^{-1}$ ,  $B = 5.08 \pm 0.10 \times 10^{-4} \text{ SNe yr}^{-1} (M_{\odot} \text{ yr}^{-1})^{-1}$ ,  $n_{\text{mass}} = 0.67 \pm 0.14$  and  $n_{\text{star-forming}} = 1.01 \pm 0.25$  and  $\chi^2 = 47$  for 37 d.o.f. This produces a probability of  $P(\chi^2) = 0.126$ , indicating that this parameterisation is favoured. From the best-fit results, a suitable simplification of this model is,

$$\text{SNR}_{\text{Ia}} = A \times M^{0.5} + B \times \text{SFR}. \quad (5.20)$$

By fitting this parameterisation with a bivariate fit we find  $A = 2.60 \pm 0.37 \times 10^{-9} \text{ SNe yr}^{-1} M_{\odot}^{-1}$  and  $B = 4.86 \pm 0.53 \times 10^{-4} \text{ SNe yr}^{-1} (M_{\odot} \text{ yr}^{-1})^{-1}$  with a  $\chi^2$  value of

51 for 39 d.o.f. This produces  $P(\chi^2) = 0.094$ , comparable with that found for Equation 5.19. The difference in probabilities between Equations 5.20 and 5.17 indicate that the data is unable to accurately constrain this additional parameter in the case where  $n_{\text{mass}} = 0.5$ .

Finally it possible to test two additional hypotheses. One, unphysical model, could be that the supernova rate is solely related to the ongoing star-formation rate in the host galaxy. This seems unlikely as type Ia supernovae explode in galaxies with no recent star-formation activity. However, it allows us to determine the importance of the mass component to the supernova rate. This parameterisation is of the form,

$$\text{SNR}_{\text{Ia}} = B \times \text{SFR}^{\text{n}_{\text{star-forming}}}. \quad (5.21)$$

For this we find  $5.95 \pm 0.62 \times 10^{-4} \text{ SNe yr}^{-1} (\text{M}_{\odot} \text{ yr}^{-1})^{-1}$  and  $n_{\text{star-forming}} = 0.98 \pm 0.07$ , with a  $\chi^2$  value of 99 for 39 d.o.f. The probability produced from this combination is  $P(\chi^2) = 4.0 \times 10^{-7}$ , a strong indication that this model is highly disfavoured.

Our alternative model concerns the possibility of cross-terms in Equation 5.18. Our data does not cover a sufficient mass range and does not contain enough elements to justify the determination of cross terms in Equation 5.19, although the determination of any cross-correlation in Equation 5.18 will allow us to constrain its overall contribution. Thus, for the parameterisation,

$$\text{SNR}_{\text{Ia}} = A \times M + B \times \text{SFR} + C \times M \times \text{SFR}, \quad (5.22)$$

we find a best-fit  $A = 1.18 \pm 0.18 \times 10^{-14} \text{ SNe yr}^{-1} \text{M}_{\odot}^{-1}$ ,  $B = 5.51 \pm 0.52 \times 10^{-4} \text{ SNe yr}^{-1} (\text{M}_{\odot} \text{ yr}^{-1})^{-1}$  and  $C = 1.00 \times 10^{-19}$ , with a  $\chi^2$  statistic of 56 for 38 d.o.f., or  $P(\chi^2) = 0.030$ . Alternatively, this could be parameterised to fit,

$$\text{SNR}_{\text{Ia}} = A \times M^{1/2} + B \times \text{SFR} + C \times M \times \text{SFR}. \quad (5.23)$$

Here we find  $A = 2.60 \pm 0.37 \times 10^{-9} \text{ SNe yr}^{-1} \text{M}_{\odot}^{-1}$ ,  $B = 4.86 \pm 0.05 \times 10^{-3} \text{ SNe yr}^{-1} (\text{M}_{\odot} \text{ yr}^{-1})^{-1}$  and  $C = 1.00 \times 10^{-19}$ , with a  $\chi^2$  statistic of 51 for 39 d.o.f., or  $P(\chi^2) = 0.094$ .

The  $\chi^2$  values from Equations 5.22 and 5.23 do not indicate that any contribution from these cross-correlation can be ignored. However, it is possible that the addition of these

extra parameters can lead to an over-fitting of the data.

Hence, we find that the results from §5.4 and §5.6 are consistent with those found here. This robust technique gives values of  $n_{\text{mass}} = 0.67$  and  $n_{\text{star-forming}} = 1.01$  in Equation 5.9, and when we enforce  $n_{\text{mass}} = 0.5$  and  $n_{\text{star-forming}} = 1$ , we find that  $A = 2.60 \pm 0.37 \times 10^{-9} \text{ SNe yr}^{-1} M_{\odot}^{-1}$  and  $B = 4.86 \pm 0.53 \times 10^{-4} \text{ SNe yr}^{-1} (M_{\odot} \text{ yr}^{-1})^{-1}$ . These fits give the best  $\chi^2$  per degree of freedom and the highest probabilities.

The extremely high value of the  $\chi^2$  statistic for the parameterisation of the type Ia supernova rate as being purely a function of host galaxy mass means that this model is effectively ruled out for this dataset. With the other models considered, there is obvious tension between results when extra parameters are included in the model. None of the models produce a high probability of representing the correct distribution. This may indicate that the assumption of the ‘‘A+B’’ formalism, that the probability distribution of a type Ia event can be modelled as a delta function at time  $t = 0$  and a constant term is not valid. However, with the current dataset we are unable to determine if this is the case.

## 5.8 Comparison to Other Results

As noted in §5.2, the determination of the derived properties of our type Ia supernova host galaxies has been determined in a similar fashion to the method described in Sullivan et al. (2006b), so that our results can be comparable to those found at higher redshift.

In §5.3 we investigated the type Ia supernova rate in passive galaxies as a function of specific star-formation rate. Our determined best-fit value of  $1.49 \pm 0.25(\text{statistical}) \pm 0.20(\text{systematic}) \times 10^{-14}$  per unit mass per year is  $2.2\sigma$  different to the result found in Sullivan et al. (2006b). Further to this, we do not see a linear trend with specific star-formation rate as it shown in Sullivan et al. (2006b) and  $1.6\sigma$  different from that of Mannucci et al. (2005a), who found a value of  $3.83 \pm 1.4 \times 10^{-14} \text{ SNe yr}^{-1} M_{\odot}^{-1}$ . All three analyses do show a difference in the type Ia supernova rate for galaxies with recent star-formation activity when compared to passively evolving objects, although both Sullivan et al. (2006b) and Mannucci et al. (2005a) show a linear trend with this parameter.

In §5.4 and §5.6 we investigated if the type Ia supernova rate can be expressed as a function of the host galaxy mass and star-formation rate. Sullivan et al. (2006b) found that a two-component model, the ‘‘A+B’’ model provides a good fit, with values of  $A = 5.3 \pm 1.1 \times 10^{-14} \text{ SNe yr}^{-1} M_{\odot}^{-1}$  and  $B = 3.9 \pm 0.7 \times 10^{-4} \text{ SNe yr}^{-1} (M_{\odot} \text{ yr}^{-1})^{-1}$

when  $n_{\text{pass}}$  and  $n_{\text{star-forming}}$  are enforced to be unity. In our example we find that  $A = 1.18 \pm 0.18 \times 10^{-14} \text{ SNe yr}^{-1} \text{ M}_{\odot}^{-1}$  and  $B = 5.51 \pm 0.51 \times 10^{-4} \text{ SNe yr}^{-1} (\text{M}_{\odot} \text{ yr}^{-1})^{-1}$ . These values were seen not to be a good fit to the data. However, it is interesting to note that our value for  $A$  is lower than that found by [Sullivan et al. \(2006b\)](#). This is consistent with the lower value found in §5.3 for the passive rate, and indicates that the rate in passive galaxies is lower than that seen in [Sullivan et al. \(2006b\)](#) for all masses of passive galaxies. The value of  $B$  found by both surveys differs by  $1.86\sigma$ .

However, our analysis in §5.7 show that the type Ia supernova host galaxies in our sample are not well described by a type Ia supernova rate that is linearly dependent on mass. [Sullivan et al. \(2006b\)](#) find that  $n_{\text{mass}} = 1.00 \pm 0.11$  and  $n_{\text{star-forming}} = 0.98 \pm 0.12$  when a bivariate fit is used. We find values of  $n_{\text{mass}} = 0.67 \pm 0.14$  and  $n_{\text{star-forming}} = 1.01 \pm 0.25$ . The values of  $n_{\text{star-forming}}$  are consistent between the two survey's, but the value of  $n_{\text{pass}}$  differ by  $1.85\sigma$ .

Thus whilst the analysis of [Sullivan et al. \(2006b\)](#) indicates a type Ia supernova rate that corresponds to the ‘‘A+B’’ model, our analysis prefers,

$$\text{SNR}_{\text{Ia}} = A \times M^{\frac{1}{2}} + B \times \text{SFR}. \quad (5.24)$$

The tension between these two results, and the low values of the probabilities found in §5.7, may indicate that the type Ia supernova rate cannot be parameterised in this way for our dataset, and instead a different parameterisation may be required.

It should be noted that the only difference of note between the analysis shown above and that of [Sullivan et al. \(2006b\)](#) is the rest-frame covered by each survey, with our rest-frame being slightly wider than that of [Sullivan et al. \(2006b\)](#). In §D we discuss the effect of this difference, and show that it does not significantly affect the results given in this chapter.

# Chapter 6

## Supernova Properties as a Function of Host Galaxy Properties

### 6.1 Introduction

Diversity in the type Ia supernova population is a well studied topic. These so called standard candles are known to show differences beyond their known luminosity versus light-curve decline rate relationship (§1).

[Hamuy et al. \(1996c\)](#) showed that whilst the photometric properties of these Ia events can be well described from this one parameter, there are still significant differences in their light-curves which suggest that another parameter may influence the observed properties of type Ia supernova. [Oemler & Tinsley \(1979\)](#) showed that these explosions are substantially more common in galaxies who exhibit large amounts of recent star formation activity. Further to this, results from [Hamuy et al. \(1995\)](#) and [Hamuy et al. \(2000\)](#) suggest that bright SNe Ia events occur preferentially in young stellar environments, and that the brightest events are found in the lowest luminosity galaxies. Further to this, [Hamuy et al. \(1996b\)](#) showed that there is a strong correlation between the light-curve decline rate the morphological class of galaxy in which the supernova occurs. [Mannucci et al. \(2005b\)](#) also show that the rate of Ia events is a factor of  $\sim 20$  times higher in galaxies that are visually determined to be late-type when compared to early type galaxies.

[Sullivan et al. \(2006b\)](#) determined that the light-curve decline rate (or stretch parameter) for a sample of SNe Ia's both at low redshift, from the literature, and at high redshift, using data from the first two seasons of the SNLS, is correlated with the host galaxy type in which it occurred. In particular, they found that type Ia SNe were less likely to occur in passive galaxies exhibiting no sign of recent star-formation activity and were found

to have low stretch values, and are thus fainter than their counterparts in star-forming environments.

[Benetti et al. \(2005\)](#) looked at the photometric and spectroscopic properties of a local sample of these events and managed to split their sample into three distinct categories. The first group contained faint objects, such as 1991bg ([Leibundgut et al. \(1993\)](#), [Krisciunas et al. \(2004\)](#)) like events with low expansion velocities and rapid growth of the SiII velocity, based on optical spectra. The second group consisted of normal events with high velocity gradients and brighter mean absolute magnitudes ( $\langle M_B \rangle = -19.3$ ) and larger expansion velocities than the fainter sample. The third group consisted of 1991T ([Phillips et al. \(1992\)](#)) like events and normal Ia's, who populate a thin strip in the SiII expansion rate and have small velocity gradients, but have similar absolute magnitudes to the second group.

[Foley et al. \(2008b\)](#) show that the velocity of the FeII line in the Ultra-Violet (UV) part of the spectrum, does not correlate with light-curve decline rate, and that differences are seen between objects which decline quickly when compared to those which are slow decliners, and thus that the UV ratio is highly correlated with SN Ia luminosity, and further to that these objects have a UV excess.

This diversity within the type Ia population shows that the physics of these events is not fully understood. Further to this, any discovered correlations maybe used to reduce the intrinsic scatter of these events, and thus lead to better estimations of cosmological parameters. [Sullivan et al. \(2003\)](#) found that type Ia supernovae that occur in early-type galaxies are less scattered from the best-fit Hubble diagram than supernovae that occur in late-type galaxies.

To accurately determine the cosmological parameters, the efficiency of each supernova survey needs to be estimated. Unless the type Ia supernova population is properly understood, these efficiency corrections may be incorrect and thus results in a biased, or skewed cosmology analysis.

In §5 we showed that the SN Ia rate from the SDSS-II Supernova Survey at intermediate redshift depends on both the mass and star formation rate of the host galaxy in which it occurs. Whilst not perfectly matching the results at higher redshift from [Sullivan et al. \(2006b\)](#), it is clear that a “two-component” distribution is required as we cannot reconcile the SN Ia rate in star-forming galaxies with a rate purely dependent on the mass of the host. This implies that two distinct populations of type Ia supernova events may

exist, and if this hypothesis is true, we would expect to see a diversity of the supernova properties related to this.

As mentioned by [Scannapieco & Bildsten \(2005\)](#) and [Mannucci et al. \(2006\)](#) it is understandable that a range of delay times will occur for observed SN Ia events, due to variations on the progenitor system, with the companion star being drawn from a separate and distinct set dependent on the stellar population of the host galaxy. Passive galaxies are far more likely to contain older and more evolved stars, such as red giant stars or other white dwarfs, whilst star forming galaxies are seen to contain more main sequence stars. This difference in delay-times maybe seen in the decline rate relation.

In this chapter we use the incompleteness corrected sample from the first two years of the SDSS-II Supernova sample, as defined in §3 and as listed in §4.8 to look at how the properties of the supernova event, as estimated by the MLCS2k2 light-curve fitter (and the SALT2 light-curve fitter), correlate with the properties of their host galaxies, as determined from the PEGASE SED's (§4.4). In particular we shall see if the galaxy type is correlated with the light-curve decline rate, extinction and colour of the supernova event.

## 6.2 Investigating the Light-Curve Decline Rate as a Function of Host Galaxy Type

The most important factor affecting the shape of an SN Ia is the light-curve decline rate. this connects the rate of decline of the light-curve to the peak luminosity. This determines how bright the SN Ia is, and thus the distances to which it can be seen.

The relationship between the peak brightness of a type Ia supernova and its decline rate is well known and has been well measured. There are several methods for doing this. These include the  $\Delta m_{15}(B)$  parameterisation of [Phillips \(1993\)](#) which determines the amount of magnitudes that the B-band magnitude decreases in brightness during the first 15 days after maximum.

This work will consider two parameterisations. In the analysis described previously we have used the MLCS2k2 light-curve fitter (§3.2.3, [Jha et al. \(2007\)](#) and [Kessler et al. \(2009\)](#)) to determine the best-fit parameters for our SN Ia events. This method uses a training set of sample low redshift light-curves to fit a multi-dimensional parameter space including the luminosity correction  $\Delta$ , which is treated to have quadratic dependence. This is discussed in §6.2.1. As a comparison to the result found in §6.2.1 we

shall consider the stretch and  $x_1$  parameters, as determined from the SALT and SALT2 lightcurve fitters, which use the traditional “stretch” method (Perlmutter et al. (1997)). The results using this method are discussed in §6.2.2

### 6.2.1 The Delta Distribution of Type Ia Supernovae

The MLCS2k2 light-curve fitter (Jha et al. (2007)) is discussed in §3.2.3. The luminosity correction for this method is contained in the parameter,  $\Delta$ . This is used in a least squares fit. This model attempts to use a physically motivated method to separate extinction by dust from the usually measured colour correlation.

The MLCS2k2 model fits the observed light curves in a specific passband X using the model,

$$\vec{m}_X(t - t_0) = \vec{M}_X^0 + \mu_0 + \vec{\zeta}_X(\alpha_X + \beta_X/R_V)A_V^0 + \vec{P}_X\Delta + \vec{Q}_X\Delta^2 \quad (6.1)$$

where  $\Delta$  is the luminosity / light-curve shape parameter, and  $\vec{P}_X$  and  $\vec{Q}_X$  are vectors describing the change in light-curve shape as a function of  $\Delta$  (Jha et al. (2007)).  $\vec{P}_X$  and  $\vec{Q}_X$  are solved using a low redshift training set. The  $\Delta$  parameter is such that larger values indicate intrinsically fainter events.

In this section we shall investigate how the light-curve decline rate, using the  $\Delta$  parameterisation from MLCS, is related to the host galaxy in which the supernova event occurs.

Figure 6.1 shows how the peak luminosity / decline rate parameter is related to host galaxy type. For this analysis we have split up our incompleteness corrected sample as determined in §3 by specific star-formation rate, as defined in §5.2. We have then binned each of the  $\Delta$  distributions and included the efficiency correction (§3.3) to determine the relationship between the  $\Delta$  distribution for each galaxy type.

Further to this, we have then fitted a Gaussian function to each distribution. The determined mean and width of each Gaussian is shown in Table 6.1 along with the number of elements in each galaxy category.

From the Gaussian fits, it appears that there is a difference between the three distributions, and in particular a difference between the passive galaxy set and galaxies exhibiting recent star-formation activity. However, such a difference needs to be quantified. To do this we shall use two statistical tests. These are introduced in §6.2.1 and §6.2.1.

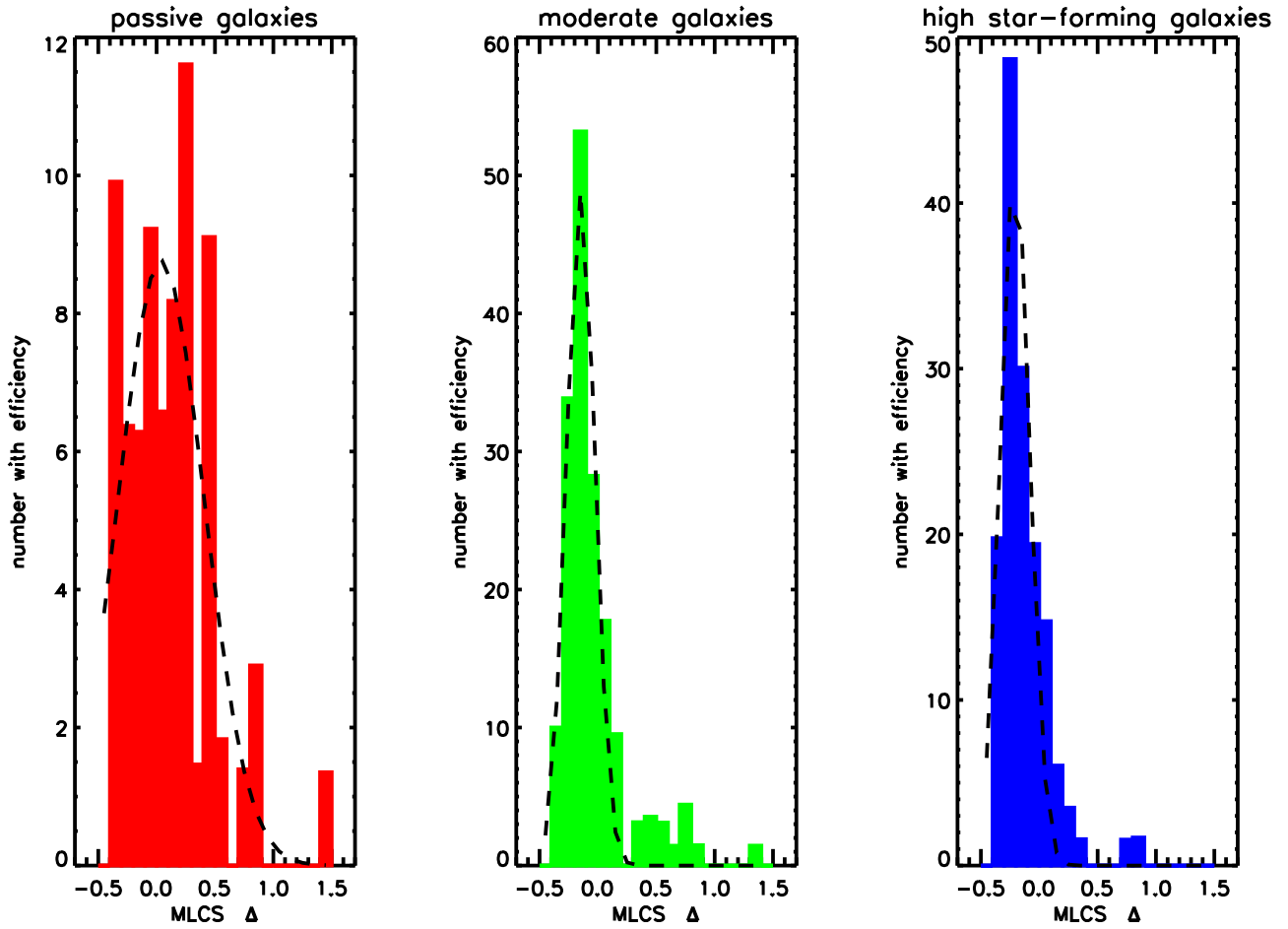


Figure 6.1: Showing the distribution of the MLCS2k2  $\Delta$  parameter for the passive, moderately star-forming and highly star-forming galaxy populations. Also overplotted is the best-fit Gaussian function for each sample.

Galaxy Type	Number of Elements	Gaussian Mean	Gaussian Width
Passive	48	0.0382	0.3693
Moderately Star-forming	106	-0.1474	0.1213
Highly Star-forming	92	-0.2070	0.1255

Table 6.1: Shows the number of elements and mean and width of the fitted Gaussians for the MLCS2k2  $\Delta$  parameter for various galaxy types

### The Kolmogorov-Smirnov test

A Kolmogorov-Smirnov test (K-S test), [Chakravarti et al. \(1967\)](#), attempts to determine if two datasets differ significantly. This test is non-parametric and independent of the distribution. The K-S test statistic determines the distance between the empirical distribution functions for the two distributions, where the empirical distribution function is defined as,

$$F_n(x) = \frac{\text{number of elements in the sample} \leq x}{n} = \frac{1}{n} \sum_{i=1}^n I(X_i \leq x), \quad (6.2)$$

where  $I(x)$  is the characteristic function, and thus the K-S statistic is given by,

$$D_n = \sup_x |F_n(x) - F(x)|, \quad (6.3)$$

where  $\sup S$ , the supremum of  $S$ , is the least upper bound, ([James & Roos \(1991\)](#)).

The null hypothesis for this statistic is the hypothesis that the two input distributions are drawn from the same distribution. This test is sensitive to any differences in shape and location between the two distributions.

Thus this test is able to successfully determine if two distributions are not drawn from the same parent distribution, but is unable to accurately confirm if they come from the same parent distribution.

### The Anderson-Darling test

An Anderson-Darling test (A-D test), [Stephens \(1974\)](#), [Scholz & Stephens \(1987\)](#), is a powerful statistical test that is used for detecting differences between two data-sets. It is designed to be more sensitive to discrepancies between two datasets with a special focus on the tails of the distributions. The K-S test (§6.2.1) is conversely more sensitive to the mean of the distributions.

The A-D test statistic is defined as,

$$A_n^2 = n \int_{-\infty}^{\infty} \frac{[F_n(x) - F(x)]^2}{F(x)[1 - F(x)]} dF(x), \quad (6.4)$$

where  $F$  is as described in Equation 6.2.

For the two sample extension, the statistic is defined as (Pettitt (1976)),

$$A_{nm}^2 = \frac{nm}{N} \int_{-\infty}^{\infty} \frac{[F_n(x) - G_m(x)]^2}{H_N(x)[1 - H_N(x)]} dH_N(x), \quad (6.5)$$

where  $N = n + m$  and  $F_n(x)$ ,  $G_m(x)$ ,  $H_N(x)$  are the sample distribution functions of the  $X$ -sample,  $Y$ -sample and combined sample, such that,

$$H_N(x) = \{nF_n(x) + mG_m(x)\}N. \quad (6.6)$$

This statistic is compared to the critical values to determine the P-value, or probability of obtaining a value of the test statistic given the null hypothesis that the two distributions are drawn from the same distribution.

As with the K-S test (§6.2.1), the A-D test is able to determine if two distributions are drawn from different parent distributions, with special attention given to the tails of the distribution in this case, but is unable to provide evidence that the two samples are the same.

### Statistical Results

Having introduced the statistical tests we are now able to investigate if the observed differences between the  $\Delta$  distributions are statistically important. To do this the two star-forming datasets are combined. Thus we are able to compare the  $\Delta$  distributions of passive galaxies to that of star-forming galaxies. A K-S test yields a probability of  $1.037 \times 10^{-5}$  that the two distributions are not drawn from different distributions. A corresponding A-D test yields a value of  $5.143 \times 10^{-6}$ . These two values are clear indications that the two distributions are drawn from different parent distributions. Statistically, SNe Ia's that occur in passive galaxies are seen to have a wider variety of values of  $\Delta$  than those that occur in star-forming galaxies, which are predominately fast-decliners. Those in elliptical galaxies have high values of decline rate, and thus are intrinsically fainter events.

### 6.2.2 The $x_1$ and stretch distributions of Type Ia Supernovae

To confirm this result, and to be able to compare our distribution of decline rate's to other published results, we need to use another light-curve fitter. The SALT light-curve fitter

(Guy et al. (2005)) uses the stretch parameterisation, whilst the SALT2 light-curve fitter (Guy et al. (2007)) uses the  $x_1$  parameterisation.

### The SALT and SALT2 Lightcurve Fitters

The SALT light-curve fitter (Guy et al. (2005)) is used by the SNLS (Pritchett & For The Snls Collaboration (2005)). It uses broadband corrections to the spectral sequence, as a function of phase, wavelength and stretch factor, so that the light-curves obtained from the spectral templates, when run through the filter response curves, match the measured light-curves.

The SALT2 light-curve fitter (Guy et al. (2007)) uses a similar framework with multi-colour light curves being used to train the model. In this case spectroscopic data is used to allow the model to be fully independent of the spectral template provided by Nugent et al. (2002). The model aims to provide the best average template, so that any variation in type Ia supernova spectra can be discounted. By leaving the normalisation of the spectra as a free parameter, type Ia events at both low redshift and high redshift can be used to train the model. The following form is used for the flux,

$$F = x_0 \times [M_0(p, \lambda) + x_1 M_1(p, \lambda) + \dots] \times \exp[cCL(\lambda)], \quad (6.7)$$

where  $p$  is the rest-frame time since the date of maximum luminosity in the B-band, and  $\lambda$  is the rest-frame wavelength of the supernova.  $M_0(p, \lambda)$  is the mean spectral sequence, whilst  $M_1(p, \lambda)$  and other terms (such as  $M_k(p, \lambda)$ ) describe the variability of the SN Ia event.  $CL(\lambda)$  is the average colour correction law, whilst,

$$c = (B - V)_{MAX} - \langle B - V \rangle \quad (6.8)$$

is the colour offset with respect to the colour at maximum light in the B-band. In this model,  $x_0$ ,  $x_1$  and  $c$  are the parameters specific to each supernova event, with  $c$  indicating the intrinsic colour of the supernova event, broadly corresponding to the MLCS2k2  $A_V$  extinction term.  $x_1$  represents the peak luminosity / light-curve decline rate parameter (corresponding to the MLCS2k2  $\Delta$  parameter).

The SALT light-curve fitter uses the stretch method. Its peak luminosity / light-curve decline rate parameter is known as “stretch”. This can be related to the SALT2  $x_1$  using the transformation (Guy et al. (2007)),

$$s(SALT) = 0.98 + 0.091x_1 + 0.003x_1^2 - 0.00075x_1^3 \quad (6.9)$$

This transformation is not perfect as it carries a scatter of approximately 0.02.

To investigate whether the result in §6.2.1 is independent of light-curve fitter, the objects in our sample (as described in §4.8) were run through the SALT2 light-curve fitter. For this process, the objects with a spectroscopic redshift were evaluated at the particular redshift, whilst objects with only a photometric identification from the MLCS2k2 were identified at that particular redshift. For the fitting process, a wavelength range of 3000Å to 7000Å was considered, and only the period  $-15$  days to  $+40$  days from maximum was used. Following the example set by the MLCS2k2 light-curve fitter only that  $g$ ,  $r$  and  $i$  filter's data was used.

### The $x_1$ Distribution of Type Ia Supernovae

Having evaluated the light-curves of our objects using the SALT2 light-curve fitter, we are now able to investigate the light-curve decline rate in this parameterisation.

Figure 6.2 shows how the luminosity / light-curve decline rate parameter  $x_1$  is related to host galaxy type. For this analysis, we have split our incompleteness corrected sample as determined in §3 by specific star-formation rate, as defined in §5.2. We have then binned each of the  $x_1$  distributions and included the efficiency correction (§3.3) to determine the relationship between the  $x_1$  distribution for each galaxy type.

Further to this, we have then fitted a Gaussian function to each distribution. The determined mean and width of each Gaussian is shown in Table 6.2 along with the number of elements in each galaxy category.

Following the procedure used in §6.2.1 we are interested to determine if there is any statistically significant difference between these different distributions, and in particular

Galaxy Type	Number of Elements	Gaussian Mean	Gaussian Width
Passive	48	-1.5027	1.4104
Moderately Star-forming	106	-0.0801	0.7822
Highly Star-forming	92	-0.1961	0.8768

Table 6.2: Shows the number of elements and mean and width of the fitted Gaussians for the SALT2  $x_1$  parameter for various galaxy types

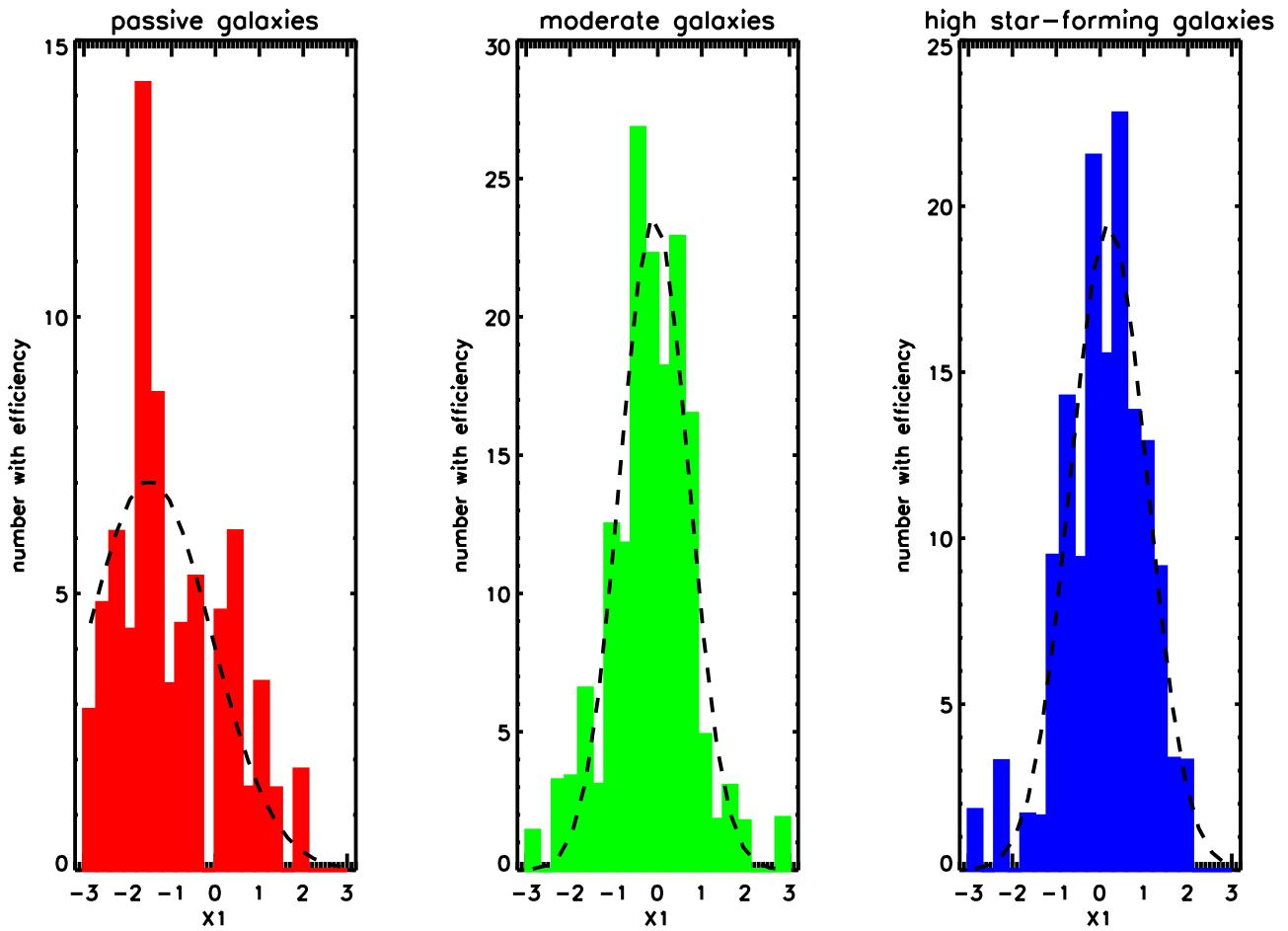


Figure 6.2: Showing the distribution of the SALT2  $x_1$  parameter for the passive, moderately star-forming and highly star-forming galaxy populations. Also overplotted is the best-fit Gaussian function for each sample.

between the passive galaxies and the star-forming set, which we are confident of being able to differentiate between. Having combined the two star-forming sets, a K-S test (§6.2.1) and an A-D test (§6.2.1) was run. The K-S test produced a probability of  $2.07 \times 10^{-7}$  of the two distributions being drawn from the same parent data-set, whilst the A-D test produced a similar statistic of  $4.55 \times 10^{-7}$ . These results confirm the findings in §6.2.1 that the two datasets are drawn from different distributions to a high degree of certainty.

### Transformation to the stretch parameterisation

Equation 6.9 shows the method for transforming between the  $x_1$  parameterisation and the stretch parameter from the SALT light-curve fitter. Figure 6.3 shows the result of this transformation. This result, whilst not being statistically different to that in §6.2.2 is useful for comparisons between different published results, which are mostly seen in this parameterisation. Table 6.3 shows the outputs of the Gaussian fitting that is overplotted on Figure 6.3. The mean and width of the Gaussian is shown.

### Using a Low redshift Approximation

Another method for transforming between  $\Delta$  and  $x_1$  and further to stretch, is by using an observed low redshift relationship. This relationship is shown in Figure 6.4 and has been obtained by Jha (2008) from the measurements of a set of well-measured light-curves of supernovae at low redshift. It shows that with a small level of scatter, the MLCS2k2  $\Delta$  parameter can be converted to the SALT2  $x_1$  parameter using the equation:

$$x_1 = -0.49(\pm 0.03) - 5.16(\pm 0.19) * \Delta + 2.90(\pm 0.33) * \Delta^2 \quad (6.10)$$

As stated in §6.2.2, Equation 6.9 allows us to convert between the  $x_1$  and stretch parameterisation.

Galaxy Type	Number of Elements	Gaussian Mean	Gaussian Width
Passive	48	0.8637	0.0906
Moderately Star-forming	106	0.9648	0.0718
Highly Star-forming	92	0.9945	0.0844

Table 6.3: Shows the number of elements and mean and width of the fitted Gaussians for the SALT2 stretch parameter for various galaxy types when converted from the SALT2  $x_1$  parameter

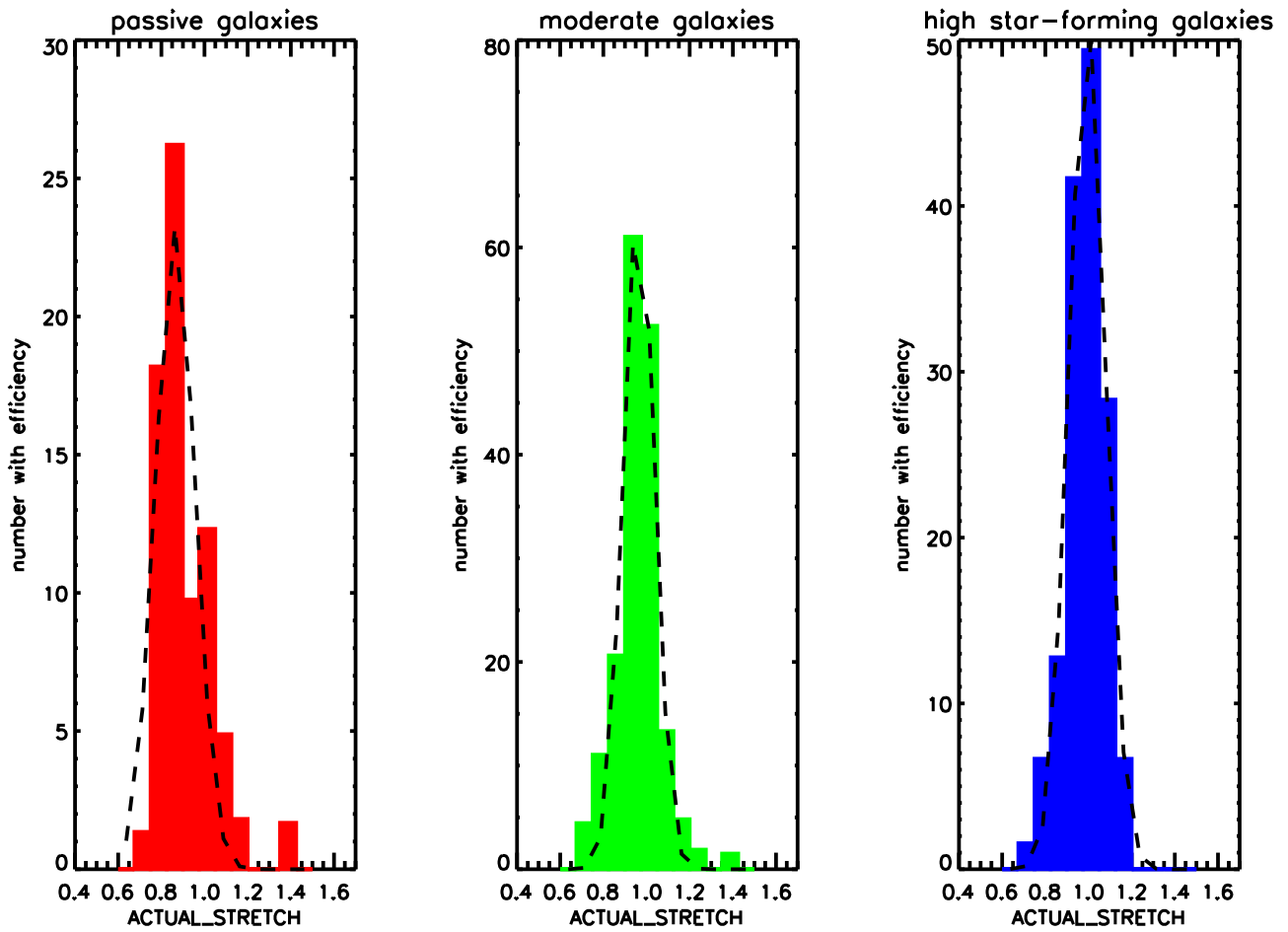


Figure 6.3: Showing the distribution of the SALT stretch parameter  $s$  for the passive, moderately star-forming and highly star-forming galaxy populations. Also overplotted is the best-fit Gaussian function for each sample.

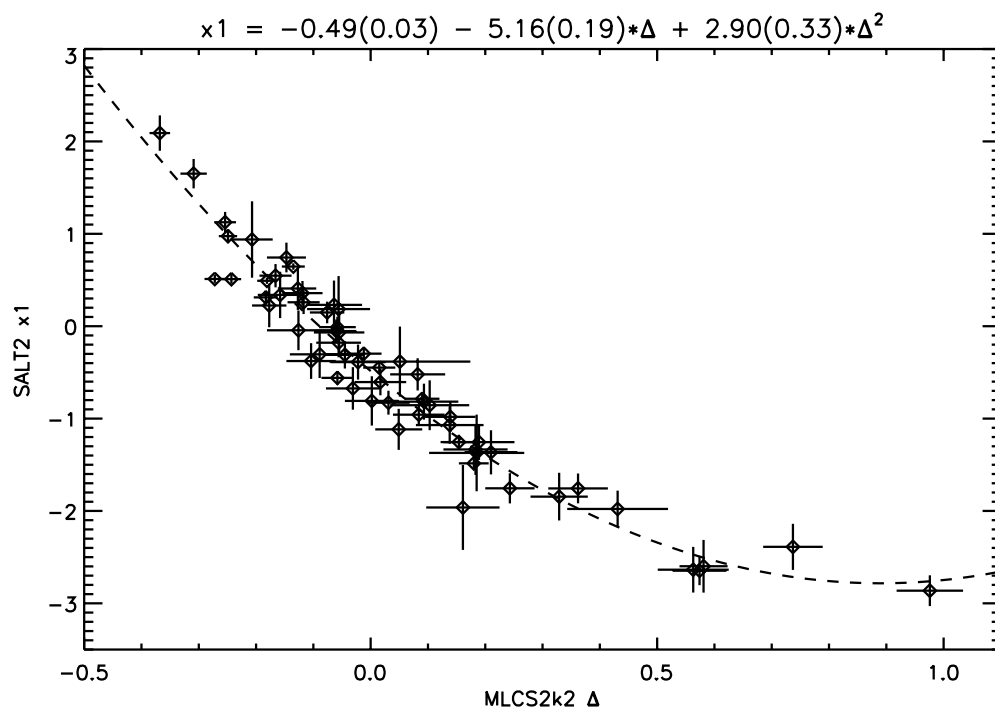


Figure 6.4: Showing the low redshift approximation relating the SALT2 parameter  $x_1$  to the MLCS2k2 parameter  $\Delta$ . This relationship has been determined by [Jha \(2008\)](#) using a set of well-measured low redshift supernovae from the literature.

Using Equation 6.10, the distribution of  $x_1$  when converted from the MLCS2k2 values for  $\Delta$  allows us to make Figure 6.5, which shows us the distribution of  $x_1$  when converted from  $\Delta$  as a function of host galaxy type. Table 6.4 shows the parameters of the fitted Gaussians in this case. This figure is not statistically different from Figure 6.1, but allows us to confirm that the values obtained from Figure 6.2 and Table 6.2 are accurate and in agreement with those from the  $\Delta$  distribution.

In a similar fashion to Figure 6.5, Figure 6.6 shows the distribution for the objects in our sample when the values of  $\Delta$  from MLCS2k2 are converted to the stretch parameterisation using Equation 6.10 and Equation 6.9 as a function of host galaxy type, and specifically specific star-formation rate. Table 6.5 shows the parameters of the fitted Gaussians in this case. This figure allows us to confirm that the values obtained from Figure 6.3 and Table 6.3 are accurate and in agreement with those from the  $\Delta$  distribution.

### 6.2.3 Summary

In this section we have looked at how the luminosity / light-curve decline rate parameter is related to host galaxy type. We have used the incompleteness corrected sample as described in §3 and looked at both the MLCS2k2  $\Delta$  parameter and SALT2  $x_1$  parameter along with the associated and commonly used, stretch parameter from SALT.

We have seen that there is a clear difference between the decline-rates for SNe events that occur in passive galaxies when compared to those that occur in star-forming galaxies. Using a K-S and A-D test we have been able to confirm that the two distributions are not drawn from the same dataset. Type Ia supernovae are predominantly fast decliners whilst similar events that occur in passive galaxies show a greater range in decline rates, but are generally far more slowly declining. This implies that the properties of a type Ia

Galaxy Type	Number of Elements	Gaussian Mean	Gaussian Width
Passive	48	-1.2987	2.1587
Moderately Star-forming	106	0.2526	0.7959
Highly Star-forming	92	0.6876	0.7682

Table 6.4: Shows the number of elements and mean and width of the fitted Gaussians for the SALT2  $x_1$  parameter for various galaxy types when converted from the MLCS2k2  $\Delta$  parameter using a low redshift approximation.

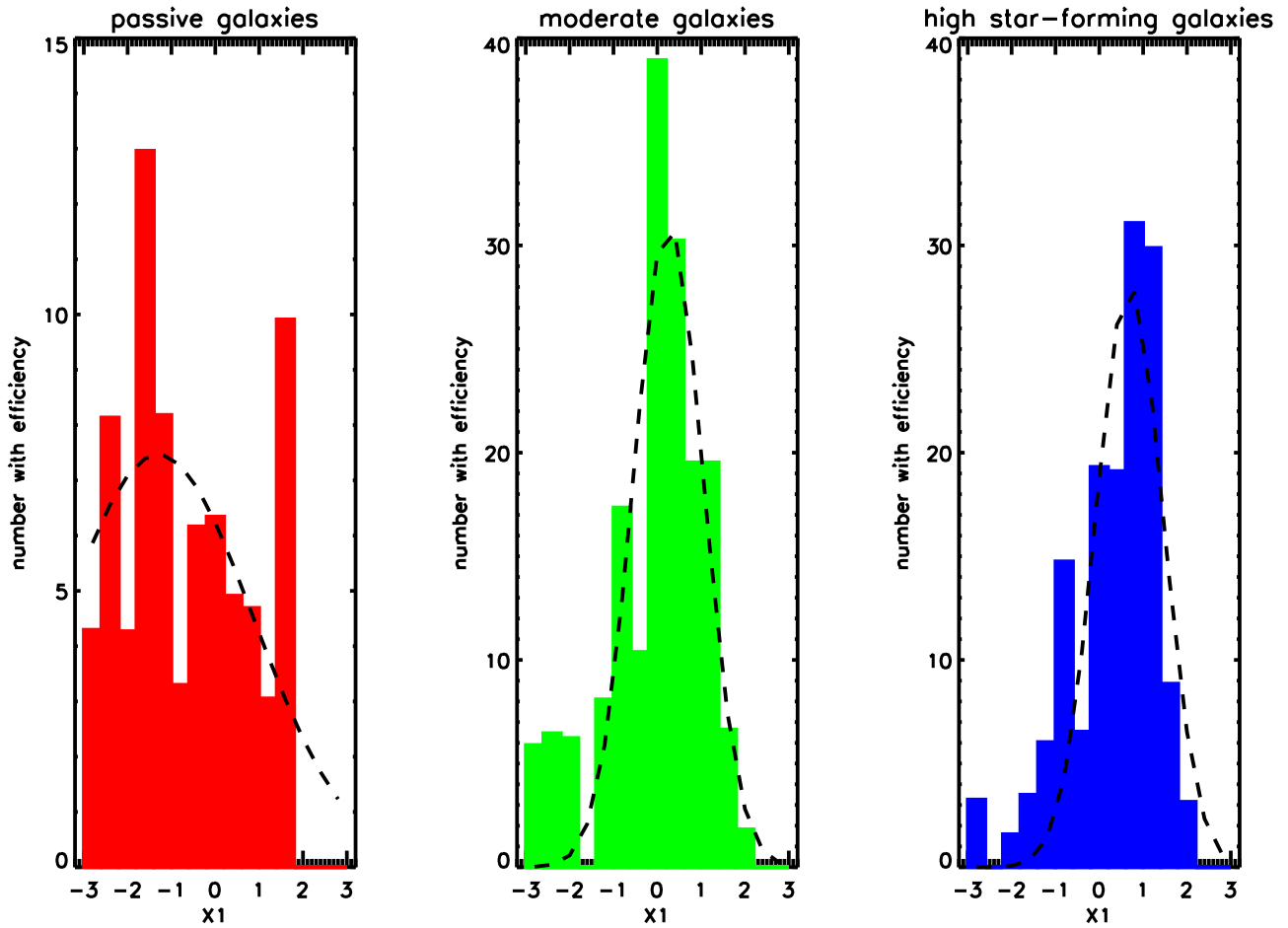


Figure 6.5: Showing the distribution of the SALT2 parameter  $x_1$  as determined from the low redshift approximation (Figure 6.4) for the passive, moderately star-forming and highly star-forming galaxy populations. Also overplotted is the best-fit Gaussian function for each sample.

Galaxy Type	Number of Elements	Gaussian Mean	Gaussian Width
Passive	48	0.8897	0.1434
Moderately Star-forming	106	1.0049	0.0714
Highly Star-forming	92	1.0397	0.0765

Table 6.5: Shows the number of elements mean and width of the fitted Gaussians for the SALT2 stretch parameter for various galaxy types when converted from the MLCS2k2  $\Delta$  parameter using a low redshift approximation.

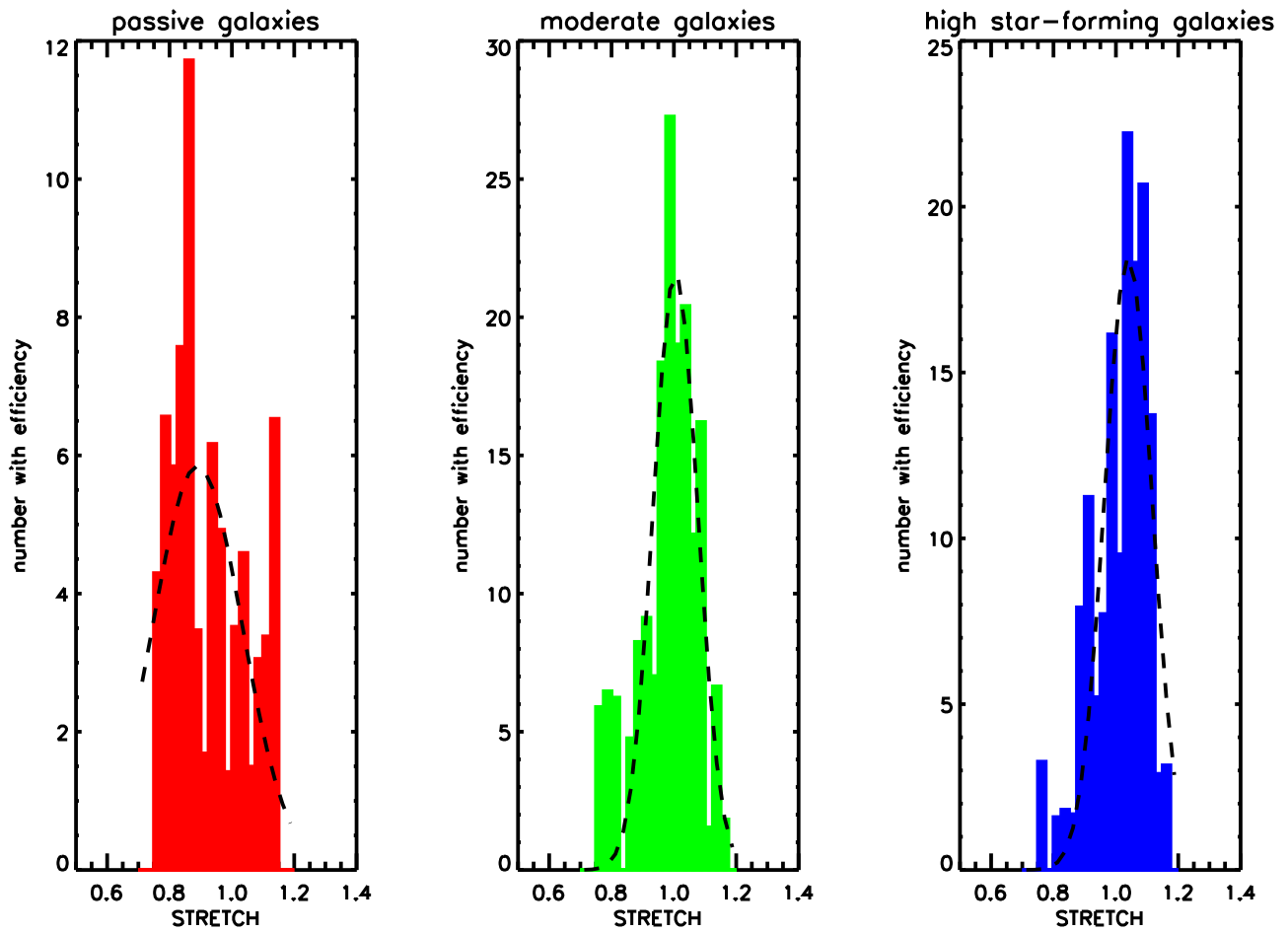


Figure 6.6: Showing the distribution of the SALT stretch parameter  $s$  as determined from the low redshift approximation (Figure 6.4) for the passive, moderately star-forming and highly star-forming galaxy populations. Also overplotted is the best-fit Gaussian function for each sample.

supernova are related to the host galaxy, and with the properties differing between galaxy types, this implies that the progenitors for each supernovae may be different.

### 6.3 Extinction and Colour in the Supernova

In §6.2, we showed that independent of light-curve fitter, the light-curve decline rate is strongly correlated with host galaxy type, specifically with faint, and slowly declining objects primarily seen in passive galaxies, whilst objects which have declined quickly are seen in objects with recent signs of star-formation. This result is consistent in moderate and highly star-forming objects.

We now move on to investigate whether or not a correlation is seen with extinction and colour in the supernova event. We would suspect that with passive galaxies being relatively free of dust, especially when compared to dusty, star-forming galaxies, that a possible correlation may exist.

Extinction by dust along the line of sight to a SN Ia is seen by its reddening effect on the colours of the supernova. As noted in Phillips et al. (1999) and Jha et al. (2007), the spectra of a type Ia supernova evolves over time. This will lead to variations in the extinction dependent on the pass-band used. Thus the reddening is a non-linear function of the of the total extinction. In the case of the SALT2 light-curve fitter, the colour variation of each supernova event is considered. This means that any colour variation (that is independent of time) will be included in the SALT2 colour term. Any differences in the two distributions may lead us to be able to infer if the primary cause of colour in type Ia supernova light-curves is due to line of sight extinction or another unknown parameter that does not follow the same dust law.

In this section we shall attempt to determine if the measured dust / colour from the light-curve of a type Ia event is strongly correlated to the host of the event. We shall start by considering the distribution of  $A_V$  as determined by the MLCS2k2 light-curve fitter (§6.3.1) and then its counterpart for from the SALT2 light-curve fitter, the colour correction, in §6.3.2.

#### 6.3.1 The $A_V$ distribution of type Ia SNe

The MLCS2k2 light-curve fitter parameterises the dust extinction along a line of sight by the extinction in a given band X,  $A_X$  and by the amount of reddening, given by the colour excess, typically  $E(B - V)$ .

The MLCS2k2 model fits the observed light curves in a specific passband X using the following model,

$$\vec{m}_X(t - t_0) = \vec{M}_X^0 + \mu_0 + \vec{\zeta}_X(\alpha_X + \beta_X/R_V)A_V^0 + \vec{P}_X\Delta + \vec{Q}_X\Delta^2, \quad (6.11)$$

where  $R_V$  and  $A_V^0$  ( $A_V$  at maximum light) are the host galaxy extinction parameters. As discussed in §3.2.3, using the extinction law as seen in other surveys, and as well matches the first year SDSS data,  $R_V$  is held constant to  $R_V = 1.9$ .

For the default analysis the  $A_V$  distribution has a prior of the form  $A_V = \exp(-A_V/0.35)$  (as discussed in §3.2.3), which is the default for the SDSS-II first year cosmology sample. The effect of this choice is shown in §6.5.

In this section we shall investigate how the extinction, in the form of the  $A_V$  parameterisation is related to the host galaxy in which the supernova event occurs.

Figure 6.7 shows how the extinction parameter is related to host galaxy type. For this analysis we have split up our incompleteness corrected sample as determined in §3 by specific star-formation rate, as defined in §5.2. We have then binned each of the  $A_V$  distributions and included the efficiency correction (§3.3) to determine the relationship between the  $A_V$  distribution for each galaxy type.

Further to this, we have then fitted a Gaussian function to each distribution. The determined mean and width of each Gaussian is shown in Table 6.6 along with the number of elements in each galaxy category.

Following the procedure used in §6.2.1 we are interested to determine if there is any statistically significant difference between these different distributions, and in particular

Galaxy Type	Number of Elements	Gaussian Mean	Gaussian Width
Passive	48	0.1464	0.2373
Moderately Star-forming	106	0.1645	0.1788
Highly Star-forming	92	-0.0659	0.2384

Table 6.6: Shows the number of elements and mean and width of the fitted Gaussians for the MLCS2k2  $A_V$  parameter for various galaxy types.

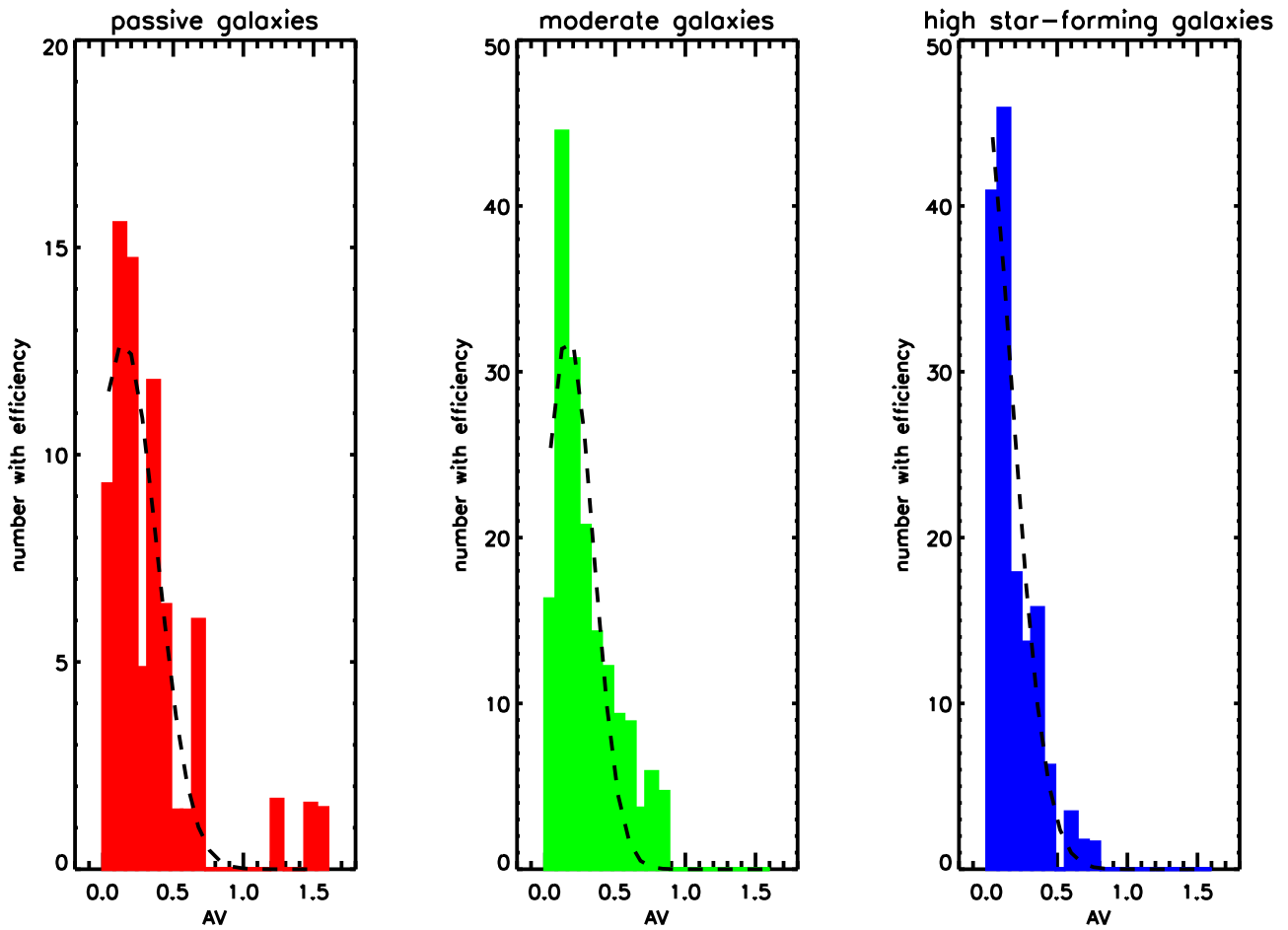


Figure 6.7: Showing the distribution of the MLCS2k2  $A_V$  parameter for the passive, moderately star-forming and highly star-forming galaxy populations when a standard  $A_V$  prior is used. Also overplotted is the best-fit Gaussian function for each sample.

between the passive galaxies and the star-forming set, which we are confident of being able to differentiate between. Thus a K-S test (§6.2.1) and an A-D test (§6.2.1) was run. For these tests the two star-forming distributions (moderately star-forming and strongly star-forming) were combined to be compared to the passive distribution. The K-S test produced a probability of 0.1663 of the two distributions being drawn from the same parent data-set, whilst the A-D test produced a similar statistic of 0.0889. These two results show little evidence (approximately a  $\sim 10\%$  probability), that the distribution of  $A_V$  as seen in the passive galaxies differ from that seen in galaxies which exhibit recent signs of star-formation.

### 6.3.2 The Colour Correction of type Ia SNe

Following the analysis in §6.2.2, we are able to determine if the result above in §6.3.1 is due to the light-curve fitter used. In §6.2.2 we described how each of the objects in our sample were fitted with the SALT2 light-curve fitter. This model deals with the extinction term in the model differently from MLCS2k2. The functional form for the SALT2 model is (Guy et al. (2007))

$$F = x_0 \times [M_0(p, \lambda) + x_1 M_1(p, \lambda) + \dots] \times \exp[cCL(\lambda)], \quad (6.12)$$

where  $CL(\lambda)$  represents the average colour correction law, and is kept constant throughout the whole sample, whilst the optical depth is expressed using a colour offset with respect to the average at the date maximum luminosity in the B-band, i.e.

$$c = (B - V)_{MAX} - \langle B - V \rangle. \quad (6.13)$$

This colour term,  $c$ , differs from the  $A_V$  term from MLCS. Whilst the MLCS  $A_V$  parameter attempts to purely describe the dust content, and thus must follow a dust law, the  $c$  parameter from SALT2 attempts to model the colour variation of the supernova event that is independent of time, and thus is able to include any variation that is not due to dust. Here we discuss how the colour term is correlated with galaxy type for the galaxies in our dataset.

Figure 6.8 shows how the SALT2 colour parameter, as described above, is related to host galaxy type. Following the analysis in §6.3.1 the incompleteness corrected sample is split based upon specific star-formation rate, as defined in §5.2. Each sample is then binned based upon the SALT2 colour term and an efficiency correction is included, to determine the relationship between the colour term for each galaxy type.

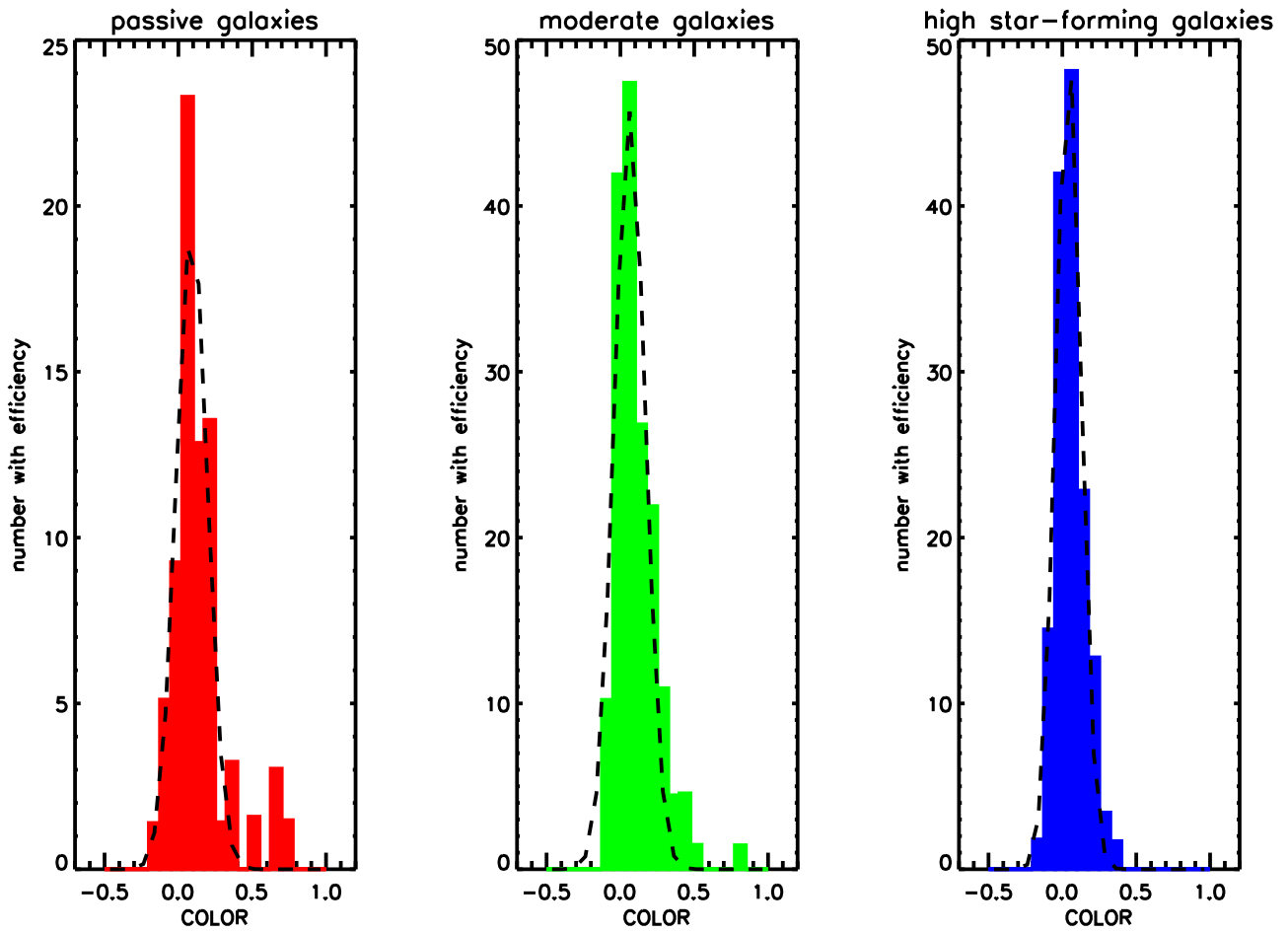


Figure 6.8: Showing the distribution of the SALT2 colour parameter  $c$  for the passive, moderately star-forming and highly star-forming galaxy populations. Also overplotted is the best-fit Gaussian function for each sample.

Further to this, we have then fitted a Gaussian function to each distribution. The determined mean and width of each Gaussian is shown in Table 6.7 along with the number of elements in each galaxy category.

As discussed previously, these Gaussian parameters provide us with an indication as to whether the three distributions are similar, but to quantify any difference between them we need to carry out several statistical tests. To that end the two star-forming datasets were merged, and a K-S test and A-D test were carried out on the passive and star-forming galaxies to determine probability that the two datasets are drawn from the same distribution. The probability from the K-S test is 0.0726 and the probability from the A-D test is 0.0265. These two values are lower than those for the  $A_V$  analysis, but still show little evidence that the two datasets are drawn from different datasets. That is we have no reason to say that the null hypothesis, that both the colour from the passive galaxies and the star-forming galaxies are drawn from the same distribution, is not correct.

### 6.3.3 Summary

We have looked at the  $A_V$  and SALT2 colour term for the hosts of the type Ia supernova events in our sample. By splitting the hosts by specific star-formation rate and investigating the relation between the samples for both the  $A_V$  and colour term, we have shown that there is no statistical reason to believe that the extinction for type Ia supernovae that occur in passive galaxies is different to that of star-forming galaxies.

This result is slightly surprising as the extinction of a type Ia supernova is expected to be related to the level of dust in the host galaxy. Passive galaxies are primarily seen to be deficient of dust (Zhang et al. (2008)), as opposed to the high levels of dust in spiral galaxies (Salim et al. (2005)). This therefore implies that the host galaxy dust levels is a sub-dominant parameter in the supernova light-curve, especially when compared to the intrinsic colour.

The effect of our chosen  $A_V$  prior on this result is discussed in §6.4.

Galaxy Type	Number of Elements	Gaussian Mean	Gaussian Width
Passive	48	0.0911	0.1057
Moderately Star-forming	106	0.0633	0.1051
Highly Star-forming	92	0.0414	0.0866

Table 6.7: Shows the number of elements and mean and width of the fitted Gaussians for the SALT2 colour parameter for various galaxy types.

## 6.4 The Effect of the $A_V$ Prior on the Results

In §6.3 and §6.2, we showed how the light-curve decline rate (in the form of the MLCS  $\Delta$  parameter, SALT2  $x_1$  parameter and SALT stretch parameter  $s$ ) and the extinction (in the form of the MLCS  $A_V$  parameter and SALT2 colour parameter) are correlated with host galaxy type. However, this result may be partially dependent on our choice of  $A_V$  in the MLCS light-curve fitting process.

As discussed in §3.2.3, our sample is determined using an  $A_V$  prior of  $A_V = \exp(-A_V/0.35)$ . This is chosen as it well matches the distribution seen in the first year SDSS cosmology analysis. However this assumption is presuming that we have prior knowledge of the  $A_V$  distribution, which is not the cosmology sample. Thus it is important to determine if our results found in the previous sections are consistent, independent of this prior. The effect of altering this prior will not only change the values of  $A_V$  for each dataset, but will also alter the number of galaxies in our sample. With the prior relaxed more elements are likely to pass the criteria set in §3.2.

To determine if this is the case there are two options. We could instead use a flat  $A_V$  prior. This assumes no knowledge of the  $A_V$  distribution of our sample, except for the fact that it must be positive. This is a sensible approach, as any negative extinction term is clearly unphysical. The other approach is to consider no  $A_V$  prior at all. This assumes no knowledge of the distribution of the  $A_V$  within our sample. We shall discuss the results under these two conditions in §6.4.1 and §6.4.2.

### 6.4.1 Using a Flat $A_V$ Prior

Here we discuss the effect of using a flat  $A_V$  prior. By using such a criteria our data set increases in size from 246 host galaxies to 257. This increase may be because it allows objects which do not follow the standardly enforced  $A_V$  prior in to the sample, or because this extra degree of freedom in the light-curve fitting process enables low signal-to-noise, or poorly sampled light-curves to pass the criteria with a high dust content. The differences between the two samples is highlighted in §4.8. An identical procedure to that described in §3.2 and §4.3 is used to determine the supernova hosts and their derived properties. The change in prior also affects the redshift of several of our objects which do not have a spectroscopic redshift.

Figure 6.9 shows the distribution of  $A_V$  for our three different galaxy types, as defined in §5.2. This plot is analogous to Figure 6.7, except that a flat  $A_V$  prior is used.

It shows how the  $A_V$  extinction parameter from MLCS is related to galaxy type for our three samples that have been split by specific star-formation rate.

Overplotted on Figure 6.9 are Gaussian fits to the distributions. The number of elements in each sample along with the fitted mean and width of the Gaussian function is shown in Table 6.8. From this table it is apparent that the extra hosts in the sample due to the change in  $A_V$  prior are distributed with galaxy type. Thus there is no bias introduced by using the standard  $A_V$  prior as described above, when compared to the flat prior. For the  $A_V$  distributions, the fitted Gaussian's have larger widths in all three cases. This is not surprising as there is now an extra degree of freedom in the determination of extinction. It would appear that the 3 distributions are similar to those in Table 6.6 .

As an extension to this, Figure 6.10 shows the distribution of the MLCS  $\Delta$  parameter for these three datasets. This is analogous to Figure 6.1. A similar procedure to that described above is used.

Table 6.9 shows the values of the fitted Gaussians for the delta distribution shown in figure 6.10. The mean value and width are shown along with the number of elements in each dataset. In this case the mean values and widths are extremely similar to those in table 6.1. This shows that the value of  $\Delta$  for each object is not particularly sensitive to the choice of the  $A_V$  parameter. The main difference between Table 6.9 and Table 6.1 is caused by the addition of new elements that have now passed the selection criteria, due to the less stringent  $A_V$  requirements.

To determine whether this change in  $A_V$  affects the statistical differences between the two datasets a K-S test and A-D test has been carried out on each dataset, in a similar fashion to that in §6.2 and §6.3.1. The two star-forming datasets have been combined and compared to the passive dataset. The probabilities that the two distributions (as determined from the K-S and A-D tests) are drawn from the same dataset are shown in Table

Galaxy Type	Number of Elements	Gaussian Mean	Gaussian Width
Passive	54	0.1767	0.3144
Moderately Star-forming	108	0.1695	0.2957
Highly Star-forming	95	-0.2091	0.3529

Table 6.8: Table showing the number of elements and mean and width of the fitted Gaussians for the MLCS  $A_V$  parameter when a Flat  $A_V$  prior is used in the light-curve fitting procedure.

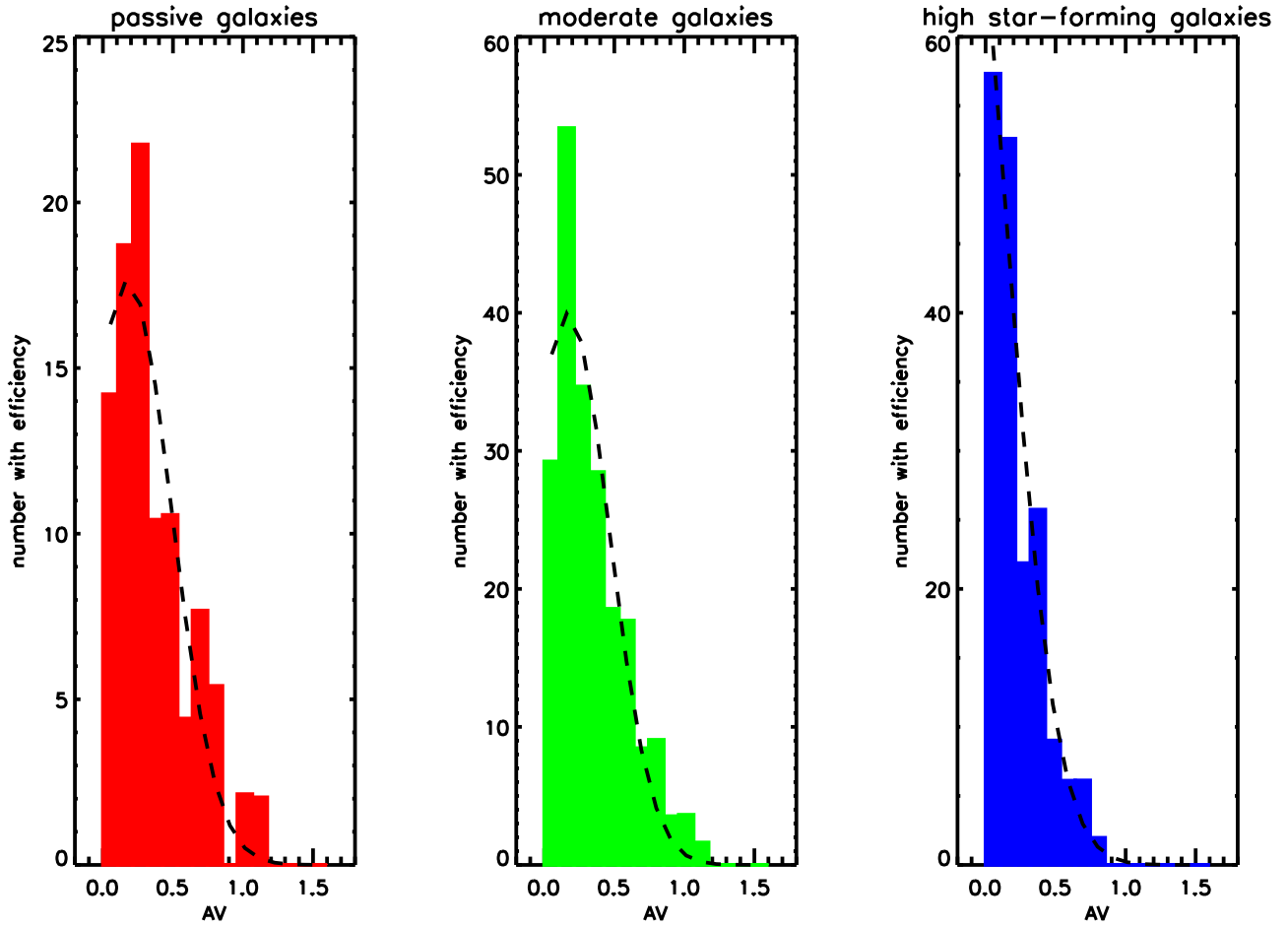


Figure 6.9: Showing the distribution of the MLCS2k2  $A_V$  parameter for the passive, moderately star-forming and highly star-forming galaxy populations when a flat  $A_V$  prior is used. Also overplotted is the best-fit Gaussian function for each sample.

Galaxy Type	Number of Elements	Gaussian Mean	Gaussian Width
Passive	54	-0.0371	0.3763
Moderately Star-forming	108	-0.1397	0.1254
Highly Star-forming	95	-0.2044	0.1352

Table 6.9: Table showing the number of elements and mean and width of the fitted Gaussians for the MLCS  $\Delta$  parameter when a Flat  $A_V$  prior is used in the light-curve fitting procedure.

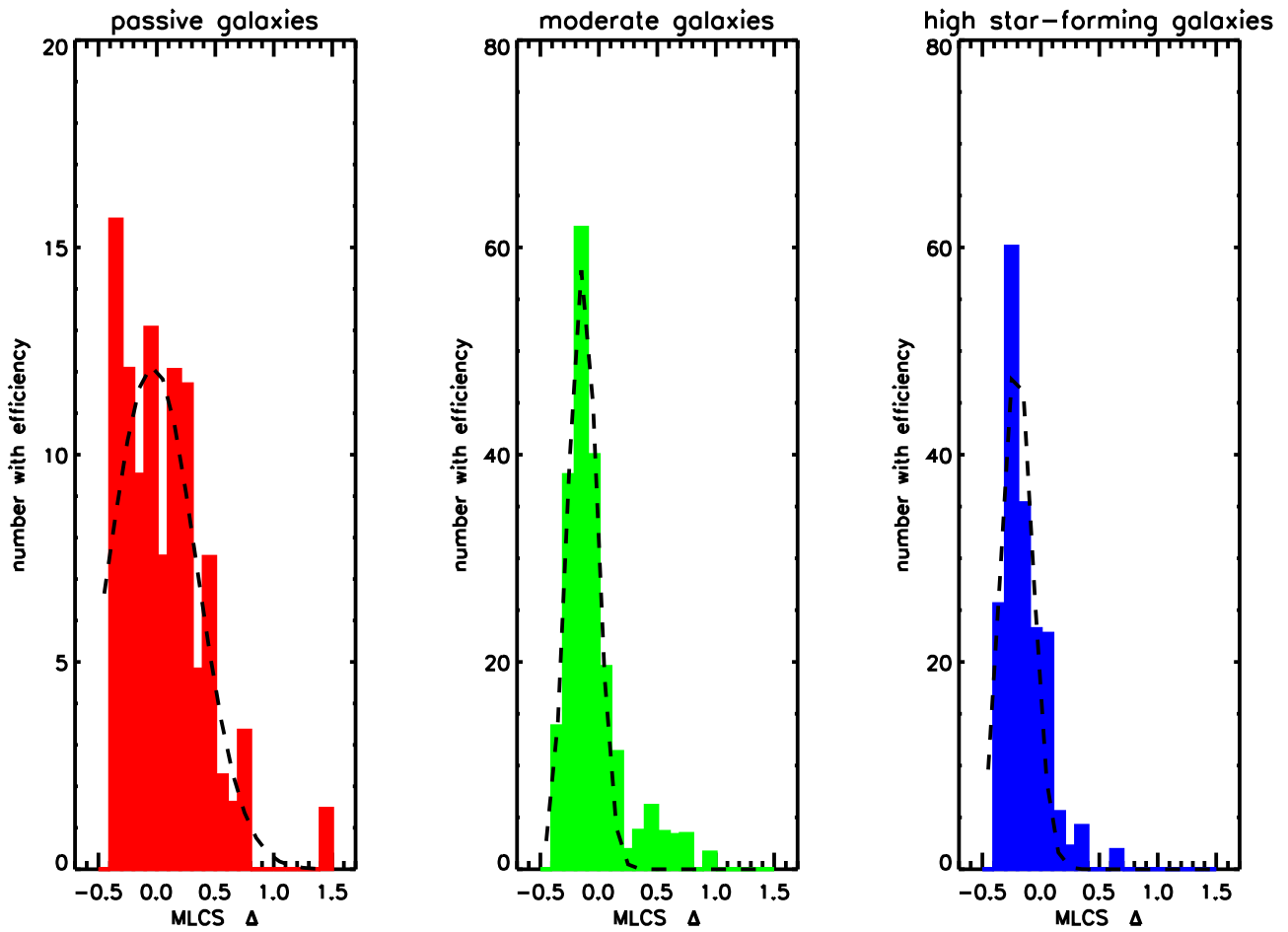


Figure 6.10: Showing the distribution of the MLCS2k2  $\Delta$  parameter for the passive, moderately star-forming and highly star-forming galaxy populations when a flat  $A_V$  prior is used. Also overplotted is the best-fit Gaussian function for each sample.

6.10 . Both the results for the  $A_V$  and MLCS  $\Delta$  distributions are shown. These results are extremely similar to those in §6.2 and §6.3.1. These statistics show that in the case of a flat  $A_V$  prior, there is significant evidence to believe that the  $\Delta$  distributions of SNe that occur in passive galaxies is significantly different to that of similar events that occur in galaxies with recent star-formation activity. As shown in Figure 6.10, type Ia events that occur in passive galaxies are seen at more values of  $\Delta$  than those found in star-forming environments, which only seem to exhibit fast declining objects. For the  $A_V$  distribution there is no evidence to suggest that the different galaxy types exhibit different distributions of extinction, and that the extinction seen in passive galaxies does not differ to that seen in star-forming galaxies, when using a  $A_V$  prior which only enforces the  $A_V$  value to be positive.

### 6.4.2 Using No $A_V$ Prior

We now move on to the case where no  $A_V$  prior is used. In this case, the fitted value of  $A_V$  in the MLCS light-curve fitter is allowed to take any value of  $A_V$  including negative values. The same criteria as that set out in §3 is used to define the sample, and the host's are identified and derived quantities are calculated using the method laid out in §3.2 and §4.3. The change in prior also affects the redshift of several of our objects which do not have a spectroscopic redshift.

By using such a criteria our data set increases in size from 246 host galaxies with the standard  $A_V$  prior to 252. This is slightly lower than the case for a flat  $A_V$  prior, possibly because several of the objects that passed the cut for a flat  $A_V$  prior now have  $\Delta$  values outside of the allowed range. The differences between the two samples is highlighted in §4.8.

Figure 6.11 shows the distribution of  $A_V$  for our three different galaxy types, as defined in §5.2. This plot is analogous to Figure 6.7 and Figure 6.9, except that no  $A_V$  prior is used. It shows how the  $A_V$  extinction parameter from MLCS is related to galaxy type for our three samples that have been split by specific star-formation rate.

Parameter	K-S test probability	A-D test probability
MLCS $\Delta$	$6.02 \times 10^{-5}$	$5.48 \times 10^{-5}$
MLCS $A_V$	0.0710	0.0222

Table 6.10: Table showing the K-S and A-D test statistics for the MLCS  $\Delta$  and  $A_V$  parameters when a Flat  $A_V$  prior is used in the light-curve fitting procedure.

Overplotted on Figure 6.11 are Gaussian fits to the distributions. The number of elements in each sample along with the fitted mean and width of the Gaussian function is shown in Table 6.11. It is clear that the extra hosts picked up by using this prior are evenly distributed amongst galaxy type, and thus no bias has been introduced by using a standard  $A_V$  prior as opposed to no prior at all.

For the  $A_V$  distributions, the fitted Gaussian's have higher mean values in all three cases and larger widths in both star-forming cases when compared to the standard  $A_V$  prior. This is because in the standard case the prior is in the form of an exponential decay, and when this is modelled as a Gaussian it underestimates the mean value. In the case where there is no  $A_V$  prior, the  $A_V$  distribution becomes two-sided and more Gaussian in nature.

As an extension to this Figure 6.12 shows the distribution of the MLCS  $\Delta$  parameter for these three datasets. This is analogous to Figure 6.1 and Figure 6.10. A similar procedure to that described above is used.

Table 6.12 shows the values of the fitted Gaussians for the delta distribution shown in figure 6.12. The mean value and width are shown along with the number of elements in each dataset. In this case the mean values and widths are similar to those in table 6.1. This again shows that the value of  $\Delta$  for each object is not particularly sensitive to the choice of the  $A_V$  parameter. The main difference between Table 6.12 and Table 6.1 is caused by the addition of new elements that have now passed the selection criteria, due to the less stringent  $A_V$  requirements.

To determine whether this change in  $A_V$  affects the statistical differences between the two datasets a K-S test and A-D test has been carried out on each dataset, in a similar fashion to that in §6.2 and §6.3.1. The two star-forming datasets have been combined and

Galaxy Type	Number of Elements	Gaussian Mean	Gaussian Width
Passive	50	0.249	0.334
Moderately Star-forming	109	0.207	0.224
Highly Star-forming	93	0.119	0.217

Table 6.11: Table showing the number of elements and mean and width of the fitted Gaussians for the MLCS  $A_V$  parameter when No  $A_V$  prior is used in the light-curve fitting procedure.

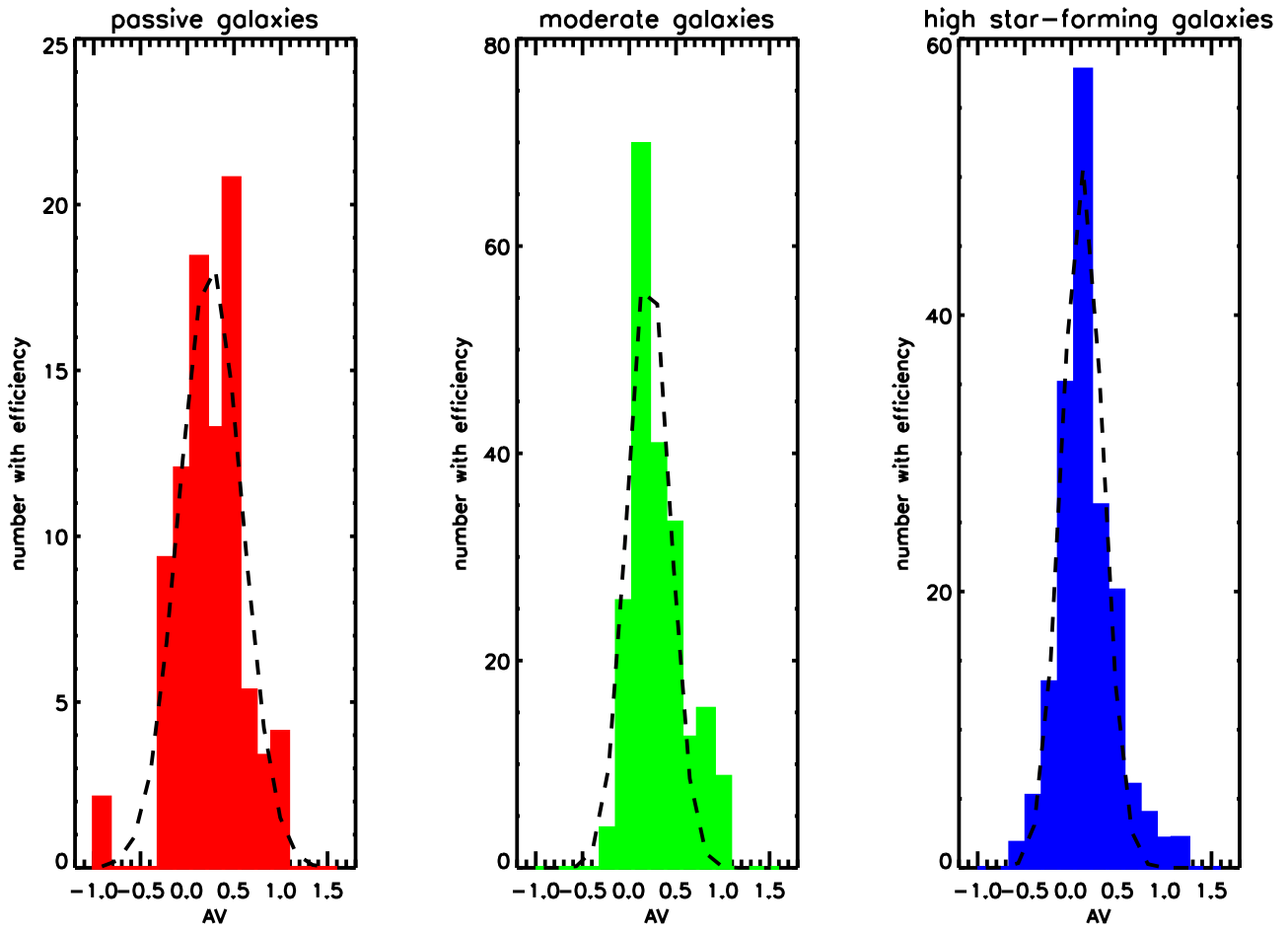


Figure 6.11: Showing the distribution of the MLCS2k2  $A_V$  parameter for the passive, moderately star-forming and highly star-forming galaxy populations when no  $A_V$  prior is used. Also overplotted is the best-fit Gaussian function for each sample.

Galaxy Type	Number of Elements	Gaussian Mean	Gaussian Width
Passive	50	-0.0020	0.414
Moderately Star-forming	109	-0.146	0.122
Highly Star-forming	93	-0.223	0.098

Table 6.12: Table showing the number of elements and mean and width of the fitted Gaussians for the MLCS  $\Delta$  parameter when No  $A_V$  prior is used in the light-curve fitting procedure.

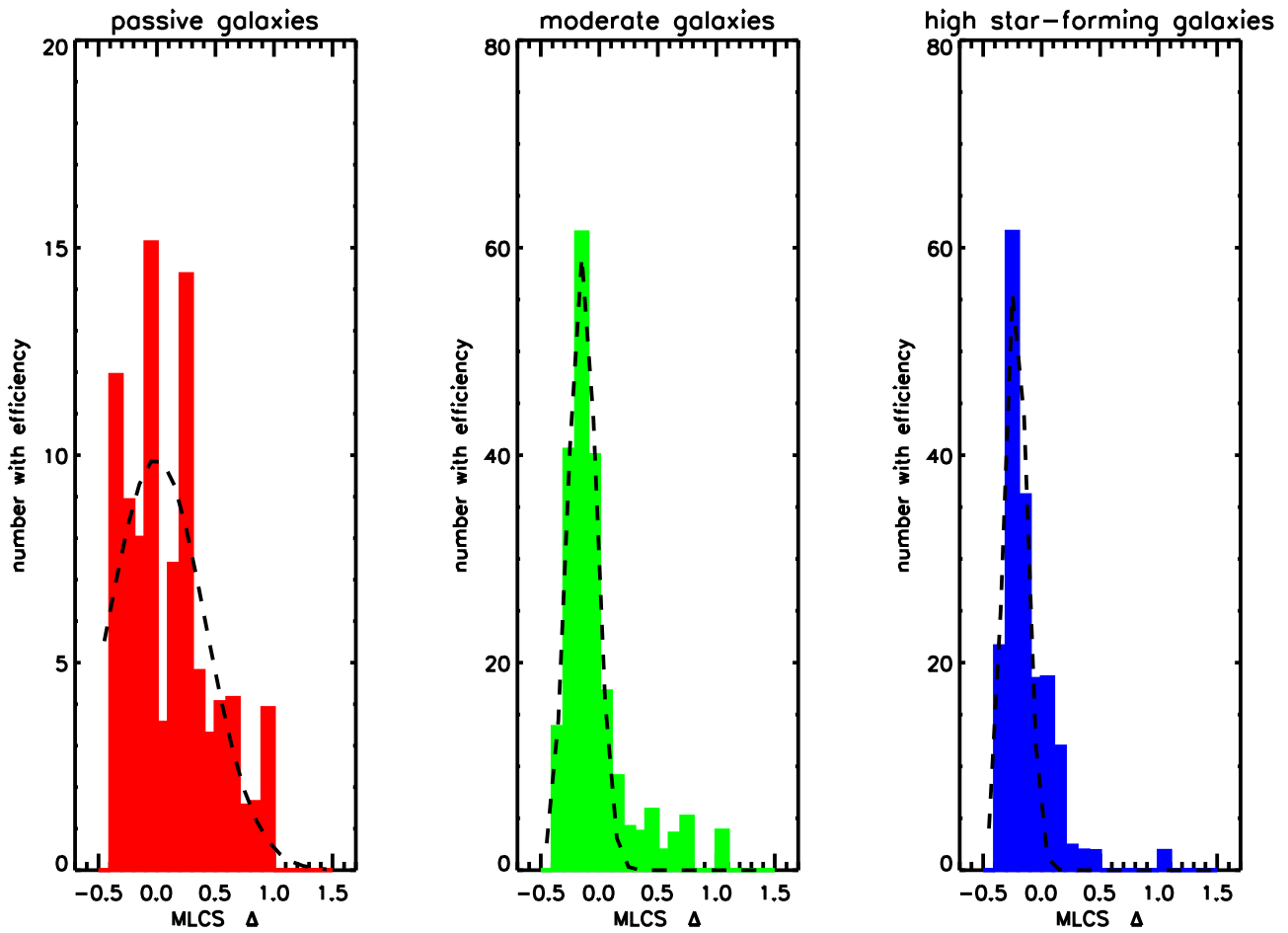


Figure 6.12: Showing the distribution of the MLCS2k2  $\Delta$  parameter for the passive, moderately star-forming and highly star-forming galaxy populations when no  $A_V$  prior is used. Also overplotted is the best-fit Gaussian function for each sample.

compared to the passive dataset. The probabilities that the two distributions are drawn from the same dataset are shown in Table 6.13. Both the results for the  $A_V$  and MLCS  $\Delta$  distributions are shown. These results are close to those in §6.2 and §6.3.1. These statistics show that in the case of no  $A_V$  prior, there is significant evidence to believe that the  $\Delta$  distributions of SNe that occur in passive galaxies is significantly different to that of similar events that occur in galaxies with recent star-formation activity. As shown in Figure 6.12, type Ia events that occur in passive galaxies are seen at more values of  $\Delta$  than those found in star-forming environments, which only seem to exhibit fast declining objects. For the  $A_V$  distribution there is no evidence to suggest that the different galaxy types exhibit different distributions of extinction, and that the extinction seen in passive galaxies does not differ to that seen in star-forming galaxies, when not using an  $A_V$  prior.

This analysis considers the case where no  $A_V$  prior is used. In many ways, this approach to the SALT2 light-curve fitter, since it uses no prior information on the dust content of the supernova explosion. However, the MLCS analysis still considers that each event must follow a well defined dust-law. We can compare the results shown above with those of the SALT2 light-curve fitter. Previously we have seen that there is no evidence that the distribution of the  $c$  parameter for the objects used in this analysis varies as a function of host galaxy type. This matches the result found above, with both approaches producing similar values for the K-S and A-D tests. However, when we compare the Gaussian distributions for the two methods, we see that the dust content inferred from the MLCS analysis is higher in all three cases than the colour levels found using the SALT2 light-curve fitter. Further to this, we also find that the distributions show larger scatter for the MLCS approach, implying that the distribution of  $c$  is less scattered than the distribution of  $A_V$ . This may be due to the value of  $R_V$  used in forming the MLCS dataset. Alternatively, since the SALT2  $c$  parameter is intended to model all colour variation, these differences may mean that either the dust content of the events used in this sample is not constant with time or that another unknown factor, not obeying the observed dust law is required in the MLCS analysis.

Parameter	K-S test probability	A-D test probability
MLCS $\Delta$	$7.73 \times 10^{-6}$	$7.31 \times 10^{-6}$
MLCS $A_V$	0.250	0.131

Table 6.13: Table showing the K-S and A-D test statistics for the MLCS  $\Delta$  and  $A_V$  parameters when No  $A_V$  prior is used in the light-curve fitting procedure.

### 6.4.3 Summary

We have shown that the results in §6.2 and §6.3.1 are not due to the choice of prior for the  $A_V$  distribution. It is clear that there is no evidence for the distribution of extinction to be different in different galaxy types, in particular in the case of passive and star-forming galaxies. Conversely, there is significant reason to believe that the MLCS  $\Delta$  distribution is different for SNe Ia's that occur in passive galaxies when compared to those that occur in star-forming environments. Independent of the choice of  $A_V$  prior, it is clear that SNe Ia events are more likely to be found in galaxies exhibiting signs of star-formation, although the level of star-formation in the host galaxy does not seem to be relevant. Further to this, we have shown that these Ia events that occur in star-forming galaxies are predominantly fast-decliners, whilst those in passive galaxies exhibit a large range, but are centered on slowly declining events.

## 6.5 The Effect of the cuts

In §6.2 and §6.3 we investigated how the properties of a type Ia supernova are related to the host galaxy in which it occurs. We found that, independent of light-curve fitter, type Ia supernovae that occur in passive galaxies show a greater range of luminosity / light curve decline rate parameter (such as the MLCS2k2  $\Delta$ , SALT2  $x_1$  or SALT2 stretch parameters) than that of star-forming galaxies. The SNe Ia's in star-forming galaxies are dominated by fast decliners whilst those in passive environments are generally slowly declining. Conversely our sample shows no difference in the extinction parameter dependent on galaxy type. All types of galaxy seem to exhibit the same distribution of  $A_V$  and colour independent of light-curve fitter. §6.4 confirmed that this result, and particularly the observation concerning extinction, is not due to the prior on  $A_V$  that was used in the MLCS2k2 light-curve fitting. This is true in both the case where a flat, but positive  $A_V$  prior is used and in the case with no  $A_V$  prior.

Here we look at the effect of correcting our sample for incompleteness. Our final sample of 246 objects contains events which have a supernova spectrum (and thus are spectroscopically confirmed), events with a measured spectroscopic redshift (from the host galaxy) and events which are purely photometrically measured. Each of these additions may introduce a bias into the sample, and thus this section will determine if the results are dependent on these non-spectroscopically confirmed events.

Table 6.14 shows the results of the Gaussian fitting for the various parameters discussed in this chapter when only objects with a spectroscopic redshift are considered. These are

objects with either a supernova spectrum or a host galaxy spectroscopic redshift. Table 6.16 shows the corresponding K-S and A-D statistics for these samples, following the method laid out in §6.2. The number of elements in each dataset is also shown.

Table 6.15 shows the results of the Gaussian fitting for the various parameters discussed in this chapter when only objects with a spectroscopic confirmation are considered. These are only objects with a supernova spectrum. Table 6.17 shows the corresponding K-S and A-D statistics for these samples, following the method laid out in §6.2. The number of elements in each dataset is also shown.

These tables show that the results found in 6.2 and 6.3 are unaffected when only a specific subset containing only objects with a spectroscopic redshift or those with a supernova spectrum are considered. With less objects in the analysis there is an increase in the diversity of the fitted Gaussian parameters, but in all cases the K-S test and A-D test statistics show the same results as in 6.2 and 6.3. In the case of the SALT2 color term  $c$  there is some evidence to suggest that the two distributions are drawn from different parent distributions. However, this difference is far less pronounced (or non-existent) than that of the peak-luminosity / light-curve decline rate parameter, so the primary difference between the type Ia supernovae seen in passive galaxies when compared to star-forming events, is the distribution in the maximum luminosity of the event.

## 6.6 Comparison with other results

In this chapter we have shown that the distribution of the light-curve decline rate parameter for type Ia supernovae differs for supernovae that occur in passive galaxies when compared to those found in star-forming galaxies. This has been shown independently of the light-curve fitting method, by considering both the MLCS2k2  $\Delta$  parameter and SALT2 parameter  $x_1$ . We have shown that fainter supernovae occur primarily in passive galaxies, whilst the brightest type Ia supernovae (with low  $\Delta$  values) occur in star-forming galaxies.

This has been observed for a set of low redshift supernovae when galaxy morphology is considered (Hamuy et al. (1995), Hamuy et al. (1996d), Hamuy et al. (2000) and Riess et al. (1999)) and by Sullivan et al. (2006b) at high redshift using the same method as described in this analysis.

The results from this analysis are directly comparable with those presented in Sullivan

Parameter	Passive		Moderately Star-forming		Highly Star-forming	
	Mean	Width	Mean	Width	Mean	Width
MLCS2k2 $\Delta$	0.101	0.410	-0.144	0.149	-0.204	0.090
SALT2 stretch	0.831	0.0594	0.960	0.0776	1.007	0.077
SALT2 $x_1$	-1.673	1.685	-0.0741	0.701	0.261	0.872
stretch (from MLCS)	0.871	0.136	1.006	0.0674	1.046	0.0702
$x_1$ (from MLCS)	-1.718	2.110	0.258	0.793	0.822	0.633
MLCS2k2 $A_v$	0.141	0.301	0.0711	0.253	-0.351	0.310
SALT2 colour	0.122	0.0911	0.0520	0.112	0.0368	0.087
Number of elements	35		86		67	

Table 6.14: Shows Gaussian outputs for various parameters when only objects with a spectroscopic redshift (supernova or host) are considered.

Parameter	Passive		Moderately Star-forming		Highly Star-forming	
	Mean	Width	Mean	Width	Mean	Width
MLCS2k2 $\Delta$	0.158	0.3112	-0.130	0.191	-0.237	0.211
SALT2 stretch	0.845	0.1000	0.966	0.0726	1.004	0.073
SALT2 $x_1$	-1.615	1.1350	-0.0124	0.791	0.315	0.876
stretch (from MLCS)	0.840	0.123	1.0176	0.0727	1.062	0.058
$x_1$ (from MLCS)	-1.284	1.353	0.3814	0.975	0.795	0.668
MLCS2k2 $A_v$	-0.8207	0.637	-0.138	0.3338	-0.468	0.302
SALT2 colour	0.1528	0.126	0.0800	0.109	0.0462	0.0970
Number of elements	15		55		51	

Table 6.15: Shows Gaussian outputs for various parameters when only objects that have been spectroscopically confirmed to be SNe Ia events are considered.

Parameter	K-S test probability	A-D test probability
MLCS2k2 $\Delta$	$9.05 \times 10^{-6}$	$2.40 \times 10^{-6}$
SALT2 stretch	$5.42 \times 10^{-7}$	$2.29 \times 10^{-6}$
MLCS2k2 $A_v$	0.0296	0.0453
SALT2 color	0.0101	0.0031

Table 6.16: Shows the K-S and A-D test statistics for various parameters when only objects with a spectroscopic redshift (supernova or host) are considered

et al. (2006b) , who use the same template fitting method to obtain the derived properties of each host galaxy. This study used the SiFTO (Conley et al. (2008)) light-curve fitting method and hence found that the distribution of stretch values differ for type Ia supernovae found in differing galaxies. This results found in the Sullivan et al. (2006b) analysis are shown in Figure’s 6.13 for a set of low redshift supernovae from the literature, and 6.14 for supernovae from the first two years of the SNLS survey in the redshift range  $0.3 < z < 0.7$ . These figures are directly comparable to the results from this analysis, and in particular to Figure’s 6.3 and 6.6 and the best-fit Gaussian functions found in Tables 6.3 and 6.5.

Our analysis showed considerable evidence that the population of type Ia supernovae as characterised by their stretch parameter found in passive galaxies differs from that of star-forming events, and matches that seen at both low and high redshift. The best-fit mean Gaussian values for the stretch parameter for our sample of objects matches those found in Sullivan et al. (2006b) for all galaxy types, thus indicating that the population of type Ia events seen at high redshift have not evolved to different stretch values at low redshift.

## 6.7 Conclusions

In this chapter we have shown that the observed properties of the light-curves of type Ia events differ based on the galaxy in which they explode. We have shown conclusively that the peak-luminosity / decline rate parameter differs for supernova that occur in passive galaxies than star-forming galaxies, with the brightest type Ia events seen in star-forming galaxies, whilst passive galaxies contribute the faintest events. This has been seen when both the MLCS2k2 and SALT2 / SALT light-curve fitters are used, and when the  $A_V$  prior used to describe the sample (§3.2.3) is changed so that no prior information is considered. These results match previous analyses seen at low and high redshift, including those of Riess et al. (1999), whose analysis techniques match ours.

Parameter	K-S test probability	A-D test probability
MLCS2k2 $\Delta$	$2.42 \times 10^{-5}$	$1.32 \times 10^{-6}$
SALT2 stretch	$4.73 \times 10^{-5}$	$7.77 \times 10^{-6}$
MLCS2k2 $A_V$	0.289	0.0921
SALT2 color	0.0197	0.0084

Table 6.17: Shows the K-S and A-D test statistics for various parameters when only objects that have been spectroscopically confirmed to be SNe Ia events are considered

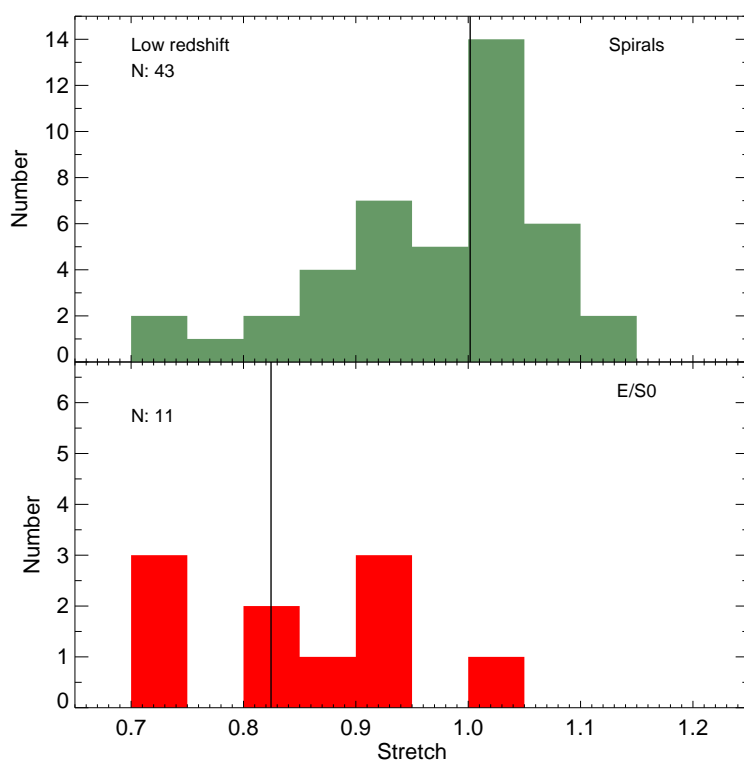


Figure 6.13: This is figure 11b is re-printed from [Sullivan et al. \(2006b\)](#). It shows the "stretch" distribution for a set of low redshift SN Ia.

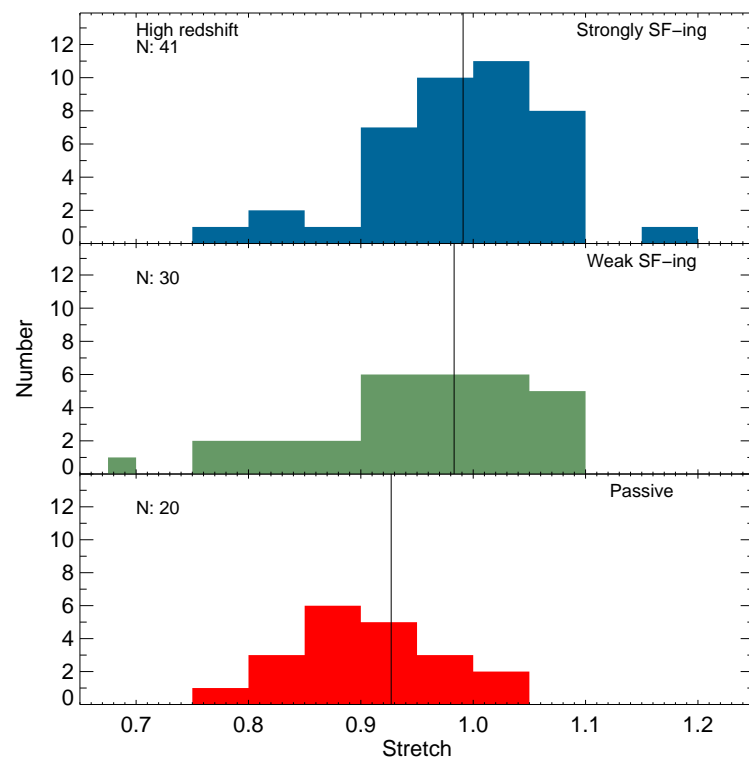


Figure 6.14: This is figure 11b is re-printed from [Sullivan et al. \(2006b\)](#). It shows the "stretch" distribution for objects in the SNLS complete SN Ia sample.

Any bias in this sample due to selection effects are not expected to affect the overall distribution of type Ia events, since the primary supernovae that are missing from our analysis would need to be the brightest events; supernovae that would conversely be more likely to be spectroscopically observed.

Further to this, we have investigated the estimated extinction in each of these type Ia supernovae. We have found that the distribution of extinction in type Ia supernovae is not affected by the host galaxy in which it occurs. Since the levels of dust in late-type galaxies is seen to differ from that found in early-type galaxies (Salim et al. (2005)) this indicates that the primary source of the extinction parameter as defined by the MLCS2k2 light-curve fitter is not due to the host galaxy, but instead due to the intrinsic variation of the type Ia supernova event. This result has been verified by considering a range of prior information on the  $A_V$  parameter and by looking at the SALT2 colour term  $c$ . This colour term shows some variety between passive and star-forming galaxies. However, any variation in this parameter is subdominant to that seen in the light-curve decline rate parameter.

# Chapter 7

## Effect of Host Galaxy Properties on the Hubble Diagram

*This work is carried out in collaboration with Hubert Lampeitl.*

*Note that in this section we shall refer to the Hubble constant,  $H_0$ . In all cases this is not the absolute value of the  $H_0$ , and thus cannot be compared to values found, for instance by the HST ([Freedman et al. \(2001\)](#)), since the absolute value of the Hubble constant is degenerate with the absolute magnitude of type Ia supernovae, and is highly uncertain. A value of  $H_0 = 62 \text{ km s}^{-1} \text{ Mpc}^{-1}$  is used in the light-curve fitting method to normalise the Hubble diagram. Thus, all measurements should only be considered relative to each other.*

### 7.1 Introduction

In §5 and §6 we investigated how the type Ia population is distributed with respect to their rates and properties. This analysis indicates that the type Ia population is not homogeneous, and shows diversity as a function of its environment, with type Ia events being more prevalent in star-forming galaxies than galaxies with no evidence of recent star-formation events. Further to this, there is strong evidence to suggest that the distribution of the peak-magnitude / light-curve decline rate parameter,  $\Delta$  (also possibly  $x_1$  and  $s$ ) is related to the host galaxy properties of the type Ia supernova event; with type Ia supernovae that occur in star-forming galaxies having higher intrinsic absolute magnitudes, than those seen in passive galaxies. Thus, there seems to be at least two populations of type Ia events. This “two-population” scenario indicates that it may be possible to improve the constraints on cosmological parameters by focusing the analysis of hubble diagrams on particular galaxies, and possibly that observing Ia events in different host galaxy types may lead

to differing preferred cosmologies. Work by [Greggio & Renzini \(1983\)](#) on two possible channels for type Ia supernovae suggest that different explosion mechanisms would be host galaxy dependent, and would produce events of different absolute luminosity, thus implying that without taking this in to account, type Ia supernovae measured in different environments would produce different best-fitting cosmologies, in particular with respect to the normalisation of the Hubble diagram, or the parameter,  $H_0$ . In previous chapters we saw that the observed properties (both in rate and light-curve) of type Ia supernovae are host galaxy dependent, possibly indicating different explosion mechanisms.

[Sullivan et al. \(2003\)](#) investigated the host galaxies of 25 low redshift supernovae observed by [Riess et al. \(1999\)](#) and [Hamuy et al. \(1996a\)](#), and set of 39 high redshift events from the SCP ([Perlmutter et al. \(1999\)](#)) using HST imaging and KECK spectroscopy to classify the type Ia host galaxies and discovered that the scatter on the Hubble diagram, relative to the best-fitting cosmological model, correlates with host galaxy type, such that early-type galaxies are minimally scattered when compared to late time events.

In §3 and §4 we selected a sample of type Ia events that are free of bias due to spectroscopic incompleteness from the first two years of the SDSS-II supernova survey, and described the method used for determining the host galaxy and its derived properties for each event. We were then able to split this sample into three distinct groups, based on the ongoing level of star-formation activity in each host. Using a sample similar to this, we will be able to determine if the result from [Sullivan et al. \(2003\)](#) is consistent with observations from the SDSS-II supernova survey.

## 7.2 Sample Section

In §3.2.5 we described a sample of 246 events that comprise a complete sample of type Ia events from the first two years of the SDSS-II supernova survey, when spectroscopic incompleteness is taken into account. However, this sample was created using the MLCS2k2 light-curve fitter, with a photometric fit that uses an assumed cosmological model and therefore cannot be used to derive cosmological parameters.

Thus to create a sample that can be used to look at the Hubble diagram, we use the same constraints as described in §3.2.2 to produce a sample of 1175 possible type Ia events, and the light-curve coverage requirements described in §3.2.4, with the exception that in this case, every object is analysed by the MLCS2k2 light-curve fitter using a cosmological fit. That is the best estimate of the redshift of each event is used and

the distance modulus is returned as a fit parameter. In §3.2.5 all objects were considered, irrespective of the redshift information available. In this case, the same approach is possible, however, for objects which do not have a spectroscopic redshift (either from the supernova event itself, or measured from the host galaxy) the input redshift used by the MLCS2k2 light-curve fitter is a photometric redshift of the host galaxy as derived by Oyaizu et al. (2008). These redshift estimates are determined using a Neural Network technique, and a Nearest Neighbor Error estimator is used to calculate the associated errors. The resulting redshifts are accurate to  $\Delta z \sim 0.05$ , with considerable scatter for low signal-to-noise galaxies. With the host galaxy identification for each object being determined using a simple targeting algorithm, and the best-fit distance modulus obtained from the MLCS2k2 light-curve fitter being partially dependent on the redshift estimate, objects without a spectroscopic redshift are excluded from this analysis. However, since objects with a spectroscopic host galaxy redshift are included in our final sample, the effect of incompleteness on our results is considered to be small. Thus, using the method described in §3, a sample of objects that is primarily complete from the first two years of the SDSS-II supernova survey has been created.

Having determined the objects in this sample, we follow the method described in §4 to determine the derived properties of the host galaxies of objects in this sample. In §4.4, we showed that the assumed cosmological model used to determine the masses and star-formation rates of the host galaxies does not significantly affect the distribution of properties. Using the criteria from §5.2, we are able to split the population of type Ia supernovae into three distinct groups based upon their ongoing star-formation activity.

In §3, a maximum redshift of  $0.05 < z < 0.25$  is enforced since the SDSS-II supernova survey is primarily complete and the aim was to probe the type Ia supernova population. However, the purpose of this investigation is to determine if there exists biases in Hubble diagram analyses, and whether the host galaxies of type Ia supernovae can be used to minimise the scatter on future cosmological results by focusing on supernovae that occur in specific galaxies. Thus for this analysis, we shall consider every object in the SDSS-II supernova survey, and extend our redshift range to  $z \simeq 0.4$ . This increase may lead to the introduction of non-type Ia events from objects that have not been spectroscopically observed. However, in §7.3, §7.4 and §7.5 we shall show that our results are unaffected by this increase in redshift cut-off, and the inclusion of non-confirmed events. Using this criteria, we form a sample of 303 objects with a spectroscopic redshift in the range  $0 < z < 0.5$ , of which 194 have been spectroscopically confirmed as type Ia events, and 188 are found in the redshift range  $0 < z < 0.25$ .

Table 7.1 shows how the objects in this sample are distributed amongst the different galaxy types. This also shows the number of objects that have been spectroscopically confirmed, and as the characteristics of the sample in the low redshift range  $0 < z < 0.25$ .

Lampeitl et al. (2009) has shown that the first year data from the SDSS-II supernova survey is able to show that the expansion rate of the Universe is accelerating, independent of information from very low redshift and high redshift samples, with a  $2\sigma$  significance. However, this sample alone is not able to accurately determine the value of the equation of state of Dark Energy ( $\omega$ ), and thus the analysis of this chapter shall focus on the differences in the residuals from a default cosmology of  $\Omega_M = 0.27, \Omega_\Lambda = 0.73$  as a function of host galaxy type. The effect of selecting a value of  $\omega \neq -1$  is expected to be insignificant, since any cosmological model with  $\omega \simeq -1$  is virtually indistinguishable from  $\Lambda$ CDM in this redshift range. The value for the Hubble constant is allowed to vary in the fitting process since it simply acts as a normalisation in the determination of the best-fit cosmology. In this determination of the best-fit value for the Hubble constant an additional dispersion of 0.077 magnitudes has been added to each event. This matches the required value discovered in Kessler et al. (2009) and Lampeitl et al. (2009) in order to produce a reasonable  $\chi^2$  statistic ( $\chi^2/\text{d.o.f.} \simeq 1$ ). This additional dispersion does not affect the residuals from the best-fitting cosmology, since only the best-fitting distance modulus value is considered for each event, and not the error values for this measurement.

Thus we have described a sample of type Ia events that covers the redshift range  $0 < z < 0.5$ . These objects have been split according to their galaxy type. A best-fit cosmology has been calculated for the complete sample. In the following sections we shall discuss these cosmological results.

### 7.3 Hubble Diagram for Confirmed Events

In this section we shall only focus on objects that have been spectroscopically confirmed as type Ia events. This sample is free of contamination from other supernova-like events, but may be biased due to spectroscopic resource priorities and allocation.

Figure 7.1 shows a Hubble diagram for these events as a function of host galaxy type and the residuals from the best-fitting cosmological models, which have a value of  $H_0 = 60.80 \text{ km s}^{-1} \text{ Mpc}^{-1}$ . (Note that, following the warning at the beginning of this chapter, this measurement can only be compared to subsamples of this dataset, since it is only

a relative measurement, degenerate with the absolute magnitude of type Ia supernovae). Following the example of §5 and §6 the objects that have been classified as passive galaxies are shown in red, with moderately star-forming objects shown in green and highly star-forming events plotted in blue. Following the information of Table 7.1, the sample is dominated by objects with recent levels of star-formation, especially at high redshift, thus confirming the result from §6 that objects seen in these environments are intrinsically brighter than those in passive galaxies.

The analysis of this chapter is primarily concerned with the residuals from this best-fitting cosmology. This is shown as a function of host galaxy type in Figure 7.2. Here histograms of the individual residual plots for each of the galaxy types are shown along with the best-fitting Gaussian functions for each. Following the method described in §6 a Gaussian distribution has been plotted to each of these histograms. The best-fitting Gaussian distribution is overplotted on each individual figure.

From Figure 7.2 it is clear that the distribution of residuals from the best-fitting Hubble diagram is different for each galaxy type, with passive galaxies being primarily considered to be closer to the observer than the best fit cosmology (i.e.  $\mu_{\text{supernova}} < \mu_{\Lambda\text{CDM}}$ ) and the opposite effect seen for star-forming objects. This can be alternatively interpreted as the supernovae in passive galaxies being considered brighter than their counterparts in star-forming environments.

The best-fitting Gaussian parameters for the fits shown in Figure 7.2 are given in Table 7.2. The results when a redshift cut-off of  $z < 0.25$  is enforced is also given. From these results it is clear that the passive galaxies are seen to have less scatter than those of star-forming objects, apparently confirming the observations of Sullivan et al. (2003) for a morphologically classified sample. However, it also appears that the best fitting cosmology, or at least the best fitting value of  $H_0$  for passive galaxies is different than for star-forming events.

To determine the statistical significance of this result, a K-S (§6.2.1) and A-D tests (§6.2.1) were carried out on these samples. These two tests determine the significance that two distributions are drawn from different parent distributions. Thus to do this, the distribution of the passive galaxies was compared to that of the star-forming events (moderately star-forming and highly star-forming combined) and that of the highly star-forming sample when considered separately. The resultant statistics are shown in Table 7.3. This was done for both the complete sample and the sample with a redshift cut-off of  $z, 0.25$ .

Cuts / Selection Criteria	# Passive <sup>a</sup>	# moderates <sup>b</sup>	# highly star-forming <sup>c</sup>
No redshift cut <sup>d</sup>	71	120	112
Of which confirmed <sup>e</sup>	31	79	84
$0 < z < 0.25$ <sup>f</sup>	36	86	66
Of which confirmed <sup>g</sup>	18	60	52

<sup>a</sup>From §5.2, these are objects with no ongoing star-formation activity

<sup>b</sup>These, moderately star-forming objects are defined to have  $-12.5 < sSFR < -9.5$

<sup>c</sup>These objects have  $sSFR > -9.5$

<sup>d</sup>The complete sample

<sup>e</sup>These objects are spectroscopically confirmed as type Ia events. The remaining objects possess a spectroscopic redshift

<sup>f</sup>Objects with either a spectroscopic confirmation of host galaxy redshift lying in the low redshift sample

<sup>g</sup>Spectroscopically confirmed objects in the low redshift sample

Table 7.1: Shows the distribution of objects that pass our cosmological fit, and selection criteria described §3.2.4 and §3.2.2, as a function of host galaxy type for both the low and high redshift samples. The number of objects in each set that have been spectroscopically confirmed is also shown.

	# Passive	# moderates	# highly star-forming
	Complete Sample <sup>a</sup>		
Number of Objects	31	79	84
Gaussian Central Value	$-0.115 \pm 0.012$	$-0.024 \pm 0.010$	$0.030 \pm 0.011$
Gaussian Width	0.101	0.169	0.131
	$0 < z < 0.25$		
Number of Objects	18	60	52
Gaussian Central Value	$-0.143 \pm 0.008$	$-0.035 \pm 0.019$	$0.037 \pm 0.007$
Gaussian Width	0.085	0.157	0.130

<sup>a</sup> $0 < z < 0.5$

Table 7.2: Shows the Gaussian fitting parameters for the three distributions shown in Figure 7.2. The values for Gaussian mean and width for the complete dataset ( $0 < z < 0.5$ ), and that of a low redshift cut-off, ( $0 < z < 0.25$ ) are given.

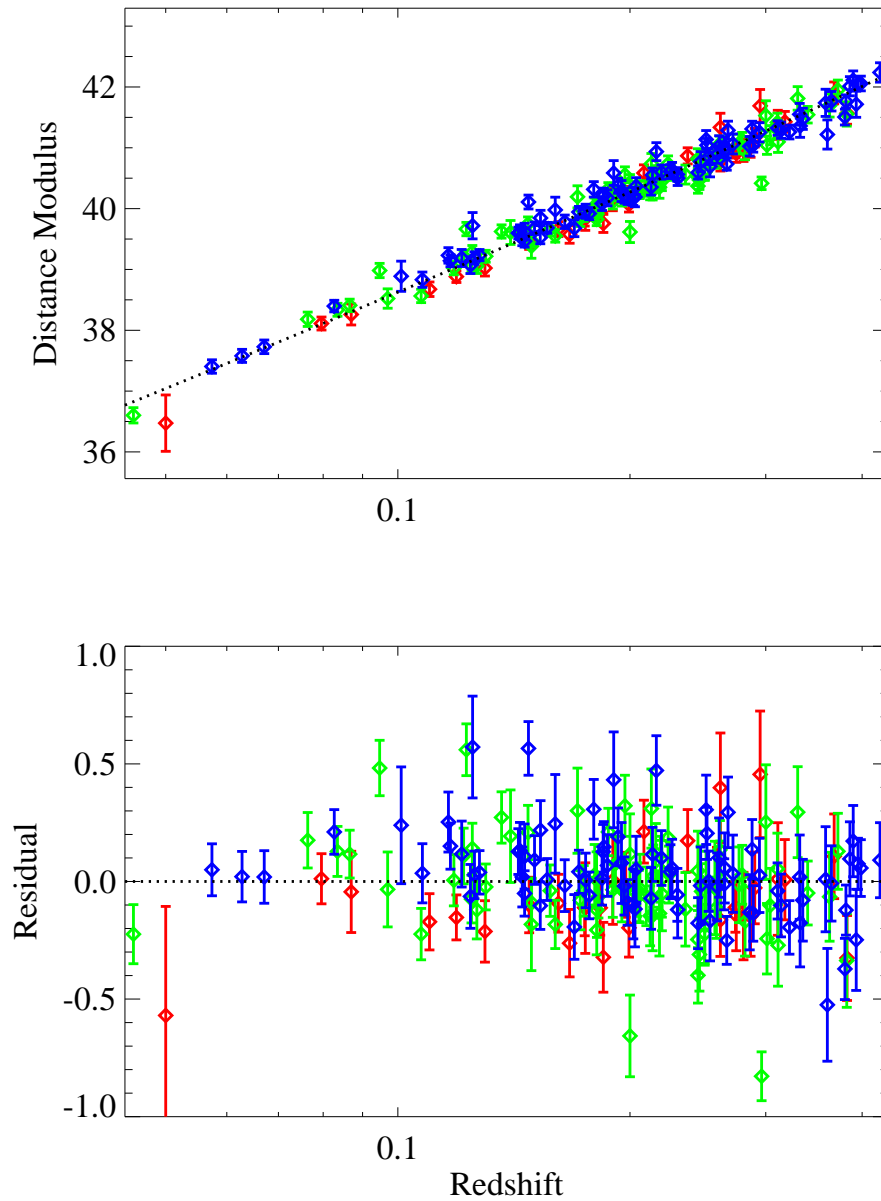


Figure 7.1: The top panel shows the Hubble diagram for the spectroscopically confirmed objects defined by using a cosmological fit, and the selection criteria described in §3.2.4 and §3.2.2, as a function of host galaxy type. The bottom panel shows the residuals from this fit. Passively evolving objects are plotted in red, whilst moderately star-forming and highly star-forming objects are shown in green and blue respectively. The dotted line is the best-fitting cosmology was a value of  $H_0 = 60.8 \text{ km s}^{-1} \text{ Mpc}^{-1}$ .

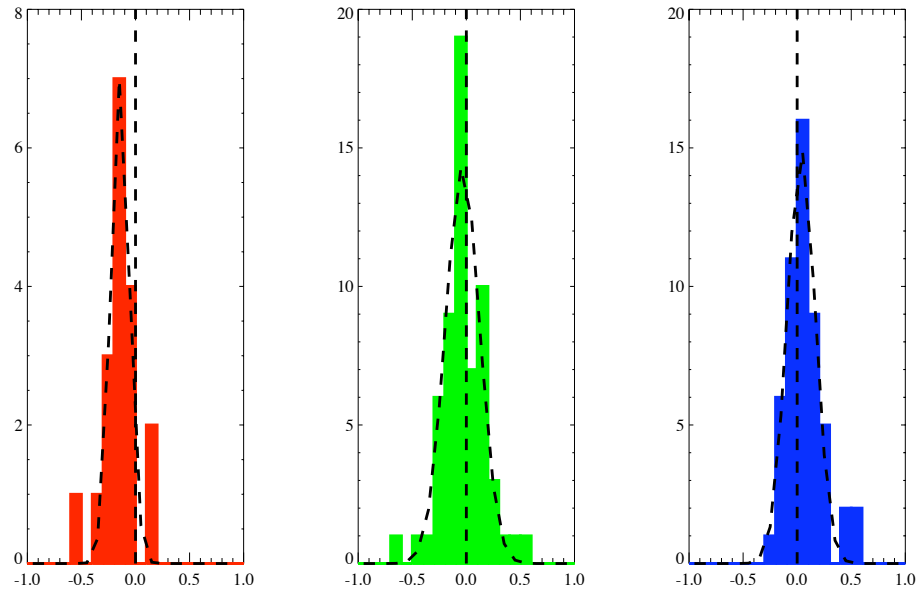


Figure 7.2: This shows the residuals from the best-fit cosmology shown in Figure 7.1 as a function of host galaxy type. The three distributions are shown separately with the best-fitting Gaussian distribution overplotted on each one. Also shown is a line indicating no residual from the fit as a guide.

	K-S statistic	A-D statistic
	Complete Sample <sup>a</sup>	
Passive vs. Star-forming	$5.16 \times 10^{-3}$	$6.27 \times 10^{-3}$
Passive vs. Highly Star-forming	$0.38 \times 10^{-3}$	$0.43 \times 10^{-3}$
	$0 < z < 0.25$	
Passive vs. Star-forming	$1.64 \times 10^{-3}$	$1.14 \times 10^{-3}$
Passive vs. Highly Star-forming	$2.12 \times 10^{-4}$	$1.63 \times 10^{-5}$

<sup>a</sup> $0 < z < 0.5$

Table 7.3: K-S and A-D test statistics for the residuals from the best-fit cosmology to the Hubble diagram (shown in Figure 7.2) for passive galaxies when compared to objects with ongoing star-formation activity and highly star-forming objects respectively. The values are given for both the complete dataset ( $0 < z < 0.5$ ) and a low redshift sample ( $0 < z < 0.25$ ). This is for a sample of type Ia's that have been spectroscopically confirmed.

The values given in Tables 7.2 and 7.3 indicate that the distribution of passive and star-forming objects are drawn from a different distribution, especially at low redshift ( $0.05 < z < 0.25$ ). Specifically, passive galaxies appear to show less scatter on the Hubble diagram and be systematically biased towards smaller values of the Hubble constant. However, it is not clear if this is due to observational biases in the dataset.

## 7.4 Hubble Diagram for Events with a Spectroscopic Redshift

In the previous section, we indicate that the residuals from the best-fit cosmology to the Hubble diagram for type Ia supernovae are different for different host galaxy types. However, the sample considered in that section were only spectroscopically confirmed events, and as shown in §3 there may exist biases in this sample. Here, we extend these results to include objects that have not been spectroscopically confirmed, but as discussed in §7.2 have spectroscopic host redshifts and light-curves that closely follow the peak luminosity / light-curve decline rate relationship that indicate that they are likely type Ia events.

Figure 7.3 shows the Hubble diagram for these events. The best fitting cosmology for these objects has a value of  $H_0 = 61.2 \text{ km s}^{-1} \text{ Mpc}^{-1}$ , which is not statistically different to the objects in §7.3. Similarly to that of Figure 7.1, the passive galaxies (plotted in red) are seen at lower redshifts than star-forming events (shown in green and blue).

Figure 7.4 shows the residuals from Figure 7.3 as a function of host galaxy type. This figure is analogous to Figure 7.2 for the spectroscopically confirmed events, with the best-fitting Gaussian functions plotted on each figure.

Similarly to the result from §7.3, with Figures 7.1 and 7.4, the distributions are clearly dependent on host galaxy type. This is shown in Tables 7.4 and 7.5 which show the central values and widths of the Gaussian functions plotted in Figure 7.4, and the values of the K-S and A-D statistics quantifying the probability that the distribution for passive galaxies is drawn from the same dataset as that of the star-forming objects (when both are combined, or only the highly star-forming objects are considered). These tables show the results when the entire sample is considered and when only a low redshift component of it ( $0 < z < 0.25$ ) is used.

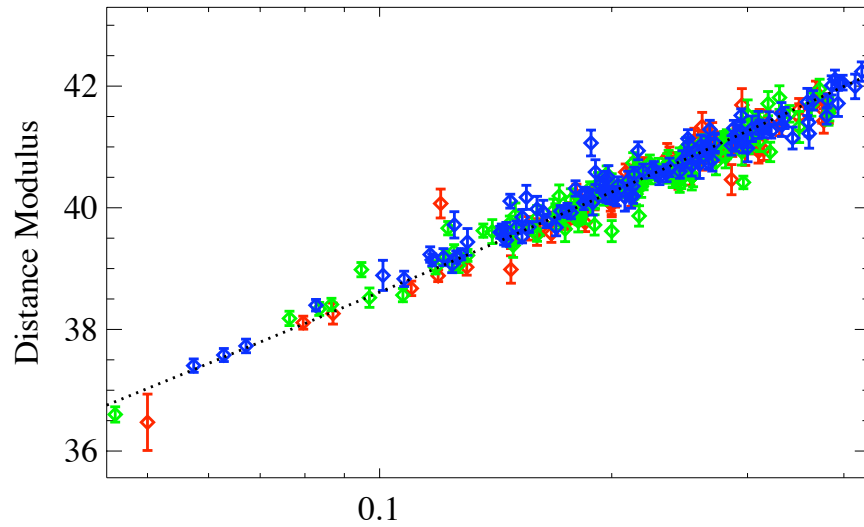


Figure 7.3: The Hubble diagram for objects with a spectroscopic redshift (of any type) that have been fit with a cosmological fit, and satisfy the selection criteria described in §3.2.4 and §3.2.2 as a function of host galaxy type. Passively evolving objects are plotted in red, whilst moderately star-forming and highly star-forming objects are shown in green and blue respectively. The best-fitting cosmology has  $H_0 = 61.2 \text{ km s}^{-1} \text{ Mpc}^{-1}$ .

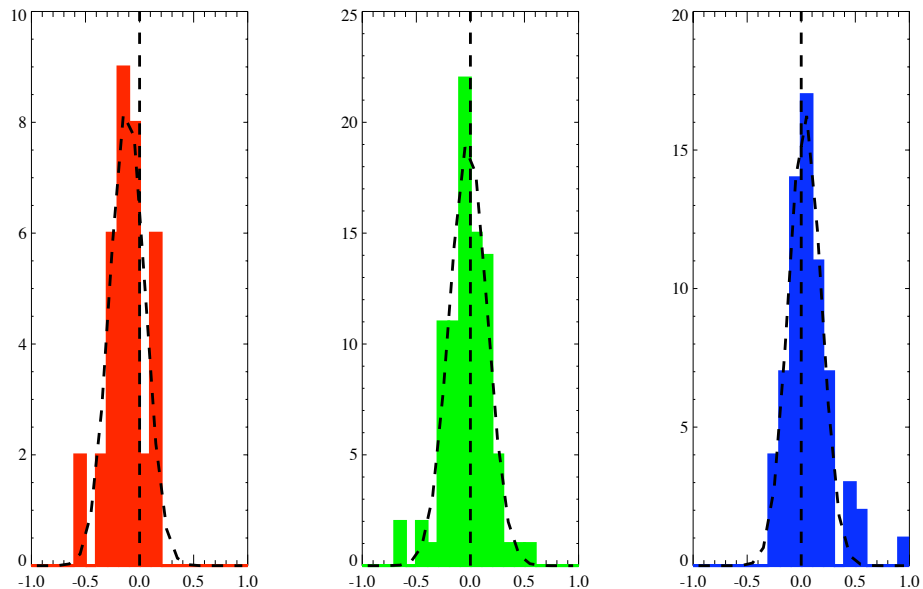


Figure 7.4: Shows the residuals from the Hubble diagram shown in Figure 7.3 as a function of host galaxy type. The three distributions are shown separately with the best-fitting Gaussian distribution overplotted.

	# Passive	# moderates	# highly star-forming
	Complete Sample <sup>a</sup>		
Number of Objects	71	120	112
Gaussian Central Value	$-0.075 \pm 0.012$	$-0.020 \pm 0.009$	$0.027 \pm 0.009$
Gaussian Width	0.166	0.195	0.154
	$0 < z < 0.25$		
Number of Objects	36	86	66
Gaussian Central Value	$-0.113 \pm 0.021$	$-0.019 \pm 0.013$	$0.033 \pm 0.009$
Gaussian Width	0.161	0.173	0.151

<sup>a</sup> $0 < z < 0.5$

Table 7.4: This shows the Gaussian fitting parameters for the three distributions shown in Figure 7.2. The values for Gaussian mean and width for the complete dataset ( $0 < z < 0.5$ ) and a low redshift sample, ( $0 < z < 0.25$ ) are given.

	K-S statistic	A-D statistic
	Complete Sample <sup>a</sup>	
Passive vs Star-forming	$9.96 \times 10^{-4}$	$12.81 \times 10^{-4}$
Passive vs Highly Star-forming	$1.81 \times 10^{-4}$	$0.64 \times 10^{-4}$
	$0 < z < 0.25$	
Passive vs Star-forming	$6.55 \times 10^{-3}$	$3.33 \times 10^{-3}$
Passive vs Highly Star-forming	$7.70 \times 10^{-4}$	$5.92 \times 10^{-5}$

<sup>a</sup> $0 < z < 0.5$

Table 7.5: K-S and A-D test statistics for the residuals from the best-fit to the Hubble diagram (shown in Figure 7.2) for passive galaxies when compared to objects with ongoing star-formation activity and highly star-forming objects respectively. The values are given for both the complete dataset ( $0 < z < 0.5$ ) and a low redshift sample ( $0 < z < 0.25$ ). This is for a sample of objects with a spectroscopic redshift.

These results show us that the best-fitting cosmologies for type Ia supernovae are statistically significantly different from the cosmology (or at least the value of  $H_0$ ) that will be obtained if the set of objects that are seen in spiral galaxies are fit separately. This is in agreement with the result found in §7.3, and is independent of the redshift limit considered. However, the scatter on the diagram is not different for passive galaxies when compared to star-forming objects. This is different from the result found in §7.3 and Sullivan et al. (2003). This may be explained by the possible introduction of contamination into the sample, or conversely, since this sample is significantly less affected by biases due to spectroscopic targeting selection effects, objects with a larger scatter are introduced into the sample. These may have been biased against, since target selection for type Ia supernovae commonly biased against passive galaxies, and in particular events that are found in the cores of these galaxies.

However, another possible explanation involves the implied dust content of these objects which we briefly explore below.

## 7.5 Altering the $A_V$ Distribution for Passive Galaxies

In §3.2.3, we introduced the light-curve fitting method used for this analysis. As part of this we described the prior information that was assumed in the light-curve fitting process. A key part of this fitting was the  $A_V$  prior distribution, which was assumed to have the form,

$$P(A_V) = \exp(-A_V/\tau_V), \quad (7.1)$$

where  $\tau_V = 0.35$ . This was chosen to match the observed distribution of  $A_V$  in the first year cosmological results from the SDSS-II supernova survey. However, this distribution does not consider the host galaxy type of each event. It has long been observed that early-type galaxies contain less dust content (Zhang et al. (2008), Salim et al. (2005)), especially when compared to star-forming galaxies. If this assumption is true, then the distribution of  $A_V$  in these galaxies will not be well described by the relationship described in Equation 7.1. By requiring supernova events in all galaxies to follow the same relationship we could be biasing the  $A_V$ 's for passive galaxies which are subdominant.

To determine if this is the case, the sample of 1175 objects described in §3 were fit by the MLCS2k2 light-curve fitter with an  $A_V$  prior of the same form as that of Equation 7.1, but this time with a value of  $\tau_V = 0.05$ . This value of the exponential decay is steeper than the standard  $A_V$  prior, thus encouraging these objects to be fit with values of  $A_V$  far closer to zero. Having done this, the host galaxy of each supernova was determined,

following the methods in §4. For passive galaxies, the value of the distance modulus derived from this new  $A_V$  distribution, whilst for star-forming galaxies, the value of  $\mu$  was considered to be the value determined from the standard  $A_V$  prior. This combined sample should better represent the distribution of  $A_V$  for each object, and thus the derived distance moduli should be more accurate. With these new constraints on  $A_V$  for passive galaxies, the number of supernova passing the criteria described in §3.2.2, specifically the requirement that MLCS2k2 light-curve fit probability  $> 0.01$ , has been altered, although not significantly; 68 objects passing the criteria when all objects with a spectroscopic redshift are considered (from 71).

Figure 7.5 shows the Hubble diagram from the events described above. This figure considers both objects that have been spectroscopically confirmed, and those with just a spectroscopic host galaxy redshift. Also shown on this figure are the residuals from the best-fitting cosmology, with a value of  $H_0 = 61.00 \text{ km s}^{-1} \text{ Mpc}^{-1}$  (not statistically different from the results of §7.3 and §7.4). Figure 7.6 shows a histogram of these residuals for each of the three galaxy types (as defined in §5.2), with the best fitting Gaussian function overplotted.

In this example the differences between the three distributions shown in Figure 7.6 appear to be reduced from that of Figures 7.2 and 7.4. To quantify this, the Gaussian fits are given in Table 7.6. The results for both the complete sample, and that with a maximum redshift of  $z = 0.25$ , are given along with the cases where only objects with a confirmed supernova spectra are considered.

As an extension of this, Table 7.7 shows the K-S and A-D test statistics for the cases described in Table 7.6, where either the two star-forming sample have been combined and compared to the distribution of passive galaxies, or the passive distribution has been simply compared to the highly star-forming dataset. Primarily these values provide no indication that the distribution of passive galaxies differs to that of objects with ongoing star-formation activity. However, especially at low redshift, there is an indication that whilst the differences between the distributions are smaller than those seen when the same  $A_V$  prior was used for all objects, there is still diversity between the two samples. From Table 7.6, there is still evidence at low redshift, that the scatter on the Hubble diagram may be smaller for supernovae that occur in passive environments. However, the evidence for this is less when the sample is extended to include objects at high redshift.

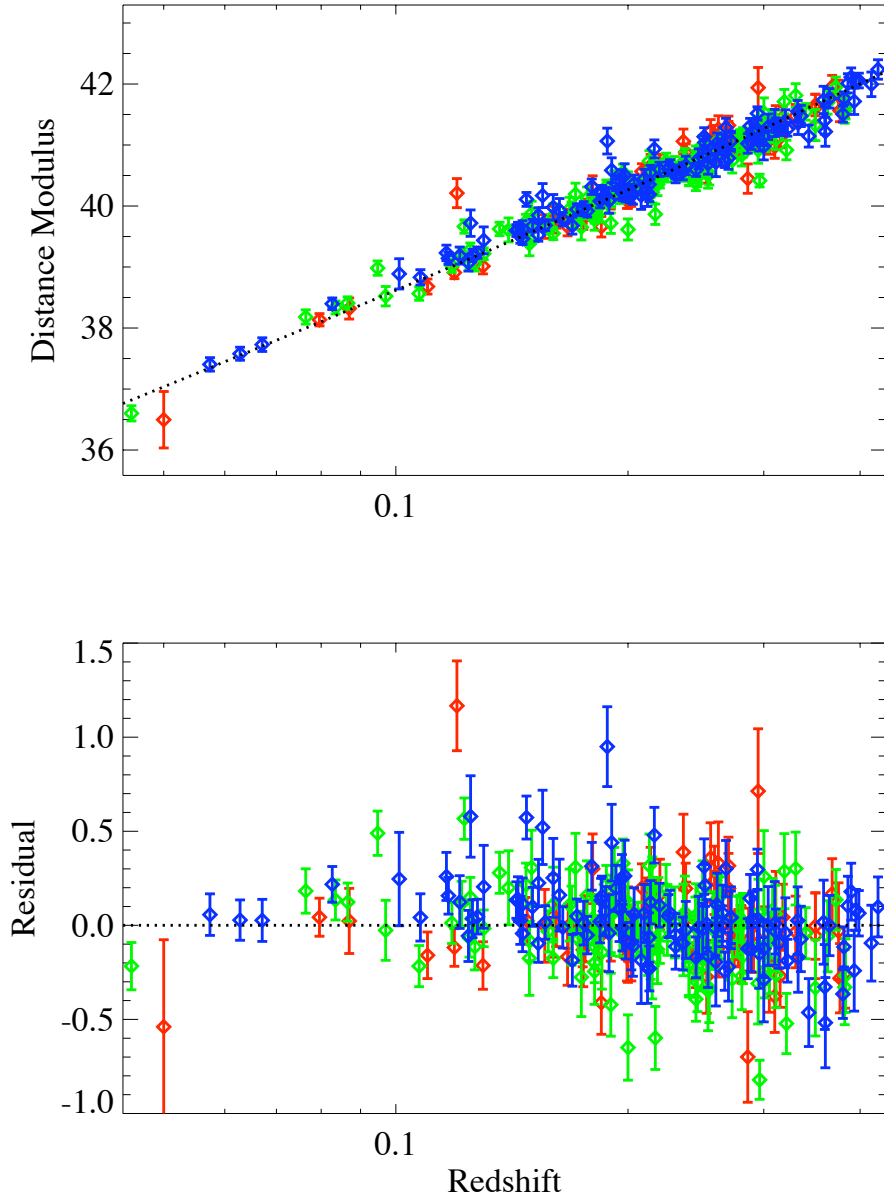


Figure 7.5: The hubble diagram for objects where the  $A_V$  distribution has been determined by either a standard  $A_V$  prior for star-forming objects, or a steeper exponential decline for passive events (see text). All of these events pass the selection criteria defined in §3.2.4 and §3.2.2. This figure includes all objects with a spectroscopic redshift. Also shown are the residuals from the fit as a function of redshift. Passively evolving objects are plotted in red, whilst moderately star-forming and highly star-forming objects are shown in green and blue respectively. The best-fitting cosmology has  $H_0 = 61.0 \text{ km s}^{-1} \text{ Mpc}^{-1}$ .

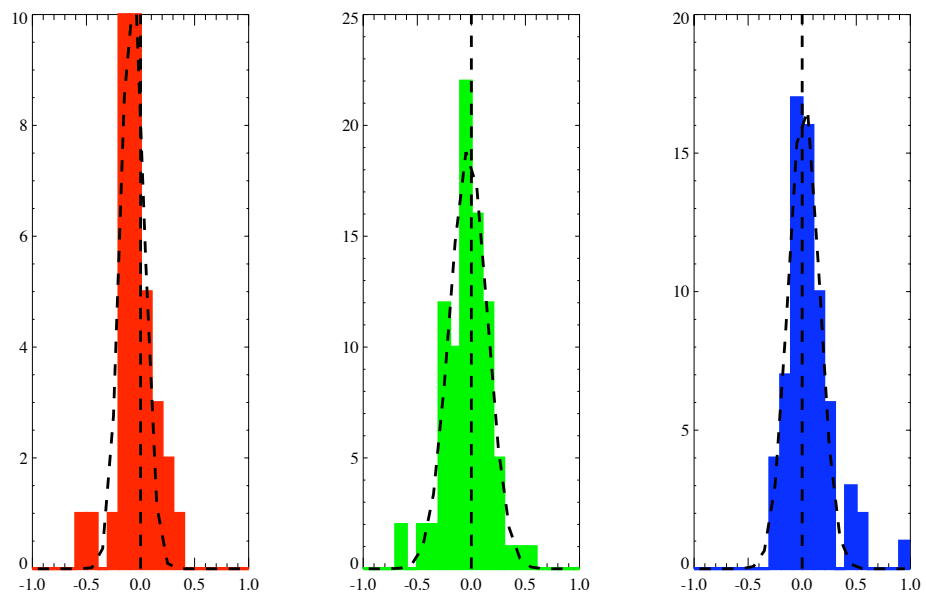


Figure 7.6: Residuals from the fit to the Hubble diagram (Figure 7.5) for objects where the  $A_V$  distribution has been determined either by a standard  $A_V$  prior for star-forming objects, or a steeper exponential decline for passive events (see text). All of these events pass the selection criteria defined in §3.2.4 and §3.2.2. This figure includes all objects with a spectroscopic redshift. The three distributions are shown separately with the best-fitting Gaussian distribution overplotted.

	# Passive	# moderates	# highly star-forming
	Complete Sample <sup>a</sup>		
	All objects <sup>b</sup>		
Number of Objects	68	120	112
Gaussian Central Value	$-0.038 \pm 0.010$	$-0.022 \pm 0.009$	$0.018 \pm 0.007$
Gaussian Width	0.129	0.194	0.149
	Confirmed events <sup>c</sup>		
Number of Objects	31	79	84
Gaussian Central Value	$-0.042 \pm 0.010$	$-0.024 \pm 0.014$	$0.030 \pm 0.009$
Gaussian Width	0.149	0.169	0.131
	$0 < z < 0.25$		
	All objects <sup>d</sup>		
Number of Objects	35	86	66
Gaussian Central Value	-0.075	-0.026	0.015
Gaussian Width	0.105	0.174	0.142
	Confirmed events <sup>e</sup>		
Number of Objects	18	60	52
Gaussian Central Value	-0.100	-0.040	0.016
Gaussian Width	0.077	0.160	0.123

<sup>a</sup> $0 < z < 0.5$

<sup>b</sup>All objects with either a spectroscopic redshift from the supernova event or a host galaxy redshift

<sup>c</sup>Only objects with a spectra of the supernova event are considered

<sup>d</sup>All objects with either a spectroscopic redshift from the supernova event or a host galaxy redshift

<sup>e</sup>Only objects with a spectra of the supernova event are considered

Table 7.6: Shows the Gaussian fitting parameters for the three distributions shown in Figure 7.6. These objects have been fitted with a standard  $A_V$  prior for star-forming objects, and a steeper exponential for passive galaxies. The values for the complete dataset ( $0 < z < 0.5$ ) and a low redshift sample ( $0 < z < 0.25$ ) are given, along with the results where only confirmed events are considered, and the case where objects with a known spectral redshift.

	K-S statistic	A-D statistic
	Complete Sample <sup>a</sup>	
	All objects <sup>b</sup>	
Passive vs. Star-forming	0.344	0.372
Passive vs. Highly Star-forming	0.114	0.068
	Confirmed events <sup>c</sup>	
Passive vs. Star-forming	0.084	0.116
Passive vs. Highly Star-forming	0.035	0.014
	$0 < z < 0.25$	
	All objects <sup>d</sup>	
Passive vs. Star-forming	0.217	0.228
Passive vs. Highly Star-forming	0.047	0.015
	Confirmed events <sup>e</sup>	
Passive vs. Star-forming	0.040	0.010
Passive vs. Highly Star-forming	$2.06 \times 10^{-3}$	$0.281 \times 10^{-3}$

<sup>a</sup> $0 < z < 0.5$

<sup>b</sup>All objects with either a spectroscopic redshift from the supernova event or a host galaxy redshift

<sup>c</sup>Only objects with a spectra of the supernova event are considered

<sup>d</sup>All objects with either a spectroscopic redshift from the supernova event or a host galaxy redshift

<sup>e</sup>Only objects with a spectra of the supernova event are considered

Table 7.7: K-S and A-D test statistics for the residuals from the best-fit to the Hubble diagram (shown in Figure 7.6). These objects have been fitted with a standard  $A_V$  prior for star-forming objects, and a steep exponential for passive galaxies. Here passive galaxies are compared to objects with ongoing star-formation activity and highly star-forming objects, respectively. This includes objects with and without spectroscopic confirmation. The values are given for both the complete dataset ( $0 < z < 0.5$ ) and that of a low redshift cut-off,  $0 < z < 0.25$

## 7.6 Comparison to SALT2

The Analysis of §7.3, §7.4 and §7.5 use the framework of the MLCS light-curve fitter. This light-curve fitting technique uses a fitted  $A_V$  prior in the fitting process. However, the SALT2 light-curve fitter does not attempt to fit the  $A_V$  content of the supernova as a separate function and thus no prior information is involved. Here we investigate the residuals from the best-fitting Hubble diagram for the sample discussed in §7.2 when the SALT2 light-curve fitter is used in the fitting process.

To carry out this analysis we use the sample described in §7.2. However, to ensure that our results are not biased by combining the results with the MLCS light-curve fitter we shall only consider objects with a spectroscopic redshift. Each supernova event is run through the SALT2 light-curve fitter to produce values of the peak magnitude in the B band ( $m_B$ ), the peak luminosity / light-curve decline rate parameter ( $x_1$ ) and the colour of the supernova event ( $c$ ). As described in §3.2.3, the distance to each supernova event is governed by the equation,

$$\mu_i = m_{B_i}^* - M_B + \alpha \times x_{1,i} - \beta \times c_i \quad (7.2)$$

where  $m_B^*$ ,  $x_1$ ,  $c$  are determined for each supernova, as described above, and  $M_B$ ,  $\alpha$  and  $\beta$  are global parameters that describe type Ia supernova in general.

For this analysis we adopt values of  $M$ ,  $\alpha$  and  $\beta$  that have been determined from the first-year SDSS-II Supernova Survey Cosmological Results (Kessler et al. (2009)). These are  $\alpha = 0.127 \pm 0.026$ ,  $\beta = 2.52 \pm 0.19$  and  $M_B = -19.44$ . Note that these values are consistent with those found from other cosmological results (see for instance Hicken et al. (2009)), and  $M_B$  is a parameter which purely affects the normalisation of the type Ia events. Since we are purely concerned with the relative normalisations for different populations, this parameter has no effect on the relative value of  $H_0$  that shall be discussed later. Ideally, a global fit would be carried out on each of the subsamples considered to determine their own values of  $\alpha$  and  $\beta$ . However, with the small number of objects, and the small redshift range covered by the sample considered here, the results would be inconclusive.

Having determined the distances to each of the supernova in our sample using the SALT2 light-curve fitter, we can follow the method laid out in §7.2 to split the sample by redshift and spectroscopic identification and discuss the cosmological results.

### 7.6.1 SALT2 Analysis for Confirmed Events

In this section we shall only consider supernovae that have been spectroscopically identified. That is, we shall not consider objects whose light-curve matches that of a type Ia supernova but lack a supernova spectrum. In previous sections we have seen that this sample may be biased due to spectroscopic resources, but this sample is free of contamination from non-type Ia events.

Figure 7.7 shows a Hubble diagram for these events along with the residuals from the best-fitting cosmology as a function of host galaxy type. The best fitting cosmological model (assuming  $\Omega_M = 0.27$  and  $\Omega_\Lambda = 0.73$  as before) has a value of  $H_0 = 65.8 \text{ km s}^{-1} \text{ Mpc}^{-1}$ . Note that the different value of  $H_0$  compared to that found in §7.3 purely due to the value of  $M_B$ , the absolute magnitude of a type Ia supernova, which is degenerate with the normalisation of the Hubble diagram.

We now consider the residuals from the best-fitting cosmology. This is shown as a function of host galaxy type in Figure 7.8. Histograms for each of the galaxy types are plotted along with the best-fitting Gaussian functions for each.

The best-fitting Gaussian parameters for the fits shown in Figure 7.8 are given in Table 7.8. The results for a low redshift cut-off of  $z < 0.25$  are also given. From these results it is clear that whilst there is a small difference between the distributions for passive galaxies compared to that of galaxies with ongoing star-formation (either moderately or highly star-forming) this effect is dramatically smaller than that for the MLCS analysis given in §7.3. Further to this, the evidence that passive galaxies exhibit less scatter from the best fit value of  $H_0$  than that of star-forming galaxies, is reduced. There is no evidence for this in the low redshift dataset, whilst the reduced scatter in the full redshift range may be better explained by the smaller number of detected events in passive galaxies.

To confirm such a claim, a K-S and A-D test (§6.2.1) are carried out on these samples to determine the significance that two distributions are drawn from different parent datasets. Following the method laid out in §7.3, we combine the moderately and highly star-forming datasets in to one distribution. This star-forming dataset is compared to that of the passive galaxies. We also consider the case where the highly star-forming objects are compared to the passive galaxy distribution. The resultant statistical values are found in Table 7.9.

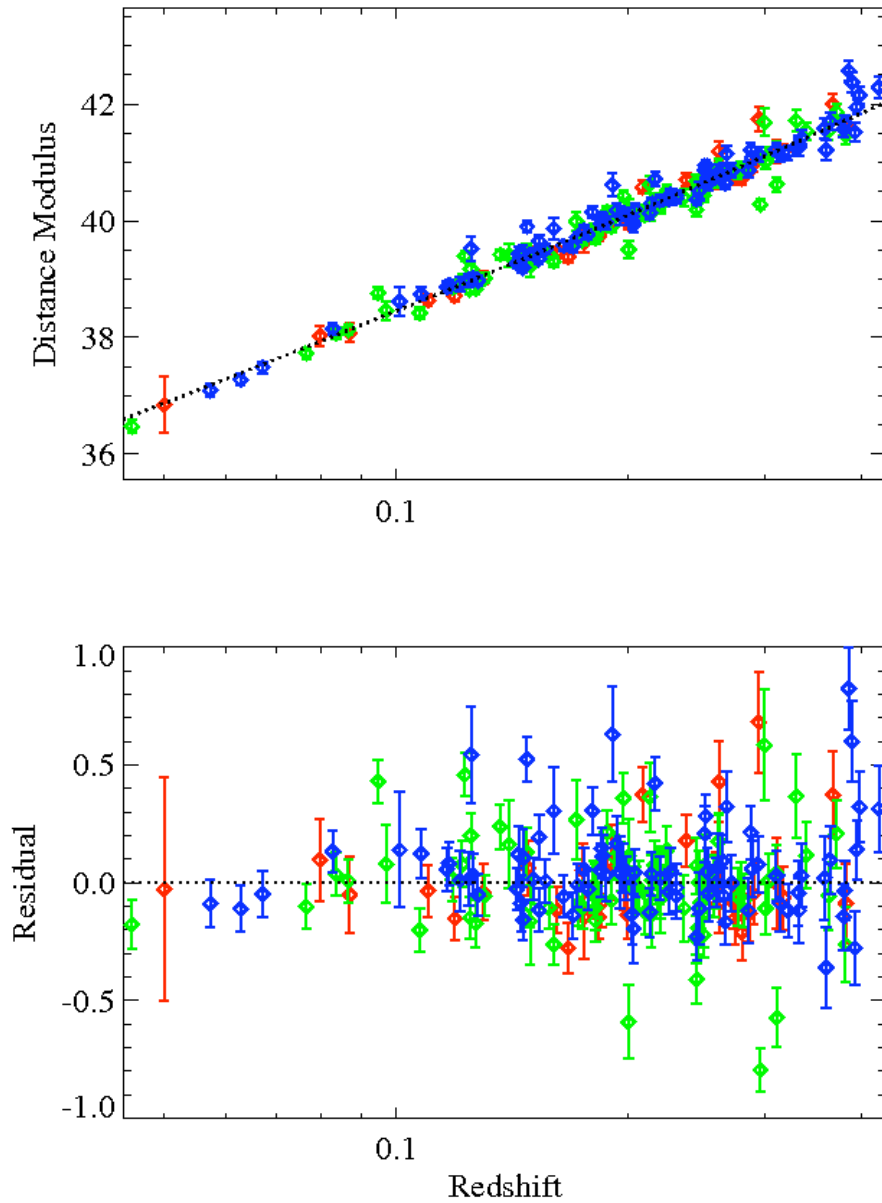


Figure 7.7: The top panel shows the Hubble diagram for the spectroscopically confirmed objects defined by using the SALT2 light-curve fitter (as described in §7.6), as a function of host galaxy type. The bottom panel shows the residuals from this fit. Passively evolving objects are plotted in red, whilst moderately star-forming and highly star-forming objects are shown in green and blue respectively. The dotted line is the the best-fitting cosmology has  $H_0 = 65.8 \text{ km s}^{-1} \text{ Mpc}^{-1}$ .

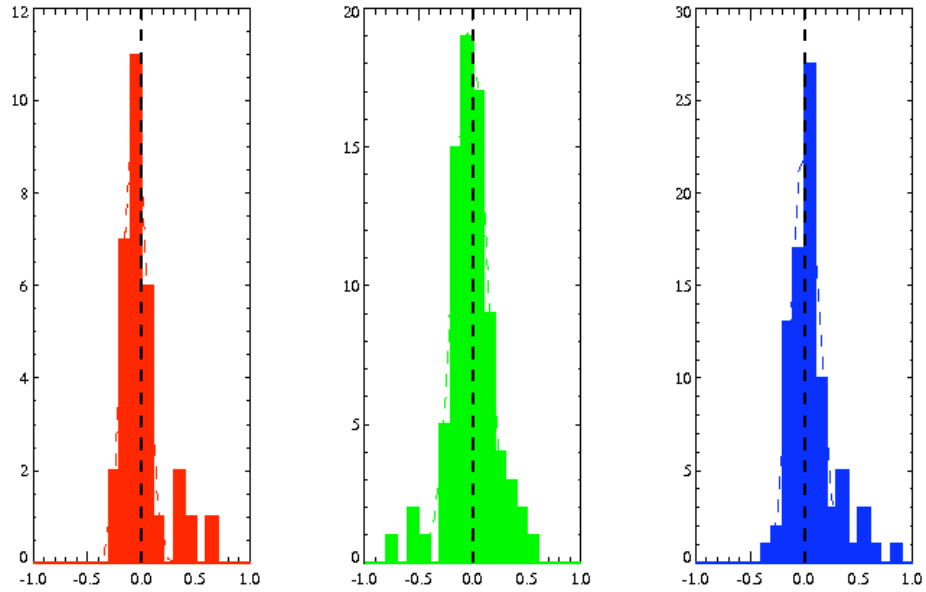


Figure 7.8: The residuals from the best-fit cosmology shown in Figure 7.7 as a function of host galaxy type. The three distributions are plotted separately with the best-fitting Gaussian distributions overplotted. This figure is for objects that have been fit with the SALT2 light-curve fitter.

	# Passive	# moderates	# highly star-forming
	Complete Sample <sup>a</sup>		
Number of Objects	31	79	84
Gaussian Central Value	$-0.059 \pm 0.006$	$-0.025 \pm 0.007$	$0.012 \pm 0.011$
Gaussian Width	0.099	0.147	0.123
	$0 < z < 0.25$		
Number of Objects	18	60	52
Gaussian Central Value	$-0.050 \pm 0.009$	$-0.040 \pm 0.009$	$0.020 \pm 0.009$
Gaussian Width	0.121	0.145	0.119

<sup>a</sup> $0 < z < 0.5$

Table 7.8: Shows the Gaussian fitting parameters for the three distributions shown in Figure 7.8. The values for Gaussian mean and width for the complete dataset ( $0 < z < 0.5$ ), and that of a low redshift cut-off, ( $0 < z < 0.25$ ) are given. This analysis is for the SALT2 light-curve fitter and contains only objects that have been spectroscopically confirmed as a type Ia supernova.

The values given in Table 7.9 indicate that there is no statistical evidence that the distribution of passive galaxies differs from that of galaxies with ongoing star-formation activity, when the sample is analysed with the SALT2 light-curve fitter. This is especially true at low redshift - where the distributions are seen to be extremely similar. This result contrasts that of §7.3 and §7.5 using the MLCS light-curve fitter. To determine if this result is due to biases and incompleteness in the sample (as discussed in §3) we now consider objects with a spectroscopic redshift, but not necessarily a spectroscopic identification.

## 7.6.2 SALT2 Analysis for Objects with a Spectroscopic Redshift

In §7.6.1 we discussed the results from fitting using the SALT2 light-curve fitter for a sample where only spectroscopically confirmed objects are considered. However, a large part of this work has been to determine the effect of incompleteness on spectroscopic samples of type Ia and thus this issue needs to be addressed with this analysis. Here we follow the analysis of §7.4 to include objects that have not been spectroscopically confirmed, but as discussed in §7.2 have spectroscopic host redshifts and light-curves that closely follow the peak luminosity / light-curve decline rate relationship that is seen in type Ia events.

The Hubble diagram for these events is shown in Figure 7.9, with the resulting residuals from the best-fit cosmology as a function of host galaxy type shown in Figure 7.10. The best-fitting Gaussian functions for each are overplotted.

The best-fitting Gaussian parameters for Figure 7.10 are given in Table 7.10. The results for a low redshift cut-off of  $z < 0.25$  are also given.

Following the method of §7.6.1, a K-S and A-D test is carried out on the various distributions to determine if there is evidence that they are drawn from different parent distributions. These statistical tests are carried out between the passive galaxy dataset and the set of galaxies with ongoing star-formation activity, and between the passive galaxy set and that of that highly star-forming galaxies. The results of these statistical tests are given in Table 7.11

These results match those found in §7.6.1 that there is no statistical evidence that when using the SALT2 light-curve fitter, the distribution of passive galaxies differs from that of galaxies with some level of ongoing-star-formation activity. This analysis contains objects that have not been spectroscopically identified, and thus is thought to be relatively

	K-S statistic	A-D statistic
	Complete Sample <sup>a</sup>	
Passive vs. Star-forming	0.185	0.209
Passive vs. Highly Star-forming	0.056	0.049
	$0 < z < 0.25$	
Passive vs. Star-forming	0.573	0.547
Passive vs. Highly Star-forming	0.192	0.088

<sup>a</sup> $0 < z < 0.5$

Table 7.9: K-S and A-D test statistics for the residuals from the best-fit cosmology to the Hubble diagram (shown in Figure 7.8) for passive galaxies when compared to objects with ongoing star-formation activity and highly star-forming objects respectively. The values are given for both the complete dataset ( $0 < z < 0.5$ ) and a low redshift sample ( $0 < z < 0.25$ ). This is for a sample of type Ia's that have been spectroscopically confirmed and analysed using the SALT2 light-curve fitter.

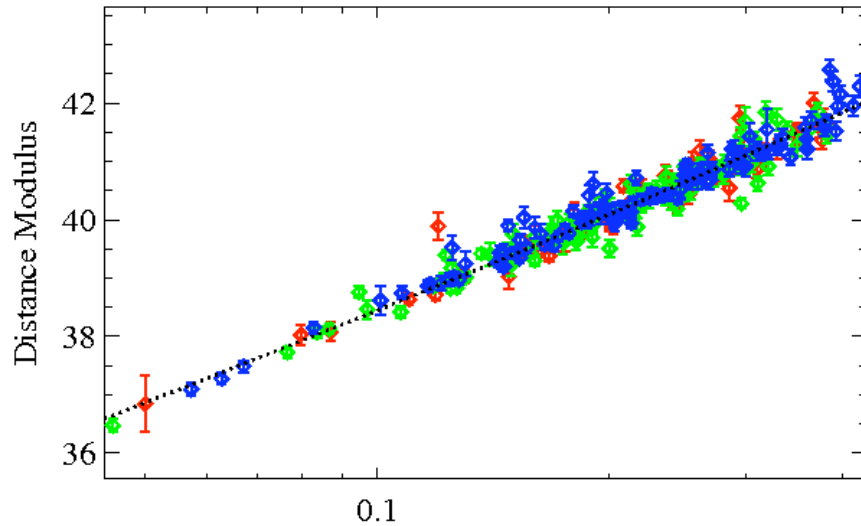


Figure 7.9: The Hubble diagram for objects with a spectroscopic redshift (of any type) defined by using the SALT2 light-curve fitter (as described in §7.6), as a function of host galaxy type. The dotted line is the the best-fitting cosmology has  $H_0 = 66.0 \text{ km s}^{-1} \text{ Mpc}^{-1}$ .

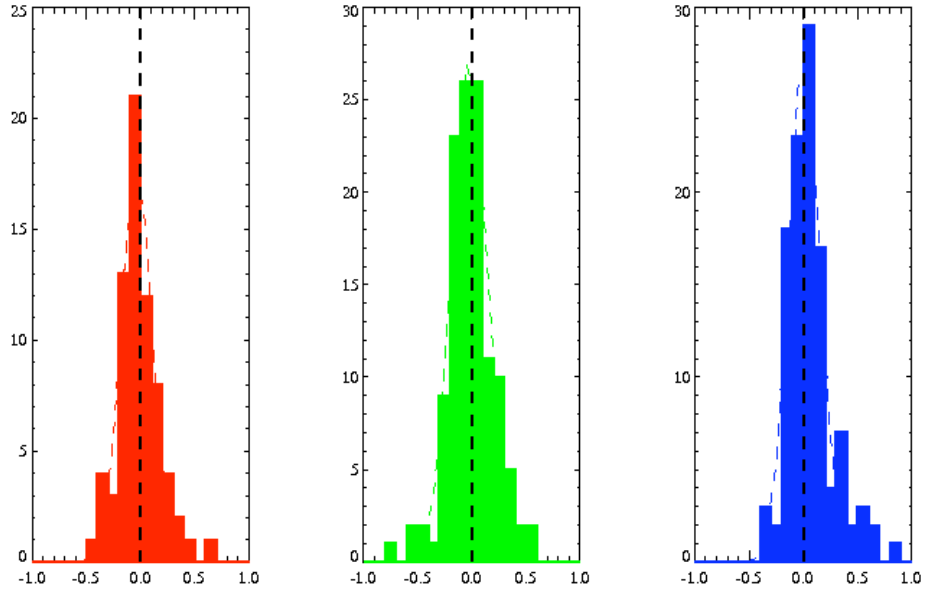


Figure 7.10: The residuals from the best-fit cosmology shown in Figure 7.9 as a function of host galaxy type. The three distributions are plotted separately with the best-fitting Gaussian distributions overplotted. This figure is for objects that have been fit with the SALT2 light-curve fitter.

	# Passive	# moderates	# highly star-forming
	Complete Sample <sup>a</sup>		
Number of Objects	71	120	112
Gaussian Central Value	$-0.038 \pm 0.010$	$-0.025 \pm 0.010$	$0.011 \pm 0.010$
Gaussian Width	0.137	0.164	0.143
	$0 < z < 0.25$		
Number of Objects	36	86	66
Gaussian Central Value	$-0.043 \pm 0.011$	$-0.026 \pm 0.009$	$0.020 \pm 0.010$
Gaussian Width	0.134	0.165	0.126

<sup>a</sup> $0 < z < 0.5$

Table 7.10: Shows the Gaussian fitting parameters for the three distributions shown in Figure 7.10. The values for Gaussian mean and width for the complete dataset ( $0 < z < 0.5$ ), and that of a low redshift cut-off, ( $0 < z < 0.25$ ) are given. This analysis is for the SALT2 light-curve fitter.

free of biases due to selection criteria or spectroscopic incompleteness. This result can be compared to that of §7.4 and §7.5 using the MLCS light-curve fitter. It is also clear that there is no significant evidence that passive galaxies show less scatter on the Hubble diagram than those with recent star-formation activity. This is true for both the full dataset and that with a low redshift cut-off.

The differences in the result between that of the MLCS light-curve fitter and that of the SALT2 light-curve fitter may best be explained by the lack of an  $A_V$  prior in the SALT2 light-curve fitter. The use of such a prior by the MLCS light-curve fitter may have the effect of causing type Ia supernova seen in passive galaxies to have a positive value of  $A_V$  in order to match the prior distribution. This effect is not required in the SALT2 case. Note that this result does not preclude the possibility that type Ia supernova in passive galaxies require a different value of the  $\alpha$ ,  $\beta$  and  $M$  parameters than that of type Ia events in star-forming galaxies. Such a test requires a larger number of type Ia events covering a wider redshift range than is available for this study.

## 7.7 Conclusions

Sullivan et al. (2003) found that for a set of morphologically classified host galaxies, the scatter on the Hubble diagram was smallest for supernovae occurring in passive galaxies. Whilst it is not entirely appropriate to compare objects which have been classified by eye to those in this sample whose properties have been determined through a study of their optical properties, it is reasonable to equate early-type galaxies to passive galaxies, and star-forming objects to late-type events. Assuming this for our sample, we would expect to see less scatter from the best fit Hubble diagram for passive galaxies. Whilst there is some evidence for this, it is not clear if this is due to observational bias or the reduced sample size, since this effect seems to be removed when objects which are not spectroscopically confirmed are included in any cosmological fit.

Further to this, we have seen evidence that the mean residual offset from the Hubble diagram are different for passive galaxies than star-forming objects when using the MLCS light-curve fitter. That is passive events primarily have distance moduli that are lower than those expected from the best-fit cosmology, whilst the opposite effect has been seen for star-forming objects. This can be interpreted to be that either type Ia supernovae in passive galaxies have different absolute magnitudes than those found in areas with recent star-formation activity, or that an assumption in the fitting process is host galaxy dependent, such as the level of dust in the supernova explosion. An attempt to model the

dust in these passive objects separately from those in star-forming events, appears to partially resolve this issue, although further study is required to determine if the remaining diversity is due to the light-curve fitting process, or whether another undetected process is responsible, possibly indicating a further lack of homogeneity in the type Ia population.

When this result is contrasted with that of the SALT2 light-curve fitter, no evidence of an offset in the best-fitting cosmology is seen. This may be due to the lack of an  $A_V$  prior in the SALT2 fitting process, which causes type Ia supernova in passive galaxies to have larger values of  $A_V$  than would be expected from the levels of dust in these environments. The SALT2 light-curve fitter confirms the result from the MLCS light-curve fitter, that there is no evidence of less scatter from the best-fitting Hubble diagram for passive galaxies when compared to that of star-forming galaxies.

	K-S statistic	A-D statistic
	Complete Sample <sup>a</sup>	
Passive vs. Star-forming	0.190	0.294
Passive vs. Highly Star-forming	0.052	0.044
	$0 < z < 0.25$	
Passive vs. Star-forming	0.636	0.639
Passive vs. Highly Star-forming	0.195	0.149

---

<sup>a</sup> $0 < z < 0.5$

Table 7.11: K-S and A-D test statistics for the residuals from the best-fit cosmology to the Hubble diagram (shown in Figure 7.10) for passive galaxies when compared to objects with ongoing star-formation activity and highly star-forming objects respectively. The values are given for both the complete dataset ( $0 < z < 0.5$ ) and a low redshift sample ( $0 < z < 0.25$ ). This is for a sample of type Ia's that have been spectroscopically confirmed and analysed using the SALT2 light-curve fitter.

# Chapter 8

## Conclusions

In this thesis we have investigated the diversity of the type Ia supernova population. To this end, we have used data from the first two years of the SDSS-II Supernova Survey which is outlined in §2.

In §3, we outlined a method for correcting the spectroscopic sample of supernovae produced by this survey for incompleteness. The multi-colour light-curves of every detected object were used to produce a sample of candidates free from bias due to spectroscopic incompleteness that was efficient in our redshift range of interest.

### 8.1 The Type I Supernova Rate

In this thesis we have considered two formalisms for the type Ia supernova rate.

#### 8.1.1 The Volumetric Type Ia Supernova Rate

Using the incompleteness corrected sample described in §3.2.5, and the determined efficiency of the SDSS-II Supernova Survey (§3.3), we were able to calculate the volumetric supernova rate in the range  $0.05 < z < 0.25$ . Our results are consistent with those found for the low- $z$  rate from the first year SDSS-II Supernova Survey data (Dilday et al. (2008)) and that of Dilday et al. (2009), who extended this calculation to  $z \simeq 0.3$ . Assuming a constant rate, we find that  $r_V = 2.24 \pm 0.49 \times 10^{-5} \text{ SNe yr}^{-1} \text{ Mpc}^{-3} h_{70}^3$  for  $z < 0.12$ .

Extending this measurement with redshift (each bin assuming a constant rate), we are able to rule out a constant supernova rate at the  $\sim 2.1 - \sigma$  level (when only statistical errors are considered). Figure 3.9 shows the redshift evolution of the supernova rate,

which is seen to increase with a slope of  $1.63 \pm 0.76 \times 10^{-4} \text{SNe yr}^{-1} \text{Mpc}^{-3} h_{70}^3$ . This measurement represents the largest single sample of supernova that have been used to determine the volumetric rate, and the results are consistent with those found at high redshift, such as [Neill et al. \(2006\)](#).

### 8.1.2 The Type Ia Supernova Rate as a Function of Host Galaxy Properties

In §4, we identified the host galaxies of each of the 246 type Ia supernovae in the incompleteness corrected sample. Using a template fitting method, we were able to calculate the derived properties, of stellar mass and star-formation rate, of each galaxy in our sample. A large comparison field sample was also produced from a coadded image covering the same area of the sky as the SDSS-II Supernova Survey. This sample, was then used to constrain the type Ia supernova rate as a function of these host galaxies.

In §5, we showed that, the type Ia supernova rate in passive galaxies is lower than that of galaxies exhibiting signs of recent star-formation activity, in agreement [Mannucci et al. \(2005a\)](#) and [Sullivan et al. \(2006b\)](#). However, in contrast to other results, we do not see that the type Ia supernova rate increases linearly with specific star-formation rate. Instead our results indicate a step between passive and active galaxies. Further to this, we then studied how the type Ia supernova rate in passive galaxies is related to their mass and found that,

$$\text{SNR}_{\text{Ia}} \propto M^{\frac{1}{2}}, \quad (8.1)$$

which does not agree with the results of [Sullivan et al. \(2006b\)](#), who found that  $\text{SNR}_{\text{Ia}} \propto M$  for passive galaxies. We found that for star-forming galaxies a linear relationship was followed with star-formation rate, indicating that a one component model of the supernova rate was unable to replicate the observations.

[Scannapieco & Bildsten \(2005\)](#) introduced a model to describe the type Ia supernova rate, called the ‘‘A+B’’ model, which considers the type Ia supernova rate to have two components, namely a ‘‘delayed component’’, related to the mass of the host and a ‘‘prompt component’’, related to the star-formation rate. This is written as,

$$\text{SNR}_{\text{Ia}} = A \times M_{\text{stellar}}^{\text{n}_{\text{mass}}} + B \times \text{SFR}^{\text{n}_{\text{SFR}}}, \quad (8.2)$$

with, in the simplest case,  $\text{n}_{\text{mass}} = \text{n}_{\text{SFR}} = 1$ . From the passive galaxy sample, it was clear that  $\text{n}_{\text{mass}} = 1$  does not represent a good fit to the data. For star-forming galaxies, once the ‘‘delayed’’ component contribution is removed, we find  $\text{n}_{\text{SFR}} \simeq 1$ . This matches

the results of [Sullivan et al. \(2006b\)](#) and [Mannucci et al. \(2005a\)](#). It also shows that the type Ia supernova rate in star-forming galaxies dominates over that of passive galaxies.

We then used a bivariate fit to the data to simultaneously constrain both the “delayed” and “prompt” components. We find best fit values of  $n_{\text{mass}} = 0.67 \pm 0.14$  and  $n_{\text{SFR}} = 1.01 \pm 0.25$ , with constants  $A = 4.35 \pm 0.31 \times 10^{-11} \text{ SNe yr}^{-1} M_{\odot}^{-1}$  and  $B = 5.08 \pm 0.10 \times 10^{-4} \text{ SNe yr}^{-1} (M_{\odot} \text{ yr}^{-1})^{-1}$ . These results are consistent with those found in §5.4 and §5.6 (and given above), except the value of  $n_{\text{mass}}$  is inconsistent with that of [Sullivan et al. \(2006b\)](#).

When we consider the  $\chi^2$  probabilities for these bivariate fits, we are able to rule out a supernova rate that is solely dependent on mass ( $P(\chi^2) = 0$ ). For the “A+B” model, we also find it is not a good fit with  $P(\chi^2) = 0.038$ , but is preferred to the case where we force  $n_{\text{mass}} = 0.5$  ( $P(\chi^2) = 2.4 \times 10^{-7}$ ). Better fits are seen for the general case (Equation 8.2),  $P(\chi^2) = 0.13$  and the that where  $n_{\text{mass}} = 0.5$  and  $n_{\text{SFR}} = 1$ , where  $P(\chi^2) = 0.094$ .

However, the addition of two additional parameters considered in the general case may lead to over-fitting of the data. The relatively high  $\chi^2$  values for all of the fit parameters may indicate some tension between the modelling of the probability distribution function and the data. However, the bivariate fitting considered only statistical errors, and the systematic uncertainties on these measurements are important.

Thus, we have shown that if the host galaxy properties are used to determine the type Ia supernova rate, then there is some tension between the results seen in our redshift range at those at higher redshift.

## 8.2 Photometric Properties of Type Ia Supernovae

Using two light-curve fitting methods, we are able to confirm the result that the distribution of the peak luminosity / light-curve decline rate parameter (for instance,  $\Delta$ ) is dependent on host galaxy type. Using a K-S test, we find significant evidence that the distribution of the  $\Delta$  parameter is different for supernovae that occur in passive galaxies than star-forming galaxies. When these results were compared to those in [Sullivan et al. \(2006b\)](#), for a set of supernovae at higher redshift, the distributions significantly matched, indicating that the type Ia supernova population has not evolved with redshift.

We then considered the extinction distributions of type Ia supernovae. Using two independent methods to determine the level of extinction in each supernova event, we showed there is little evidence for this parameter to be dependent on host galaxy type. Since the dust content of passive galaxies differs from that of star-forming galaxies, this may indicate that the levels of extinction in type Ia events is not dominated by the host galaxy, and instead is primarily concerned with the intrinsic dispersion of these events. This result was verified by considering a range of  $A_V$  priors on the light-curve fitting method. Independent of the choice of prior, there was little evidence that the distribution of  $A_V$  for supernovae in passive galaxies differs from those in star-forming galaxies.

### 8.3 Hubble Diagram Residuals

Finally, we present results on the residuals from the best-fit cosmology as a function of host galaxy type. [Sullivan et al. \(2003\)](#) found that for a set of morphologically classified galaxies, the scatter on the Hubble diagram was smallest for type Ia's in early-type galaxies.

Using a standard  $A_V$  prior, and considering only type Ia supernovae that had been spectroscopically confirmed, we find that the mean residual offset from the best-fit cosmology to the Hubble diagram differs for supernovae seen in passive galaxies, when compared to those seen in star-forming galaxies, with “passive supernovae” being closer to the observer than the best fit cosmology. Using a K-S test, we are able to show that there is significant evidence that the distribution of residuals from this best-fit cosmology is different for supernovae seen passive and star-forming galaxies. There is also an indication that supernova seen in passive galaxies are less scattered about the best-fit. However, when objects with a spectroscopic redshift (but are not necessarily spectroscopically confirmed events) are included, the scatter of the two populations is seen to be similar, indicating potential observational bias in the confirmed sample. However, when these additional objects are considered, the differences in the mean residual offset are still observed.

To determine if this effect is related to the choice of  $A_V$  prior for the light-curve fitting, we then refit “passive supernovae” with a stepper exponential decline for the  $A_V$  distribution. This selection allows the supernovae in passive galaxies to be fit with an  $A_V$  prior matching their expected dust content. When the residuals from this best-fit Hubble diagram were examined, the difference in the mean residual offset has decreased in both of the cases described above. Again the scatter from the best-fit Hubble diagrams are smaller for supernovae in passive galaxies, when only spectroscopically confirmed

objects are considered, but this effect is reduced when further objects are considered.

This result indicates that the differences in the residuals from the Hubble diagram between supernovae seen in passive and star-forming galaxies is partially related to the modelling of the dust content of these events, although further study is required to determine if the remaining diversity is due to the light-curve fitting process, or intrinsic to the supernovae.

When the SALT2 light-curve fitter is used in place of the MLCS fitter, no evidence of the offset described above. This may be due to the lack of an  $A_V$  prior in the SALT2 fitter, meaning that the supernova in passive environments are not forced to have higher values of  $A_V$  than the dust content of such galaxies would infer. When the SALT2 light-curve fitter is used, there is still no evidence that supernova in passive galaxies exhibit less scatter from the best-fit Hubble diagram than their counterparts in star-forming environments. This result is consistent independent of the sample selection used, implying that biases due to selection effects and spectroscopic incompleteness is not the primary cause of these results. Further study is required to determine if the values of the  $\alpha$ ,  $\beta$  and  $M$  parameters are dependent on host galaxy type, since the sample used in this analysis does not cover a large enough redshift range to accurately constrain them.

## 8.4 Future Work

This work has answered many questions concerning the type Ia supernova population. In solving some of these problems, new questions are now to be considered.

Concerning the type Ia supernova rate, we have seen that the simplistic “A+B” model is able to fit the available data, but some tension is clearly seen. Thus it would be useful to investigate different parameterisations of the probability distribution function that for the “A+B” case has been modelled as a constant rate combined with a delta function at  $t = 0$ . These different models would allow us to constrain the “delay time” distribution of type Ia supernovae.

The “A+B” model considers the two most important parameters that affect the evolution of a galaxy. However, there are degeneracies between these two parameters, including considering the age of the stellar population. By using SED templates that more accurately determine the ages of the stellar populations of galaxies, such as [Maraston et al. \(2006\)](#) the evolution of this population of galaxies can be better determined .

Finally for the result concerning the residuals from the best-fit Hubble diagram, an analysis including the error estimates on each supernova event would allow a proper determination of this effect. Further to this, light-curve fitting models (such as MLCS2k2) use a low redshift training set to infer the properties of type Ia supernova at other redshifts. The sample of low redshift supernovae used from this, are primarily gathered from searches of bright galaxies in the local Universe. These searches are known to preferentially discover type Ia supernovae in late-type galaxies, and thus these training sets are under-represented by type Ia supernovae in passive environments. Re-training these light-curve fitters with an unbiased sample of type Ia events would lead to a more accurate determination of the  $A_V$  distribution of type Ia supernova in the Universe and so we would be able to determine if the effect seen in §8 is solely due to the light-curve fitting technique, or if another parameter is required.

Future large scale survey's such as DES, PanSTARRS and LSST will find samples of 1,000s of type Ia supernovae. The results of this work indicate that when a full sample of objects is considered, the motivation to focus these searches on passive galaxies, such as clusters, due to their apparently reduced scatter from the best-fit Hubble diagram, is reduced.

These samples will be dominated by events that have not been spectroscopically confirmed, and thus it is vitally important to quantify the diversity of the type Ia supernova population, so that the distances to these objects can be accurately determined. Any additional parameter that can lead to a reduced scatter on future Hubble diagrams will lead to more accurate determinations of the cosmological parameters, and may influence our understanding of "Dark Energy"

# Appendix A

## The Accuracy of the Photometric Redshift estimates for the Host Sample

In this Appendix, we test the accuracy of the photometric redshifts produced by the PÉGASE.2 SEDs. To do this we have fit the host galaxy population with the redshift left as a free parameter. Figures A.1 and A.2 shows these photometric redshifts compared to the those produced when the spectroscopic redshift of the host galaxy is constrained. Figure A.2 shows a histogram of the residuals. A Gaussian fit to this distribution has a mean value of  $0.044 \pm 0.0022$  and a standard deviation  $0.068 \pm 0.0022$ .

These plots clearly shows a bias in the photometric redshifts obtained from the PÉGASE.2 light-curve SEDs. If the sample used in §5 was obtained using these photometric redshifts then the sample size would increase by  $\simeq 30\%$ .

However, to quantify the effect of this on our final results presented in §5 we consider the derived properties in these two cases. This is shown in Figures A.3 and A.4. These figures show the mass and star-formation rate estimates in the case where the redshift is left as a free parameter compared to that when the redshift is fixed.

There is considerable scatter in Figure A.3. The two estimates are in good agreement for high mass galaxies, but a deviation is seen for lower mass galaxies, with the mass obtained when the spectroscopic redshift is fixed being greater than those when the redshift is left as a free parameter. This is expected, since the photometric redshifts indicate that on an average objects is at lower redshift than the spectroscopic redshift allows, have a lower absolute magnitude and mass. When a Gaussian is fitted to the residuals from this result, a mean value of  $0.11 \pm 0.006$  and a standard deviation of  $0.27 \pm 0.006$  is found.

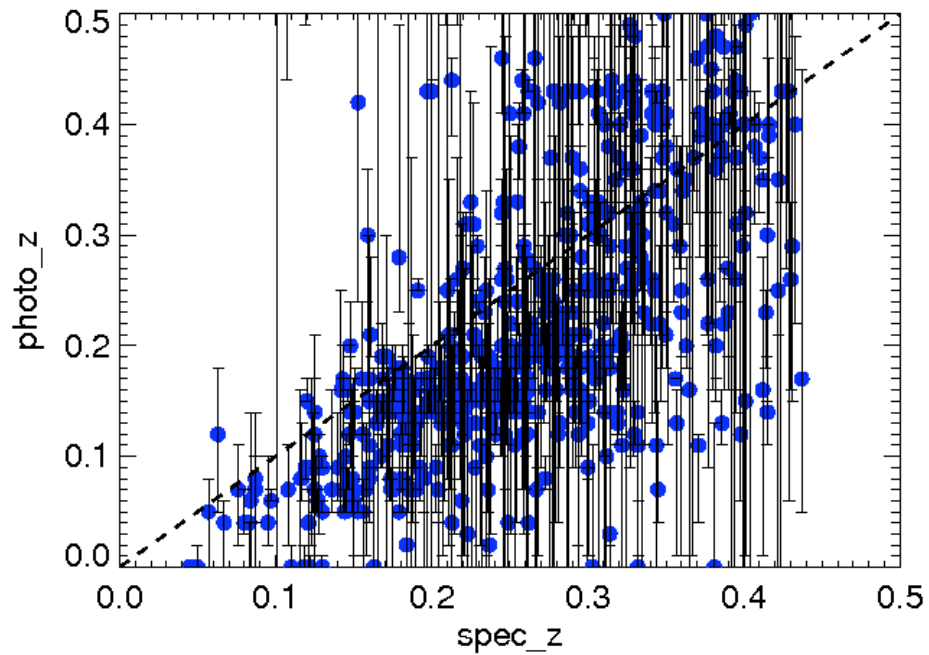


Figure A.1: A comparison of the host galaxy photometric redshift estimates and the spectroscopic redshifts. This plot considers all SDSS-II supernova survey host galaxies. Plotted is the the photometric redshifts vs. the spectroscopic redshifts.

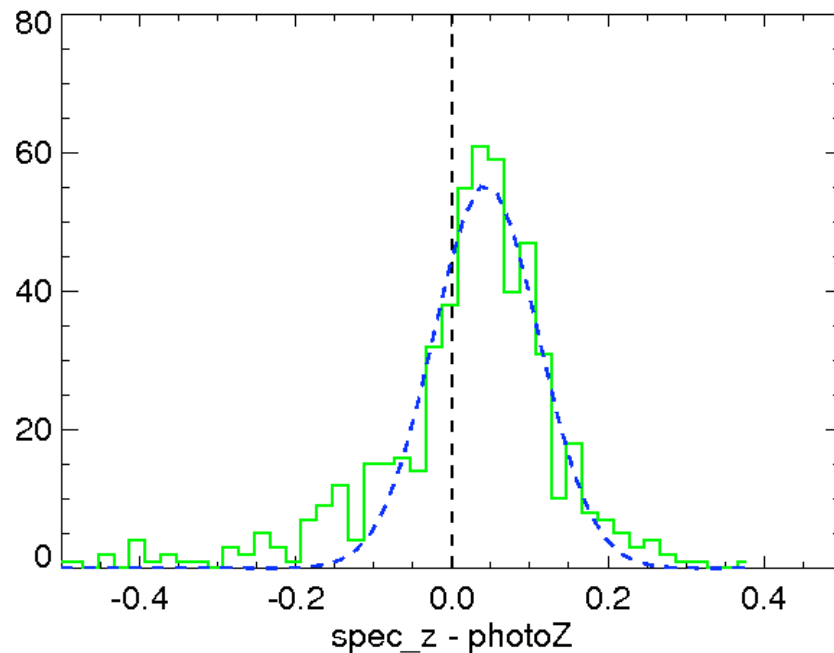


Figure A.2: A comparison of the host galaxy photometric redshift estimates and the spectroscopic redshifts. The plot shows a histogram of the residuals. Overplotted in a Gaussian with mean 0.044 and standard deviation 0.068.

For the star-formation rate analysis in Figure A.4, there is considerable scatter, especially in the case where the redshift is left as a free parameter. This is expected, since there is extra freedom allowed in the galaxy fitting process. When only objects with current star-formation activity are considered, a Gaussian fit to the residuals gives a mean of  $0.27 \pm 0.04$  and a standard deviation of  $0.71 \pm 0.04$ . This indicates the considerable scatter in this relationship, and tentatively shows that the star-formation rate estimates, when the redshift is fixed, are higher than when it is allowed to float.

As an extension to the above analysis we can consider the specific star-formation rate. Again, once passive galaxies have been excluded, we find that the differences in specific star-formation rate between estimates when the redshift is fixed compared to when it is a free parameter, are well described by a Gaussian of mean  $-0.02 \pm 0.003$  and standard deviation  $0.008 \pm 0.001$ .

It is clear that we have identified a bias in the results obtained from the PÉGASE.2 SED fits. The redshift estimates differ for the host galaxy population when the redshift is allowed to float, such that it is lower than the observed redshift. The corresponding mass estimates are higher when the redshift is fixed. There is considerable scatter in the star-formation rate when the redshift is allowed to be a free parameter. This implies that the PÉGASE.2 SEDs are unable to accurately constrain the star-formation history of objects when the redshift is unknown. A larger discussion of this is considered in Appendix C, when this analysis is repeated for a large sample of bright objects with known redshift. In Appendix E we shall introduce the Maraston models, and use them to infer that this redshift offset is constant as a function of apparent magnitude. The effect of this offset on the results found in §5 is discussed fully in Appendix F.

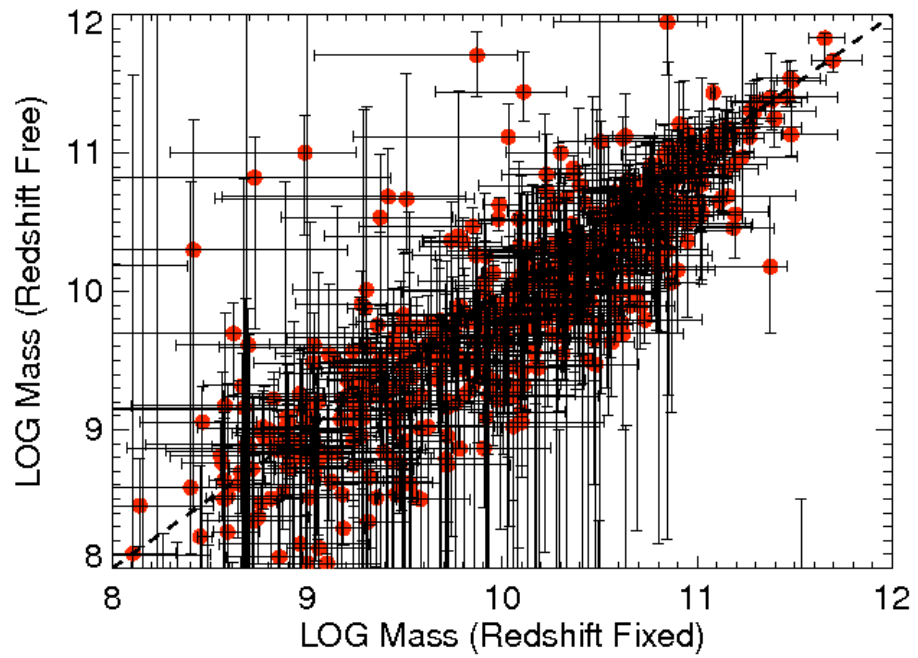


Figure A.3: A comparison of the mass determined by a host galaxy photometric redshift and those estimated by a spectroscopic redshift. Plotted are the mass distributions when the redshift is fixed compared to when it is a free parameter.

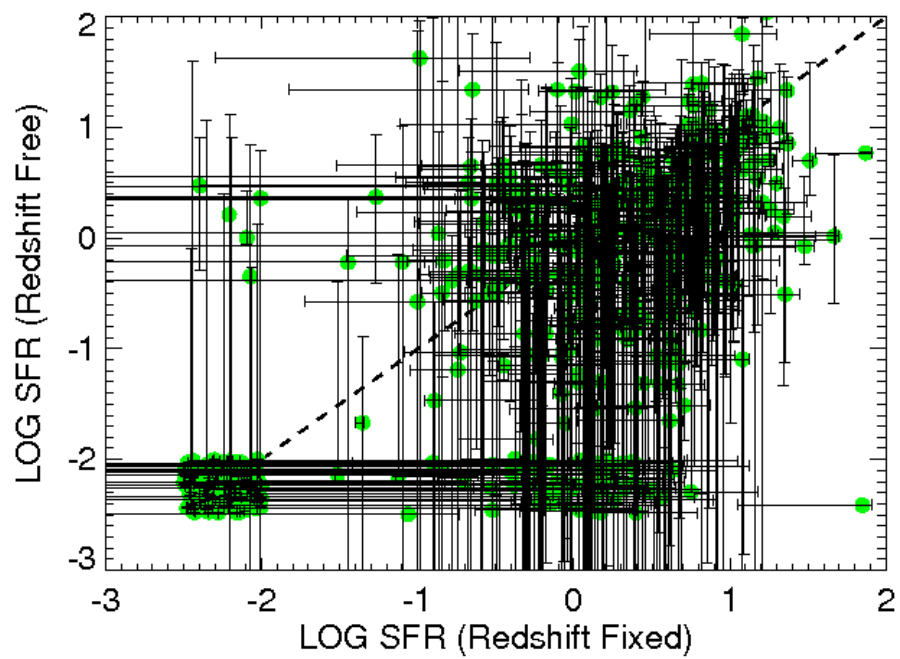


Figure A.4: A comparison of the star-formation rates determined by a host galaxy photometric redshift and those estimated by a spectroscopic redshift. This figure shows the star-formation rate distributions when the redshift is fixed, compared to when it is a free parameter. The passive galaxies are plotted for effect between  $-2.5 < \log(SFR) < -2$ .

# Appendix B

## Comparison of the Derived Measurements from PÉGASE.2 with Other Measurements

### B.1 Introduction

In §4 we introduced the PÉGASE.2 SED galaxy templates. These are used to determine the derived properties of the objects in our sample. In this section we shall attempt to determine how these results compare with those obtained using other methods.

To do this we use a sample of galaxies whose redshift, mass and star-formation rates have been determined from other spectral features. [Kauffmann et al. \(2003\)](#) and [Brinchmann et al. \(2004\)](#) have determined the stellar mass and ongoing star-formation activity for a set of low redshift galaxies, whose spectra were observed as part of the SDSS-I survey. These spectroscopic observations have high signal-to-noise ratios and their derived properties are inferred using the models of [Bruzual & Charlot \(2003\)](#), which have the same underlying physics as the PÉGASE models used in this analysis, but which do not include the TP-AGB phase of stellar evolution. The masses and star-formation rates calculated for the spectra are determined using the 4000Å break index, denoted  $D(4000)$  ([Bruzual A. \(1983\)](#)), which is defined as the ratio of the average flux density  $F_V$  in the range 3850 – 3950Å and 4000 – 4100Å ([Balogh et al. \(1999\)](#)) and the Balmer absorption line index  $H\delta_A$  ([Worthey & Ottaviani \(1997\)](#)), which quantifies  $H\delta$  absorption. However, the spectral resolution of the [Bruzual & Charlot \(2003\)](#) models is poor, and these features can be broad, so the accuracy of these determinations, especially due to the age / metallicity degeneracy, is uncertain. There is significant variation on the star-formation rate estimates, partially due to the measurement and template method and also since it

is possible to measure this parameter using many different methods. Since these objects have been observed as part of the SDSS-I survey, they all have measured magnitudes and redshifts. We use these estimates to determine their derived properties using the PÉGASE.2 galaxy evolution tracks. The matched sample contains over 400,000 galaxies. Several estimates of the stellar mass and star-formation rates are estimated from the spectra. We choose the median value of dust-corrected stellar mass and the median of the likelihood distribution for the star-formation rate.

This test will provide an indication of the effect of using different parts of the spectrum to determine the mass and star-formation rates for a set of galaxies, using models with the same underlying physics. (The PÉGASE and Bruzual & Charlot (2003) templates use the same evolutionary tracks). The PÉGASE models cover a greater range of the rest-frame spectrum than the analysis carried out by Kauffmann et al. (2003) and Brinchmann et al. (2004). The star-formation rates produced by Brinchmann et al. (2004) are likely to be more indicative of the instantaneous star-formation rate than those produced by PÉGASE, which estimate the average star-formation rate over an extended period. Since the redshift of each object has already been determined, this test will describe the level of agreement between these two different techniques.

In this Appendix, we consider the case when the redshift is a known parameter in the fitting process. However, for the field sample considered in the previous analysis, this is not the case, so Appendix C investigates the effect when the redshift is left as a free parameter.

## B.2 The Mass Estimates

Figure's B.1 and B.2 show the distribution of the mass estimates from the PÉGASE.2 templates when compared to that measured by Kauffmann et al. (2003), and shows the residuals as a function of redshift.

The two figure's both show an extremely tight correlation, indicating that once the redshift of an object has been constrained, the PÉGASE.2 templates are able to accurately match the results determined by Kauffmann et al. (2003) using a spectral feature. This is clear for all masses of galaxies, and as shown in Figure B.2, no systematic offset is seen as a function of redshift.

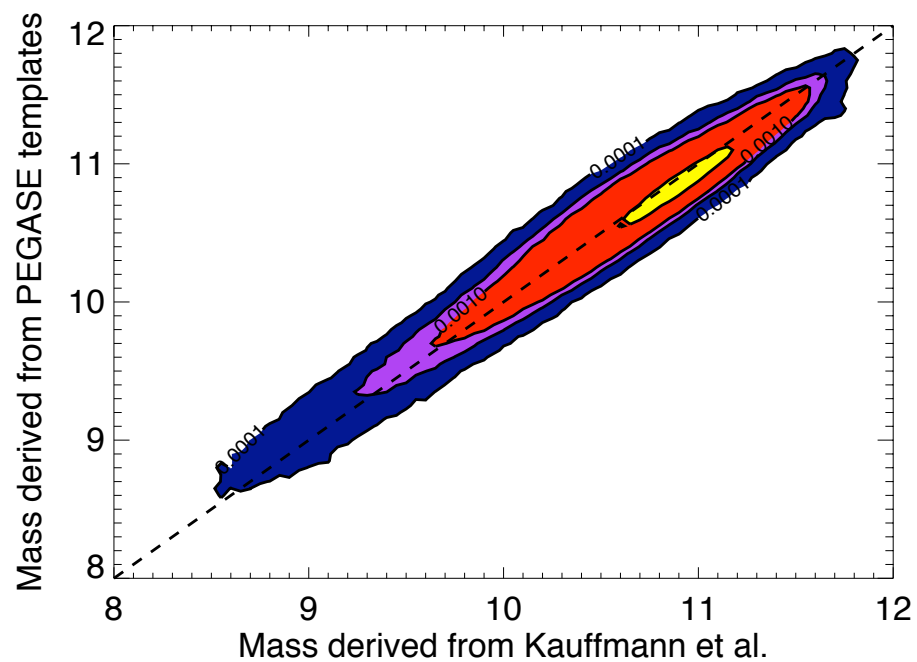


Figure B.1: The mass as estimated from the PÉGASE.2 templates compared to the values determined from [Kauffmann et al. \(2003\)](#). For this analysis the redshift of the object fitted by the PÉGASE.2 SEDs is enforced to be the measured redshift, such that this sample mimics the host galaxy sample. The mass as determined by [Kauffmann et al. \(2003\)](#) is estimated using the strength of the  $4000\text{\AA}$  break feature in each galaxy's spectrum, whilst the estimate from PÉGASE uses the information from the  $u, g, r, i, z$  bands - ensuring that it covers a wider range of the spectrum.

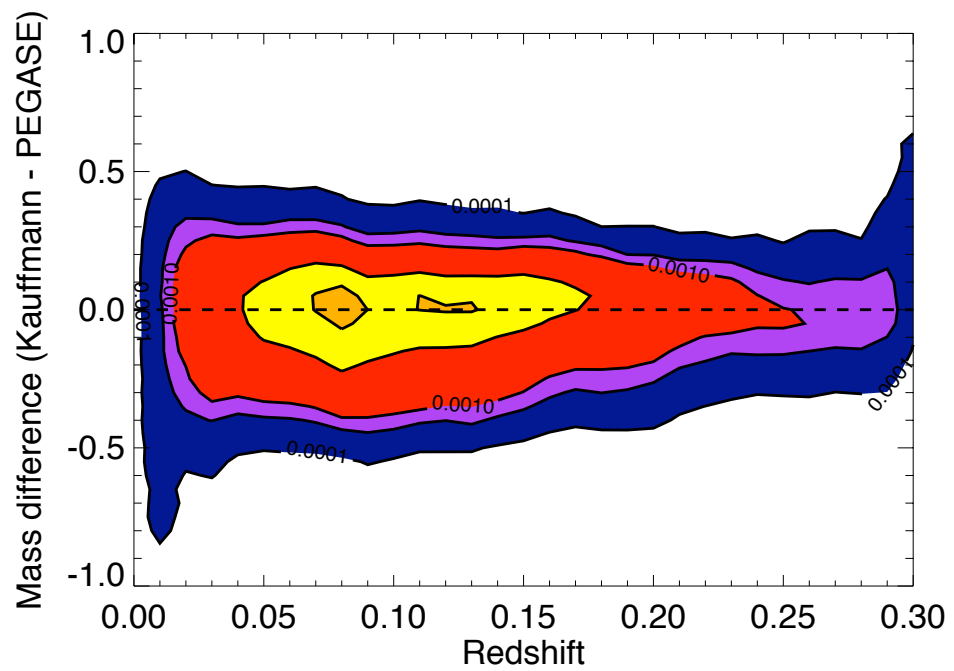


Figure B.2: The difference between the mass as estimated from the PÉGASE.2 templates compared to the values determined by [Kauffmann et al. \(2003\)](#) as a function of the redshift of each object. For this analysis the redshift of the object fitted by the PÉGASE.2 SED's is enforced to be the measured redshift, such that this sample mimics the host galaxy sample. The mass as determined by [Kauffmann et al. \(2003\)](#) is estimated using the strength of the  $4000\text{\AA}$  break feature in each galaxy's spectrum, whilst the estimate from PÉGASE uses the information from the  $u, g, r, i, z$  bands - ensuring that it covers a wider range of the spectrum.

### B.3 The Star-Formation Rate Estimates

Figure's [B.3](#) and [B.4](#) show the distribution of the star-formation rate estimates from the PÉGASE.2 templates when compared to that measured by [Brinchmann et al. \(2004\)](#), and shows the residuals as a function of redshift.

Figure [B.3](#) shows that there is considerable dispersion on this relationship. The star-formation rates as derived from the PÉGASE.2 templates are not statistically different from those derived by [Brinchmann et al. \(2004\)](#), using a spectral feature. However, the correlation between these two parameters is weak, especially compared to that of the mass distribution. It should be noted, that the star-formation rate measured by [Brinchmann et al. \(2004\)](#), using the level of  $H\delta$  absorption, is more a measure of the instantaneous star-formation rate, whilst that obtained from the PÉGASE.2 templates is an estimate of the mean star-formation over the last 0.5 Gyr of the galaxy's existence, and thus are not expected to be perfectly correlated. It is also possible that these differences may be heightened by the lack of the TP-AGB phase of stellar evolution in the evolutionary tracks used by the PÉGASE and [Bruzual & Charlot \(2003\)](#).

This relationship implies that the derived value of the star-formation rate from the SED fitting technique is able to accurately determine whether the galaxy is star-forming or passive (since a negligible proportion of the sample are considered to be passive by the PÉGASE templates), however, the separation between moderately star-forming and highly star-forming galaxies is less well defined, with galaxies being able to easily cross this threshold when errors are considered.

Figure [B.4](#) shows that the mean difference between the two estimated star-formation rates is not zero. Star-formation rates as predicted by the PÉGASE.2 templates are lower than those measured from the  $H\delta$  absorption line by [Brinchmann et al. \(2004\)](#). This is not entirely surprising, since the sample of objects only contains galaxies that show indications of star-formation activity in their spectra today, with no passive galaxies included. The estimate from the PÉGASE.2 templates is the mean value from the last 0.5 Gyr, and since the star-formation rate is unlikely to be constant over that time period, which may include times of passive evolution, will be smaller than the instantaneous rate.

There is an observed increase in the dispersion of this relationship with apparent magnitude. However, since the sample is dominated by objects with  $r \sim 17.5$ , this indicates that for an average galaxy, the star-formation rate estimates from PÉGASE.2 will need to include an error of approximately unity in  $\log\text{SFR}$ . This is consistent with the error

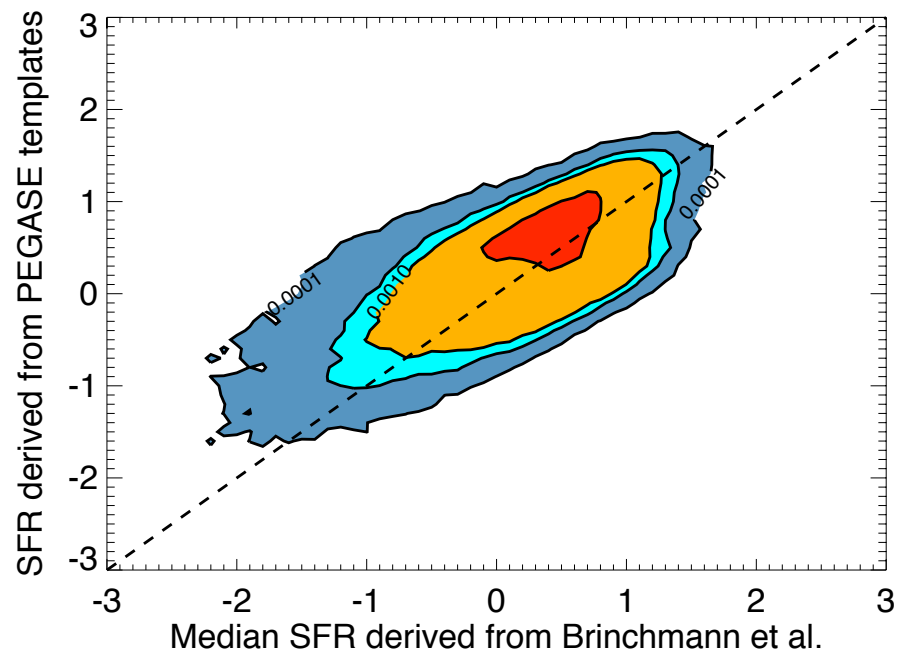


Figure B.3: The star-formation rate as estimated from the PÉGASE.2 templates compared to the median value determined by Brinchmann et al. (2004). For this analysis the redshift of the object fitted by the PÉGASE.2 SEDs is enforced to be the measured redshift, such that this sample mimics the host galaxy sample. The star-formation rate that has been determined by Brinchmann et al. (2004) is estimated through the level of  $H\delta$  absorption in the spectrum of each object, whilst the estimate from PÉGASE uses the information from the  $u, g, r, i, z$  bands - ensuring that it covers a wider range of the spectrum.

values returned by the PÉGASE.2 templates.

Thus, the star-formation rate returned by the template fitting method provides an indication, but not an accurate determination of the ongoing star-formation activity in the galaxy, when compared to results determined from the level of  $H\delta$  absorption in the spectra. As described in §B.1, the estimates of Brinchmann et al. (2004) only cover a small range of the observed spectrum, especially when compared to those produced by PÉGASE, and thus the measurements of the ongoing level of star-formation activity in these systems do take in to account any other features in the spectrum, such as the level of  $H\alpha$  emission. The PÉGASE templates are able to accurately distinguish between passive and star-forming galaxies, but when a split in sSFR is considered, the error values of each galaxy must be considered.

It should also be noted that the method used by Kauffmann et al. (2003) and Brinchmann et al. (2004) to determine the mass and star-formation rates of this set of galaxies is taken using a fiber of  $3''$  in diameter. Since these galaxies are primarily in the local Universe (typically  $z < 0.1$ ), they can be highly extended, and thus the observed spectra, and thus derived measurements, may only be able to determine the properties of the centre of these galaxies. For star-forming galaxies, the vast majority of recent star-formation activity is seen to occur in the spiral arms, and thus this may not be accounted for in the observed spectra.

Nevertheless, we have been able to show that for a set of local galaxies, the estimates of mass and star-formation rate from the PÉGASE.2 templates are similar to those produced by Kauffmann et al. (2003) and Brinchmann et al. (2004), who used different spectral features to determine their estimates. This is especially true for the estimates of mass, and with a small level of scatter, possibly due to the different timescales involved, the galaxy's star-formation rates. These two methods use the same input physics, and thus we have been able to show that the method used to determine the derived properties does not cause a bias in the final result.

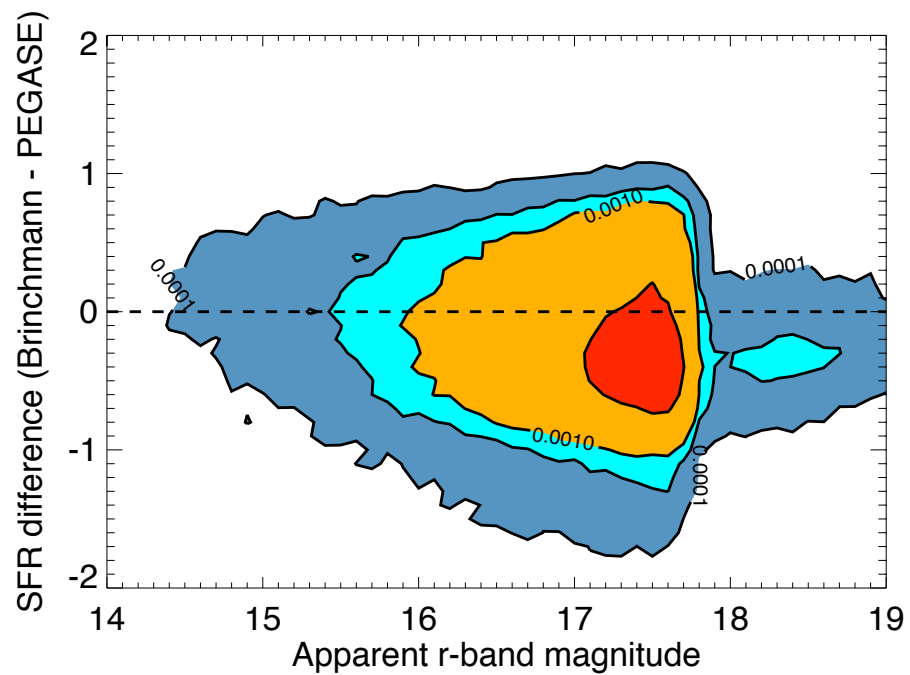


Figure B.4: The difference between the star-formation rates as estimated from the PÉGASE.2 templates compared to the median value determined by Brinchmann et al. (2004) as a function of the redshift of each object. For this analysis the redshift of the object fitted by the PÉGASE.2 SED's is enforced to be the measured redshift, such that this sample mimics the host galaxy sample. The star-formation rate that has been determined by Brinchmann et al. (2004) is estimated through the level of  $H\delta$  absorption in the spectrum of each object, whilst the estimate from PÉGASE uses the information from the  $u, g, r, i, z$  bands - ensuring that it covers a wider range of the spectrum.

# Appendix C

## The Differences in Derived Properties when the Redshift is Known Compared to When it is Left Free

### C.1 Introduction

The photometry of the host galaxy and field samples used in §5 are obtained from the same source, and thus no systematic differences should be introduced. However, whilst the two samples are analysed in similar fashions, with their derived properties calculated from the PÉGASE.2 templates, one difference remains. The redshifts of each object in the host galaxy sample is known, unlike that of the field sample. In this section, we shall investigate the different result produced by the PÉGASE templates for a sample of galaxies whose redshift has been measured. We shall contrast the mass and star-formation rate estimates in the cases where the redshift is considered and when it is left as a free parameter in the fitting process.

An ideal sample to use for this analysis is the SDSS-I spectroscopic sample ([Strauss et al. \(2002\)](#)). Therefore, a sample of over 400,000 galaxies is selected with measured spectral redshifts and magnitudes in each of the SDSS filters. Thus we are able (after correcting the magnitude estimates for galactic extinction) to use the PÉGASE.2 templates to determine the derived properties of these objects in the two cases of interest; when the redshift of each object is considered and when it is left as a free parameter. This sample, however, does not include events at the same magnitude limit as our coadded image, since these events are too faint for measured spectroscopic redshifts. Thus this test provides only an indication of the accuracy of the PÉGASE.2 templates.

## C.2 Differences

Figure's C.1, C.2, C.3 and C.4 show the differences between the derived properties from the PÉGASE.2 templates for a range of outputs.

Figure C.1 shows how the estimated masses for each object are distributed. This relationship shows an extremely tight correlation for objects with high mass estimates, whilst for masses below  $M = 1 \times 10^{11} M_{\odot}$  there is a difference between the mass estimates. The masses are primarily accurate (as shown by the galaxies whose mass estimates are identical), however when differences are seen, the determined masses when the redshift is fixed are higher than that when the redshift is left free. However, this does not represent a large part of the sample ( $\sim 10\%$ ).

Figure C.2 shows the differences between the two estimates discussed in Figure C.1 as a function of the apparent magnitude of the host galaxy as measured in the SDSS  $r$ -band. Here we see that for the vast majority of galaxies, the mass estimates are identical or at least not statistically different. We also see that the observed scatter of these results is small. However, for a small percentage of the sample, the mass estimates differ, such that the mass determined when the redshift is fixed is bigger than when it is free. This plot shows that this effect becomes more prominent for fainter objects (this sample is primarily composed of bright events, and thus a very small fraction of events have  $r > 18$ ), although the mean value of the mass is consistent with that estimated when the redshift is fixed.

Figure C.3 shows the difference between the redshift of each object when estimated by the PÉGASE.2 templates and the known redshift as a function of apparent  $r$ -band magnitude. This plot shows that the redshift as estimated by the template fitting method is smaller than the redshift as measured from the spectra of objects. The difference is not statistically significant. The mean value of this difference is  $\Delta z = 0.02$ , and is identical when calculated as a function of apparent magnitude. The scatter on this difference is seen to increase with increasing magnitudes. This figure seems to follow that seen in Figure C.2 for the mass estimates of the hosts, with the effect seen in the opposite direction. The effect on this conclusion is discussed in §C.3.

Figure C.4 shows the differences between the star-formation rates as estimated by the template fitting process when the redshift is known and when it is left free as a function of apparent magnitude of the object. This figure is similar to those shown above. Objects with no indication of current star-formation activity are not plotted on the figure, although

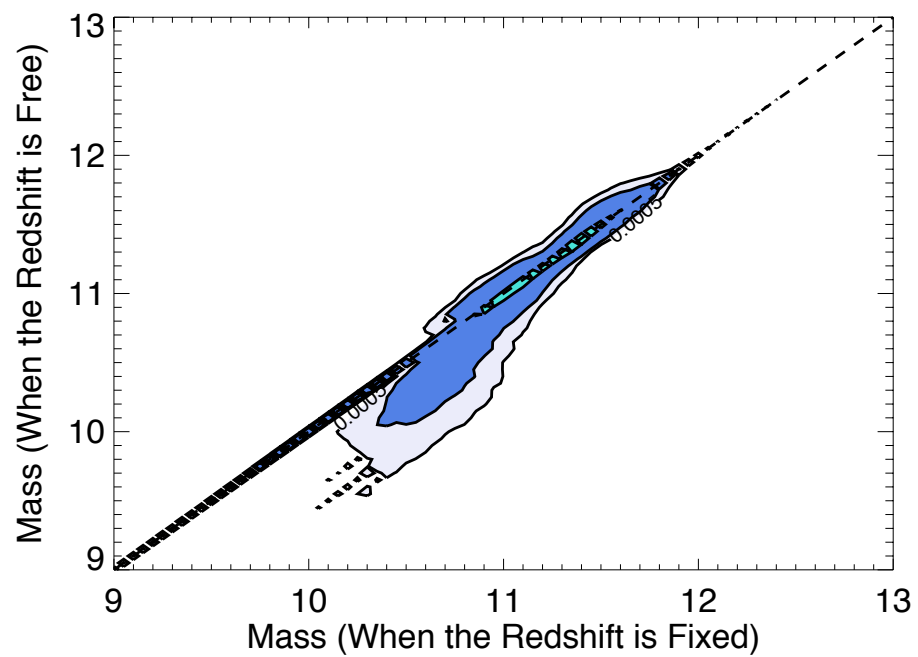


Figure C.1: The mass as estimated from the PÉGASE.2 templates for a sample of objects, whose redshifts have been determined spectroscopically, when the redshift is left as a free parameter in the fitting process compared to the case when the redshift is fixed to its known value. This figure is shown in logarithmic units, of  $1M_{\odot}$ . The contours are the 0.05, 0.5 and 5% levels, respectively.

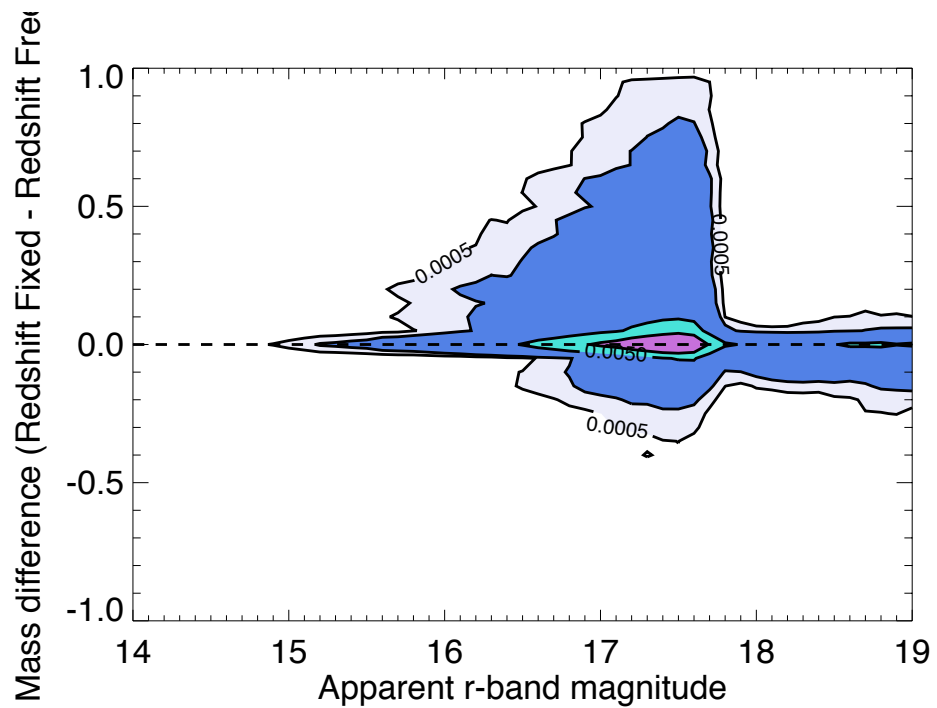


Figure C.2: The mass differences between the estimates from the PÉGASE.2 templates for a sample of objects whose redshifts have been determined spectroscopically, when the redshift is left as a free parameter and when when the redshift is fixed to its known value as a function of the apparent  $r$ -band magnitude. The contours are the 0.05, 0.1, 0.5 and 5% levels, respectively.

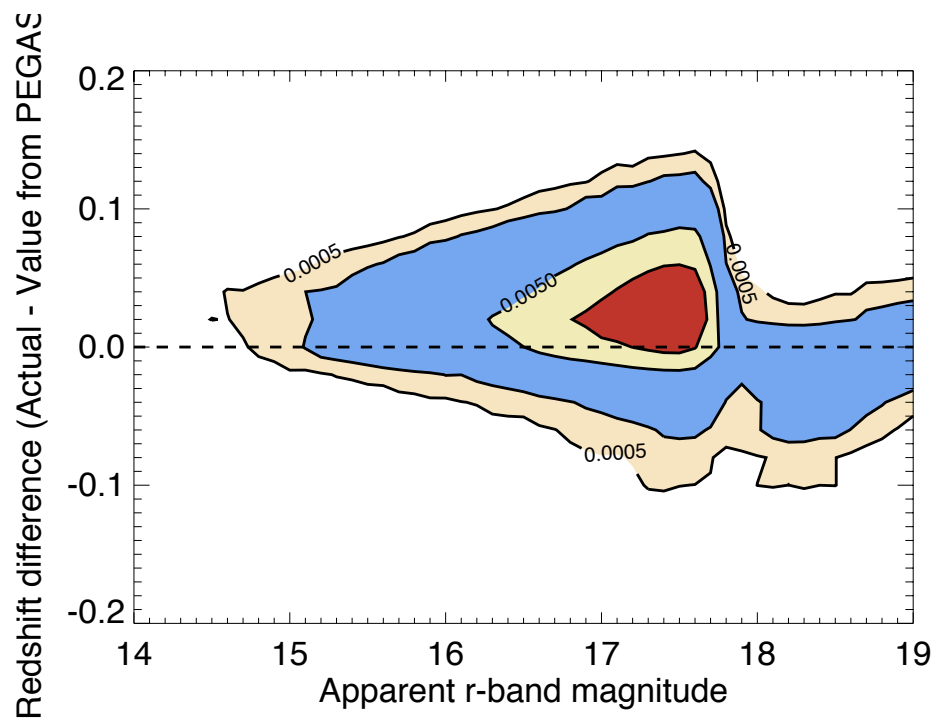


Figure C.3: The difference between the estimated redshift from the PÉGASE.2 templates and the measured redshift as a function of the apparent  $r$ -band magnitude. The contours are the 0.05, 0.1, 0.5 and 5% levels, respectively.

there is little scatter between the determinations when the redshift is fixed or not. This figure shows that the estimated star-formation rates are not especially affected by whether the redshift of the object is known or not, with the differences being small. However, similarly to that seen in Figure’s C.3 and C.2 there is an increase in the observed scatter as the magnitude of the objects increase. This is not unexpected, since these objects are lower signal-to-noise events, and from Figure C.3 the redshift determination of these objects may be incorrect.

### C.3 Summary

In the section above we discussed the differences between the estimated derived properties in the cases where the redshift is fixed or left as a free parameter in the template fitting process. We have shown that there is some indication that the estimates may not be accurate. We found that the redshift determined by PÉGASE is different to that from the spectra, and is lower than the observed value. The scatter on this difference increases as a function of the apparent magnitude of the object, as would be expected since these events have larger uncertainties. By fitting a function to this relationship we find that the differences are  $\Delta z \simeq 0.02$  for all apparent magnitudes. However, by fitting a similar function to the mass differences as shown in Figure C.2, we find that a small difference is seen. By extrapolating this difference to the galaxy field sample used in the analysis of §5, we find that any difference in the number of objects in the field sample, due to this increase in redshift, is offset by the corresponding increase in mass. Since the star-formation rate determination is accurate, or at least is accurately able to distinguish between passive and star-forming objects, this means that the results of §5 are unaffected by this redshift and mass offset. Also, since the differences between the mass estimates are primarily seen in low mass systems (Figure C.1) which contribute a small percentage to the overall sample, and do not significantly affect the total mass of the field sample, these differences do not influence the results seen in §5.3.

This analysis has produced results similar to those found in Appendix A, which used the host galaxy sample to extend this measurement to fainter magnitudes. With results in this Appendix indicating that any offset in the redshift distribution of field galaxies will be offset by a corresponding decrease in their mass, this can be tentatively extended to the field sample used in §5, to suggest that this will not cause a large difference in the results. From Appendix A we also saw that there was considerable scatter in the specific star-formation rate of galaxies when the redshift was allowed to float. Since this scatter

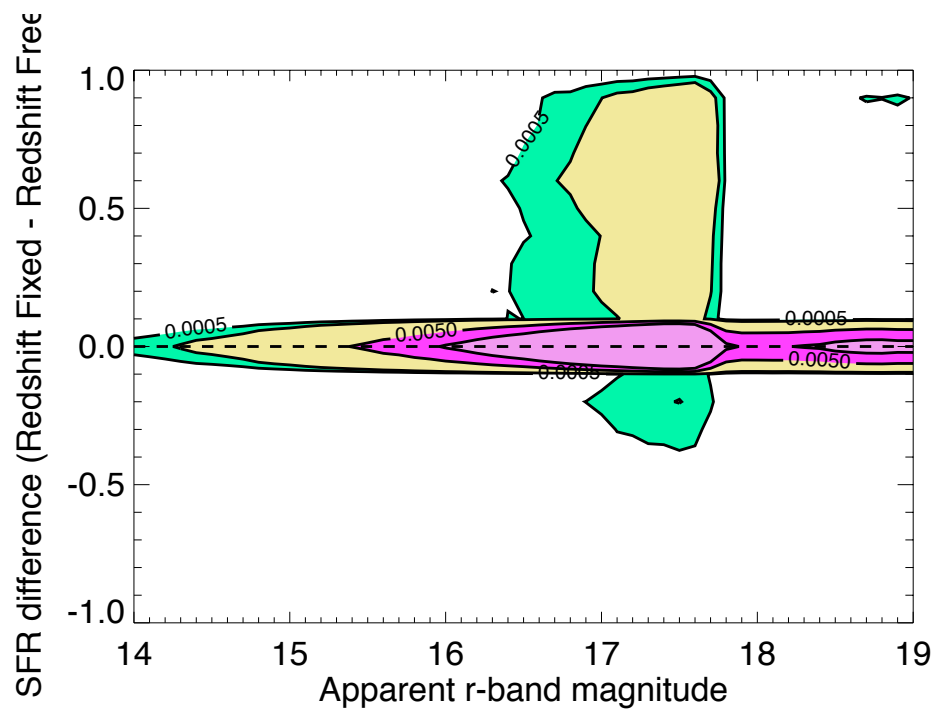


Figure C.4: The difference between the estimated star-formation rate from the PÉGASE.2 templates when the redshift of each object is left as a free parameter and the case where the measured redshift is enforced as a function of the apparent  $r$ -band magnitude for a sample of objects whose redshift has been determined spectroscopically. The contours are the 0.05, 0.1, 0.5 and 5% levels, respectively.

is not obviously skewed, the distribution of galaxies in each galaxy type should not be affected, and thus the results of §5 will not be systematically different.

# Appendix D

## The Influence on the Rest-Wavelength Coverage of the SDSS Filter Bands

### D.1 Introduction

One of the main aims of this work has been to determine the validity of the results found by [Sullivan et al. \(2006b\)](#) when converted to another redshift range. We have shown that there are significant differences.

However, it is possible that any variation in results may be due to the derived properties being systematically different. The SNLS survey detects and measures type Ia supernovae at higher redshifts than the SDSS-II survey, and thus the host galaxy population is primarily found at higher redshifts. The SNLS uses filter bands that cover a similar wavelength range to that of the SDSS filters. It is therefore clear that observed colours of the host galaxies in the sample of [Sullivan et al. \(2006b\)](#) probe a different rest wavelength range to that of objects measured in this work. More precisely, objects detected in the SNLS survey are probed at bluer rest wavelengths than those observed as part of SDSS-II. It is possible that the PÉGASE.2 templates, rigorously tested at high redshift may be biased at lower redshifts, due to the shapes of the template spectra being incorrect. Stellar population models of [Maraston \(2005\)](#) have indicated that the TP-AGB phase of stellar evolution is important in determining stellar masses, and can contribute up to 40% of the bolometric luminosity and 80% to the luminosity in the K-band (and other NIR bands). This phase is not included in the PÉGASE.2 SEDs. Since this phase of stellar evolution is primarily seen in redder parts of the stellar spectrum it is not probed by the objects that comprise the sample of [Sullivan et al. \(2006b\)](#). However, with the SDSS-II survey observing the redder parts of the spectrum, the mass estimates may be systematically different to those of [Sullivan et al. \(2006b\)](#). More discussion of the models of [Maraston](#)

(2005) can be found in §B

Thus to accurately determine if our observed host properties match those of the SNLS survey we need to measure a set of objects in a bluer filter than the SDSS  $u$ -band, in order to mimic the rest wavelength range covered by the SNLS survey. By comparing mass and star-formation estimates for a set of objects whose masses have been calculated both from optical measurements to those whose masses have been calculated from observations at bluer wavelengths, we shall be able to determine if there exists a bias in the mass estimates. For this we shall use the GALEX survey.

## D.2 The GALEX survey

The Galaxy Evolution Explorer (GALEX) (Bianchi & The GALEX Team (1999)) is an orbiting space telescope observing galaxies in ultraviolet filters. This NASA mission is aimed at investigating how star formation in galaxies evolved from the early Universe up to the present day, and images objects in two filters; near-UV (NUV) and far-UV (FUV). This mission has covered the survey area of the SDSS-I survey, and objects have been cross-matched to the nearest primary object from SDSS-I within a radius of  $4''$ .

Thus with the redshift information from the SDSS-I survey, this combined dataset allows us to investigate the effect of using bluer filter sets to mimic the rest wavelength range covered by Sullivan et al. (2006b). Measurements of the magnitude of each object detected in the NUV and SDSS filters was obtained. For this we used the SDSS DR5 data release (Adelman-McCarthy et al. (2007)) to obtain photometry and redshift information for the cross-matched objects. Since the GALEX mission has only covered the SDSS-I area to shallow depths, the matched objects do not cover the same magnitude range of our comparison field sample, and the objects detected are high signal-to-noise events. Thus we will only be able to determine if our estimates of mass and other properties are incorrect for the brightest objects. The combined sample includes over 10,000 galaxies.

For this analysis we shall fit the galaxies with SEDs assuming the spectroscopic redshift. An alternative approach would be to leave this free in the fitting process. However, this is a bright sample of objects, and as we saw in Appendix C the PÉGASE.2 templates are able to accurately estimate the redshift of objects in this case.

### D.3 The Difference Between Six and Five Filters

Figure's [D.1](#) and [D.2](#) show the difference in the mass as estimated by the PÉGASE.2 SEDs when six filters (NUV and *ugriz*) are used and the case where only five are considered (*ugriz*) as a function of apparent magnitude in the *r*-band. These values were obtained by enforcing the redshift in the PÉGASE fitting process to be the redshift of the object.

From these figures, it is clear that the derived parameters as estimated by the PÉGASE.2 SED's do not show significant levels of scatter, when extra filters are considered. In both cases the scatter is seen to be small, with the vast majority of objects following a tight relationship. In the case of the mass estimation, the distribution is slightly skewed, such that the mass obtained when extra information is included in the fitting process is smaller than when only five bands are considered. However, the mean value of this relationship is zero, and no indication of deviation with apparent magnitude is seen.

In the case of the star-formation estimates a tight relationship is also seen. This result is consistent for all magnitudes considered. A small level of scatter is seen. This sample is comprised primarily of star-forming galaxies since a detection is required in the UV part of the spectrum. In both cases the PÉGASE.2 SED's have estimated a negligible proportion of the sample to be passive, indicating that the template fitting method is accurately able to distinguish between passive and star-forming galaxies.

### D.4 Summary

In the above section, we have considered the case where all five SDSS filters are used in the fitting process. An alternative approach would be to compare the estimates of mass and star-formation rates when several filters are excluded. This analysis was carried out in the case where the three bluest SDSS filters were considered. The mass and star-formation rate estimates in this case were compared to those from the section above, and the case where the template fitting was carried out with 4 filters; NUV, *ugr*. In all of these cases, no deviation was seen for both the mass and star-formation rate parameters. The scatter on this relationship was seen to increase when few filters were considered. This is not surprising since a loss of information means that fewer degeneracies can be broken in the template fitting process.

This analysis has shown that for the PÉGASE.2 SEDs, when a different part of the rest

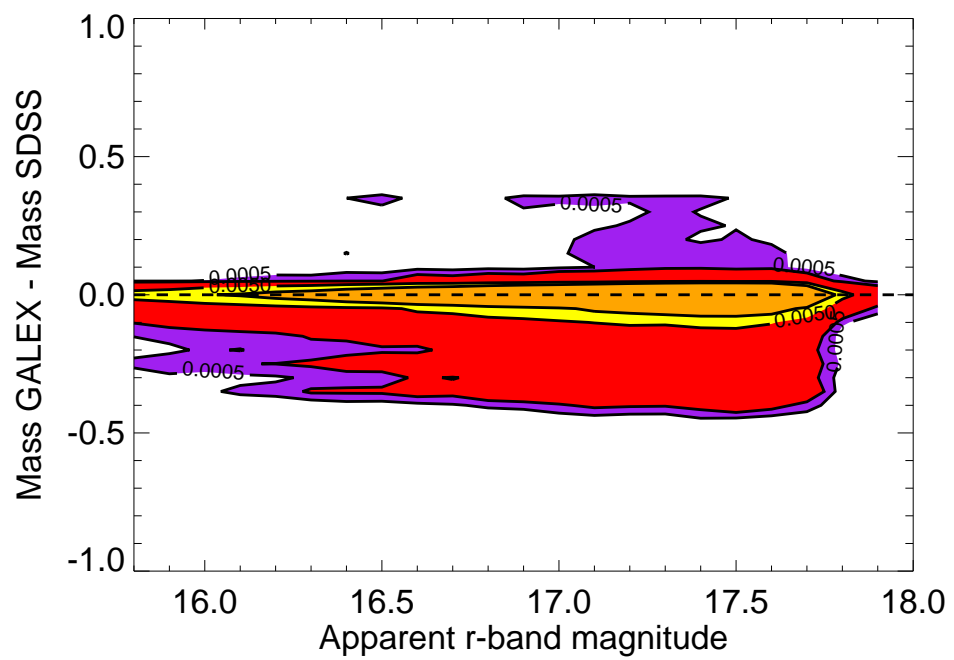


Figure D.1: The difference between the mass estimates as determined when including GALEX data in the fit, and the case where only SDSS data is considered. This is plotted as a function of apparent  $r$ -band magnitude. This plot is the result of fitting when the redshift is constrained to be the spectroscopic redshift from SDSS.

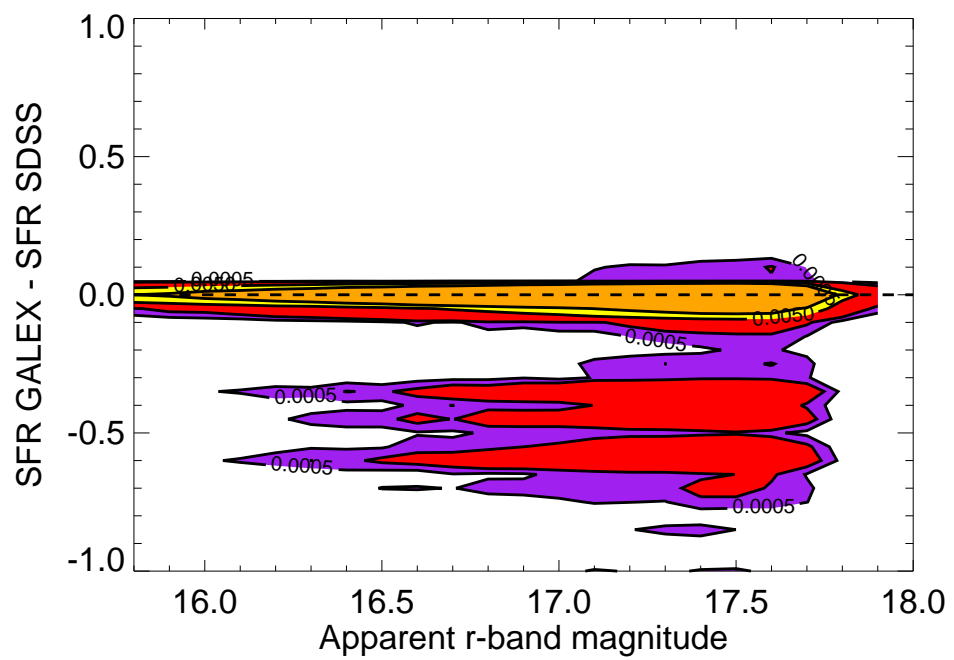


Figure D.2: The difference between the star-formation rate estimates as determined when including GALEX data in the fit, and the case where only SDSS data is considered. This is plotted as a function of apparent  $r$ -band magnitude. This plot is the result of fitting when the redshift is constrained to be the spectroscopic redshift from SDSS.

wavelength spectrum is probed through the introduction or removal of filters in the fitting process then no systematic difference is seen in the mass and star-formation rate estimates. This implies that the derived parameters used in this analysis can be directly compared to those used at higher redshift in the analysis of [Sullivan et al. \(2006b\)](#).

# Appendix E

## Other SED Templates

*This work is carried out in collaboration with Janine Pforr and Dr Claudia Maraston*

In Appendices [A](#), [C](#) and [E](#), we have determined that the photometric quantities determined for the field sample from PÉGASE are offset from the correct values. However, this analysis involves a limited sample of galaxies. However, in order to accurately correct for this, we need to determine if the offsets are constant with apparent magnitude. Ideally, to estimate this, we require a large set of galaxies with known redshift to compare to the photometric redshifts. However, such a sample does not exist. Instead we shall introduce another set of template SED's to compare with the PÉGASE.2 template models.

### E.1 The Maraston Galaxy Templates

In this thesis we have used the PÉGASE.2 model spectra to determine the properties of galaxies in our sample. However, several other template fitting methods are available. These include the models of [Bruzual & Charlot \(2003\)](#). However these models do not fully include the thermally-pulsing asymptotic giant branch (TP-AGB), which is better understood by the models of [Maraston \(2005\)](#).

These models are based on the “Fuel Consumption Theorem”, which calculates the luminosity contribution of each stellar evolutionary phase by the amount of hydrogen and / or helium that is burned. The models include the TP-AGB evolutionary stage of stellar systems, which can often produce younger ages as the best-fit template.

For this analysis we use a variety of template spectra based on the [Maraston \(2005\)](#) models, including star-formation histories of simple stellar populations (initial star-burst

events followed by passive evolution), exponentially declining star-formation rate, truncated star-formation rate (constant star-formation rate followed by no star-formation) and constant star-formation rate for a range of metallicities from a fifth to twice the solar metallicity. A total of thirty-two templates on an age grid of 51 ages is used in the analysis. The model templates are fit to the observed fluxes of galaxies using the publicly available `HYPERZ` code (Bolzonella et al. (2000)) which allows several parameters to be varied in the fitting process. A Kroupa (2001) IMF is used to ensure results that are comparable to those found for the PÉGASE.2 templates.

## E.2 Analysis of the Maraston Models

In Appendix C we introduced a large sample of objects with spectroscopic redshifts, the SDSS-I spectroscopic sample. This sample was used to determine if the derived properties of the PÉGASE.2 SEDs are accurate. We are able to repeat this analysis for the Maraston models. However, since the photometric properties of galaxies using the Maraston models are obtained from the `HYPERZ` code, instead of the `ZPEG` galaxy fitting code, we are only able to determine the accuracy of these models with respect to redshift.

Figure E.1 shows the differences between the spectroscopic and photometric redshifts (produced using the Maraston models) as a function of apparent magnitude for the sample of galaxies described in Appendix C. This figure shows considerable scatter in the redshift determination. However, the mean difference is consistent with zero for all magnitude ranges. For comparison the result for the PÉGASE.2 SED's is shown in Figure E.2. This figure shows the redshift offset of  $\Delta z \sim 0.05$  observed in Appendix A and C.

These results suggest that the redshifts obtained using the Maraston models better reproduce the spectroscopic redshifts than the PÉGASE.2 SEDs for a set of objects with  $r \leq 17.7$ . No deviation from the spectroscopic redshift is observed for these models as a function of apparent magnitude.

### E.2.1 The Difference Between the PEGASE and Maraston Models as a Function of Apparent Magnitude

In Appendix A and C we determined that the derived properties for the comparison field sample are offset from the expected values when a spectroscopic redshift is available. However, the samples used to determine this are either too small or too faint to accurately determine if this offset is constant with apparent magnitude, which is required if

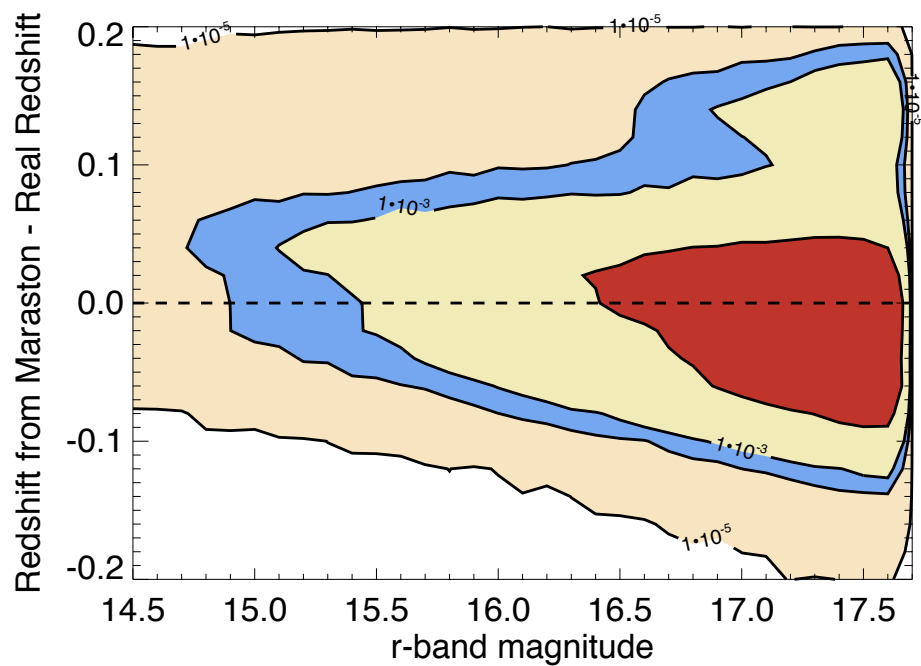


Figure E.1: The differences between the photometric redshift from the Maraston models when compared to the spectroscopic redshift as a function of apparent magnitude for a set of galaxies from the SDSS spectroscopic sample, as described in Appendix C.

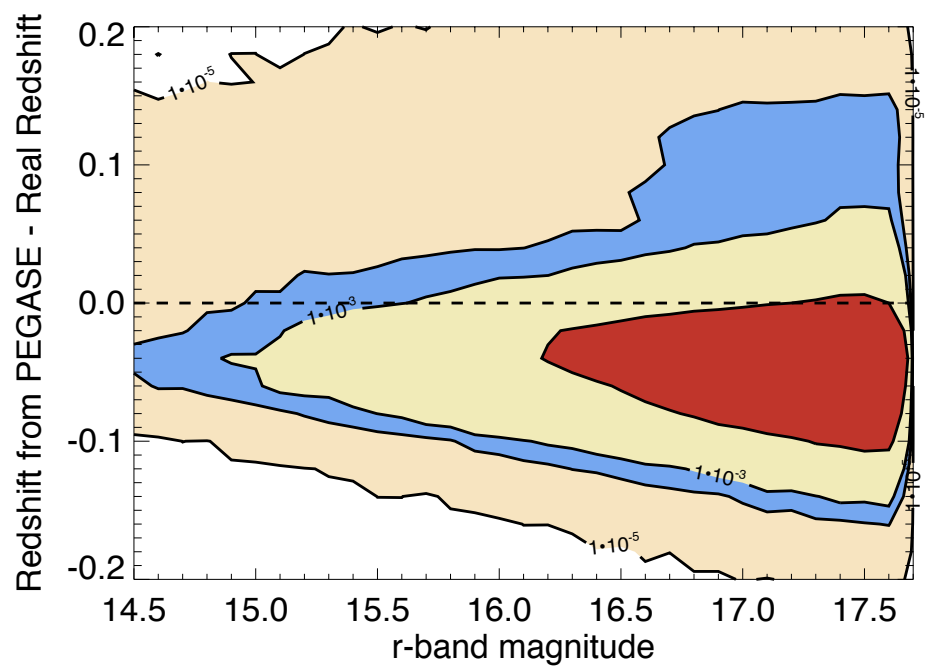


Figure E.2: The differences between the photometric redshift from the PEGASE.2 models when compared to the spectroscopic redshift as a function of apparent magnitude for a set of galaxies from the SDSS spectroscopic sample, as described in Appendix C.

we intend to determine how this offset affects the results in §5.

No large spectroscopic sample is available that covers the magnitude range used for the analysis of §5. However in the section above we determined that the Maraston models are accurately able to determine the redshift of a set of objects with known spectroscopic redshift, and that for this sample of objects the difference between the redshift from the PÉGASE and Maraston models is constant with apparent magnitude. Thus, should the differences between these two methods for determining photometric redshift be constant as a function of apparent magnitude for a sample of fainter objects, it is reasonable to infer that the redshifts obtained from the PÉGASE.2 models are constantly offset as a function of apparent magnitude.

To do this, we obtain photometric redshift estimates using both template SEDs for a sample of the coadded image described in §2.2.1. This image provides the basis for the field sample used in §5.

Figure E.3 shows the difference between these two redshift estimates as a function of apparent magnitude. A constant offset matching that seen in Figure E.2 is observed. This offset of  $\Delta z \simeq 0.05$  suggests that the photometric redshift returned from the PÉGASE.2 SEDs is constantly offset from the value produced using the Maraston models as a function of apparent magnitude. Thus, to correct for this effect, or at least to quantify the error caused by this difference, we can consider the photometric redshifts obtained by the PÉGASE.2 models to be constantly offset by a value of  $\Delta z = 0.045$  from the Maraston models, independent of the apparent magnitude of a galaxy. As observed in Appendix A and C, the mass estimates from the PÉGASE.2 templates are also offset from the actual values. It is impossible to determine if this offset is constant as a function of apparent magnitude. However, since the log mass determination of a galaxy corresponds to its absolute magnitude, which is related to its redshift, we can assume that the log mass offset observed in Appendix A is constant with apparent magnitude in a similar fashion to the redshift estimates.

The effect of this redshift offset on the results obtained in §5 is investigated in Appendix F.

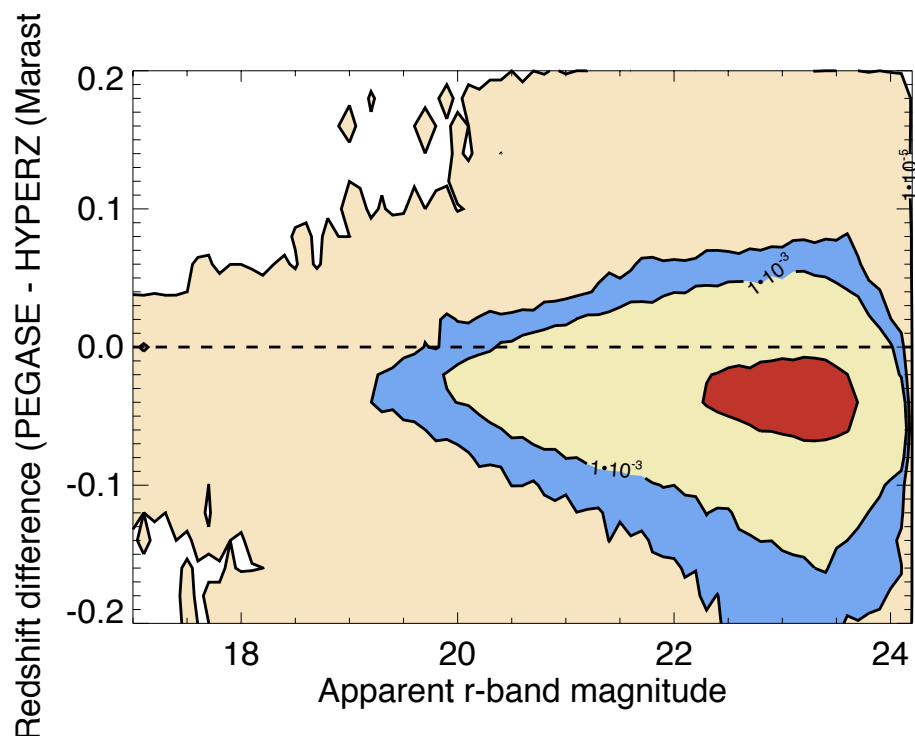


Figure E.3: The differences between the redshift from the PÉGASE.2 models and the Maraston models as a function of apparent magnitude for a set of galaxies from the coadded image described in §2.2.1.

# Appendix F

## The Effect of the Observed Offset

In Appendix [A](#) and [C](#) we determined that the redshift and mass estimates from the PÉGASE.2 SEDs are offset from the values expected when the redshift is known. In Appendix [E](#) we used the Maraston SEDs to infer that this offset is constant as a function of apparent magnitude.

Having identified offsets in the differences between the photometric redshifts produced by the PÉGASE.2 SEDs we can attempt to quantify the effect that these have on our results. This analysis is used to determine whether the results given in [§5](#) are accurate, however, they are unable to accurately determine the systematic error since it is uncertain how the offsets detected in Appendix [A](#) are related to the galaxy type, since it is likely that the best-fit template of a galaxy is likely to change when the redshift is altered. Thus the proportion of passive and star-forming galaxies in our sample will not change in this analysis, but we have no method of determining if this ratio is correct.

To carry out this analysis we use the offsets calculated in Appendix [A](#). That is a redshift offset of  $\Delta z = 0.045$  is applied to each galaxy in the comparison field sample. Further to this, an offset of  $\delta \log \text{Mass} = 0.107$  is applied to each field galaxy. This offset was determined in Appendix [A](#) and is a natural consequence of the increase in redshift of each object.

These alterations to the redshift distribution of galaxies in our field sample will alter the number of objects in the field sample and total mass of this sample. Table [F.1](#) describes the parameters calculated in [§5](#) when both the default field sample is used and when the offsets described above are added to the sample. Both the case where just the offset in redshift is applied, and that when both the redshift and mass offsets are considered. The errors quoted on this table are purely statistical and do not include the Monte-Carlo or

bootstrap analysis described in §5.

The values on this table suggest that the results determined in §5 are robust, especially in the determination of the best-fit gradients for the components of the “A+B” model. By altering the redshift distribution of the field sample the number of galaxies in the sample has been changed. This is partially counteracted by the corresponding change in the mass distribution, which increases the mean mass of galaxies in the sample.

This change in the field sample has altered the value for the type Ia supernova rate in passive galaxies, with both new values obtained being higher than that found in §5. However, neither value is comparable to that found by Sullivan et al. (2006b) of  $4.93 \pm 1.20 \times 10^{-14}$  per unit mass per year. Further to this, unlike that observed by Sullivan et al. (2006b), the type Ia supernova rate shows no indication of being linearly dependent on specific star-formation rate in either case, with all three distributions being well represented by a step function.

In all three cases considered, the best-fit values for  $n_{\text{pass}}$ ,  $n_{\text{SFR}}$  and  $n_{\text{star-forming}}$  (when either  $n_{\text{pass}} = 1$  or the best-fit value of  $n_{\text{pass}}$  is considered) are statistically identical. This implies that these results are robust independent of the redshift distribution of the field sample.

A small variation in the best-fit values of  $A$  and  $B$  is seen when the distribution of the comparison field sample is altered. This is not statistically significant, but is not unexpected, since these values are calculated from the normalisation due to the mass of the field sample.

The values given in Table F.1 show that the redshift and mass offsets detected in Appendix A do not significantly affect the results determined in §5. This analysis has been able to determine the effect of these offsets under the assumption that it is constant with redshift (as inferred from Appendix E), but has not been able to quantify the effect on changes in the star-formation rate, since this is governed by changes in the best-fit templates.

Parameter	Standard Setup <sup>a</sup>	$0.05 < z_{\text{PÉGASE}} + 0.045 < 0.25$ <sup>b</sup>	Corrected Field Sample <sup>c</sup>
# field galaxies	958294	897289	897289
Total field mass <sup>d</sup>	1.61	1.07	1.38
Passive Rate <sup>e f</sup>	$1.49 \pm 0.25$	$2.10 \pm 0.35$	$1.64 \pm 0.27$
$n_{\text{pass}}$ <sup>g</sup>	$0.58 \pm 0.14$	$0.58 \pm 0.13$	$0.51 \pm 0.15$
$n_{\text{SFR}}$ <sup>h i</sup>	$0.85 \pm 0.06$	$0.80 \pm 0.05$	$0.73 \pm 0.07$
$n_{\text{star-forming}}$ <sup>j k</sup>	$0.67 \pm 0.08$	$0.60 \pm 0.08$	$0.60 \pm 0.08$
$n_{\text{star-forming}}$ <sup>l m</sup>	$0.92 \pm 0.10$	$0.85 \pm 0.10$	$0.85 \pm 0.10$
$\log A$ <sup>n o</sup>	$-13.53 \pm 0.20$	$-13.41 \pm 0.20$	$-13.46 \pm 0.20$
$\log B$ <sup>p q</sup>	$-3.01 \pm 0.18$	$-2.92 \pm 0.19$	$-2.92 \pm 0.19$
$\log B$ <sup>r s</sup>	$-2.98 \pm 0.17$	$-2.89 \pm 0.18$	$-2.90 \pm 0.18$

<sup>a</sup>As described throughout this work

<sup>b</sup>When the photometric redshift derived from PÉGASE is offset

<sup>c</sup>When the redshift and mass derived from PÉGASE are corrected for with an offset of  $\Delta z = 0.045$  and  $\Delta \log Mass = 0.107$ .

<sup>d</sup> $\times 10^{16}$

<sup>e</sup>As described in §5.3

<sup>f</sup> $\times 10^{14}$  per unit mass per year

<sup>g</sup>As described in §5.4

<sup>h</sup>When the moderately star-forming and highly star-forming sets are combined

<sup>i</sup>As described in §5.4

<sup>j</sup>When the best-fit value of  $n_{\text{pass}}$  is considered

<sup>k</sup>As described in §5.6

<sup>l</sup>When  $n_{\text{pass}} = 1$  is enforced

<sup>m</sup>As described in §5.6

<sup>n</sup>As derived from the passive component

<sup>o</sup>As described in §5.6

<sup>p</sup>When the best-fit value of  $n_{\text{pass}}$  is considered

<sup>q</sup>As described in §5.6

<sup>r</sup>When  $n_{\text{pass}} = 1$  and the value of A is enforced

<sup>s</sup>As described in §5.6

Table F.1: Values for the parameters described in this work when different comparison field samples are considered. Specifically, the field sample is corrected for the observed redshift offset. The errors quoted on this table are purely statistical and do not include the Monte-Carlo or bootstrap analysis described in §5.

# Appendix G

## List of Supernovae

SDSS ID	RA	Dec.	$\Delta$	Av	Redshift	Origin	fitprob
911	38.691	-0.116	0.024	0.740	0.208	Galaxy Spectrum	0.822
762	15.535	-0.879	-0.173	0.072	0.192	SN Ia spectrum	0.935
779	26.674	-1.021	-0.223	0.161	0.238	Galaxy Spectrum	0.931
822	40.561	-0.862	0.426	0.122	0.211	Lightcurve	0.064
1008	28.278	1.114	-0.280	0.107	0.120	Galaxy Spectrum	0.814
1032	46.796	1.120	0.804	0.235	0.130	SN Ia spectrum	0.415
1241	-22.327	-0.777	-0.001	0.454	0.087	SN Ia spectrum	0.993
1371	-10.626	0.429	-0.194	0.048	0.119	SN Ia spectrum	0.906
1415	6.106	0.599	-0.360	0.399	0.212	Galaxy Spectrum	0.030
1580	45.323	-0.644	-0.228	0.140	0.183	SN Ia spectrum	1.000
1740	5.404	-0.881	0.296	0.105	0.167	Galaxy Spectrum	0.369
2031	-47.957	-1.171	-0.096	0.041	0.153	SN Ia spectrum	0.946
2057	-39.600	-0.317	-0.272	0.623	0.212	Galaxy Spectrum	0.728
2162	15.443	-0.134	0.476	0.063	0.176	Galaxy Spectrum	0.853
2246	50.090	-0.886	-0.178	0.324	0.195	SN Ia spectrum	0.981
2308	34.273	0.280	-0.174	0.013	0.148	SN Ia spectrum	0.951
2319	55.466	0.346	-0.223	0.058	0.159	Lightcurve	0.999
2330	6.807	1.121	0.378	0.157	0.213	SN Ia spectrum	0.884
2372	40.521	-0.541	-0.156	0.383	0.181	SN Ia spectrum	0.989
2440	42.634	0.808	-0.151	0.049	0.193	SN Ia spectrum	0.972
2561	46.343	0.858	-0.083	0.381	0.118	SN Ia spectrum	1.000
2635	52.704	-1.238	-0.275	0.061	0.143	SN Ia spectrum	0.985
2639	-29.536	0.665	-0.118	0.154	0.215	Galaxy Spectrum	0.332
2734	48.207	-0.695	-0.349	0.185	0.155	Galaxy Spectrum	0.862

*continued on next page*

Table G.1: *continued*

SDSS ID	RA	Dec.	$\Delta$	$A_v$	Redshift	Origin	fitprob
2855	16.175	-0.356	-0.066	0.143	0.229	Lightcurve	0.994
2864	-0.549	-1.240	-0.313	0.326	0.244	Galaxy Spectrum	0.371
2916	-44.078	0.570	0.109	0.434	0.124	SN Ia spectrum	0.675
2992	55.497	-0.783	0.042	0.465	0.127	SN Ia spectrum	0.685
3049	-29.777	-1.237	-0.168	0.070	0.168	Galaxy Spectrum	0.880
3077	-30.956	0.215	-0.123	0.721	0.159	Lightcurve	0.919
3080	16.932	-1.040	-0.077	0.121	0.174	SN Ia spectrum	1.000
3087	20.407	-0.977	-0.225	0.230	0.165	SN Ia spectrum	1.000
3256	-30.732	-0.223	-0.056	0.378	0.108	SN Ia spectrum	0.633
3331	34.561	0.797	-0.106	0.443	0.206	SN Ia spectrum	0.839
3377	54.156	1.079	-0.276	0.065	0.245	SN Ia spectrum	0.571
3451	-25.931	0.708	-0.103	0.105	0.250	SN Ia spectrum	0.542
3452	-25.329	0.639	-0.227	0.060	0.230	SN Ia spectrum	0.909
3488	-46.445	-1.010	-0.084	0.570	0.160	Galaxy Spectrum	0.018
3506	-23.749	-0.978	-0.206	0.071	0.211	Lightcurve	0.962
3592	19.052	0.792	-0.088	0.087	0.087	SN Ia spectrum	1.000
3746	10.162	-0.840	-0.125	0.365	0.203	Lightcurve	0.195
3901	14.850	0.003	-0.258	0.169	0.063	SN Ia spectrum	1.000
4019	1.262	1.145	-0.154	0.525	0.181	Galaxy Spectrum	0.876
4281	33.367	-0.968	-0.139	0.337	0.213	Galaxy Spectrum	0.998
4676	18.824	0.788	-0.104	0.105	0.245	Galaxy Spectrum	0.089
4690	32.930	0.688	-0.362	1.503	0.200	Galaxy Spectrum	0.285
5103	-0.116	0.737	-0.033	0.357	0.146	SN Ia spectrum	0.996
5199	-11.208	-0.995	-0.208	0.426	0.248	Lightcurve	0.749
5235	-22.776	0.636	0.206	0.399	0.219	Lightcurve	0.037
5378	37.737	-1.252	-0.084	0.023	0.234	Lightcurve	0.044
5395	49.641	0.123	-0.265	0.082	0.117	SN Ia spectrum	1.000
5533	-31.330	0.413	-0.260	0.290	0.220	SN Ia spectrum	0.919
5549	3.251	0.248	-0.194	0.182	0.121	SN Ia spectrum	0.997
5550	3.598	0.333	-0.307	0.027	0.156	SN Ia spectrum	0.994
5635	-26.817	-0.035	-0.118	0.097	0.180	SN Ia spectrum	0.876
5702	12.583	-0.919	-0.370	0.073	0.223	Lightcurve	0.984
5735	-48.341	0.651	-0.155	0.212	0.225	Lightcurve	0.603
5751	11.634	0.838	-0.225	0.518	0.130	SN Ia spectrum	0.991

*continued on next page*

Table G.1: *continued*

SDSS ID	RA	Dec.	$\Delta$	$A_v$	Redshift	Origin	fitprob
5785	-31.403	0.084	0.456	0.687	0.148	Galaxy Spectrum	0.419
5792	-31.286	-1.238	-0.023	0.343	0.248	Lightcurve	0.329
5890	-27.484	0.609	-0.106	0.085	0.177	Galaxy Spectrum	1.000
5916	5.437	-0.325	0.031	0.223	0.172	SN Ia spectrum	0.985
5959	38.060	-0.308	-0.110	0.143	0.198	Galaxy Spectrum	0.930
5963	11.081	0.479	-0.133	0.207	0.236	Galaxy Spectrum	0.997
5994	-47.398	-0.168	-0.186	0.190	0.187	SN Ia spectrum	0.991
6057	52.554	-0.975	0.054	0.425	0.067	SN Ia spectrum	1.000
6295	23.673	-0.605	1.484	0.127	0.080	SN Ia spectrum	0.026
6304	26.498	1.196	-0.104	0.478	0.190	SN Ia spectrum	0.902
6406	46.089	-1.063	-0.106	0.220	0.125	SN Ia spectrum	1.000
6422	-10.861	-0.663	-0.206	0.046	0.184	SN Ia spectrum	0.935
6479	-39.593	0.584	-0.043	0.165	0.236	Galaxy Spectrum	0.888
6491	16.649	0.543	0.024	0.100	0.232	Lightcurve	0.034
6530	14.329	0.021	0.707	0.119	0.151	Lightcurve	0.614
6558	21.702	-1.238	-0.226	0.090	0.057	SN Ia spectrum	0.999
6614	26.647	0.867	0.626	0.578	0.169	Galaxy Spectrum	0.249
6780	-31.931	0.267	0.386	0.307	0.202	SN Ia spectrum	0.994
6861	-10.568	-1.114	0.024	0.799	0.190	Galaxy Spectrum	0.281
6933	11.352	1.076	-0.180	0.261	0.213	SN Ia spectrum	0.871
6936	-36.766	-0.700	-0.158	0.230	0.181	SN Ia spectrum	0.901
7092	-43.720	1.221	0.065	0.094	0.225	Galaxy Spectrum	0.975
7102	-35.380	-0.616	-0.040	0.034	0.196	Galaxy Spectrum	0.048
7147	-9.982	-0.055	0.411	0.217	0.110	SN Ia spectrum	0.363
7243	-31.921	0.472	-0.243	0.145	0.204	SN Ia spectrum	0.994
7335	-41.115	-0.355	0.444	0.216	0.198	SN Ia spectrum	0.639
7363	17.964	-0.782	-0.314	0.368	0.180	Galaxy Spectrum	0.440
7444	27.703	0.430	-0.256	0.182	0.250	Galaxy Spectrum	0.898
7473	4.326	-0.257	-0.070	0.068	0.216	SN Ia spectrum	0.808
7479	7.226	-0.409	0.269	0.172	0.207	Lightcurve	0.794
7512	52.090	-0.326	-0.252	0.295	0.219	SN Ia spectrum	0.511
7527	-24.744	-1.204	-0.369	0.703	0.237	Galaxy Spectrum	0.933
7847	32.460	-0.062	-0.142	0.563	0.212	SN Ia spectrum	0.888
7876	19.183	0.795	-0.354	0.125	0.076	SN Ia spectrum	0.296

*continued on next page*

Table G.1: *continued*

SDSS ID	RA	Dec.	$\Delta$	$A_v$	Redshift	Origin	fitprob
8213	-2.479	-0.921	0.172	0.669	0.185	SN Ia spectrum	0.861
8254	-8.836	0.820	-0.136	0.396	0.189	Galaxy Spectrum	0.012
8297	24.975	0.692	-0.239	0.304	0.249	Lightcurve	0.759
8495	-24.739	-0.748	-0.294	0.107	0.214	SN Ia spectrum	0.882
10559	-5.883	-1.227	-0.060	0.320	0.241	Lightcurve	0.693
8555	2.916	-0.415	0.110	0.405	0.198	Galaxy Spectrum	0.312
8719	7.721	-0.719	-0.327	0.135	0.116	SN Ia spectrum	0.233
9052	21.041	-0.483	-0.228	0.142	0.237	Lightcurve	0.940
9467	-31.049	1.181	0.172	0.191	0.218	SN Ia spectrum	0.357
9739	-36.306	-0.879	-0.289	0.856	0.204	Lightcurve	0.939
9954	6.584	-0.425	0.128	0.124	0.228	Galaxy Spectrum	0.595
10106	47.693	-0.205	-0.230	0.605	0.147	SN Ia spectrum	0.163
12780	-37.845	1.228	-0.060	0.488	0.050	SN Ia spectrum	0.139
12804	18.202	1.040	-0.128	0.142	0.130	Galaxy Spectrum	0.959
12843	-36.122	-0.980	0.186	0.459	0.167	SN Ia spectrum	0.997
12853	-43.235	0.723	0.145	0.127	0.169	SN Ia spectrum	0.524
12856	-27.135	0.756	-0.215	0.054	0.172	SN Ia spectrum	0.950
12860	-36.306	1.176	-0.133	0.519	0.122	SN Ia spectrum	0.755
12874	-6.035	-0.177	-0.256	0.084	0.245	SN Ia spectrum	0.356
12898	26.793	-0.147	-0.053	0.257	0.084	SN Ia spectrum	0.989
12930	-50.317	-0.475	-0.267	0.080	0.148	SN Ia spectrum	0.999
12950	-8.333	-0.840	-0.089	0.147	0.083	SN Ia spectrum	0.114
12977	13.696	-0.251	-0.116	0.142	0.247	SN Ia spectrum	0.994
12978	7.167	0.148	-0.340	0.156	0.166	Lightcurve	0.999
12987	25.534	0.129	-0.356	0.449	0.237	Lightcurve	0.982
13016	25.589	0.980	0.087	0.098	0.246	Lightcurve	0.796
13025	-18.433	0.416	-0.173	0.263	0.224	SN Ia spectrum	0.672
13038	-12.173	0.505	-0.279	0.047	0.101	SN Ia spectrum	0.997
13044	-27.457	0.503	0.044	0.044	0.126	SN Ia spectrum	0.998
13045	-14.975	0.538	-0.250	0.177	0.181	SN Ia spectrum	0.760
13064	-16.327	-1.140	-0.138	0.145	0.233	Lightcurve	0.970
13070	-2.215	-0.746	-0.273	0.042	0.199	SN Ia spectrum	0.718
13072	-25.041	0.024	-0.093	0.055	0.231	SN Ia spectrum	0.677
13152	7.052	0.118	-0.276	0.318	0.203	SN Ia spectrum	0.954

*continued on next page*

Table G.1: *continued*

SDSS ID	RA	Dec.	$\Delta$	$A_v$	Redshift	Origin	fitprob
13174	13.235	0.448	0.015	0.059	0.236	SN Ia spectrum	0.989
13224	47.495	-0.246	-0.208	0.382	0.236	Galaxy Spectrum	0.881
13254	42.059	-0.347	-0.171	0.138	0.181	SN Ia spectrum	0.073
13305	-28.900	0.691	-0.314	0.122	0.214	SN Ia spectrum	0.770
13323	-36.949	-0.135	-0.073	0.229	0.246	Lightcurve	0.779
13354	27.565	-0.887	-0.283	0.359	0.158	SN Ia spectrum	0.352
13411	-44.810	0.192	-0.260	0.146	0.163	Galaxy Spectrum	0.980
13432	-41.547	-1.076	0.767	0.342	0.173	Lightcurve	0.624
13506	25.243	-0.728	-0.200	0.215	0.245	SN Ia spectrum	0.055
13578	17.395	0.704	0.099	0.101	0.200	SN Ia spectrum	0.413
13615	-48.588	1.187	-0.077	0.357	0.250	Lightcurve	0.964
13641	-14.781	-0.981	-0.291	0.163	0.220	SN Ia spectrum	0.831
14157	51.137	1.022	-0.146	0.059	0.214	SN Ia spectrum	0.055
13689	4.016	0.808	-0.226	0.038	0.250	Galaxy Spectrum	0.870
13703	39.014	1.253	-0.070	0.274	0.240	Galaxy Spectrum	0.608
13716	-45.046	0.488	0.241	0.210	0.235	Lightcurve	0.208
13727	-42.412	0.933	-0.308	0.098	0.226	SN Ia spectrum	0.227
13736	-23.167	1.031	-0.385	0.077	0.150	SN Ia spectrum	0.956
13740	-48.783	-1.089	-0.291	0.290	0.247	Lightcurve	0.494
13768	-36.924	-0.763	0.061	0.134	0.246	Lightcurve	0.739
13796	-9.308	0.533	-0.270	0.104	0.145	SN Ia spectrum	0.981
13813	-41.679	-0.405	0.110	0.068	0.242	Lightcurve	0.305
13835	6.060	-0.248	-0.193	0.102	0.248	SN Ia spectrum	0.706
13840	-46.294	0.125	-0.179	0.368	0.240	Galaxy Spectrum	0.015
13894	1.691	-0.037	-0.220	0.592	0.125	SN Ia spectrum	0.881
13896	2.713	-0.070	-0.027	0.382	0.207	Lightcurve	0.019
13907	14.179	0.232	-0.061	0.648	0.200	Galaxy Spectrum	0.838
14019	-43.358	-0.648	-0.085	0.065	0.216	SN Ia spectrum	0.580
14024	-41.801	0.916	0.566	0.276	0.200	SN Ia spectrum	0.826
14108	53.595	-1.123	-0.121	0.168	0.123	SN Ia spectrum	0.571
14113	28.445	-0.818	0.335	0.631	0.168	Lightcurve	0.037
14206	17.395	0.704	0.082	0.116	0.222	Lightcurve	0.407
14212	-29.530	1.045	0.057	0.208	0.205	SN Ia spectrum	0.828
14231	57.650	0.788	0.067	0.188	0.168	Lightcurve	0.924

*continued on next page*

Table G.1: *continued*

SDSS ID	RA	Dec.	$\Delta$	$A_v$	Redshift	Origin	fitprob
14284	49.049	-0.601	0.165	0.105	0.181	SN Ia spectrum	0.229
14317	-44.429	0.330	-0.040	0.407	0.181	Galaxy Spectrum	0.999
14377	48.264	-0.472	-0.116	0.404	0.140	SN Ia spectrum	0.536
14402	54.285	0.236	-0.292	1.265	0.214	Lightcurve	0.086
14437	-27.919	-1.196	-0.257	0.129	0.149	SN Ia spectrum	0.914
14444	-23.298	-0.816	0.232	0.084	0.247	Lightcurve	0.861
14445	-19.037	-0.754	0.575	0.208	0.238	Galaxy Spectrum	0.260
14463	3.145	-0.350	-0.194	0.225	0.209	Lightcurve	0.962
14470	44.215	-0.352	-0.028	0.270	0.179	Lightcurve	0.493
14525	16.883	0.477	-0.183	0.565	0.150	Galaxy Spectrum	0.839
14549	8.181	0.963	-0.167	0.671	0.240	Lightcurve	0.031
14561	46.699	0.950	0.855	0.761	0.160	Lightcurve	0.593
14750	34.519	0.653	-0.097	0.394	0.219	Lightcurve	0.713
14784	-36.202	-0.348	-0.175	0.226	0.192	Galaxy Spectrum	0.340
14816	-23.284	0.506	0.104	0.430	0.107	SN Ia spectrum	0.189
14846	7.663	0.142	-0.208	0.111	0.225	SN Ia spectrum	0.985
14871	54.277	0.009	-0.300	0.044	0.128	SN Ia spectrum	0.991
14979	54.946	0.993	-0.107	0.090	0.177	SN Ia spectrum	0.951
14984	-46.166	-0.093	-0.312	0.288	0.197	SN Ia spectrum	0.249
15055	58.499	-0.052	0.052	0.135	0.182	Lightcurve	0.950
15057	17.881	0.409	0.708	0.082	0.191	SN Ia spectrum	0.165
15132	-30.300	0.198	-0.253	0.024	0.144	SN Ia spectrum	0.589
15136	-8.837	-0.718	0.041	0.537	0.149	SN Ia spectrum	0.073
15160	-1.571	-0.579	0.062	0.655	0.221	Lightcurve	0.930
15161	35.843	0.819	-0.055	0.294	0.250	SN Ia spectrum	0.194
15201	-22.481	0.004	0.270	0.116	0.209	SN Ia spectrum	0.252
15203	15.735	0.183	-0.339	0.202	0.204	SN Ia spectrum	0.992
15219	34.611	0.227	-0.012	0.057	0.247	SN Ia spectrum	0.918
15222	2.853	0.703	0.178	0.376	0.199	SN Ia spectrum	0.958
15229	4.832	1.091	-0.231	0.161	0.227	SN Ia spectrum	0.083
15234	16.958	0.828	-0.230	0.449	0.136	SN Ia spectrum	0.908
15259	-22.456	-0.408	-0.136	0.253	0.210	SN Ia spectrum	0.536
15260	-20.823	-0.276	-0.254	0.504	0.230	Lightcurve	1.000
15272	-9.227	0.084	0.226	0.417	0.217	Lightcurve	0.524

*continued on next page*

Table G.1: *continued*

SDSS ID	RA	Dec.	$\Delta$	$A_v$	Redshift	Origin	fitprob
15325	32.298	-0.742	0.054	0.069	0.214	Galaxy Spectrum	0.846
15343	-36.328	0.685	0.501	0.875	0.174	Galaxy Spectrum	0.962
15359	-12.544	0.311	-0.094	0.449	0.235	Lightcurve	0.032
15365	-5.443	1.249	-0.256	0.025	0.188	SN Ia spectrum	0.625
15369	-11.167	-0.563	-0.213	0.155	0.245	SN Ia spectrum	0.805
15419	19.905	0.886	-0.111	0.319	0.244	Lightcurve	0.969
15421	33.742	0.603	-0.109	0.104	0.185	SN Ia spectrum	0.947
15425	55.561	0.478	-0.226	0.149	0.160	SN Ia spectrum	0.094
15433	14.880	-0.257	-0.085	0.126	0.220	SN Ia spectrum	0.691
15443	49.868	-0.318	-0.308	0.048	0.182	SN Ia spectrum	0.212
15448	52.380	-1.147	-0.348	0.487	0.227	Lightcurve	0.930
15453	-40.332	-1.024	-0.324	0.066	0.148	SN Ia spectrum	0.999
15459	-19.299	-0.902	-0.190	0.378	0.125	SN Ia spectrum	0.632
15461	-33.153	-0.495	-0.067	0.132	0.180	SN Ia spectrum	0.980
15466	-42.355	-0.123	0.089	0.392	0.246	SN Ia spectrum	0.765
15467	-39.980	-0.177	-0.212	0.053	0.210	Galaxy Spectrum	0.811
15496	8.074	0.275	-0.278	0.082	0.239	Lightcurve	0.924
15508	27.169	-0.577	-0.320	0.055	0.146	SN Ia spectrum	0.999
15583	37.731	0.946	-0.062	0.385	0.175	SN Ia spectrum	0.905
15587	54.417	0.998	-0.172	0.174	0.219	Galaxy Spectrum	0.101
15648	-46.282	-0.195	0.279	0.715	0.175	SN Ia spectrum	0.194
15674	-19.171	0.263	0.114	0.113	0.197	SN Ia spectrum	0.365
15675	-16.826	0.364	0.180	0.111	0.220	Galaxy Spectrum	0.895
15722	55.351	1.195	-0.072	0.166	0.190	Galaxy Spectrum	0.331
15748	48.115	-0.131	0.379	0.086	0.156	Galaxy Spectrum	0.831
15806	24.092	-0.831	0.457	0.286	0.250	Galaxy Spectrum	0.684
15823	-45.747	0.199	-0.167	0.071	0.215	Galaxy Spectrum	0.938
15850	0.668	-1.165	0.214	0.182	0.232	Lightcurve	0.510
15872	36.722	-0.328	-0.300	0.137	0.185	SN Ia spectrum	0.075
15892	-36.801	0.689	0.173	0.805	0.185	Galaxy Spectrum	0.431
15897	11.682	-1.033	0.812	0.069	0.175	SN Ia spectrum	0.699
15901	31.976	-0.535	-0.187	0.139	0.171	SN Ia spectrum	0.436
15909	11.315	0.797	0.014	0.264	0.218	Galaxy Spectrum	0.030
15994	11.932	0.100	0.884	0.276	0.215	Lightcurve	0.141

*continued on next page*

Table G.1: *continued*

SDSS ID	RA	Dec.	$\Delta$	$A_v$	Redshift	Origin	fitprob
16021	13.844	-0.389	-0.149	0.257	0.095	SN Ia spectrum	0.347
16032	44.069	-0.411	0.129	0.131	0.195	SN Ia spectrum	0.432
16052	58.600	-0.721	-0.264	0.761	0.142	Lightcurve	0.964
16073	8.108	-1.054	-0.202	0.142	0.153	SN Ia spectrum	0.982
16100	30.436	-1.032	0.013	0.203	0.190	SN Ia spectrum	0.535
16103	-47.025	-1.050	0.086	0.244	0.202	Galaxy Spectrum	0.340
16111	-30.683	0.935	-0.195	0.300	0.228	Lightcurve	0.954
16152	46.909	0.988	-0.342	0.219	0.249	Lightcurve	0.729
16163	31.499	-0.856	0.797	0.225	0.160	Galaxy Spectrum	0.338
16185	16.868	-0.269	0.703	0.177	0.097	SN Ia spectrum	0.994
16199	-27.056	1.135	-0.182	0.610	0.231	Lightcurve	0.342
16259	-7.970	0.856	0.412	0.399	0.119	SN Ia spectrum	0.154
16276	20.579	1.011	-0.200	0.159	0.160	SN Ia spectrum	0.995
16302	-28.233	0.184	-0.191	0.081	0.198	Lightcurve	1.000
16452	-37.443	-0.282	-0.340	1.577	0.161	Lightcurve	0.100
16462	17.041	-0.386	0.487	0.231	0.245	Galaxy Spectrum	0.084
16466	-40.592	0.103	0.053	0.038	0.188	Galaxy Spectrum	0.018
16768	-37.299	0.693	1.347	0.381	0.143	Lightcurve	0.022

Table G.1: Table of a list of objects passing the selection criteria described in §3.2, including the parameters  $\Delta$  and  $A_v$  derived from the MLCS light-curve fitter

# Appendix H

## Properties of the Host Galaxies in this Analysis

SDSS Id	Redshift	Mass	SFR	sSFR	Template
703	0.300	10.002	0.437	-9.565	Sd
911	0.208	10.287	0.800	-9.487	Sb
762	0.192	11.023	0.381	-10.642	S0
779	0.238	10.102	0.925	-9.177	S0
822	0.211	9.801	-0.841	-10.642	S0
841	0.292	10.060	0.573	-9.487	S0
1008	0.120	9.954	-99.000	-99.000	Elliptical
1032	0.130	10.466	-99.000	-99.000	Elliptical
1112	0.258	11.157	1.288	-9.869	S0
1166	0.382	10.874	-99.000	-99.000	Elliptical
1241	0.087	10.525	-99.000	-99.000	S0
1253	0.262	11.013	-99.000	-99.000	Elliptical
1342	0.284	9.477	-0.375	-9.852	Sa
1371	0.119	10.764	-99.000	-99.000	S0
1415	0.212	11.461	-99.000	-99.000	S0
1580	0.183	10.362	-99.000	-99.000	Elliptical
1658	0.266	9.573	0.665	-8.908	S0
1688	0.359	10.244	1.084	-9.159	Sa
1740	0.167	10.705	-99.000	-99.000	S0
1921	0.367	9.679	0.286	-9.393	S0
2017	0.262	10.414	0.545	-9.869	S0
2031	0.153	9.278	-0.105	-9.383	Irr

*continued on next page*

Table H.1: *continued*

SDSS Id	Redshift	Mass	SFR	sSFR	Template
2057	0.212	10.158	0.671	-9.487	S0
2081	0.259	9.940	0.758	-9.183	Sbc
2162	0.176	10.920	-99.000	-99.000	S0
2165	0.288	9.393	0.216	-9.177	S0
2246	0.195	10.899	0.257	-10.642	S0
2308	0.148	10.263	-99.000	-99.000	Elliptical
2319	0.159	8.828	-0.542	-9.370	Elliptical
2330	0.213	9.764	0.075	-9.688	S0
2372	0.181	10.311	-0.331	-10.642	S0
2422	0.265	8.898	0.088	-8.810	Elliptical
2440	0.193	10.399	1.024	-9.376	Sb
2532	0.270	11.184	-99.000	-99.000	Elliptical
2533	0.340	9.693	-0.202	-9.895	Elliptical
2561	0.118	10.636	-0.006	-10.642	S0
2632	0.296	10.231	1.054	-9.177	S0
2635	0.143	9.907	0.730	-9.177	S0
2639	0.215	10.821	0.179	-10.642	S0
2734	0.155	8.574	-0.623	-9.197	Elliptical
2784	0.382	10.219	1.042	-9.177	S0
2789	0.290	10.774	-99.000	-99.000	Elliptical
2806	0.259	10.804	-99.000	-99.000	Elliptical
2855	0.229	9.360	-0.443	-9.803	Elliptical
2864	0.244	10.396	-99.000	-99.000	Elliptical
2871	0.313	11.160	-99.000	-99.000	S0
2916	0.124	9.855	1.045	-8.810	Elliptical
2943	0.265	8.826	0.195	-8.632	Elliptical
2992	0.127	9.954	-0.006	-9.960	Elliptical
3049	0.168	9.888	0.248	-9.640	Elliptical
3077	0.159	8.960	-0.569	-9.529	Sc
3080	0.174	10.790	0.148	-10.642	S0
3087	0.165	9.393	0.196	-9.197	Elliptical
3195	0.300	10.869	-99.000	-99.000	Elliptical
3199	0.251	8.592	-0.040	-8.632	Elliptical
3241	0.259	11.231	1.205	-10.026	S0

*continued on next page*

Table H.1: *continued*

SDSS Id	Redshift	Mass	SFR	sSFR	Template
3256	0.108	9.719	0.233	-9.487	S0
3331	0.206	10.740	0.098	-10.642	S0
3368	0.327	9.310	0.064	-9.245	Sd
3377	0.245	9.142	0.333	-8.810	Elliptical
3417	0.260	9.664	-99.000	-99.000	Elliptical
3451	0.250	10.732	0.090	-10.642	S0
3452	0.230	9.177	0.171	-9.006	Elliptical
3488	0.160	9.832	-99.000	-99.000	Elliptical
3506	0.211	8.717	-0.289	-9.006	Elliptical
3535	0.308	10.286	0.101	-10.185	Elliptical
3592	0.087	10.470	-0.097	-10.567	Elliptical
3746	0.203	9.354	0.177	-9.177	S0
3881	0.318	9.847	-0.119	-9.966	Sa
3892	0.350	11.490	-99.000	-99.000	Elliptical
3901	0.063	9.739	0.243	-9.496	Irr
3945	0.263	9.539	0.169	-9.370	Elliptical
3975	0.395	10.676	0.648	-10.028	Elliptical
3983	0.287	9.804	0.754	-9.050	S0
4019	0.181	10.856	0.987	-9.869	S0
4028	0.316	10.245	-0.397	-10.642	S0
4035	0.341	11.130	-99.000	-99.000	Elliptical
4044	0.382	9.562	0.277	-9.285	Sbc
4046	0.277	8.912	-0.891	-9.803	Elliptical
4059	0.300	10.025	0.740	-9.285	Sbc
4079	0.416	10.379	1.089	-9.291	S0
4181	0.290	10.554	1.178	-9.376	Sb
4236	0.343	10.319	0.832	-9.487	S0
4241	0.332	9.018	0.386	-8.632	Elliptical
4281	0.213	9.124	0.314	-8.810	Elliptical
4307	0.272	9.029	0.023	-9.006	Elliptical
4311	0.295	10.614	1.026	-9.588	Sbc
4360	0.324	8.647	-0.723	-9.370	Elliptical
4572	0.407	10.793	-99.000	-99.000	Elliptical
4577	0.363	10.425	-0.218	-10.642	S0

*continued on next page*

Table H.1: *continued*

SDSS Id	Redshift	Mass	SFR	sSFR	Template
4578	0.334	10.949	0.306	-10.642	S0
4676	0.245	10.005	0.136	-9.869	S0
4679	0.332	9.434	0.526	-8.908	S0
4690	0.200	10.359	-99.000	-99.000	Elliptical
4714	0.433	9.328	-0.312	-9.640	Elliptical
4757	0.424	9.714	0.537	-9.177	S0
4803	0.398	10.620	0.751	-9.869	S0
5103	0.146	9.228	0.178	-9.050	S0
5199	0.248	9.459	0.408	-9.050	S0
5235	0.219	9.285	-0.172	-9.457	Sd
5378	0.234	9.607	0.354	-9.253	Sb
5395	0.117	8.877	0.245	-8.632	Elliptical
5468	0.281	10.110	-99.000	-99.000	Elliptical
5473	0.280	10.932	-99.000	-99.000	Elliptical
5524	0.320	10.544	1.152	-9.393	S0
5533	0.220	9.760	0.582	-9.177	S0
5543	0.332	11.533	1.849	-9.684	Sb
5549	0.121	8.489	-0.065	-8.553	S0
5550	0.156	9.311	0.771	-8.540	Elliptical
5635	0.180	9.559	0.651	-8.908	S0
5702	0.223	8.923	0.113	-8.810	Elliptical
5717	0.252	9.040	0.408	-8.632	Elliptical
5731	0.376	8.780	-0.030	-8.810	Elliptical
5735	0.225	9.632	-99.000	-99.000	Elliptical
5736	0.253	8.858	0.108	-8.749	S0
5737	0.393	9.783	0.624	-9.159	Sa
5751	0.130	10.495	-0.147	-10.642	S0
5785	0.148	11.697	-99.000	-99.000	S0
5792	0.248	8.992	-0.206	-9.197	Elliptical
5802	0.287	9.003	0.458	-8.545	Elliptical
5803	0.276	9.375	-0.585	-9.960	Elliptical
5844	0.311	9.234	0.602	-8.632	Elliptical
5890	0.177	10.582	-0.060	-10.642	S0
5916	0.172	10.713	0.071	-10.642	S0

*continued on next page*

Table H.1: *continued*

SDSS Id	Redshift	Mass	SFR	sSFR	Template
5917	0.262	7.916	-0.904	-8.820	Irr
5957	0.280	10.129	0.326	-9.803	Elliptical
5959	0.198	10.853	0.211	-10.642	S0
5963	0.236	10.099	0.706	-9.393	S0
5993	0.377	10.927	-99.000	-99.000	Elliptical
5994	0.187	8.153	-0.744	-8.897	Irr
6055	0.404	9.015	-0.471	-9.487	S0
6057	0.067	9.992	0.815	-9.177	S0
6108	0.260	9.044	0.499	-8.545	Elliptical
6275	0.273	10.674	0.031	-10.642	S0
6192	0.272	9.237	0.691	-8.545	Elliptical
6196	0.281	10.900	-99.000	-99.000	Elliptical
6225	0.337	9.475	0.567	-8.908	S0
6249	0.294	10.025	0.866	-9.159	Sa
6282	0.369	10.847	-99.000	-99.000	Elliptical
6295	0.080	10.847	-99.000	-99.000	S0
6304	0.190	10.798	1.025	-9.773	Sb
6315	0.267	9.102	0.544	-8.558	Elliptical
6406	0.125	10.216	0.187	-10.028	Elliptical
6422	0.184	9.521	0.613	-8.908	S0
6479	0.236	10.279	0.410	-9.869	S0
6491	0.232	10.846	0.818	-10.028	Elliptical
6501	0.350	10.197	0.804	-9.393	S0
6530	0.151	9.803	-99.000	-99.000	Elliptical
6558	0.057	9.403	0.226	-9.177	S0
6560	0.291	9.540	0.791	-8.749	S0
6614	0.169	10.749	0.880	-9.869	S0
6618	0.307	9.524	-99.000	-99.000	Elliptical
6649	0.314	8.989	0.081	-8.908	S0
6699	0.311	10.375	-0.192	-10.567	Elliptical
6714	0.414	9.483	0.526	-8.957	Sa
6780	0.202	8.699	-0.677	-9.376	Sb
6807	0.295	10.945	0.303	-10.642	S0
6813	0.286	10.209	-99.000	-99.000	Elliptical

*continued on next page*

Table H.1: *continued*

SDSS Id	Redshift	Mass	SFR	sSFR	Template
6851	0.305	11.115	0.473	-10.642	S0
6861	0.190	9.920	-0.266	-10.185	Elliptical
6889	0.295	10.154	-99.000	-99.000	Elliptical
6903	0.253	11.109	-99.000	-99.000	Elliptical
6912	0.357	10.480	1.080	-9.400	Sa
6914	0.415	10.584	0.399	-10.185	Elliptical
6933	0.213	8.232	-0.517	-8.749	Irr
6936	0.181	9.888	0.084	-9.803	Elliptical
6939	0.315	10.986	-99.000	-99.000	Elliptical
7205	0.314	8.659	-0.538	-9.197	Elliptical
7051	0.330	10.981	-99.000	-99.000	Elliptical
7092	0.225	10.605	0.579	-10.026	S0
7102	0.196	10.661	1.174	-9.487	Sb
7119	0.323	10.322	0.634	-9.688	S0
7143	0.304	10.576	0.893	-9.684	Sb
7147	0.110	10.291	-99.000	-99.000	Elliptical
7243	0.204	8.930	0.120	-8.810	Elliptical
7258	0.256	10.919	-99.000	-99.000	Elliptical
7304	0.257	7.605	-0.987	-8.591	Irr
7335	0.198	11.010	-99.000	-99.000	Elliptical
7357	0.401	10.756	-99.000	-99.000	Elliptical
7363	0.180	10.484	-99.000	-99.000	Elliptical
7365	0.401	10.643	1.319	-9.325	Sa
7373	0.282	10.709	1.127	-9.582	Sc
7431	0.350	11.016	-99.000	-99.000	Elliptical
7444	0.250	10.085	0.059	-10.026	S0
7473	0.216	9.375	-1.267	-10.642	S0
7475	0.322	8.490	-0.076	-8.566	Elliptical
7479	0.207	11.067	-99.000	-99.000	Elliptical
7512	0.219	9.711	-0.185	-9.895	Elliptical
7527	0.237	10.424	0.842	-9.582	Sc
7550	0.332	9.016	0.447	-8.569	S0
7636	0.400	9.495	0.318	-9.177	S0
7644	0.310	9.953	0.889	-9.065	Sa

*continued on next page*

Table H.1: *continued*

SDSS Id	Redshift	Mass	SFR	sSFR	Template
7654	0.387	9.239	0.649	-8.590	S0
7656	0.336	10.400	-99.000	-99.000	Elliptical
7701	0.360	10.331	1.087	-9.244	Sa
7712	0.382	10.390	-0.253	-10.642	S0
7717	0.329	10.222	-0.420	-10.642	S0
7779	0.381	9.236	0.127	-9.109	Sb
7802	0.305	10.577	-99.000	-99.000	Elliptical
7803	0.395	10.927	0.285	-10.642	S0
7824	0.291	10.870	-99.000	-99.000	Elliptical
7847	0.212	10.336	-0.231	-10.567	Elliptical
7857	0.415	10.119	1.055	-9.065	Sa
7876	0.076	10.537	0.888	-9.650	Sbc
7884	0.344	10.800	-99.000	-99.000	Elliptical
7947	0.368	11.382	-99.000	-99.000	Elliptical
7954	0.255	10.791	0.922	-9.869	S0
8030	0.422	9.440	0.532	-8.908	S0
8046	0.259	11.070	-99.000	-99.000	Elliptical
8092	0.327	8.573	0.033	-8.540	Elliptical
8114	0.375	10.932	-99.000	-99.000	Elliptical
8118	0.412	10.060	0.667	-9.393	S0
8138	0.334	10.720	-99.000	-99.000	Elliptical
8165	0.319	10.579	0.012	-10.567	Elliptical
8213	0.185	10.287	-99.000	-99.000	S0
8226	0.430	8.747	0.196	-8.551	Elliptical
8254	0.189	9.626	0.576	-9.050	S0
8280	0.356	11.186	1.869	-9.316	Sb
8297	0.249	8.332	-0.219	-8.551	Elliptical
8323	0.422	9.151	0.086	-9.065	Sa
8351	0.432	10.417	-0.225	-10.642	S0
8495	0.214	10.714	0.845	-9.869	S0
10559	0.241	10.424	-0.218	-10.642	S0
8555	0.198	9.960	0.588	-9.372	Sbc
8598	0.361	10.081	1.031	-9.050	S0
8607	0.260	9.836	0.583	-9.253	Sb

*continued on next page*

Table H.1: *continued*

SDSS Id	Redshift	Mass	SFR	sSFR	Template
8679	0.294	8.555	-0.330	-8.885	Sd
8700	0.390	10.108	0.783	-9.325	Sa
8705	0.371	10.056	0.569	-9.487	S0
8707	0.395	9.753	0.429	-9.325	Sa
8719	0.116	8.590	-0.042	-8.632	Elliptical
8793	0.385	10.857	-99.000	-99.000	Elliptical
9032	0.254	8.814	0.263	-8.551	Elliptical
9045	0.390	10.651	1.258	-9.393	S0
9052	0.237	7.861	-0.849	-8.711	Irr
9109	0.259	9.233	-0.407	-9.640	Elliptical
9117	0.307	8.683	-0.323	-9.006	Elliptical
9155	0.304	10.292	0.899	-9.393	S0
9218	0.268	9.911	-0.656	-10.567	Elliptical
9326	0.350	11.011	0.369	-10.642	S0
9334	0.329	9.188	-0.103	-9.291	S0
9467	0.218	10.466	-0.177	-10.642	S0
9594	0.298	10.802	-99.000	-99.000	Elliptical
9739	0.204	11.376	1.668	-9.707	Sbc
9817	0.254	10.480	0.611	-9.869	S0
9895	0.323	10.259	-0.383	-10.642	S0
9954	0.228	9.974	0.410	-9.565	Sd
10106	0.147	9.444	-0.452	-9.895	Elliptical
10113	0.294	8.262	-0.296	-8.558	Elliptical
10450	0.299	10.092	0.361	-9.732	Sa
10550	0.300	10.561	0.973	-9.588	Sbc
11306	0.256	11.082	0.440	-10.642	S0
11864	0.303	8.615	-0.342	-8.957	Sa
12780	0.050	10.173	-99.000	-99.000	Elliptical
12804	0.130	9.477	0.300	-9.177	S0
12843	0.167	11.004	-99.000	-99.000	Elliptical
12852	0.264	10.971	0.689	-10.283	S0
12853	0.169	10.592	1.105	-9.487	Sb
12856	0.172	10.291	1.001	-9.291	S0
12860	0.122	10.410	0.127	-10.283	S0

*continued on next page*

Table H.1: *continued*

SDSS Id	Redshift	Mass	SFR	sSFR	Template
12874	0.245	10.842	1.154	-9.688	S0
12879	0.395	9.877	0.718	-9.159	Sa
12898	0.084	10.080	0.222	-9.859	Sb
12930	0.148	11.020	1.370	-9.650	Sbc
12950	0.083	9.721	0.656	-9.065	Sa
12972	0.261	9.180	-0.317	-9.496	Irr
12977	0.247	9.527	0.778	-8.749	S0
12987	0.237	10.484	-99.000	-99.000	Elliptical
13016	0.246	9.304	0.060	-9.244	Sa
13025	0.224	10.950	1.301	-9.650	Sbc
13044	0.126	9.672	0.495	-9.177	S0
13045	0.181	10.324	-0.243	-10.567	Elliptical
13064	0.233	10.169	-99.000	-99.000	Elliptical
13070	0.199	10.194	0.904	-9.291	S0
13072	0.231	9.985	1.236	-8.750	Sa
13073	0.320	9.870	-99.000	-99.000	Elliptical
15386	0.262	10.758	-99.000	-99.000	Elliptical
13096	0.363	9.955	0.778	-9.177	S0
13098	0.279	8.729	-0.179	-8.908	S0
13108	0.258	10.090	0.062	-10.028	Elliptical
13136	0.372	9.766	-0.086	-9.852	Sa
13144	0.278	7.818	-1.002	-8.820	Irr
13152	0.203	9.270	-0.226	-9.496	Irr
13168	0.370	9.208	-0.162	-9.370	Elliptical
13174	0.236	10.787	0.144	-10.642	S0
13224	0.236	10.409	-99.000	-99.000	Elliptical
13254	0.181	10.011	0.834	-9.177	S0
13305	0.214	10.059	0.882	-9.177	S0
13323	0.246	10.168	0.883	-9.285	Sbc
13329	0.320	8.622	-0.335	-8.957	Sa
13354	0.158	10.690	1.006	-9.684	Sb
13411	0.163	9.290	-0.110	-9.400	Sa
13432	0.173	10.023	0.154	-9.869	S0
13441	0.276	11.053	-99.000	-99.000	Elliptical

*continued on next page*

Table H.1: *continued*

SDSS Id	Redshift	Mass	SFR	sSFR	Template
13460	0.301	9.206	0.457	-8.749	S0
13474	0.328	10.031	-99.000	-99.000	S0
13476	0.308	9.854	0.563	-9.291	S0
13477	0.407	9.870	0.761	-9.109	Sb
13491	0.377	10.034	0.970	-9.065	Sa
13495	0.304	10.036	-99.000	-99.000	Elliptical
13506	0.245	10.374	0.786	-9.588	Sbc
13554	0.329	9.928	0.684	-9.244	Sa
13578	0.200	8.675	-1.098	-9.773	Sb
13615	0.250	10.201	-99.000	-99.000	Elliptical
13633	0.416	11.655	-99.000	-99.000	Elliptical
13641	0.220	8.904	-0.736	-9.640	Elliptical
13646	0.300	9.715	0.690	-9.025	Sb
13649	0.317	8.810	-0.830	-9.640	Elliptical
14157	0.214	10.847	0.662	-10.185	Elliptical
13675	0.289	8.141	-0.669	-8.811	Sc
13689	0.250	10.528	1.155	-9.372	Sbc
13703	0.240	11.024	0.382	-10.642	S0
13716	0.235	9.436	0.605	-8.831	S0
13727	0.226	9.684	0.853	-8.831	S0
13729	0.332	8.963	0.397	-8.566	Elliptical
13736	0.150	9.499	0.209	-9.291	S0
13737	0.348	10.750	-99.000	-99.000	Elliptical
13740	0.247	8.960	0.150	-8.810	Elliptical
13757	0.289	8.890	0.080	-8.810	Elliptical
13768	0.246	8.700	-0.306	-9.006	Elliptical
13796	0.145	10.118	0.632	-9.487	S0
13813	0.242	10.109	-99.000	-99.000	Elliptical
13835	0.248	10.619	1.037	-9.582	Sc
13840	0.240	11.128	0.486	-10.642	S0
13843	0.429	8.106	-0.497	-8.603	Elliptical
13859	0.330	8.563	-0.247	-8.810	Elliptical
13861	0.376	9.439	0.279	-9.159	Sa
13864	0.270	10.650	-99.000	-99.000	Elliptical

*continued on next page*

Table H.1: *continued*

SDSS Id	Redshift	Mass	SFR	sSFR	Template
13867	0.334	10.589	-99.000	-99.000	Elliptical
13894	0.125	9.269	-0.599	-9.869	S0
13896	0.207	9.040	-0.010	-9.050	S0
13907	0.200	10.646	-99.000	-99.000	Elliptical
13908	0.288	11.144	-99.000	-99.000	Elliptical
13934	0.330	10.657	0.631	-10.026	S0
13952	0.346	11.190	-99.000	-99.000	Elliptical
13956	0.262	10.334	-99.000	-99.000	Elliptical
14019	0.216	9.679	0.869	-8.810	Elliptical
14024	0.200	10.218	0.034	-10.184	Sa
14074	0.313	9.663	1.110	-8.553	S0
14093	0.255	10.274	-99.000	-99.000	Elliptical
14108	0.123	8.450	-1.353	-9.803	Elliptical
14113	0.168	9.916	-0.366	-10.283	S0
14206	0.222	8.897	-0.300	-9.197	Elliptical
14212	0.205	10.393	0.316	-10.077	Sa
14231	0.168	9.479	-0.132	-9.611	Sd
14250	0.395	10.323	0.923	-9.400	Sa
14261	0.286	9.396	0.213	-9.183	Sbc
14268	0.259	9.485	-0.080	-9.565	Sd
14279	0.045	10.526	-0.116	-10.642	S0
14284	0.181	10.494	-0.073	-10.567	Elliptical
14298	0.268	9.322	0.032	-9.291	S0
14303	0.278	10.713	0.070	-10.642	S0
14304	0.322	9.509	-0.014	-9.523	Sbc
14317	0.181	10.772	0.489	-10.283	S0
14322	0.389	9.029	0.072	-8.957	Sa
14333	0.271	10.627	-99.000	-99.000	Elliptical
14340	0.290	11.477	-99.000	-99.000	S0
14342	0.387	10.898	-99.000	-99.000	Elliptical
14343	0.278	9.886	0.709	-9.177	S0
14347	0.291	8.463	-0.495	-8.957	Sa
14357	0.423	9.415	-0.868	-10.283	S0
14375	0.321	10.781	0.215	-10.567	Elliptical

*continued on next page*

Table H.1: *continued*

SDSS Id	Redshift	Mass	SFR	sSFR	Template
14377	0.140	10.610	0.447	-10.162	S0
14397	0.386	10.629	1.143	-9.487	S0
14402	0.214	10.228	-99.000	-99.000	Elliptical
14403	0.293	10.030	0.341	-9.688	S0
14404	0.391	10.972	-99.000	-99.000	Elliptical
14437	0.149	9.935	-0.707	-10.642	S0
14444	0.247	10.551	-99.000	-99.000	Elliptical
14445	0.238	10.854	-99.000	-99.000	Elliptical
14453	0.348	9.913	0.736	-9.177	S0
14463	0.209	8.667	-0.658	-9.325	Sa
14467	0.351	9.286	0.236	-9.050	S0
14470	0.179	10.098	-99.000	-99.000	S0
14522	0.407	11.139	1.366	-9.773	Sb
14524	0.274	10.616	0.589	-10.026	S0
14525	0.150	10.165	0.577	-9.588	Sbc
14528	0.348	8.887	-0.448	-9.335	Sc
14531	0.363	10.034	0.183	-9.852	Sa
14539	0.386	10.930	1.078	-9.852	Sa
14545	0.278	11.398	-99.000	-99.000	S0
14548	0.304	10.126	0.835	-9.291	S0
14549	0.240	10.446	-0.197	-10.642	S0
14561	0.160	9.053	-1.514	-10.567	Elliptical
14588	0.379	9.563	0.498	-9.065	Sa
14589	0.270	11.086	-99.000	-99.000	Elliptical
14617	0.262	10.120	-0.522	-10.642	S0
14708	0.348	10.780	-99.000	-99.000	Elliptical
14735	0.301	10.468	0.886	-9.582	Sc
14750	0.219	9.831	-0.028	-9.859	Sb
14760	0.321	11.271	-99.000	-99.000	Elliptical
14763	0.343	10.658	-99.000	-99.000	Elliptical
14784	0.192	10.337	0.152	-10.185	Elliptical
14786	0.330	10.423	-99.000	-99.000	Elliptical
14809	0.319	10.365	0.180	-10.185	Elliptical
14816	0.107	10.498	0.210	-10.287	Sa

*continued on next page*

Table H.1: *continued*

SDSS Id	Redshift	Mass	SFR	sSFR	Template
14823	0.320	11.075	-99.000	-99.000	Elliptical
14846	0.225	10.747	0.562	-10.185	Elliptical
14871	0.128	9.277	-0.194	-9.471	Sc
14888	0.325	9.686	1.020	-8.666	S0
14900	0.437	10.035	0.548	-9.487	S0
14965	0.255	9.823	0.773	-9.050	S0
14979	0.177	9.968	0.677	-9.291	S0
14984	0.197	10.401	1.008	-9.393	S0
15002	0.380	9.368	0.318	-9.050	S0
15009	0.295	11.309	-99.000	-99.000	S0
15055	0.182	8.416	-0.649	-9.065	Sa
15057	0.191	8.978	-0.029	-9.006	Elliptical
15075	0.372	10.852	-99.000	-99.000	Elliptical
15103	0.380	10.830	0.188	-10.642	S0
15108	0.412	9.718	0.761	-8.957	Sa
15132	0.144	9.455	0.624	-8.831	S0
15136	0.149	11.195	1.512	-9.684	Sb
15137	0.273	10.386	0.103	-10.283	S0
15291	0.311	9.931	0.444	-9.487	S0
15160	0.221	9.919	0.629	-9.291	S0
15161	0.250	10.775	0.747	-10.028	Elliptical
15198	0.291	9.591	0.683	-8.908	S0
15201	0.209	11.144	-99.000	-99.000	S0
15203	0.204	10.115	-0.528	-10.642	S0
15213	0.311	10.507	0.819	-9.688	S0
15219	0.247	10.814	0.172	-10.642	S0
15222	0.199	11.152	-99.000	-99.000	Elliptical
15229	0.227	9.170	-0.326	-9.496	Irr
15234	0.136	10.321	0.632	-9.688	S0
15259	0.210	9.111	-0.577	-9.688	S0
15260	0.230	10.187	0.161	-10.026	S0
15263	0.387	10.739	-99.000	-99.000	Elliptical
15264	0.314	10.376	1.004	-9.372	Sbc
15268	0.266	9.494	0.174	-9.320	Irr

*continued on next page*

Table H.1: *continued*

SDSS Id	Redshift	Mass	SFR	sSFR	Template
15272	0.217	10.961	-99.000	-99.000	S0
15287	0.274	10.387	-99.000	-99.000	Elliptical
15289	0.360	10.566	-99.000	-99.000	Elliptical
15294	0.347	10.185	-99.000	-99.000	Elliptical
15301	0.296	10.310	0.745	-9.565	Sd
15325	0.214	10.637	-99.000	-99.000	Elliptical
15343	0.174	10.681	0.039	-10.642	S0
15345	0.259	10.511	1.024	-9.487	S0
15351	0.341	10.767	1.179	-9.588	Sbc
15353	0.310	11.066	-99.000	-99.000	Elliptical
15356	0.275	10.159	-99.000	-99.000	Elliptical
15357	0.281	9.776	-0.083	-9.859	Sb
15359	0.235	10.082	0.553	-9.529	Sc
15363	0.345	9.907	1.354	-8.553	S0
15365	0.188	10.891	0.249	-10.642	S0
15366	0.308	10.500	-99.000	-99.000	Elliptical
15369	0.245	9.800	-0.482	-10.283	S0
15401	0.329	10.362	-99.000	-99.000	Elliptical
15417	0.312	9.529	-0.059	-9.588	Sb
15419	0.244	9.441	-1.126	-10.567	Elliptical
15421	0.185	10.174	0.801	-9.372	Sbc
15423	0.328	10.227	0.740	-9.487	S0
15425	0.160	10.417	-0.150	-10.567	Elliptical
15433	0.220	10.760	0.118	-10.642	S0
15436	0.344	9.718	0.536	-9.183	Sbc
15440	0.262	10.589	-0.054	-10.642	S0
15443	0.182	10.477	0.889	-9.588	Sbc
15448	0.227	10.633	0.764	-9.869	S0
15453	0.148	8.772	-0.519	-9.291	S0
15456	0.382	10.781	0.912	-9.869	S0
15459	0.125	8.850	0.040	-8.810	Elliptical
15461	0.180	10.167	0.139	-10.028	Elliptical
15466	0.246	10.454	0.766	-9.688	S0
15467	0.210	10.397	1.220	-9.177	S0

*continued on next page*

Table H.1: *continued*

SDSS Id	Redshift	Mass	SFR	sSFR	Template
15483	0.330	11.269	-99.000	-99.000	Elliptical
15489	0.258	10.302	-99.000	-99.000	Elliptical
15496	0.239	9.034	-0.211	-9.244	Sa
15508	0.146	9.856	0.679	-9.177	S0
15511	0.258	9.100	-0.009	-9.109	Sb
15522	0.324	8.770	-0.237	-9.006	Elliptical
15525	0.349	10.364	-99.000	-99.000	Elliptical
15553	0.290	10.366	-99.000	-99.000	Elliptical
15569	0.341	9.352	0.061	-9.291	S0
15583	0.175	9.061	-0.230	-9.291	S0
15584	0.282	10.619	-0.023	-10.642	S0
15587	0.219	10.841	1.253	-9.588	Sbc
15592	0.360	10.398	0.431	-9.966	Sa
15648	0.175	11.084	-99.000	-99.000	S0
15674	0.197	8.578	-1.448	-10.026	S0
15675	0.220	10.611	-99.000	-99.000	Elliptical
15776	0.318	10.897	-99.000	-99.000	Elliptical
15777	0.295	8.402	-0.843	-9.245	Sd
15704	0.365	8.998	-0.377	-9.376	Sb
15719	0.279	10.137	0.111	-10.026	S0
15722	0.190	10.965	0.323	-10.642	S0
15726	0.398	8.898	-0.486	-9.383	Irr
15745	0.427	9.385	0.428	-8.957	Sa
15748	0.156	10.702	-99.000	-99.000	Elliptical
15751	0.321	8.975	-0.310	-9.285	Sbc
15755	0.281	10.870	1.342	-9.529	Sc
15765	0.305	11.377	-99.000	-99.000	Elliptical
15782	0.315	9.864	-0.779	-10.642	S0
15784	0.270	10.525	1.209	-9.316	Sb
15802	0.357	11.292	-99.000	-99.000	Elliptical
15806	0.250	10.760	0.118	-10.642	S0
15812	0.325	10.487	-99.000	-99.000	Elliptical
15814	0.355	9.743	0.994	-8.749	S0
15816	0.253	9.979	0.391	-9.588	Sb

*continued on next page*

Table H.1: *continued*

SDSS Id	Redshift	Mass	SFR	sSFR	Template
15817	0.401	9.807	0.167	-9.640	Elliptical
15823	0.215	10.542	0.380	-10.162	S0
15829	0.325	9.284	0.259	-9.025	Sb
15850	0.232	10.849	-99.000	-99.000	Elliptical
15860	0.288	8.688	0.137	-8.551	Elliptical
15868	0.251	10.296	0.768	-9.529	Sc
15872	0.185	9.448	-0.039	-9.487	S0
15874	0.428	10.299	0.906	-9.393	S0
15892	0.185	10.951	1.009	-9.942	Sb
15897	0.175	10.606	-99.000	-99.000	S0
15901	0.171	9.523	-0.280	-9.803	Elliptical
15903	0.314	10.635	-99.000	-99.000	Elliptical
15909	0.218	10.893	-99.000	-99.000	Elliptical
15951	0.273	9.185	0.620	-8.566	Elliptical
15992	0.410	10.744	0.177	-10.567	Elliptical
15994	0.215	8.760	0.220	-8.540	Elliptical
16000	0.399	8.972	0.340	-8.632	Elliptical
16021	0.095	9.718	0.029	-9.688	S0
16032	0.195	10.187	0.817	-9.370	Elliptical
16052	0.142	9.492	-0.403	-9.895	Elliptical
16072	0.287	10.656	-99.000	-99.000	Elliptical
16073	0.153	9.782	0.406	-9.376	Sb
16091	0.300	9.580	0.396	-9.184	Sb
16093	0.335	10.132	0.955	-9.177	S0
16100	0.190	9.234	-99.000	-99.000	Elliptical
16103	0.202	10.131	-99.000	-99.000	Elliptical
16111	0.228	10.801	1.161	-9.640	Elliptical
16120	0.386	10.732	1.479	-9.253	Sb
16121	0.343	10.273	0.244	-10.028	Elliptical
16130	0.329	10.685	-99.000	-99.000	Elliptical
16148	0.306	10.062	0.474	-9.588	Sb
16152	0.249	10.890	0.247	-10.642	S0
16163	0.160	10.405	0.376	-10.028	Elliptical
16185	0.097	9.582	-1.060	-10.642	S0

*continued on next page*

Table H.1: *continued*

SDSS Id	Redshift	Mass	SFR	sSFR	Template
16199	0.231	9.619	0.133	-9.487	S0
16211	0.311	11.275	-99.000	-99.000	Elliptical
16220	0.329	8.730	-0.454	-9.184	Sb
16237	0.314	10.443	0.670	-9.773	Sb
16238	0.341	11.088	-99.000	-99.000	Elliptical
16259	0.119	8.988	-99.000	-99.000	Elliptical
16276	0.160	9.057	-0.336	-9.393	S0
16302	0.198	9.297	0.012	-9.285	Sbc
16398	0.308	11.482	-99.000	-99.000	Elliptical
16417	0.291	10.527	0.658	-9.869	S0
16436	0.314	9.445	0.069	-9.376	Sb
16441	0.291	10.876	-99.000	-99.000	Elliptical
16452	0.161	10.909	-99.000	-99.000	Elliptical
16460	0.285	9.317	0.266	-9.050	S0
16462	0.245	11.293	-99.000	-99.000	Elliptical
16466	0.188	10.101	0.811	-9.291	S0
16626	0.301	9.581	0.517	-9.065	Sa
16640	0.328	10.654	-99.000	-99.000	Elliptical
16768	0.143	10.657	0.798	-9.859	Sb

Table H.1: Showing the derived host galaxy parameters including Mass, SFR and sSFR.

---

## References

Abazajian, K., Adelman-McCarthy, J. K., Agüeros, M. A., Allam, S. S., Anderson, S. F., Annis, J., Bahcall, N. A., Baldry, I. K., Bastian, S., Berlind, A., Bernardi, M., Blanton, M. R., Blythe, N., Bochanski, Jr., J. J., Boroski, W. N., Brewington, H., Briggs, J. W., Brinkmann, J., Brunner, R. J., Budavári, T., Carey, L. N., Carr, M. A., Castander, F. J., Chiu, K., Collinge, M. J., Connolly, A. J., Covey, K. R., Csabai, I., Dalcanton, J. J., Dodelson, S., Doi, M., Dong, F., Eisenstein, D. J., Evans, M. L., Fan, X., Feldman, P. D., Finkbeiner, D. P., Friedman, S. D., Frieman, J. A., Fukugita, M., Gal, R. R., Gillespie, B., Glazebrook, K., Gonzalez, C. F., Gray, J., Grebel, E. K., Grodnicki, L., Gunn, J. E., Gurbani, V. K., Hall, P. B., Hao, L., Harbeck, D., Harris, F. H., Harris, H. C., Harvanek, M., Hawley, S. L., Heckman, T. M., Helmboldt, J. F., Hendry, J. S., Hennessy, G. S., Hindsley, R. B., Hogg, D. W., Holmgren, D. J., Holtzman, J. A., Homer, L., Hui, L., Ichikawa, S.-i., Ichikawa, T., Inkmann, J. P., Ivezić, Ž., Jester, S., Johnston, D. E., Jordan, B., Jordan, W. P., Jorgensen, A. M., Jurić, M., Kauffmann, G., Kent, S. M., Kleinman, S. J., Knapp, G. R., Kniazev, A. Y., Kron, R. G., Krzesiński, J., Kunszt, P. Z., Kuropatkin, N., Lamb, D. Q., Lampeitl, H., Laubscher, B. E., Lee, B. C., Leger, R. F., Li, N., Lidz, A., Lin, H., Loh, Y.-S., Long, D. C., Loveday, J., Lupton, R. H., Malik, T., Margon, B., McGehee, P. M., McKay, T. A., Meiksin, A., Miknaitis, G. A., Moorthy, B. K., Munn, J. A., Murphy, T., Nakajima, R., Narayanan, V. K., Nash, T., Neilsen, Jr., E. H., Newberg, H. J., Newman, P. R., Nichol, R. C., Nicinski, T., Nieto-Santisteban, M., Nitta, A., Odenkirchen, M., Okamura, S., Ostriker, J. P., Owen, R., Padmanabhan, N., Peoples, J., Pier, J. R., Pindor, B., Pope, A. C., Quinn, T. R., Rafikov, R. R., Raymond, S. N., Richards, G. T., Richmond, M. W., Rix, H.-W., Rockosi, C. M., Schaye, J., Schlegel, D. J., Schneider, D. P., Schroeder, J., Scranton, R., Sekiguchi, M., Seljak, U., Sergey, G., Sesar, B., Sheldon, E., Shimasaku, K., Siegmund, W. A., Silvestri, N. M., Sinisgalli, A. J., Sirko, E., Smith, J. A., Smolčić, V., Snedden, S. A., Stebbins, A., Steinhardt, C., Stinson, G., Stoughton, C., Strateva, I. V., Strauss, M. A., SubbaRao, M., Szalay, A. S., Szapudi, I., Szkody, P., Tasca, L., Tegmark, M., Thakar, A. R., Tremonti, C., Tucker, D. L., Uomoto, A., Vanden Berk, D. E., Vandenberg, J., Vogeley, M. S., Voges, W., Vogt, N. P., Walkowicz, L. M.,

- Weinberg, D. H., West, A. A., White, S. D. M., Wilhite, B. C., Willman, B., Xu, Y., Yanny, B., Yarger, J., Yasuda, N., Yip, C.-W., Yocum, D. R., York, D. G., Zakamska, N. L., Zehavi, I., Zheng, W., Zibetti, S., & Zucker, D. B. 2003, *AJ*, 126, 2081
- Adelman-McCarthy, J. K., Agüeros, M. A., Allam, S. S., Anderson, K. S. J., Anderson, S. F., Annis, J., Bahcall, N. A., Bailer-Jones, C. A. L., Baldry, I. K., Barentine, J. C., Beers, T. C., Belokurov, V., Berlind, A., Bernardi, M., Blanton, M. R., Bochanski, J. J., Boroski, W. N., Bramich, D. M., Brewington, H. J., Brinchmann, J., Brinkmann, J., Brunner, R. J., Budavári, T., Carey, L. N., Carliles, S., Carr, M. A., Castander, F. J., Connolly, A. J., Cool, R. J., Cunha, C. E., Csabai, I., Dalcanton, J. J., Doi, M., Eisenstein, D. J., Evans, M. L., Evans, N. W., Fan, X., Finkbeiner, D. P., Friedman, S. D., Frieman, J. A., Fukugita, M., Gillespie, B., Gilmore, G., Glazebrook, K., Gray, J., Grebel, E. K., Gunn, J. E., de Haas, E., Hall, P. B., Harvanek, M., Hawley, S. L., Hayes, J., Heckman, T. M., Hendry, J. S., Hennessy, G. S., Hindsley, R. B., Hirata, C. M., Hogan, C. J., Hogg, D. W., Holtzman, J. A., Ichikawa, S.-i., Ichikawa, T., Ivezić, Ž., Jester, S., Johnston, D. E., Jorgensen, A. M., Jurić, M., Kauffmann, G., Kent, S. M., Kleinman, S. J., Knapp, G. R., Kniazev, A. Y., Kron, R. G., Krzesinski, J., Kuropatkin, N., Lamb, D. Q., Lampeitl, H., Lee, B. C., Leger, R. F., Lima, M., Lin, H., Long, D. C., Loveday, J., Lupton, R. H., Mandelbaum, R., Margon, B., Martínez-Delgado, D., Matsubara, T., McGehee, P. M., McKay, T. A., Meiksin, A., Munn, J. A., Nakajima, R., Nash, T., Neilsen, Jr., E. H., Newberg, H. J., Nichol, R. C., Nieto-Santisteban, M., Nitta, A., Oyaizu, H., Okamura, S., Ostriker, J. P., Padmanabhan, N., Park, C., Peoples, J. J., Pier, J. R., Pope, A. C., Pourbaix, D., Quinn, T. R., Raddick, M. J., Re Fiorentin, P., Richards, G. T., Richmond, M. W., Rix, H.-W., Rockosi, C. M., Schlegel, D. J., Schneider, D. P., Scranton, R., Seljak, U., Sheldon, E., Shimasaku, K., Silvestri, N. M., Smith, J. A., Smolčić, V., Snedden, S. A., Stebbins, A., Stoughton, C., Strauss, M. A., SubbaRao, M., Suto, Y., Szalay, A. S., Szapudi, I., Szkody, P., Tegmark, M., Thakar, A. R., Tremonti, C. A., Tucker, D. L., Uomoto, A., Vanden Berk, D. E., Vandenberg, J., Vidrih, S., Vogeley, M. S., Voges, W., Vogt, N. P., Weinberg, D. H., West, A. A., White, S. D. M., Wilhite, B., Yanny, B., Yocum, D. R., York, D. G., Zehavi, I., Zibetti, S., & Zucker, D. B. 2007, *ApJS*, 172, 634
- Adelman-McCarthy, J. K., Agüeros, M. A., Allam, S. S., Anderson, K. S. J., Anderson, S. F., Annis, J., Bahcall, N. A., Baldry, I. K., Barentine, J. C., Berlind, A., Bernardi, M., Blanton, M. R., Boroski, W. N., Brewington, H. J., Brinchmann, J., Brinkmann, J., Brunner, R. J., Budavári, T., Carey, L. N., Carr, M. A., Castander, F. J., Connolly, A. J., Csabai, I., Czarapata, P. C., Dalcanton, J. J., Doi, M., Dong, F., Eisenstein, D. J., Evans, M. L., Fan, X., Finkbeiner, D. P., Friedman, S. D., Frieman, J. A., Fukugita, M., Gillespie, B., Glazebrook, K., Gray, J., Grebel, E. K., Gunn, J. E., Gurbani, V. K.,

- de Haas, E., Hall, P. B., Harris, F. H., Harvanek, M., Hawley, S. L., Hayes, J., Hendry, J. S., Hennessy, G. S., Hindsley, R. B., Hirata, C. M., Hogan, C. J., Hogg, D. W., Holmgren, D. J., Holtzman, J. A., Ichikawa, S.-i., Ivezić, Ž., Jester, S., Johnston, D. E., Jorgensen, A. M., Jurić, M., Kent, S. M., Kleinman, S. J., Knapp, G. R., Kniazev, A. Y., Kron, R. G., Krzesinski, J., Kuropatkin, N., Lamb, D. Q., Lampeitl, H., Lee, B. C., Leger, R. F., Lin, H., Long, D. C., Loveday, J., Lupton, R. H., Margon, B., Martínez-Delgado, D., Mandelbaum, R., Matsubara, T., McGehee, P. M., McKay, T. A., Meiksin, A., Munn, J. A., Nakajima, R., Nash, T., Neilsen, Jr., E. H., Newberg, H. J., Newman, P. R., Nichol, R. C., Nicinski, T., Nieto-Santisteban, M., Nitta, A., O'Mullane, W., Okamura, S., Owen, R., Padmanabhan, N., Pauls, G., Peoples, J. J., Pier, J. R., Pope, A. C., Pourbaix, D., Quinn, T. R., Richards, G. T., Richmond, M. W., Rockosi, C. M., Schlegel, D. J., Schneider, D. P., Schroeder, J., Scranton, R., Seljak, U., Sheldon, E., Shimasaku, K., Smith, J. A., Smolčić, V., Snedden, S. A., Stoughton, C., Strauss, M. A., SubbaRao, M., Szalay, A. S., Szapudi, I., Szkody, P., Tegmark, M., Thakar, A. R., Tucker, D. L., Uomoto, A., Vanden Berk, D. E., Vandenberg, J., Vogeley, M. S., Voges, W., Vogt, N. P., Walkowicz, L. M., Weinberg, D. H., West, A. A., White, S. D. M., Xu, Y., Yanny, B., Yocum, D. R., York, D. G., Zehavi, I., Zibetti, S., & Zucker, D. B. 2006, *ApJS*, 162, 38
- Aldering, G., Adam, G., Antilogus, P., Astier, P., Bacon, R., Bongard, S., Bonnaud, C., Copin, Y., Hardin, D., Henault, F., Howell, D. A., Lemonnier, J.-P., Levy, J.-M., Loken, S. C., Nugent, P. E., Pain, R., Pecontal, A., Pecontal, E., Perlmutter, S., Quimby, R. M., Schahmaneche, K., Smadja, G., & Wood-Vasey, W. M. 2002, in *Society of Photo-Optical Instrumentation Engineers (SPIE) Conference Series*, Vol. 4836, *Society of Photo-Optical Instrumentation Engineers (SPIE) Conference Series*, ed. J. A. Tyson & S. Wolff, 61–72
- Aldering, G., Antilogus, P., Bailey, S., Baltay, C., Bauer, A., Blanc, N., Bongard, S., Copin, Y., Gangler, E., Gilles, S., Kessler, R., Kocevski, D., Lee, B. C., Loken, S., Nugent, P., Pain, R., Pécontal, E., Pereira, R., Perlmutter, S., Rabinowitz, D., Rigaudier, G., Scalzo, R., Smadja, G., Thomas, R. C., Wang, L., & Weaver, B. A. 2006, *ApJ*, 650, 510
- Annis, J., & Strauss, M. . T. 2008, In preparation
- Arnett, D. 1996, *Supernovae and nucleosynthesis. an investigation of the history of matter, from the Big Bang to the present* (Princeton series in astrophysics, Princeton, NJ: Princeton University Press, —c1996)

- Astier, P., Guy, J., Regnault, N., Pain, R., Aubourg, E., Balam, D., Basa, S., Carlberg, R. G., Fabbro, S., Fouchez, D., Hook, I. M., Howell, D. A., Lafoux, H., Neill, J. D., Palanque-Delabrouille, N., Perrett, K., Pritchet, C. J., Rich, J., Sullivan, M., Taillet, R., Aldering, G., Antilogus, P., Arsenijevic, V., Balland, C., Baumont, S., Bronder, J., Courtois, H., Ellis, R. S., Filiol, M., Gonçalves, A. C., Goobar, A., Guide, D., Hardin, D., Luset, V., Lidman, C., McMahon, R., Mouchet, M., Mourao, A., Perlmutter, S., Ripoché, P., Tao, C., & Walton, N. 2006, *A&A*, 447, 31
- Baldry, I. K., Balogh, M. L., Bower, R. G., Glazebrook, K., Nichol, R. C., Bamford, S. P., & Budavari, T. 2006, *MNRAS*, 373, 469
- Balland, C., Mouchet, M., Pain, R., Walton, N. A., Amanullah, R., Astier, P., Ellis, R. S., Fabbro, S., Goobar, A., Hardin, D., Hook, I. M., Irwin, M. J., McMahon, R. G., Mendez, J. M., Ruiz-Lapuente, P., Sainton, G., Schahmaneche, K., & Stanishev, V. 2006, *A&A*, 445, 387
- Balogh, M. L., Morris, S. L., Yee, H. K. C., Carlberg, R. G., & Ellingson, E. 1999, *ApJ*, 527, 54
- Barris, B. J., & Tonry, J. L. 2006, *ApJ*, 637, 427
- Bell, E. F., Wolf, C., Meisenheimer, K., Rix, H.-W., Borch, A., Dye, S., Kleinheinrich, M., Wisotzki, L., & McIntosh, D. H. 2004, *ApJ*, 608, 752
- Bender, R., Ziegler, B., & Bruzual, G. 1996, *ApJ*, 463, L51
- Benetti, S., Cappellaro, E., Mazzali, P. A., Turatto, M., Altavilla, G., Bufano, F., Elias-Rosa, N., Kotak, R., Pignata, G., Salvo, M., & Stanishev, V. 2005, *ApJ*, 623, 1011
- Bianchi, L., & The GALEX Team. 1999, *Memorie della Societa Astronomica Italiana*, 70, 365
- Blanc, G., Afonso, C., Alard, C., Albert, J. N., Aldering, G., Amadon, A., Andersen, J., Ansari, R., Aubourg, É., Balland, C., Bareyre, P., Beaulieu, J. P., Charlot, X., Conley, A., Coutures, C., Dahln, T., Derue, F., Fan, X., Ferlet, R., Folatelli, G., Fouqué, P., Garavini, G., Glicenstein, J. F., Goldman, B., Goobar, A., Gould, A., Graff, D., Gros, M., Haissinski, J., Hamadache, C., Hardin, D., Hook, I. M., de Kat, J., Kent, S., Kim, A., Lasserre, T., Le Guillou, L., Lesquoy, É., Loup, C., Magneville, C., Marquette, J. B., Maurice, É., Maury, A., Milsztajn, A., Moniez, M., Mouchet, M., Newberg, H., Nobili, S., Palanque-Delabrouille, N., Perdureau, O., Prévot, L., Rahal, Y. R., Regnault, N., Rich, J., Ruiz-Lapuente, P., Spiro, M., Tisserand, P., Vidal-Madjar, A., Vigroux, L., Walton, N. A., & Zylberajch, S. 2004, *A&A*, 423, 881

- Blanton, M. R., & Roweis, S. 2007, *AJ*, 133, 734
- Blanton, M. R., Schlegel, D. J., Strauss, M. A., Brinkmann, J., Finkbeiner, D., Fukugita, M., Gunn, J. E., Hogg, D. W., Ivezić, Ž., Knapp, G. R., Lupton, R. H., Munn, J. A., Schneider, D. P., Tegmark, M., & Zehavi, I. 2005, *AJ*, 129, 2562
- Blondin, S., Dessart, L., Leibundgut, B., Branch, D., Höflich, P., Tonry, J. L., Matheson, T., Foley, R. J., Chornock, R., Filippenko, A. V., Sollerman, J., Spyromilio, J., Kirshner, R. P., Wood-Vasey, W. M., Clocchiatti, A., Aguilera, C., Barris, B., Becker, A. C., Challis, P., Covarrubias, R., Davis, T. M., Garnavich, P., Hicken, M., Jha, S., Krisciunas, K., Li, W., Miceli, A., Miknaitis, G., Pignata, G., Prieto, J. L., Rest, A., Riess, A. G., Salvo, M. E., Schmidt, B. P., Smith, R. C., Stubbs, C. W., & Suntzeff, N. B. 2006, *AJ*, 131, 1648
- Blondin, S., & Tonry, J. L. 2007, *ApJ*, 666, 1024
- Bolzonella, M., Miralles, J.-M., & Pelló, R. 2000, *A&A*, 363, 476
- Bower, R. G., Benson, A. J., Malbon, R., Helly, J. C., Frenk, C. S., Baugh, C. M., Cole, S., & Lacey, C. G. 2006, *MNRAS*, 370, 645
- Branch, D., Baron, E., Thomas, R. C., Kasen, D., Li, W., & Filippenko, A. V. 2004, *PASP*, 116, 903
- Branch, D., Dang, L. C., Hall, N., Ketchum, W., Melakayil, M., Parrent, J., Troxel, M. A., Casebeer, D., Jeffery, D. J., & Baron, E. 2006, *PASP*, 118, 560
- Branch, D., Drucker, W., & Jeffery, D. J. 1988, *ApJ*, 330, L117+
- Branch, D., Fisher, A., & Nugent, P. 1993, *AJ*, 106, 2383
- Branch, D., Livio, M., Yungelson, L. R., Boffi, F. R., & Baron, E. 1995, *PASP*, 107, 1019
- Bravo, E., & García-Senz, D. 2008, *A&A*, 478, 843
- Brinchmann, J., Charlot, S., White, S. D. M., Tremonti, C., Kauffmann, G., Heckman, T., & Brinkmann, J. 2004, *MNRAS*, 351, 1151
- Brinchmann, J., & Ellis, R. S. 2000, *ApJ*, 536, L77
- Bruzual, G., & Charlot, S. 2003, *MNRAS*, 344, 1000
- Bruzual A., G. 1983, *ApJ*, 273, 105

- Calzetti, D., Armus, L., Bohlin, R. C., Kinney, A. L., Koornneef, J., & Storchi-Bergmann, T. 2000, *ApJ*, 533, 682
- Cappellaro, E., Evans, R., & Turatto, M. 1999, *A&A*, 351, 459
- Cardelli, J. A., Clayton, G. C., & Mathis, J. S. 1989, *ApJ*, 345, 245
- Carroll, S. M. 2004, *Spacetime and geometry. An introduction to general relativity* (Spacetime and geometry / Sean Carroll. San Francisco, CA, USA: Addison Wesley, ISBN 0-8053-8732-3, 2004, XIV + 513 pp.)
- Chakravarti, I. M., Laha, R. G., & Roy, J. 1967, *Handbook of Methods of Applied Statistics*, Vol. I (USE: John Wiley and Sons)
- Chandrasekhar, S. 1931, *MNRAS*, 91, 456
- Chester, C., & Roberts, M. S. 1964, *AJ*, 69, 635
- Cole, S., Lacey, C. G., Baugh, C. M., & Frenk, C. S. 2000, *MNRAS*, 319, 168
- Colgate, S. A., & McKee, C. 1969, *ApJ*, 157, 623
- Conley, A., Carlberg, R. G., Guy, J., Howell, D. A., Jha, S., Riess, A. G., & Sullivan, M. 2007, *ApJ*, 664, L13
- Conley, A., Sullivan, M., Hsiao, E. Y., Guy, J., Astier, P., Balam, D., Balland, C., Basa, S., Carlberg, R. G., Fouchez, D., Hardin, D., Howell, D. A., Hook, I. M., Pain, R., Perrett, K., Pritchett, C. J., & Regnault, N. 2008, *ApJ*, 681, 482
- Cooray, A., & Caldwell, R. R. 2006, *Phys. Rev. D*, 73, 103002
- Cooray, A., Huterer, D., & Holz, D. E. 2006, *Physical Review Letters*, 96, 021301
- Cresswell, J. G., & Percival, W. J. 2008, *ArXiv e-prints*
- Dahlen, T., Strolger, L.-G., Riess, A. G., Mobasher, B., Chary, R.-R., Conselice, C. J., Ferguson, H. C., Fruchter, A. S., Giavalisco, M., Livio, M., Madau, P., Panagia, N., & Tonry, J. L. 2004, *ApJ*, 613, 189
- Davis, T. M., Mörtzell, E., Sollerman, J., Becker, A. C., Blondin, S., Challis, P., Clocchiatti, A., Filippenko, A. V., Foley, R. J., Garnavich, P. M., Jha, S., Krisciunas, K., Kirshner, R. P., Leibundgut, B., Li, W., Matheson, T., Miknaitis, G., Pignata, G., Rest, A., Riess, A. G., Schmidt, B. P., Smith, R. C., Spyromilio, J., Stubbs, C. W., Suntzeff, N. B., Tonry, J. L., Wood-Vasey, W. M., & Zenteno, A. 2007, *ApJ*, 666, 716

- de La Peña, M. D., White, R. L., & Greenfield, P. 2001, in *Astronomical Society of the Pacific Conference Series*, Vol. 238, *Astronomical Data Analysis Software and Systems X*, ed. F. R. Harnden, Jr., F. A. Primini, & H. E. Payne, 59–+
- De Lucia, G., & Blaizot, J. 2007, *MNRAS*, 375, 2
- de Vaucouleurs, G. 1948, *Annales d’Astrophysique*, 11, 247
- Della Valle, M., Panagia, N., Padovani, P., Cappellaro, E., Mannucci, F., & Turatto, M. 2005, in *Astronomical Society of the Pacific Conference Series*, Vol. 342, 1604-2004: *Supernovae as Cosmological Lighthouses*, ed. M. Turatto, S. Benetti, L. Zampieri, & W. Shea, 133–+
- della Valle, M., Rosino, L., Bianchini, A., & Livio, M. 1994, *A&A*, 287, 403
- Deng, J., Kawabata, K. S., Ohya, Y., Nomoto, K., Mazzali, P. A., Wang, L., Jeffery, D. J., Iye, M., Tomita, H., & Yoshii, Y. 2004, *ApJ*, 605, L37
- Dilday, B. 2008, Thesis
- Dilday, B., Kessler, R., Frieman, J. A., Holtzman, J., Marriner, J., Miknaitis, G., Nichol, R. C., Romani, R., Sako, M., Bassett, B., Becker, A., Cinabro, D., DeJongh, F., Depoy, D. L., Doi, M., Garnavich, P. M., Hogan, C. J., Jha, S., Konishi, K., Lampeitl, H., Marshall, J. L., McGinnis, D., Prieto, J. L., Riess, A. G., Richmond, M. W., Schneider, D. P., Smith, M., Takanashi, N., Tokita, K., van der Heyden, K., Zheng, N. Y. C., Barentine, J., Brewington, H., Choi, C., Crotts, A., Dembicky, J., Harvanek, M., Im, M., Ketzeback, W., Kleinman, S. J., Krzesiński, J., Long, D. C., Malanushenko, E., Malanushenko, V., McMillan, R. J., Nitta, A., Pan, K., Saurage, G., Snedden, S. A., Watters, S., Wheeler, J. C., & York, D. 2008, *ArXiv e-prints*, 801
- Dilday, B., Smith, M., Frieman, J., Bassett, B., Becker, A., Choi, C., Cinabro, D., DeJongh, F., Depoy, D. L., Dilday, B., Doi, M., Garnavich, P. M., Hogan, C. J., Holtzman, J., Im, M., Jha, S., Kessler, R., Konishi, K., Lampeitl, H., Marriner, J., Marshall, J. L., McGinnis, D., Miknaitis, G., Nichol, R. C., Prieto, J. L., Riess, A. G., Richmond, M. W., Romani, R., Sako, M., Schneider, D. P., Smith, M., Takanashi, N., Tokita, K., van der Heyden, K., Yasuda, N., Zheng, C., Adelman-McCarthy, J., Annis, J., Assef, R. J., Barentine, J., Bender, R., Blandford, R. D., Boroski, W. N., Bremer, M., Brewington, H., Collins, C. A., Crotts, A., Dembicky, J., Eastman, J., Edge, A., Edmondson, E., Elson, E., Eyler, M. E., Filippenko, A. V., Foley, R. J., Frank, S., Goobar, A., Gueth, T., Gunn, J. E., Harvanek, M., Hopp, U., Ihara, Y., Ivezić, Ž., Kahn, S., Kaplan, J., Kent, S., Ketzeback, W., Kleinman, S. J., Kollatschny, W., Kron,

- R. G., Krzesiński, J., Lamenti, D., Leloudas, G., Lin, H., Long, D. C., Lucey, J., Lupton, R. H., Malanushenko, E., Malanushenko, V., McMillan, R. J., Mendez, J., Morgan, C. W., Morokuma, T., Nitta, A., Ostman, L., Pan, K., Rockosi, C. M., Romer, A. K., Ruiz-Lapuente, P., Saurage, G., Schlesinger, K., Snedden, S. A., Sollerman, J., Stoughton, C., Stritzinger, M., Subba Rao, M., Tucker, D., Vaisanen, P., Watson, L. C., Watters, S., Wheeler, J. C., Yanny, B., & York, D. 2009, In preparation
- Donas, J., Deharveng, J. M., Laget, M., Milliard, B., & Huguenin, D. 1987, *A&A*, 180, 12
- Dunkley, J., Komatsu, E., Nolta, M. R., Spergel, D. N., Larson, D., Hinshaw, G., Page, L., Bennett, C. L., Gold, B., Jarosik, N., Weiland, J. L., Halpern, M., Hill, R. S., Kogut, A., Limon, M., Meyer, S. S., Tucker, G. S., Wollack, E., & Wright, E. L. 2008, *ArXiv e-prints*
- Eisenstein, D. J., Zehavi, I., Hogg, D. W., Scoccamarro, R., Blanton, M. R., Nichol, R. C., Scranton, R., Seo, H.-J., Tegmark, M., Zheng, Z., Anderson, S. F., Annis, J., Bahcall, N., Brinkmann, J., Burles, S., Castander, F. J., Connolly, A., Csabai, I., Doi, M., Fukugita, M., Frieman, J. A., Glazebrook, K., Gunn, J. E., Hendry, J. S., Hennessy, G., Ivezić, Z., Kent, S., Knapp, G. R., Lin, H., Loh, Y.-S., Lupton, R. H., Margon, B., McKay, T. A., Meiksin, A., Munn, J. A., Pope, A., Richmond, M. W., Schlegel, D., Schneider, D. P., Shimasaku, K., Stoughton, C., Strauss, M. A., SubbaRao, M., Szalay, A. S., Szapudi, I., Tucker, D. L., Yanny, B., & York, D. G. 2005, *ApJ*, 633, 560
- Ellis, R. S., Sullivan, M., Nugent, P. E., Howell, D. A., Gal-Yam, A., Astier, P., Balam, D., Balland, C., Basa, S., Carlberg, R. G., Conley, A., Fouchez, D., Guy, J., Hardin, D., Hook, I., Pain, R., Perrett, K., Pritchett, C. J., & Regnault, N. 2008, *ApJ*, 674, 51
- Felten, J. E. 1976, *ApJ*, 207, 700
- Filippenko, A. V., Richmond, M. W., Branch, D., Gaskell, M., Herbst, W., Ford, C. H., Treffers, R. R., Matheson, T., Ho, L. C., Dey, A., Sargent, W. L. W., Small, T. A., & van Breugel, W. J. M. 1992a, *AJ*, 104, 1543
- Filippenko, A. V., Richmond, M. W., Matheson, T., Shields, J. C., Burbidge, E. M., Cohen, R. D., Dickinson, M., Malkan, M. A., Nelson, B., Pietz, J., Schlegel, D., Schmeer, P., Spinrad, H., Steidel, C. C., Tran, H. D., & Wren, W. 1992b, *ApJ*, 384, L15
- Filippenko, A. V., & Riess, A. G. 1998, *Phys. Rep.*, 307, 31
- Fioc, M., & Rocca-Volmerange, B. 1997, *A&A*, 326, 950

- Fisher, A., Branch, D., Hofflich, P., & Khokhlov, A. 1995, *ApJ*, 447, L73+
- Fitzpatrick, E. L., & Massa, D. 1988, *ApJ*, 328, 734
- Folatelli, G. 2004, *New Astronomy Review*, 48, 623
- Foley, R. J., Filippenko, A. V., Aguilera, C., Becker, A. C., Blondin, S., Challis, P., Clocchiatti, A., Covarrubias, R., Davis, T. M., Garnavich, P. M., Jha, S. W., Kirshner, R. P., Krisciunas, K., Leibundgut, B., Li, W., Matheson, T., Miceli, A., Miknaitis, G., Pignata, G., Rest, A., Riess, A. G., Schmidt, B. P., Smith, R. C., Sollerman, J., Spyromilio, J., Stubbs, C. W., Suntzeff, N. B., Tonry, J. L., Wood-Vasey, W. M., & Zenteno, A. 2008a, *ApJ*, 684, 68
- Foley, R. J., Filippenko, A. V., & Jha, S. W. 2008b, *ArXiv e-prints*, 803
- Freedman, W. L., Madore, B. F., Gibson, B. K., Ferrarese, L., Kelson, D. D., Sakai, S., Mould, J. R., Kennicutt, Jr., R. C., Ford, H. C., Graham, J. A., Huchra, J. P., Hughes, S. M. G., Illingworth, G. D., Macri, L. M., & Stetson, P. B. 2001, *ApJ*, 553, 47
- Freeman, K. C. 1970, *ApJ*, 160, 811
- Friedmann, A. 1924, *Z. Phys.*, 21, 326
- Frieman, J. A., Bassett, B., Becker, A., Choi, C., Cinabro, D., DeJongh, F., Depoy, D. L., Dilday, B., Doi, M., Garnavich, P. M., Hogan, C. J., Holtzman, J., Im, M., Jha, S., Kessler, R., Konishi, K., Lampeitl, H., Marriner, J., Marshall, J. L., McGinnis, D., Miknaitis, G., Nichol, R. C., Prieto, J. L., Riess, A. G., Richmond, M. W., Romani, R., Sako, M., Schneider, D. P., Smith, M., Takanashi, N., Tokita, K., van der Heyden, K., Yasuda, N., Zheng, C., Adelman-McCarthy, J., Annis, J., Assef, R. J., Barentine, J., Bender, R., Blandford, R. D., Boroski, W. N., Bremer, M., Brewington, H., Collins, C. A., Crotts, A., Dembicky, J., Eastman, J., Edge, A., Edmondson, E., Elson, E., Eyler, M. E., Filippenko, A. V., Foley, R. J., Frank, S., Goobar, A., Gueth, T., Gunn, J. E., Harvanek, M., Hopp, U., Ihara, Y., Ivezić, Ž., Kahn, S., Kaplan, J., Kent, S., Ketzeback, W., Kleinman, S. J., Kollatschny, W., Kron, R. G., Krzesiński, J., Lamenti, D., Leloudas, G., Lin, H., Long, D. C., Lucey, J., Lupton, R. H., Malanushenko, E., Malanushenko, V., McMillan, R. J., Mendez, J., Morgan, C. W., Morokuma, T., Nitta, A., Ostman, L., Pan, K., Rockosi, C. M., Romer, A. K., Ruiz-Lapuente, P., Saurage, G., Schlesinger, K., Snedden, S. A., Sollerman, J., Stoughton, C., Stritzinger, M., Subba Rao, M., Tucker, D., Vaisanen, P., Watson, L. C., Watters, S., Wheeler, J. C., Yanny, B., & York, D. 2008a, *AJ*, 135, 338
- Frieman, J. A., Turner, M. S., & Huterer, D. 2008b, *ARA&A*, 46, 385

- Fu, L., Semboloni, E., Hoekstra, H., Kilbinger, M., van Waerbeke, L., Tereno, I., Mellier, Y., Heymans, C., Coupon, J., Benabed, K., Benjamin, J., Bertin, E., Doré, O., Hudson, M. J., Ilbert, O., Maoli, R., Marmo, C., McCracken, H. J., & Ménard, B. 2008, *A&A*, 479, 9
- Fukugita, M., Ichikawa, T., Gunn, J. E., Doi, M., Shimasaku, K., & Schneider, D. P. 1996, *AJ*, 111, 1748
- Galaz, G., & de Lapparent, V. 1998, *A&A*, 332, 459
- Gallagher, J. S., Garnavich, P. M., Berlind, P., Challis, P., Jha, S., & Kirshner, R. P. 2005, *ApJ*, 634, 210
- Garavini, G., Folatelli, G., Nobili, S., Aldering, G., Amanullah, R., Antilogus, P., Astier, P., Blanc, G., Bronder, T., Burns, M. S., Conley, A., Deustua, S. E., Doi, M., Fabbro, S., Fadeyev, V., Gibbons, R., Goldhaber, G., Goobar, A., Groom, D. E., Hook, I., Howell, D. A., Kashikawa, N., Kim, A. G., Kowalski, M., Kuznetsova, N., Lee, B. C., Lidman, C., Mendez, J., Morokuma, T., Motohara, K., Nugent, P. E., Pain, R., Perlmutter, S., Quimby, R., Raux, J., Regnault, N., Ruiz-Lapuente, P., Sainton, G., Schahmaneche, K., Smith, E., Spadafora, A. L., Stanishev, V., Thomas, R. C., Walton, N. A., Wang, L., Wood-Vasey, W. M., & Yasuda, N. 2007, *A&A*, 470, 411
- Geminale, A., & Popowski, P. 2005, *Journal of Physics Conference Series*, 6, 223
- Giallongo, E., D'Odorico, S., Fontana, A., Cristiani, S., Egami, E., Hu, E., & McMahon, R. G. 1998, *AJ*, 115, 2169
- Giannantonio, T., Scranton, R., Crittenden, R. G., Nichol, R. C., Boughn, S. P., Myers, A. D., & Richards, G. T. 2008, *Phys. Rev. D*, 77, 123520
- Goldhaber, G., Groom, D. E., Kim, A., Aldering, G., Astier, P., Conley, A., Deustua, S. E., Ellis, R., Fabbro, S., Fruchter, A. S., Goobar, A., Hook, I., Irwin, M., Kim, M., Knop, R. A., Lidman, C., McMahon, R., Nugent, P. E., Pain, R., Panagia, N., Pennypacker, C. R., Perlmutter, S., Ruiz-Lapuente, P., Schaefer, B., Walton, N. A., & York, T. 2001, *ApJ*, 558, 359
- Greenfield, P., & White, R. L. 2000, in *Astronomical Society of the Pacific Conference Series*, Vol. 216, *Astronomical Data Analysis Software and Systems IX*, ed. N. Manset, C. Veillet, & D. Crabtree, 59–+
- Greggio, L., & Renzini, A. 1983, *A&A*, 118, 217
- Greggio, L., Renzini, A., & Daddi, E. 2008, *MNRAS*, 388, 829

- Gunn, J. E., Carr, M., Rockosi, C., Sekiguchi, M., Berry, K., Elms, B., de Haas, E., Ivezić, Ž., Knapp, G., Lupton, R., Pauls, G., Simcoe, R., Hirsch, R., Sanford, D., Wang, S., York, D., Harris, F., Annis, J., Bartozek, L., Boroski, W., Bakken, J., Halderman, M., Kent, S., Holm, S., Holmgren, D., Petravick, D., Prosapio, A., Rechenmacher, R., Doi, M., Fukugita, M., Shimasaku, K., Okada, N., Hull, C., Siegmund, W., Mannery, E., Blouke, M., Heidtman, D., Schneider, D., Lucinio, R., & Brinkman, J. 1998, *AJ*, 116, 3040
- Gunn, J. E., Siegmund, W. A., Mannery, E. J., Owen, R. E., Hull, C. L., Leger, R. F., Carey, L. N., Knapp, G. R., York, D. G., Boroski, W. N., Kent, S. M., Lupton, R. H., Rockosi, C. M., Evans, M. L., Waddell, P., Anderson, J. E., Annis, J., Barentine, J. C., Bartoszek, L. M., Bastian, S., Bracker, S. B., Brewington, H. J., Briegel, C. I., Brinkmann, J., Brown, Y. J., Carr, M. A., Czarapata, P. C., Drennan, C. C., Dombeck, T., Federwitz, G. R., Gillespie, B. A., Gonzales, C., Hansen, S. U., Harvanek, M., Hayes, J., Jordan, W., Kinney, E., Klaene, M., Kleinman, S. J., Kron, R. G., Kresinski, J., Lee, G., Limmongkol, S., Lindenmeyer, C. W., Long, D. C., Loomis, C. L., McGehee, P. M., Mantsch, P. M., Neilsen, Jr., E. H., Neswold, R. M., Newman, P. R., Nitta, A., Peoples, J. J., Pier, J. R., Prieto, P. S., Prosapio, A., Rivetta, C., Schneider, D. P., Snedden, S., & Wang, S.-i. 2006, *AJ*, 131, 2332
- Guy, J., Astier, P., Baumont, S., Hardin, D., Pain, R., Regnault, N., Basa, S., Carlberg, R. G., Conley, A., Fabbro, S., Fouchez, D., Hook, I. M., Howell, D. A., Perrett, K., Pritchett, C. J., Rich, J., Sullivan, M., Antilogus, P., Aubourg, E., Bazin, G., Bronder, J., Filiol, M., Palanque-Delabrouille, N., Ripoche, P., & Ruhlmann-Kleider, V. 2007, *A&A*, 466, 11
- Guy, J., Astier, P., Nobili, S., Regnault, N., & Pain, R. 2005, *A&A*, 443, 781
- Hachinger, S., Mazzali, P. A., & Benetti, S. 2006, *MNRAS*, 370, 299
- Hamuy, M., Folatelli, G., Morrell, N. I., Phillips, M. M., Suntzeff, N. B., Persson, S. E., Roth, M., Gonzalez, S., Krzeminski, W., Contreras, C., Freedman, W. L., Murphy, D. C., Madore, B. F., Wyatt, P., Maza, J., Filippenko, A. V., Li, W., & Pinto, P. A. 2006, *PASP*, 118, 2
- Hamuy, M., Phillips, M., Suntzeff, N., & Maza, J. 2003a, *IAU Circ.*, 8151, 2
- Hamuy, M., Phillips, M. M., Maza, J., Suntzeff, N. B., Schommer, R. A., & Aviles, R. 1995, *AJ*, 109, 1

- Hamuy, M., Phillips, M. M., Suntzeff, N. B., Maza, J., González, L. E., Roth, M., Krisciunas, K., Morrell, N., Green, E. M., Persson, S. E., & McCarthy, P. J. 2003b, *Nature*, 424, 651
- Hamuy, M., Phillips, M. M., Suntzeff, N. B., Schommer, R. A., Maza, J., Antezan, A. R., Wischnjewsky, M., Valladares, G., Muena, C., Gonzales, L. E., Aviles, R., Wells, L. A., Smith, R. C., Navarrete, M., Covarrubias, R., Williger, G. M., Walker, A. R., Layden, A. C., Elias, J. H., Baldwin, J. A., Hernandez, M., Tirado, H., Ugarte, P., Elston, R., Saavedra, N., Barrientos, F., Costa, E., Lira, P., Ruiz, M. T., Anguita, C., Gomez, X., Ortiz, P., della Valle, M., Danziger, J., Storm, J., Kim, Y.-C., Baily, C., Rubenstein, E. P., Tucker, D., Cersosimo, S., Mendez, R. A., Siciliano, L., Sherry, W., Chaboyer, B., Koopmann, R. A., Geisler, D., Sarajedini, A., Dey, A., Tyson, N., Rich, R. M., Gal, R., Lamontagne, R., Caldwell, N., Guhathakurta, P., Phillips, A. C., Szkody, P., Prosser, C., Ho, L. C., McMahan, R., Baggley, G., Cheng, K.-P., Havlen, R., Wakamatsu, K., Janes, K., Malkan, M., Baganoff, F., Seitzer, P., Shara, M., Sturch, C., Hesser, J., Hartig, A. N. P., Hughes, J., Welch, D., Williams, T. B., Ferguson, H., Francis, P. J., French, L., Bolte, M., Roth, J., Odewahn, S., Howell, S., & Krzeminski, W. 1996a, *AJ*, 112, 2408
- Hamuy, M., Phillips, M. M., Suntzeff, N. B., Schommer, R. A., Maza, J., & Aviles, R. 1996b, *AJ*, 112, 2391
- . 1996c, *AJ*, 112, 2398
- Hamuy, M., Phillips, M. M., Suntzeff, N. B., Schommer, R. A., Maza, J., Smith, R. C., Lira, P., & Aviles, R. 1996d, *AJ*, 112, 2438
- Hamuy, M., Trager, S. C., Pinto, P. A., Phillips, M. M., Schommer, R. A., Ivanov, V., & Suntzeff, N. B. 2000, *AJ*, 120, 1479
- Hardin, D., Afonso, C., Alard, C., Albert, J. N., Amadon, A., Andersen, J., Ansari, R., Aubourg, É., Bareyre, P., Bauer, F., Beaulieu, J. P., Blanc, G., Bouquet, A., Char, S., Charlot, X., Couchot, F., Coutures, C., Derue, F., Ferlet, R., Glicenstein, J. F., Goldman, B., Gould, A., Graff, D., Gros, M., Haissinski, J., Hamilton, J. C., de Kat, J., Kim, A., Lasserre, T., Lesquoy, É., Loup, C., Magneville, C., Mansoux, B., Marquette, J. B., Maurice, É., Milsztajn, A., Moniez, M., Palanque-Delabrouille, N., Perdureau, O., Prévot, L., Regnault, N., Rich, J., Spiro, M., Vidal-Madjar, A., Vigroux, L., Zylberajch, S., & The EROS Collaboration. 2000, *A&A*, 362, 419
- Harkness, R. P., & Wheeler, J. C. 1990, in *Supernovae*, 1–29

- Hicken, M., Wood-Vasey, W. M., Blondin, S., Challis, P., Jha, S., Kelly, P. L., Rest, A., & Kirshner, R. P. 2009, ArXiv e-prints
- Hillebrandt, W., & Niemeyer, J. C. 2000, *ARA&A*, 38, 191
- Holtzman, J. A., & SDSS-II Supernova Collaboration. 2006, in *Bulletin of the American Astronomical Society*, Vol. 38, *Bulletin of the American Astronomical Society*, 941–
- Hook, I. M., Howell, D. A., Aldering, G., Amanullah, R., Burns, M. S., Conley, A., Deustua, S. E., Ellis, R., Fabbro, S., Fadeyev, V., Folatelli, G., Garavini, G., Gibbons, R., Goldhaber, G., Goobar, A., Groom, D. E., Kim, A. G., Knop, R. A., Kowalski, M., Lidman, C., Nobili, S., Nugent, P. E., Pain, R., Pennypacker, C. R., Perlmutter, S., Ruiz-Lapuente, P., Sain-ton, G., Schaefer, B. E., Smith, E., Spadafora, A. L., Stanishev, V., Thomas, R. C., Walton, N. A., Wang, L., & Wood-Vasey, W. M. 2005, *AJ*, 130, 2788
- Howell, D. A. 2001, *ApJ*, 554, L193
- Howell, D. A., Sullivan, M., Nugent, P. E., Ellis, R. S., Conley, A. J., Le Borgne, D., Carlberg, R. G., Guy, J., Balam, D., Basa, S., Fouchez, D., Hook, I. M., Hsiao, E. Y., Neill, J. D., Pain, R., Perrett, K. M., & Pritchett, C. J. 2006, *Nature*, 443, 308
- Howell, D. A., Sullivan, M., Perrett, K., Bronder, T. J., Hook, I. M., Astier, P., Aubourg, E., Balam, D., Basa, S., Carlberg, R. G., Fabbro, S., Fouchez, D., Guy, J., Lafoux, H., Neill, J. D., Pain, R., Palanque-Delabrouille, N., Pritchett, C. J., Regnault, N., Rich, J., Taillet, R., Knop, R., McMahon, R. G., Perlmutter, S., & Walton, N. A. 2005, *ApJ*, 634, 1190
- Hsiao, E. Y., Conley, A., Howell, D. A., Sullivan, M., Pritchett, C. J., Carlberg, R. G., Nugent, P. E., & Phillips, M. M. 2007, *ApJ*, 663, 1187
- Hubble, E. 1929, *Proceedings of the National Academy of Science*, 15, 168
- Hui, L., & Greene, P. B. 2006, *Phys. Rev. D*, 73, 123526
- Ivezić, Ž., Smith, J. A., Miknaitis, G., Lin, H., Tucker, D., Lupton, R. H., Gunn, J. E., Knapp, G. R., Strauss, M. A., Sesar, B., Doi, M., Tanaka, M., Fukugita, M., Holtzman, J., Kent, S., Yanny, B., Schlegel, D., Finkbeiner, D., Padmanabhan, N., Rockosi, C. M., Jurić, M., Bond, N., Lee, B., Stoughton, C., Jester, S., Harris, H., Harding, P., Morrison, H., Brinkmann, J., Schneider, D. P., & York, D. 2007, *AJ*, 134, 973
- James, F., & Roos, M. 1991, *Phys. Rev. D*, 44, 299

Jha, S. 2008, Private Communication

Jha, S., Kirshner, R. P., Challis, P., Garnavich, P. M., Matheson, T., Soderberg, A. M., Graves, G. J. M., Hicken, M., Alves, J. F., Arce, H. G., Balog, Z., Barmby, P., Barton, E. J., Berlind, P., Bragg, A. E., Briceño, C., Brown, W. R., Buckley, J. H., Caldwell, N., Calkins, M. L., Carter, B. J., Concannon, K. D., Donnelly, R. H., Eriksen, K. A., Fabricant, D. G., Falco, E. E., Fiore, F., Garcia, M. R., Gómez, M., Grogin, N. A., Groner, T., Groot, P. J., Haisch, Jr., K. E., Hartmann, L., Hergenrother, C. W., Holman, M. J., Huchra, J. P., Jayawardhana, R., Jerius, D., Kannappan, S. J., Kim, D.-W., Kleyna, J. T., Kochanek, C. S., Koranyi, D. M., Krockenberger, M., Lada, C. J., Luhman, K. L., Luu, J. X., Macri, L. M., Mader, J. A., Mahdavi, A., Marengo, M., Marsden, B. G., McLeod, B. A., McNamara, B. R., Megeath, S. T., Moraru, D., Mossman, A. E., Muench, A. A., Muñoz, J. A., Muzerolle, J., Naranjo, O., Nelson-Patel, K., Pahre, M. A., Patten, B. M., Peters, J., Peters, W., Raymond, J. C., Rines, K., Schild, R. E., Sobczak, G. J., Spahr, T. B., Stauffer, J. R., Stefanik, R. P., Szentgyorgyi, A. H., Tollestrup, E. V., Väisänen, P., Vikhlinin, A., Wang, Z., Willner, S. P., Wolk, S. J., Zajac, J. M., Zhao, P., & Stanek, K. Z. 2006, *AJ*, 131, 527

Jha, S., Riess, A. G., & Kirshner, R. P. 2007, *ApJ*, 659, 122

Johnson, B. D., & Crotts, A. P. S. 2006, *AJ*, 132, 756

Kaiser, N., Aussel, H., Burke, B. E., Boesgaard, H., Chambers, K., Chun, M. R., Heasley, J. N., Hodapp, K.-W., Hunt, B., Jedicke, R., Jewitt, D., Kudritzki, R., Luppino, G. A., Maberry, M., Magnier, E., Monet, D. G., Onaka, P. M., Pickles, A. J., Rhoads, P. H. H., Simon, T., Szalay, A., Szapudi, I., Tholen, D. J., Tonry, J. L., Waterson, M., & Wick, J. 2002, in *Society of Photo-Optical Instrumentation Engineers (SPIE) Conference Series*, Vol. 4836, *Society of Photo-Optical Instrumentation Engineers (SPIE) Conference Series*, ed. J. A. Tyson & S. Wolff, 154–164

Kauffmann, G., Heckman, T. M., White, S. D. M., Charlot, S., Tremonti, C., Brinchmann, J., Bruzual, G., Peng, E. W., Seibert, M., Bernardi, M., Blanton, M., Brinkmann, J., Castander, F., Csábai, I., Fukugita, M., Ivezić, Z., Munn, J. A., Nichol, R. C., Padmanabhan, N., Thakar, A. R., Weinberg, D. H., & York, D. 2003, *MNRAS*, 341, 33

Kennicutt, Jr., R. C. 1992, *ApJS*, 79, 255

—. 1998, *ARA&A*, 36, 189

- Kessler, R., Frieman, J., Bassett, B., Becker, A., Choi, C., Cinabro, D., DeJongh, F., Depoy, D. L., Dilday, B., Doi, M., Garnavich, P. M., Hogan, C. J., Holtzman, J., Im, M., Jha, S., Kessler, R., Konishi, K., Lampeitl, H., Marriner, J., Marshall, J. L., McGinnis, D., Miknaitis, G., Nichol, R. C., Prieto, J. L., Riess, A. G., Richmond, M. W., Romani, R., Sako, M., Schneider, D. P., Smith, M., Takanashi, N., Tokita, K., van der Heyden, K., Yasuda, N., Zheng, C., Adelman-McCarthy, J., Annis, J., Assef, R. J., Barentine, J., Bender, R., Blandford, R. D., Boroski, W. N., Bremer, M., Brewington, H., Collins, C. A., Crotts, A., Dembicky, J., Eastman, J., Edge, A., Edmondson, E., Elson, E., Eyler, M. E., Filippenko, A. V., Foley, R. J., Frank, S., Goobar, A., Gueth, T., Gunn, J. E., Harvanek, M., Hopp, U., Ihara, Y., Ivezić, Ž., Kahn, S., Kaplan, J., Kent, S., Ketzeback, W., Kleinman, S. J., Kollatschny, W., Kron, R. G., Krzesiński, J., Lamenti, D., Leloudas, G., Lin, H., Long, D. C., Lucey, J., Lupton, R. H., Malanushenko, E., Malanushenko, V., McMillan, R. J., Mendez, J., Morgan, C. W., Morokuma, T., Nitta, A., Ostman, L., Pan, K., Rockosi, C. M., Romer, A. K., Ruiz-Lapuente, P., Saurage, G., Schlesinger, K., Snedden, S. A., Sollerman, J., Stoughton, C., Stritzinger, M., Subba Rao, M., Tucker, D., Vaisanen, P., Watson, L. C., Watters, S., Wheeler, J. C., Yanny, B., & York, D. 2009, inprep
- King, I. R. 1980, *ApJ*, 241, 474
- Kirkman, D., Tytler, D., Suzuki, N., O'Meara, J. M., & Lubin, D. 2003, *ApJS*, 149, 1
- Knop, R. A., Aldering, G., Amanullah, R., Astier, P., Blanc, G., Burns, M. S., Conley, A., Deustua, S. E., Doi, M., Ellis, R., Fabbro, S., Folatelli, G., Fruchter, A. S., Garavini, G., Garmond, S., Garton, K., Gibbons, R., Goldhaber, G., Goobar, A., Groom, D. E., Hardin, D., Hook, I., Howell, D. A., Kim, A. G., Lee, B. C., Lidman, C., Mendez, J., Nobili, S., Nugent, P. E., Pain, R., Panagia, N., Pennypacker, C. R., Perlmutter, S., Quimby, R., Raux, J., Regnault, N., Ruiz-Lapuente, P., Sainton, G., Schaefer, B., Schahmaneche, K., Smith, E., Spadafora, A. L., Stanishev, V., Sullivan, M., Walton, N. A., Wang, L., Wood-Vasey, W. M., & Yasuda, N. 2003, *ApJ*, 598, 102
- Komatsu, E., Dunkley, J., Nolta, M. R., Bennett, C. L., Gold, B., Hinshaw, G., Jarosik, N., Larson, D., Limon, M., Page, L., Spergel, D. N., Halpern, M., Hill, R. S., Kogut, A., Meyer, S. S., Tucker, G. S., Weiland, J. L., Wollack, E., & Wright, E. L. 2009, *ApJS*, 180, 330
- Kowalski, M., Rubin, D., Aldering, G., Agostinho, R. J., Amadon, A., Amanullah, R., Balland, C., Barbary, K., Blanc, G., Challis, P. J., Conley, A., Connolly, N. V., Covarrubias, R., Dawson, K. S., Deustua, S. E., Ellis, R., Fabbro, S., Fadeyev, V., Fan, X.,

- Farris, B., Folatelli, G., Frye, B. L., Garavini, G., Gates, E. L., Germany, L., Goldhaber, G., Goldman, B., Goobar, A., Groom, D. E., Haissinski, J., Hardin, D., Hook, I., Kent, S., Kim, A. G., Knop, R. A., Lidman, C., Linder, E. V., Mendez, J., Meyers, J., Miller, G. J., Moniez, M., Mourao, A. M., Newberg, H., Nobili, S., Nugent, P. E., Pain, R., Perdureau, O., Perlmutter, S., Phillips, M. M., Prasad, V., Quimby, R., Regnault, N., Rich, J., Rubenstein, E. P., Ruiz-Lapuente, P., Santos, F. D., Schaefer, B. E., Schommer, R. A., Smith, R. C., Soderberg, A. M., Spadafora, A. L., Strolger, L. ., Strovink, M., Suntzeff, N. B., Suzuki, N., Thomas, R. C., Walton, N. A., Wang, L., Wood-Vasey, W. M., & Yun, J. L. 2008, ArXiv e-prints
- Krisciunas, K., Suntzeff, N. B., Phillips, M. M., Candia, P., Prieto, J. L., Antezana, R., Chassagne, R., Chen, H.-W., Dickinson, M., Eisenhardt, P. R., Espinoza, J., Garnavich, P. M., González, D., Harrison, T. E., Hamuy, M., Ivanov, V. D., Krzemiński, W., Kulesa, C., McCarthy, P., Moro-Martín, A., Muena, C., Noriega-Crespo, A., Persson, S. E., Pinto, P. A., Roth, M., Rubenstein, E. P., Stanford, S. A., Stringfellow, G. S., Zapata, A., Porter, A., & Wischnjewsky, M. 2004, *AJ*, 128, 3034
- Kroupa, P. 2001, *MNRAS*, 322, 231
- Kuznetsova, N. V., & Connolly, B. M. 2007, *ApJ*, 659, 530
- Lampeitl, H., Bassett, B., Becker, A., Choi, C., Cinabro, D., DeJongh, F., Depoy, D. L., Dilday, B., Doi, M., Garnavich, P. M., Hogan, C. J., Holtzman, J., Im, M., Jha, S., Kessler, R., Konishi, K., Lampeitl, H., Marriner, J., Marshall, J. L., McGinnis, D., Miknaitis, G., Nichol, R. C., Prieto, J. L., Riess, A. G., Richmond, M. W., Romani, R., Sako, M., Schneider, D. P., Smith, M., Takanashi, N., Tokita, K., van der Heyden, K., Yasuda, N., Zheng, C., Adelman-McCarthy, J., Annis, J., Assef, R. J., Barentine, J., Bender, R., Blandford, R. D., Boroski, W. N., Bremer, M., Brewington, H., Collins, C. A., Crotts, A., Dembicky, J., Eastman, J., Edge, A., Edmondson, E., Elson, E., Eyler, M. E., Filippenko, A. V., Foley, R. J., Frank, S., Goobar, A., Gueth, T., Gunn, J. E., Harvanek, M., Hopp, U., Ihara, Y., Ivezić, Ž., Kahn, S., Kaplan, J., Kent, S., Ketzeback, W., Kleinman, S. J., Kollatschny, W., Kron, R. G., Krzesiński, J., Lamenti, D., Leloudas, G., Lin, H., Long, D. C., Lucey, J., Lupton, R. H., Malanushenko, E., Malanushenko, V., McMillan, R. J., Mendez, J., Morgan, C. W., Morokuma, T., Nitta, A., Ostman, L., Pan, K., Rockosi, C. M., Romer, A. K., Ruiz-Lapuente, P., Saurage, G., Schlesinger, K., Snedden, S. A., Sollerman, J., Stoughton, C., Stritzinger, M., Subba Rao, M., Tucker, D., Vaisanen, P., Watson, L. C., Watters, S., Wheeler, J. C., Yanny, B., & York, D. 2009, In preparation

- Lawrence, A., Warren, S. J., Almaini, O., Edge, A. C., Hambly, N. C., Jameson, R. F., Lucas, P., Casali, M., Adamson, A., Dye, S., Emerson, J. P., Foucaud, S., Hewett, P., Hirst, P., Hodgkin, S. T., Irwin, M. J., Lodieu, N., McMahon, R. G., Simpson, C., Smail, I., Mortlock, D., & Folger, M. 2007, *MNRAS*, 379, 1599
- Le Borgne, D., & Rocca-Volmerange, B. 2002, *A&A*, 386, 446
- Le Borgne, D., Rocca-Volmerange, B., Prugniel, P., Lançon, A., Fioc, M., & Soubiran, C. 2004, *A&A*, 425, 881
- Leibundgut, B., Kirshner, R. P., Phillips, M. M., Wells, L. A., Suntzeff, N. B., Hamuy, M., Schommer, R. A., Walker, A. R., Gonzalez, L., Ugarte, P., Williams, R. E., Williger, G., Gomez, M., Marzke, R., Schmidt, B. P., Whitney, B., Coldwell, N., Peters, J., Chaffee, F. H., Foltz, C. B., Rehner, D., Siciliano, L., Barnes, T. G., Cheng, K.-P., Hintzen, P. M. N., Kim, Y.-C., Maza, J., Parker, J. W., Porter, A. C., Schmidtke, P. C., & Sonneborn, G. 1993, *AJ*, 105, 301
- Li, W., Filippenko, A. V., Chornock, R., Berger, E., Berlind, P., Calkins, M. L., Challis, P., Fassnacht, C., Jha, S., Kirshner, R. P., Matheson, T., Sargent, W. L. W., Simcoe, R. A., Smith, G. H., & Squires, G. 2003a, *PASP*, 115, 453
- Li, W., Filippenko, A. V., Chornock, R., & Jha, S. 2003b, in *Bulletin of the American Astronomical Society*, Vol. 35, *Bulletin of the American Astronomical Society*, 752–+
- Li, W., Filippenko, A. V., Gates, E., Chornock, R., Gal-Yam, A., Ofek, E. O., Leonard, D. C., Modjaz, M., Rich, R. M., Riess, A. G., & Treffers, R. R. 2001a, *PASP*, 113, 1178
- Li, W., Filippenko, A. V., Treffers, R. R., Riess, A. G., Hu, J., & Qiu, Y. 2001b, *ApJ*, 546, 734
- Lupton, R., Gunn, J. E., Ivezić, Z., Knapp, G. R., & Kent, S. 2001, in *Astronomical Society of the Pacific Conference Series*, Vol. 238, *Astronomical Data Analysis Software and Systems X*, ed. F. R. Harnden, Jr., F. A. Primini, & H. E. Payne, 269–+
- Madau, P., della Valle, M., & Panagia, N. 1998, *MNRAS*, 297, L17+
- Madgwick, D. S., Hewett, P. C., Mortlock, D. J., & Wang, L. 2003, *ApJ*, 599, L33
- Mannucci, F., Della Valle, M., & Panagia, N. 2006, *MNRAS*, 370, 773
- Mannucci, F., Della Valle, M., Panagia, N., Cappellaro, E., Cresci, G., Maiolino, R., Petrosian, A., & Turatto, M. 2005a, *A&A*, 433, 807

—. 2005b, *A&A*, 433, 807

Mannucci, F., Maoz, D., Sharon, K., Botticella, M. T., Della Valle, M., Gal-Yam, A., & Panagia, N. 2008, *MNRAS*, 383, 1121

Maoz, D., & Gal-Yam, A. 2003, *ArXiv Astrophysics e-prints*

Maraston, C. 2005, *MNRAS*, 362, 799

Maraston, C., Daddi, E., Renzini, A., Cimatti, A., Dickinson, M., Papovich, C., Pasquali, A., & Pirzkal, N. 2006, *ApJ*, 652, 85

Matheson, T., Blondin, S., Foley, R. J., Chornock, R., Filippenko, A. V., Leibundgut, B., Smith, R. C., Sollerman, J., Spyromilio, J., Kirshner, R. P., Clocchiatti, A., Aguilera, C., Barris, B., Becker, A. C., Challis, P., Covarrubias, R., Garnavich, P., Hicken, M., Jha, S., Krisciunas, K., Li, W., Miceli, A., Miknaitis, G., Prieto, J. L., Rest, A., Riess, A. G., Salvo, M. E., Schmidt, B. P., Stubbs, C. W., Suntzeff, N. B., & Tonry, J. L. 2005, *AJ*, 129, 2352

Matheson, T., Kirshner, R. P., Challis, P., Jha, S., Garnavich, P. M., Berlind, P., Calkins, M. L., Blondin, S., Balog, Z., Bragg, A. E., Caldwell, N., Dendy Concannon, K., Falco, E. E., Graves, G. J. M., Huchra, J. P., Kuraszkiewicz, J., Mader, J. A., Mahdavi, A., Phelps, M., Rines, K., Song, I., & Wilkes, B. J. 2008, *AJ*, 135, 1598

Mazzali, P. A., & Lucy, L. B. 1993, *A&A*, 279, 447

Miknaitis, G., Pignata, G., Rest, A., Wood-Vasey, W. M., Blondin, S., Challis, P., Smith, R. C., Stubbs, C. W., Suntzeff, N. B., Foley, R. J., Matheson, T., Tonry, J. L., Aguilera, C., Blackman, J. W., Becker, A. C., Clocchiatti, A., Covarrubias, R., Davis, T. M., Filippenko, A. V., Garg, A., Garnavich, P. M., Hicken, M., Jha, S., Krisciunas, K., Kirshner, R. P., Leibundgut, B., Li, W., Miceli, A., Narayan, G., Prieto, J. L., Riess, A. G., Salvo, M. E., Schmidt, B. P., Sollerman, J., Spyromilio, J., & Zenteno, A. 2007, *ApJ*, 666, 674

Milne, E. A. 1933, *Zeitschrift fur Astrophysik*, 6, 1

Minkowski, R. 1941, *PASP*, 53, 224

Misner, C. W., Thorne, K. S., & Wheeler, J. A. 1973, *Gravitation* (San Francisco: W.H. Freeman and Co., 1973)

Neill, J. D., Hudson, M. J., & Conley, A. 2007, *ApJ*, 661, L123

- Neill, J. D., Sullivan, M., Balam, D., Pritchett, C. J., Howell, D. A., Perrett, K., Astier, P., Aubourg, E., Basa, S., Carlberg, R. G., Conley, A., Fabbro, S., Fouchez, D., Guy, J., Hook, I., Pain, R., Palanque-Delabrouille, N., Regnault, N., Rich, J., Taillet, R., Aldering, G., Antilogus, P., Arsenijevic, V., Balland, C., Baumont, S., Bronder, J., Ellis, R. S., Filiol, M., Gonçalves, A. C., Hardin, D., Kowalski, M., Lidman, C., Lusset, V., Mouchet, M., Mourao, A., Perlmutter, S., Ripoche, P., Schlegel, D., & Tao, C. 2006, *AJ*, 132, 1126
- Nobili, S., & Goobar, A. 2008, *A&A*, 487, 19
- Nomoto, K., Iwamoto, K., & Kishimoto, N. 1997, *Science*, 276, 1378
- Nugent, P., Baron, E., Hauschildt, P. H., & Branch, D. 1995a, *ApJ*, 441, L33
- Nugent, P., Kim, A., & Perlmutter, S. 2002, *PASP*, 114, 803
- Nugent, P., Phillips, M., Baron, E., Branch, D., & Hauschildt, P. 1995b, *ApJ*, 455, L147+
- Oemler, Jr., A., & Tinsley, B. M. 1979, *AJ*, 84, 985
- Oke, J. B. 1974, *ApJS*, 27, 21
- Oyaizu, H., Lima, M., Cunha, C. E., Lin, H., & Frieman, J. 2007, *ArXiv e-prints*
- Oyaizu, H., Lima, M., Cunha, C. E., Lin, H., Frieman, J., & Sheldon, E. S. 2008, *ApJ*, 674, 768
- Pain, R., Fabbro, S., Sullivan, M., Ellis, R. S., Aldering, G., Astier, P., Deustua, S. E., Fruchter, A. S., Goldhaber, G., Goobar, A., Groom, D. E., Hardin, D., Hook, I. M., Howell, D. A., Irwin, M. J., Kim, A. G., Kim, M. Y., Knop, R. A., Lee, J. C., Lidman, C., McMahon, R. G., Nugent, P. E., Panagia, N., Pennypacker, C. R., Perlmutter, S., Ruiz-Lapuente, P., Schahmanche, K., Schaefer, B., & Walton, N. A. 2002, *ApJ*, 577, 120
- Peebles, P. J. E. 1993, *Principles of physical cosmology* (Princeton Series in Physics, Princeton, NJ: Princeton University Press, —c1993)
- Percival, W. J., Cole, S., Eisenstein, D. J., Nichol, R. C., Peacock, J. A., Pope, A. C., & Szalay, A. S. 2007, *MNRAS*, 381, 1053
- Perlmutter, S., Aldering, G., Goldhaber, G., Knop, R. A., Nugent, P., Castro, P. G., Deustua, S., Fabbro, S., Goobar, A., Groom, D. E., Hook, I. M., Kim, A. G., Kim, M. Y., Lee, J. C., Nunes, N. J., Pain, R., Pennypacker, C. R., Quimby, R., Lidman, C., Ellis, R. S., Irwin, M., McMahon, R. G., Ruiz-Lapuente, P., Walton, N., Schaefer, B.,

- Boyle, B. J., Filippenko, A. V., Matheson, T., Fruchter, A. S., Panagia, N., Newberg, H. J. M., Couch, W. J., & The Supernova Cosmology Project. 1999, *ApJ*, 517, 565
- Perlmutter, S., Gabi, S., Goldhaber, G., Goobar, A., Groom, D. E., Hook, I. M., Kim, A. G., Kim, M. Y., Lee, J. C., Pain, R., Pennypacker, C. R., Small, I. A., Ellis, R. S., McMahon, R. G., Boyle, B. J., Bunclark, P. S., Carter, D., Irwin, M. J., Glazebrook, K., Newberg, H. J. M., Filippenko, A. V., Matheson, T., Dopita, M., Couch, W. J., & The Supernova Cosmology Project. 1997, *ApJ*, 483, 565
- Pettitt, A. N. 1976, *Biometrika*, 63, 161
- Phillips, M. M. 1993, *ApJ*, 413, L105
- Phillips, M. M., Li, W., Frieman, J. A., Blinnikov, S. I., DePoy, D., Prieto, J. L., Milne, P., Contreras, C., Folatelli, G., Morrell, N., Hamuy, M., Suntzeff, N. B., Roth, M., González, S., Krzeminski, W., Filippenko, A. V., Freedman, W. L., Chornock, R., Jha, S., Madore, B. F., Persson, S. E., Burns, C. R., Wyatt, P., Murphy, D., Foley, R. J., Ganeshalingam, M., Serduke, F. J. D., Krisciunas, K., Bassett, B., Becker, A., Dilday, B., Eastman, J., Garnavich, P. M., Holtzman, J., Kessler, R., Lampeitl, H., Marriner, J., Frank, S., Marshall, J. L., Miknaitis, G., Sako, M., Schneider, D. P., van der Heyden, K., & Yasuda, N. 2007, *PASP*, 119, 360
- Phillips, M. M., Lira, P., Suntzeff, N. B., Schommer, R. A., Hamuy, M., & Maza, J. 1999, *AJ*, 118, 1766
- Phillips, M. M., Wells, L. A., Suntzeff, N. B., Hamuy, M., Leibundgut, B., Kirshner, R. P., & Foltz, C. B. 1992, *AJ*, 103, 1632
- Pier, J. R., Munn, J. A., Hindsley, R. B., Hennessy, G. S., Kent, S. M., Lupton, R. H., & Ivezić, Ž. 2003, *AJ*, 125, 1559
- Poggianti, B. M., Bridges, T. J., Carter, D., Mobasher, B., Doi, M., Iye, M., Kashikawa, N., Komiyama, Y., Okamura, S., Sekiguchi, M., Shimasaku, K., Yagi, M., & Yasuda, N. 2001, *ApJ*, 563, 118
- Popper, D. M. 1937, *PASP*, 49, 283
- Poznanski, D., Maoz, D., & Gal-Yam, A. 2007, *AJ*, 134, 1285
- Prieto, J. L., Garnavich, P. M., Phillips, M. M., DePoy, D. L., Parrent, J., Pooley, D., Dwarkadas, V. V., Baron, E., Bassett, B., Becker, A., Cinabro, D., DeJongh, F., Dilday, B., Doi, M., Frieman, J. A., Hogan, C. J., Holtzman, J., Jha, S., Kessler, R., Konishi, K., Lampeitl, H., Marriner, J., Marshall, J. L., Miknaitis, G., Nichol, R. C.,

- Riess, A. G., Richmond, M. W., Romani, R., Sako, M., Schneider, D. P., Smith, M., Takanashi, N., Tokita, K., van der Heyden, K., Yasuda, N., Zheng, C., Wheeler, J. C., Barentine, J., Dembicky, J., Eastman, J., Frank, S., Ketzeback, W., McMillan, R. J., Morrell, N., Folatelli, G., Contreras, C., Burns, C. R., Freedman, W. L., Gonzalez, S., Hamuy, M., Krzeminski, W., Madore, B. F., Murphy, D., Persson, S. E., Roth, M., & Suntzeff, N. B. 2007, ArXiv e-prints, 706
- Pritchett, C. J., & For The Snls Collaboration. 2005, in *Astronomical Society of the Pacific Conference Series*, Vol. 339, *Observing Dark Energy*, ed. S. C. Wolff & T. R. Lauer, 60–+
- Pskovskii, I. P. 1977, *Soviet Astronomy*, 21, 675
- Radburn-Smith, D. J., Lucey, J. R., & Hudson, M. J. 2004, *MNRAS*, 355, 1378
- Rice, W. L. 1980, PhD thesis, AA(Harvard Univ., Cambridge, MA.)
- Richardson, D., Thomas, R. C., Casebeer, D., Blankenship, Z., Ratowt, S., Baron, E., & Branch, D. 2001, in *Bulletin of the American Astronomical Society*, Vol. 33, *Bulletin of the American Astronomical Society*, 1428–+
- Riess, A. G., Filippenko, A. V., Challis, P., Clocchiatti, A., Diercks, A., Garnavich, P. M., Gilliland, R. L., Hogan, C. J., Jha, S., Kirshner, R. P., Leibundgut, B., Phillips, M. M., Reiss, D., Schmidt, B. P., Schommer, R. A., Smith, R. C., Spyromilio, J., Stubbs, C., Suntzeff, N. B., & Tonry, J. 1998, *AJ*, 116, 1009
- Riess, A. G., Kirshner, R. P., Schmidt, B. P., Jha, S., Challis, P., Garnavich, P. M., Esin, A. A., Carpenter, C., Grashius, R., Schild, R. E., Berlind, P. L., Huchra, J. P., Prosser, C. F., Falco, E. E., Benson, P. J., Briceño, C., Brown, W. R., Caldwell, N., dell'Antonio, I. P., Filippenko, A. V., Goodman, A. A., Grogin, N. A., Groner, T., Hughes, J. P., Green, P. J., Jansen, R. A., Kleyana, J. T., Luu, J. X., Macri, L. M., McLeod, B. A., McLeod, K. K., McNamara, B. R., McLean, B., Milone, A. A. E., Mohr, J. J., Moraru, D., Peng, C., Peters, J., Prestwich, A. H., Stanek, K. Z., Szentgyorgyi, A., & Zhao, P. 1999, *AJ*, 117, 707
- Riess, A. G., Press, W. H., & Kirshner, R. P. 1995, in *Bulletin of the American Astronomical Society*, Vol. 27, *Bulletin of the American Astronomical Society*, 1309–+
- Riess, A. G., Press, W. H., & Kirshner, R. P. 1996, *ApJ*, 473, 88
- Röpke, F. K., & Hillebrandt, W. 2006, in *American Institute of Physics Conference Series*, Vol. 847, *Origin of Matter and Evolution of Galaxies*, ed. S. Kubono, W. Aoki, T. Kajino, T. Motobayashi, & K. Nomoto, 190–195

- Rubin, V. C., Ford, W. K. J., & Thonnard, N. 1980, *ApJ*, 238, 471
- Sako, M., Bassett, B., Becker, A., Cinabro, D., DeJongh, F., Depoy, D. L., Dilday, B., Doi, M., Frieman, J. A., Garnavich, P. M., Hogan, C. J., Holtzman, J., Jha, S., Kessler, R., Konishi, K., Lampeitl, H., Marriner, J., Miknaitis, G., Nichol, R. C., Prieto, J. L., Riess, A. G., Richmond, M. W., Romani, R., Schneider, D. P., Smith, M., Subba Rao, M., Takanashi, N., Tokita, K., van der Heyden, K., Yasuda, N., Zheng, C., Barentine, J., Brewington, H., Choi, C., Dembicky, J., Harnavek, M., Ihara, Y., Im, M., Ketzbeck, W., Kleinman, S. J., Krzesiński, J., Long, D. C., Malanushenko, E., Malanushenko, V., McMillan, R. J., Morokuma, T., Nitta, A., Pan, K., Saurage, G., & Snedden, S. A. 2008, *AJ*, 135, 348
- Salim, S., Charlot, S., Rich, R. M., Kauffmann, G., Heckman, T. M., Barlow, T. A., Bianchi, L., Byun, Y.-I., Donas, J., Forster, K., Friedman, P. G., Jelinsky, P. N., Lee, Y.-W., Madore, B. F., Malina, R. F., Martin, D. C., Milliard, B., Morrissey, P., Neff, S. G., Schiminovich, D., Seibert, M., Siegmund, O. H. W., Small, T., Szalay, A. S., Welsh, B. Y., & Wyder, T. K. 2005, *ApJ*, 619, L39
- Salimbeni, S., Giallongo, E., & Grazian, A. 2007, in *Astronomical Society of the Pacific Conference Series*, Vol. 380, *Deepest Astronomical Surveys*, ed. J. Afonso, H. C. Ferguson, B. Mobasher, & R. Norris, 551–+
- Salpeter, E. E. 1955, *ApJ*, 121, 161
- Savage, B. D., & Mathis, J. S. 1979, *ARA&A*, 17, 73
- Scalo, J. M. 1986, *Fundamentals of Cosmic Physics*, 11, 1
- Scannapieco, E., & Bildsten, L. 2005, *ApJ*, 629, L85
- Schechter, P. 1976, *ApJ*, 203, 297
- Schechter, P. L., Mateo, M., & Saha, A. 1993, *PASP*, 105, 1342
- Schmidt, M. 1968, *ApJ*, 151, 393
- Scholz, F. W., & Stephens, M. A. 1987, *Journal of the American Statistical Association*, 82, 918
- Seaton, M. J. 1979, *MNRAS*, 187, 73P
- Smith, J. A., Tucker, D. L., Kent, S., Richmond, M. W., Fukugita, M., Ichikawa, T., Ichikawa, S.-i., Jorgensen, A. M., Uomoto, A., Gunn, J. E., Hamabe, M., Watanabe, M., Tolea, A., Henden, A., Annis, J., Pier, J. R., McKay, T. A., Brinkmann, J., Chen, B., Holtzman, J., Shimasaku, K., & York, D. G. 2002a, *AJ*, 123, 2121

- Smith, R. C., Aguilera, C., Krisciunas, K., Suntzeff, N. B., Becker, A., Covarrubias, R., Miceli, A., Miknaitis, G., Rest, A., Stubbs, C., Garnavich, P. M., Holland, S. T., Schmidt, B. P., Filippenko, A. V., Jha, S., Li, W., Challis, P., Kirshner, R. P., Matheson, T., Barris, B., Tonry, J. L., Riess, A. G., Leibundgut, B., Sollerman, J., Spyromilio, J., Clocchiatti, A., & Pompea, S. 2002b, in *Bulletin of the American Astronomical Society*, Vol. 34, *Bulletin of the American Astronomical Society*, 1232–+
- Smoot, G. F., Bennett, C. L., Kogut, A., Aymon, J., Backus, C., de Amici, G., Galuk, K., Jackson, P. D., Keegstra, P., Rokke, L., Tenorio, L., Torres, S., Gulkis, S., Hauser, M. G., Janssen, M. A., Mather, J. C., Weiss, R., Wilkinson, D. T., Wright, E. L., Boggess, N. W., Cheng, E. S., Kelsall, T., Lubin, P., Meyer, S., Moseley, S. H., Murdock, T. L., Shafer, R. A., & Silverberg, R. F. 1991, *ApJ*, 371, L1
- Spergel, D. N., Bean, R., Doré, O., Nolta, M. R., Bennett, C. L., Dunkley, J., Hinshaw, G., Jarosik, N., Komatsu, E., Page, L., Peiris, H. V., Verde, L., Halpern, M., Hill, R. S., Kogut, A., Limon, M., Meyer, S. S., Odegard, N., Tucker, G. S., Weiland, J. L., Wollack, E., & Wright, E. L. 2007, *ApJS*, 170, 377
- Stanford, S. A., Eisenhardt, P. R., & Dickinson, M. 1998, *ApJ*, 492, 461
- Stanishev, V. 2007, *Astronomische Nachrichten*, 328, 948
- Stephens, M. A. 1974, *Journal of the American Statistical Association*, 69, 730
- Stoughton, C., Lupton, R. H., Bernardi, M., Blanton, M. R., Burles, S., Castander, F. J., Connolly, A. J., Eisenstein, D. J., Frieman, J. A., Hennessy, G. S., Hindsley, R. B., Ivezić, Ž., Kent, S., Kunszt, P. Z., Lee, B. C., Meiksin, A., Munn, J. A., Newberg, H. J., Nichol, R. C., Nicinski, T., Pier, J. R., Richards, G. T., Richmond, M. W., Schlegel, D. J., Smith, J. A., Strauss, M. A., SubbaRao, M., Szalay, A. S., Thakar, A. R., Tucker, D. L., Vanden Berk, D. E., Yanny, B., Adelman, J. K., Anderson, Jr., J. E., Anderson, S. F., Annis, J., Bahcall, N. A., Bakken, J. A., Bartelmann, M., Bastian, S., Bauer, A., Berman, E., Böhringer, H., Boroski, W. N., Bracker, S., Briegel, C., Briggs, J. W., Brinkmann, J., Brunner, R., Carey, L., Carr, M. A., Chen, B., Christian, D., Colestock, P. L., Crocker, J. H., Csabai, I., Czarapata, P. C., Dalcanton, J., Davidsen, A. F., Davis, J. E., Dehnen, W., Dodelson, S., Doi, M., Dombeck, T., Donahue, M., Ellman, N., Elms, B. R., Evans, M. L., Eyer, L., Fan, X., Federwitz, G. R., Friedman, S., Fukugita, M., Gal, R., Gillespie, B., Glazebrook, K., Gray, J., Grebel, E. K., Greenawalt, B., Greene, G., Gunn, J. E., de Haas, E., Haiman, Z., Haldeman, M., Hall, P. B., Hamabe, M., Hansen, B., Harris, F. H., Harris, H., Harvanek, M., Hawley, S. L., Hayes, J. J. E., Heckman, T. M., Helmi, A., Henden, A., Hogan, C. J.,

- Hogg, D. W., Holmgren, D. J., Holtzman, J., Huang, C.-H., Hull, C., Ichikawa, S.-I., Ichikawa, T., Johnston, D. E., Kauffmann, G., Kim, R. S. J., Kimball, T., Kinney, E., Klaene, M., Kleinman, S. J., Klypin, A., Knapp, G. R., Korienek, J., Krolik, J., Kron, R. G., Krzesiński, J., Lamb, D. Q., Leger, R. F., Limmongkol, S., Lindenmeyer, C., Long, D. C., Loomis, C., Loveday, J., MacKinnon, B., Mannery, E. J., Mantsch, P. M., Margon, B., McGehee, P., McKay, T. A., McLean, B., Menou, K., Merelli, A., Mo, H. J., Monet, D. G., Nakamura, O., Narayanan, V. K., Nash, T., Neilsen, Jr., E. H., Newman, P. R., Nitta, A., Odenkirchen, M., Okada, N., Okamura, S., Ostriker, J. P., Owen, R., Pauls, A. G., Peoples, J., Peterson, R. S., Petravick, D., Pope, A., Pordes, R., Postman, M., Prosapio, A., Quinn, T. R., Rechenmacher, R., Rivetta, C. H., Rix, H.-W., Rockosi, C. M., Rosner, R., Ruthmanskorfer, K., Sandford, D., Schneider, D. P., Scranton, R., Sekiguchi, M., Sergey, G., Sheth, R., Shimasaku, K., Smee, S., Snedden, S. A., Stebbins, A., Stubbs, C., Szapudi, I., Szkody, P., Szokoly, G. P., Tabachnik, S., Tsvetanov, Z., Uomoto, A., Vogeley, M. S., Voges, W., Waddell, P., Walterbos, R., Wang, S.-i., Watanabe, M., Weinberg, D. H., White, R. L., White, S. D. M., Wilhite, B., Wolfe, D., Yasuda, N., York, D. G., Zehavi, I., & Zheng, W. 2002, *AJ*, 123, 485
- Strauss, M. A., Weinberg, D. H., Lupton, R. H., Narayanan, V. K., Annis, J., Bernardi, M., Blanton, M., Burles, S., Connolly, A. J., Dalcanton, J., Doi, M., Eisenstein, D., Frieman, J. A., Fukugita, M., Gunn, J. E., Ivezić, Ž., Kent, S., Kim, R. S. J., Knapp, G. R., Kron, R. G., Munn, J. A., Newberg, H. J., Nichol, R. C., Okamura, S., Quinn, T. R., Richmond, M. W., Schlegel, D. J., Shimasaku, K., SubbaRao, M., Szalay, A. S., Vanden Berk, D., Vogeley, M. S., Yanny, B., Yasuda, N., York, D. G., & Zehavi, I. 2002, *AJ*, 124, 1810
- Strolger, L.-G., Riess, A. G., Dahlen, T., Livio, M., Panagia, N., Challis, P., Tonry, J. L., Filippenko, A. V., Chornock, R., Ferguson, H., Koekemoer, A., Mobasher, B., Dickinson, M., Giavalisco, M., Casertano, S., Hook, R., Blondin, S., Leibundgut, B., Nonino, M., Rosati, P., Spinrad, H., Steidel, C. C., Stern, D., Garnavich, P. M., Matheson, T., Grogin, N., Hornschemeier, A., Kretchmer, C., Laidler, V. G., Lee, K., Lucas, R., de Mello, D., Moustakas, L. A., Ravindranath, S., Richardson, M., & Taylor, E. 2004, *ApJ*, 613, 200
- Sullivan, M., Ellis, R. S., Aldering, G., Amanullah, R., Astier, P., Blanc, G., Burns, M. S., Conley, A., Deustua, S. E., Doi, M., Fabbro, S., Folatelli, G., Fruchter, A. S., Garavini, G., Gibbons, R., Goldhaber, G., Goobar, A., Groom, D. E., Hardin, D., Hook, I., Howell, D. A., Irwin, M., Kim, A. G., Knop, R. A., Lidman, C., McMahon, R., Mendez, J., Nobili, S., Nugent, P. E., Pain, R., Panagia, N., Pennypacker, C. R., Perlmutter, S., Quimby, R., Raux, J., Regnault, N., Ruiz-Lapuente, P., Schaefer, B.,

- Schahmaneche, K., Spadafora, A. L., Walton, N. A., Wang, L., Wood-Vasey, W. M., & Yasuda, N. 2003, *MNRAS*, 340, 1057
- Sullivan, M., Howell, D. A., Perrett, K., Nugent, P. E., Astier, P., Aubourg, E., Balam, D., Basa, S., Carlberg, R. G., Conley, A., Fabbro, S., Fouchez, D., Guy, J., Hook, I., Lafoux, H., Neill, J. D., Pain, R., Palanque-Delabrouille, N., Pritchett, C. J., Regnault, N., Rich, J., Taillet, R., Aldering, G., Baumont, S., Bronder, J., Filiol, M., Knop, R. A., Perlmutter, S., & Tao, C. 2006a, *AJ*, 131, 960
- Sullivan, M., Le Borgne, D., Pritchett, C. J., Hodsman, A., Neill, J. D., Howell, D. A., Carlberg, R. G., Astier, P., Aubourg, E., Balam, D., Basa, S., Conley, A., Fabbro, S., Fouchez, D., Guy, J., Hook, I., Pain, R., Palanque-Delabrouille, N., Perrett, K., Regnault, N., Rich, J., Taillet, R., Baumont, S., Bronder, J., Ellis, R. S., Filiol, M., Lusser, V., Perlmutter, S., Ripoche, P., & Tao, C. 2006b, *ApJ*, 648, 868
- Taylor, E. N., Franx, M., van Dokkum, P. G., Bell, E. F., Brammer, G. B., Rudnick, G., Wuyts, S., Gawiser, E., Lira, P., Urry, C., & Rix, H.-W. 2008, *ArXiv e-prints*
- The Dark Energy Survey Collaboration. 2005, *ArXiv Astrophysics e-prints*
- Thomas, D., Maraston, C., Bender, R., & Mendes de Oliveira, C. 2005, *ApJ*, 621, 673
- Tody, D. 1986, in *Society of Photo-Optical Instrumentation Engineers (SPIE) Conference Series*, Vol. 627, *Society of Photo-Optical Instrumentation Engineers (SPIE) Conference Series*, ed. D. L. Crawford, 733–+
- Tody, D. 1993, in *Astronomical Society of the Pacific Conference Series*, Vol. 52, *Astronomical Data Analysis Software and Systems II*, ed. R. J. Hanisch, R. J. V. Brissenden, & J. Barnes, 173–+
- Tonry, J., & Davis, M. 1979, *AJ*, 84, 1511
- Tonry, J. L., Schmidt, B. P., Barris, B., Candia, P., Challis, P., Clocchiatti, A., Coil, A. L., Filippenko, A. V., Garnavich, P., Hogan, C., Holland, S. T., Jha, S., Kirshner, R. P., Krisciunas, K., Leibundgut, B., Li, W., Matheson, T., Phillips, M. M., Riess, A. G., Schommer, R., Smith, R. C., Sollerman, J., Spyromilio, J., Stubbs, C. W., & Suntzeff, N. B. 2003, *ApJ*, 594, 1
- Tyson, J. A. 2002, in *Society of Photo-Optical Instrumentation Engineers (SPIE) Conference Series*, Vol. 4836, *Society of Photo-Optical Instrumentation Engineers (SPIE) Conference Series*, ed. J. A. Tyson & S. Wolff, 10–20

- Valdes, F. 1986, in Society of Photo-Optical Instrumentation Engineers (SPIE) Conference Series, Vol. 627, Society of Photo-Optical Instrumentation Engineers (SPIE) Conference Series, ed. D. L. Crawford, 749–756
- Valdes, F. 1992, in Astronomical Society of the Pacific Conference Series, Vol. 25, Astronomical Data Analysis Software and Systems I, ed. D. M. Worrall, C. Biemesderfer, & J. Barnes, 417–+
- van den Bergh, S., Li, W., & Filippenko, A. V. 2005, *PASP*, 117, 773
- van Dokkum, P. G. 2001, *PASP*, 113, 1420
- Wang, L. 2005, *ApJ*, 635, L33
- Wang, L., Goldhaber, G., Aldering, G., & Perlmutter, S. 2002, in Bulletin of the American Astronomical Society, Vol. 34, Bulletin of the American Astronomical Society, 1305–+
- Wang, L., Hoeflich, P., & Wheeler, J. C. 1997, *ApJ*, 483, L29+
- Wang, Y. 2007, *ApJ*, 654, L123
- Wang, Y., Narayan, G., & Wood-Vasey, M. 2007, *MNRAS*, 382, 377
- Wells, L. A., Phillips, M. M., Suntzeff, B., Heathcote, S. R., Hamuy, M., Navarrete, M., Fernandez, M., Weller, W. G., Schommer, R. A., Kirshner, R. P., Leibundgut, B., Willner, S. P., Peletier, R. P., Schlegel, E. M., Wheeler, J. C., Harkness, R. P., Bell, D. J., Matthews, J. M., Filippenko, A. V., Shields, J. C., Richmond, M. W., Jewitt, D., Luu, J., Tran, H. D., Appleton, P. N., Robson, E. I., Tyson, J. A., Guhathakurta, P., Eder, J. A., Bond, H. E., Potter, M., Veilleux, S., Porter, A. C., Humphreys, R. M., Janes, K. A., Williams, T. B., Costa, E., Ruiz, M. T., Lee, J. T., Lutz, J. H., Rich, R. M., Winkler, P. F., & Tyson, N. D. 1994, *AJ*, 108, 2233
- Wheeler, J. C., & Harkness, R. P. 1986, in NATO ASIC Proc. 180: Galaxy Distances and Deviations from Universal Expansion, ed. B. F. Madore & R. B. Tully, 45–54
- Wood-Vasey, W. M., Miknaitis, G., Stubbs, C. W., Jha, S., Riess, A. G., Garnavich, P. M., Kirshner, R. P., Aguilera, C., Becker, A. C., Blackman, J. W., Blondin, S., Challis, P., Clocchiatti, A., Conley, A., Covarrubias, R., Davis, T. M., Filippenko, A. V., Foley, R. J., Garg, A., Hicken, M., Krisciunas, K., Leibundgut, B., Li, W., Matheson, T., Miceli, A., Narayan, G., Pignata, G., Prieto, J. L., Rest, A., Salvo, M. E., Schmidt, B. P., Smith, R. C., Sollerman, J., Spyromilio, J., Tonry, J. L., Suntzeff, N. B., & Zenteno, A. 2007, *ApJ*, 666, 694

- Wood-Vasey, W. M., Wang, L., & Aldering, G. 2004, *ApJ*, 616, 339
- Wosley, S. E., Almgren, A., Bell, J. B., Glatzmaier, G., Kasen, D., Kerstein, A. R., Ma, H., Nugent, P., Röpke, F., Sankaran, V., & Zingale, M. 2007, *Journal of Physics Conference Series*, 78, 012081
- Worthey, G., & Ottaviani, D. L. 1997, *ApJS*, 111, 377
- Yadav, J., Bharadwaj, S., Pandey, B., & Seshadri, T. R. 2005, *MNRAS*, 364, 601
- York, D. G., Adelman, J., Anderson, Jr., J. E., Anderson, S. F., Annis, J., Bahcall, N. A., Bakken, J. A., Barkhouser, R., Bastian, S., Berman, E., Boroski, W. N., Bracker, S., Briegel, C., Briggs, J. W., Brinkmann, J., Brunner, R., Burles, S., Carey, L., Carr, M. A., Castander, F. J., Chen, B., Colestock, P. L., Connolly, A. J., Crocker, J. H., Csabai, I., Czarapata, P. C., Davis, J. E., Doi, M., Dombeck, T., Eisenstein, D., Ellman, N., Elms, B. R., Evans, M. L., Fan, X., Federwitz, G. R., Fiscelli, L., Friedman, S., Frieman, J. A., Fukugita, M., Gillespie, B., Gunn, J. E., Gurbani, V. K., de Haas, E., Haldeman, M., Harris, F. H., Hayes, J., Heckman, T. M., Hennessy, G. S., Hindsley, R. B., Holm, S., Holmgren, D. J., Huang, C.-h., Hull, C., Husby, D., Ichikawa, S.-I., Ichikawa, T., Ivezić, Ž., Kent, S., Kim, R. S. J., Kinney, E., Klaene, M., Kleinman, A. N., Kleinman, S., Knapp, G. R., Korienek, J., Kron, R. G., Kunszt, P. Z., Lamb, D. Q., Lee, B., Leger, R. F., Limmongkol, S., Lindenmeyer, C., Long, D. C., Loomis, C., Loveday, J., Lucinio, R., Lupton, R. H., MacKinnon, B., Mannery, E. J., Mantsch, P. M., Margon, B., McGehee, P., McKay, T. A., Meiksin, A., Merelli, A., Monet, D. G., Munn, J. A., Narayanan, V. K., Nash, T., Neilsen, E., Neswold, R., Newberg, H. J., Nichol, R. C., Nicinski, T., Nonino, M., Okada, N., Okamura, S., Ostriker, J. P., Owen, R., Pauls, A. G., Peoples, J., Peterson, R. L., Petravick, D., Pier, J. R., Pope, A., Pordes, R., Prosapio, A., Rechenmacher, R., Quinn, T. R., Richards, G. T., Richmond, M. W., Rivetta, C. H., Rockosi, C. M., Ruthmansdorfer, K., Sandford, D., Schlegel, D. J., Schneider, D. P., Sekiguchi, M., Sergey, G., Shimasaku, K., Siegmund, W. A., Smee, S., Smith, J. A., Snedden, S., Stone, R., Stoughton, C., Strauss, M. A., Stubbs, C., SubbaRao, M., Szalay, A. S., Szapudi, I., Szokoly, G. P., Thakar, A. R., Tremonti, C., Tucker, D. L., Uomoto, A., Vanden Berk, D., Vogeley, M. S., Waddell, P., Wang, S.-i., Watanabe, M., Weinberg, D. H., Yanny, B., & Yasuda, N. 2000, *AJ*, 120, 1579
- Zehavi, I., Riess, A. G., Kirshner, R. P., & Dekel, A. 1998, *ApJ*, 503, 483
- Zhang, Y., Gu, Q.-S., & Ho, L. C. 2008, *A&A*, 487, 177

Zheng, C., Romani, R. W., Sako, M., Marriner, J., Bassett, B., Becker, A., Choi, C., Cinabro, D., DeJongh, F., Depoy, D. L., Dilday, B., Doi, M., Frieman, J. A., Garnavich, P. M., Hogan, C. J., Holtzman, J., Im, M., Jha, S., Kessler, R., Konishi, K., Lampeitl, H., Marshall, J. L., McGinnis, D., Miknaitis, G., Nichol, R. C., Prieto, J. L., Riess, A. G., Richmond, M. W., Schneider, D. P., Smith, M., Takanashi, N., Tokita, K., van der Heyden, K., Yasuda, N., Assef, R. J., Barentine, J., Bender, R., Blandford, R. D., Bremer, M., Brewington, H., Collins, C. A., Crotts, A., Dembicky, J., Eastman, J., Edge, A., Elson, E., Eyler, M. E., Filippenko, A. V., Foley, R. J., Frank, S., Goobar, A., Harvanek, M., Hopp, U., Ihara, Y., Kahn, S., Ketzeback, W., Kleinman, S. J., Kollatschny, W., Krzesiński, J., Leloudas, G., Long, D. C., Lucey, J., Malanushenko, E., Malanushenko, V., McMillan, R. J., Morgan, C. W., Morokuma, T., Nitta, A., Ostman, L., Pan, K., Romer, A. K., Saurage, G., Schlesinger, K., Snedden, S. A., Sollerman, J., Stritzinger, M., Watson, L. C., Watters, S., Wheeler, J. C., & York, D. 2008, *AJ*, 135, 1766

Zwicky, F. 1933, *Helvetica Physica Acta*, 6, 110